Three-Dimensional In Vitro Models To Assess Pancreatic β-Cell Function

Dissertation

der Mathematisch-Naturwissenschaftlichen Fakultät

der Eberhard Karls Universität Tübingen

zur Erlangung des Grades eines

Doktors der Naturwissenschaften

(Dr. rer. nat.)

vorgelegt von

Aline Zbinden

aus Zürich, Schweiz

Tübingen

2021

Gedruckt mit Genehmigung der Mathematisch-Naturwissenschaftlichen Fakultät der Eberhard Karls Universität Tübingen.

Tag der mündlichen Qualifikation:	23.07.2021
Dekan:	Prof. Dr. Thilo Stehle
1. Berichterstatter	Prof. Dr. Katja Schenke-Layland
2. Berichterstatter	Prof. Dr. Garry P. Duffy
3. Berichterstatter	Prof. Dr. Ulrich Rothbauer
4. Berichterstatter	Prof. Dr. med. Liliana Schaefer

„Mont Blanc, wo bisch?“

Die Käsefreunde

Table of Contents

Abstract

To ensure a healthy state, the human body relies on a tight control of its blood glucose levels ensured by pancreatic islets. Depletion and dysfunction of pancreatic β-cells are key elements of the pathogenesis of Diabetes Mellitus (DM). The life expectancy of DM patients has been considerably expanded by insulin injections; a life-long treatment approach that comes with significant risks and strongly affects patient's daily routine. Envisioned as a promising alternative, the transplantation of islets has largely failed to sustain long-term normoglycemia. Hence, the development of bioengineered solutions to support islet function and survival has been a growing focus of research in the last decades. A majority of studies, however, are entirely based on animal models, hampering clinical translation due to various species-specific differences. Current in vitro alternatives lack physiological relevance and have failed to predict clinical responses. Therefore, there is an urgent need to develop in vitro models with a human genetic origin and high physiological relevance for the DM field.

In this thesis, in vitro models were developed using aggregates of pancreatic β-cells, so-called pseudo-islets, which responded to glucose stimuli by secreting insulin. A post-transplantation model was established where hypoxia-induced damage could be identified in a time-dependent manner. Using a pancreas-on-a-chip microfluidic device, vasculature-like flow was provided to the pseudo-islets. We explored the use of Raman microspectroscopy and fluorescence lifetime imaging microscopy (FLIM) to monitor pseudo-islet function. Specific Raman spectra and FLIM metabolic profiles were identified for glucose-stimulation in a non-invasive label-free manner. In addition, FLIM could determine metabolic shifts in hypoxic pseudo-islets at an early on-set while traditional methods could not. The in vitro models developed in this thesis were used to evaluate the impact of extracellular matrix (ECM) proteins collagen type 1 (COL1) and nidogen-1 (NID1), as well as endothelial cells (ECs) in an in vitro post-transplantation model. We showed the beneficial effect of COL1, NID1 and ECs on insulin secretion, ECM expression and survival of β-cells. Importantly, for the first time, the therapeutic potential of NID1 as support for β-cells was demonstrated. The integrin αvβ3 was identified as primary NID1 binding partner which activated the MAPK pathway. Altogether, this work demonstrated the great potential of physiologically relevant in vitro models for DM research.

Zusammenfassung

Für einen allgemein guten Gesundheitszustand ist der menschliche Körper auf eine zuverlässige Blutzuckerkontrolle durch die Langerhans'schen Inselzellen im Pankreas angewiesen. Erschöpfung und Dysfunktion von β-Zellen der Bauchspeicheldrüse sind Kernelemente der Pathogenese des Diabetes Mellitus (DM). Die Lebenserwartung und -qualität von DM-Patienten wurde durch subkutane Insulininjektionen deutlich verbessert. Dieser lebenslange Therapieansatz ist allerdings mit erheblichen Risiken und Einschränkungen im Tagesablauf der Patienten verbunden. Die Transplantation von Inselzellen zur Stabilisierung des Blutzuckerspiegels, als Alternative zu subkutanen Insulininjektionen, hat sich bisher nicht durchsetzen können.

Daher lag der Fokus der DM-Forschung in den letzten Jahrzehnten auf der Entwicklung von biotechnologischen Lösungen, die das Überleben sowie die Funktion von β-Zellen unterstützen sollen. Ein Großteil aktueller Studien basiert jedoch ausschließlich auf Tiermodellen, was die klinische Umsetzbarkeit der Ergebnisse aufgrund verschiedener artspezifischer Unterschiede erschwert. Den derzeitigen in vitro Modellen mangelt es sowohl an physiologischer Relevanz als auch an der Zuverlässigkeit, das Verhalten im klinischen Setup vorherzusagen. Aufgrund dessen besteht für den Bereich der DM-Forschung ein dringender Bedarf an der Entwicklung von in vitro Modellen humangenetischen Ursprungs mit hoher physiologischer Relevanz.

In dieser Arbeit wurden in vitro Modelle auf der Basis von β-Zell-Aggregaten, sogenannten Pseudo-Inseln, entwickelt, mit deren Hilfe man die Glukose-stimulierte Insulinsekretion der β-Zellen untersuchen kann. Es wurde ein Post-Transplantationsmodell etabliert, mit welchem zeitabhängig Hypoxie-induzierte Schäden identifiziert werden konnten. Mittels einem auf Mikrofluidik basierendem Pankreas-on-a-Chip-System wurde die Pseudo-Inseln mit Zellkulturmedium umspült, welches die Durchblutung im Pankreasgewebe simuliert. Weiterhin untersuchten wir die Einsatzmöglichkeit von Raman-Mikrospektroskopie sowie Fluoreszenzlebensdauer-Mikroskopie (FLIM) zur Analyse von Pseudo-Insel-Funktionen. Spezifische Raman-Spektren und FLIM-Stoffwechselprofile von β-Zellen unter Glukosestimulation wurde nicht-invasiv und ohne Zuhilfenahme von Markern identifiziert. Darüber hinaus konnten metabolische Veränderungen in hypoxischen Pseudo-Inseln mittels FLIM früher identifiziert werden, als es mit herkömmlichen, Marker-basierten

Methoden möglich war. Die in vitro Modelle, die in dieser Arbeit entwickelt wurden, wurden außerdem verwendet, um den Einfluss der beiden extrazellulären Matrix- (EZM) Proteine Kollagen Typ 1 (COL1) und Nidogen-1 (NID1) sowie die Ko-Kultur von Pseudo-Inseln mit Endothelzellen (EZs) in einem in vitro Post-Transplantationsmodell zu untersuchen. In diesem Modell demonstrierten wir die positive Wirkung von COL1, NID1 und den EZs auf die Insulinsekretion, EZM-Expression und das Überleben der β-Zellen. Es ist hervorzuheben, dass im Rahmen dieser Arbeit zum ersten Mal das therapeutische Potential von NID1 als β-Zell-unterstützendes Protein gezeigt wurde. Wir identifizierten das Integrin αvβ3 in der β-Zellmembran als Bindungspartner für NID1, welches nach Bindung mit NID1 den MAPK-Signalweg aktiviert. Insgesamt demonstriert diese Arbeit das große Potential physiologisch relevanter in vitro Modelle für die DM-Forschung.

Abbreviations

2D	2-dimentional
3D	3-dimentional
ADP	adenosine diphosphate
ATP	adenosine triphosphate
B-cell	bursa-derived cell
BM	basement membrane
COL1	collagen type 1
COL4	collagen type 4
DigiWest	high-throughput digital western blot platform
DM	diabetes mellitus
DNA	deoxyribonucleic acid
DPP4	dipeptidyl peptidase 4
EC	endothelial cells
ECM	extracellular matrix
ELISA	enzyme-linked immunoassay
ER	endoplasmic reticulum
FACS	fluorescence-activated single cell sorting
FAD	flavin adenine dinucleotide
FLIM	fluorescence lifetime imaging microscopy
FN	fibronectin
GCK	glucokinase
GFP	green fluorescent protein
GLP-1	Glucagon-like peptide-1
GSIS	glucose-stimulated insulin secretion
HA	hyaluronic acid
hESCs	human embryonic stem cells
HIF-1α	hypoxia-inducible factor
hiPSC	human induced pluripotent stem cells
hTERT	telomerase reverse transcriptase

HUVECs	human umbilical vein endothelial cell
IBMIR	instant blood-mediated inflammatory response
LAM	laminin
M	molar [mol/L]
mM	millimolar [mmol/L]
MAF	v-maf musculoaponeurotic fibrosarcoma oncogene homologue
MI/R	myocardial infraction and reperfusion
MSC	mesenchymal stem cell
NADH	nicotinamide adenine dinucleotide
NID1	nidogen-1
NID2	nidogen-2
OoC	organ-on-a-chip
PCA	principal component analysis
PDX1	pancreatic and duodenal homeobox 1
PP	pancreatic polypeptide
SV40LT	Simian Virus 40 Large
T1DM	diabetes mellitus type 1
T2DM	diabetes mellitus type 2
TCA	true component analysis
T-cells	thymic lymphocyte
TGF-β1	transforming growth factor beta
VEGF	vascular endothelial growth factor
αSMA	alpha smooth muscle actin

List of Figures

List of Publications

§ = authors contributed equally

1. Zbinden A., Hinderer S., Layland S.L., and Schenke-Layland K., Real-Time Analysis of Biomaterials Function, Elsevier, Oxford, Paul Ducheyne, 2017; 85-100.

2. Rogal J.§, **Zbinden A.**§, Schenke-Layland K., & Loskill P., Stem-cell based organ-on-a-chip models for diabetes research, Advanced Drug Delivery Reviews, 2019; 140: 101-128.

3. Urbanczyk M., **Zbinden A.**, Layland S. L., Duffy G., & Schenke-Layland K.; Controlled Heterotypic Pseudo-Islet Assembly of Human β-Cells and Human Umbilical Vein Endothelial Cells Using Magnetic Levitation, Tissue Engineering Part A, 2019; 26(7-8): 387-399.

4. Zbinden A., Marzi J., Schlünder K., Probst C., Urbanczyk M., Black S., Brauchle E.M., Layland S.L., Kraushaar U., Duffy G.P., Schenke-Layland K., & Loskill P.; Non-invasive high content Raman analysis of a microphysiological human pancreas-on-a-chip model, Matrix Biology, 2020; 85: 205-220.

5. Zbinden A.§, Urbanczyk M.§, Layland S.L., Becker L., Marzi J., Bosch M., Loskill P., Duffy G.P. & Schenke-Layland K.; Collagen and endothelial cell co-culture improves β-cell functionality and rescues pancreatic ECM, Tissue Engineering Part A; accepted on Sept 22nd, 2020.

6. Zbinden A.§, Carvajal D.A.§, Urbanczyk M., Layland S.L., Bosch M., Fliri S., Lu C., Jeyagaran A., Loskill P., Duffy G.P. & Schenke-Layland K.; Fluorescence lifetime metabolic mapping of hypoxia-induced damage in pancreatic pseudo-islets, Journal of Biophotonics, 2020; e202000375.

7. Zbinden A.§, Layland S.L.§, Urbanczyk M., Carvajal D.A., Marzi J., Zauner M., Hammerschmidt A., Brauchle E.M., Sudrow K., Fink S., Templin M., Liebscher S., Klein G., Deb A., Duffy G.P., Crooks G.M., Eble J.A., Mikkola H.K.A., Seifert M. and Schenke-Layland K.; Nidogen-1 Mitigates Ischemia and Promotes Tissue Survival and Regeneration, Advanced Science, 2021; 8(4): 2170016.

Contribution

B.C = Book Chapter; R = Review

No.	1	2	3	4	5	6	7
Accepted for publication	yes	yes	yes	yes	yes	yes	yes
Number of authors	4	4	5	12	9	11	19
Position of the candidate in the list of authors	1	1	2	1	1	1	1
Scientific ideas by candidate (%)	B.C	R.	10	45	30	45	25
Data generation (%)	B.C	R.	10	55	40	30	30
Interpretation and analysis by candidate (%)	B.C	R.	10	55	40	45	40
Paper writing by candidate (%)	80	50	10	70	50	70	45

Chapter 1

Introduction

1. Introduction

1.1. Human pancreas

The pancreas plays an essential role in the control of energy consumption and metabolism[1]. It is composed of two unique parts, the exocrine and endocrine pancreas, which are morphologically different and exert distinct functions in the human body (**Figure 1**). The exocrine pancreas is composed of acini. They produce digestive enzymes, such as lipases, proteinase and amylases that travel via the pancreatic ducts and are responsible for breakdown fats, proteins, and carbohydrates in the small intestine[2].

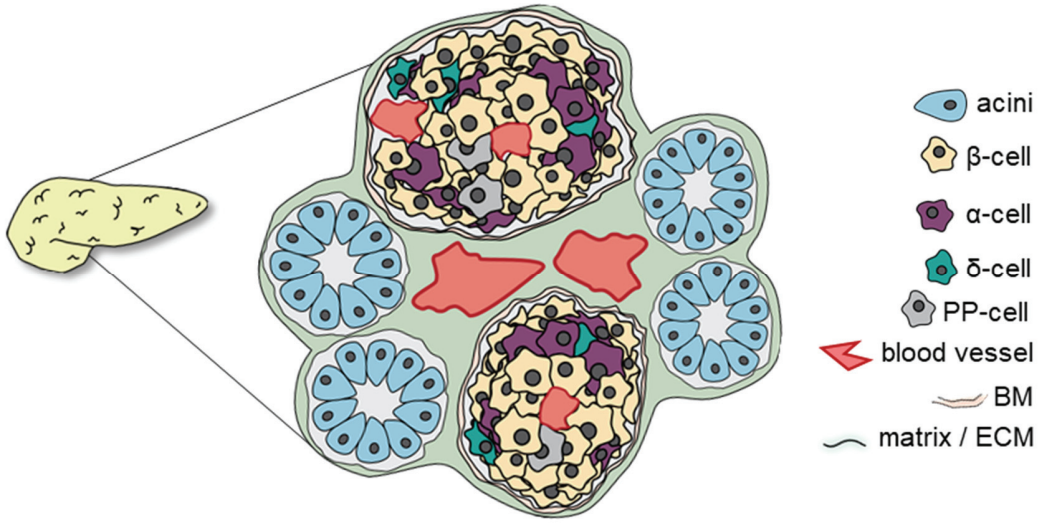

Figure 1: Human pancreas. The pancreas is highly vascularized. The endocrine pancreas is composed of the Langerhans islets, which regulate blood glucose level. The exocrine pancreas is made primarily of acini, which secrete a variety of digestive enzymes. Illustration adapted from Efrat et al.[3]

The Langerhans islets are highly vascularized endocrine clusters, which quickly respond to blood glucose level variations by secreting regulating endocrine hormones, such as insulin by β-cells and glucagon by α-cells[4]. In the human pancreas, the total number of islets is estimated between 3.6 and 14.8 million[5,6]. In humans, the different cell types are randomly distributed throughout the islets, while in rodents, β-cells are always located in the islet's center[7]. The islets are surrounded by two distinct basement membranes (BM): the peri-islet BM, which delimits the endocrine-exocrine interface, and the vascular BM bridging mostly α- and β-cells with intra-islet capillaries[8]. In humans, the vascular BM is a double BM, while in rodent islets, a single BM delimits endocrine cells and vasculature. The

main components of the pancreatic BM are collagen type 4 (COL4), laminin (LAM), nidogen-1 (NID1), nidogen-2 (NID2), and heparan sulfates proteoglycans such as perlecan[9,10]. Other extracellular matrix (ECM) components such as collagen type 1 (COL1) or fibronectin (FN) are present in the pancreatic interstitial ECM[11]. ECM proteins can stimulate the activation of different pathways, such as MAPK, Rho/ROCK and Akt/PKB pathways in vitro, indicating that ECM proteins can support β-cell function, survival and proliferation[12–14]. These interactions are mediated via the ligation of the ECM proteins to different cellular receptors, such as integrins[15]. For instance, the RGD sequence is present on a large variety of ECM proteins such as the nidogens, FN or LAM, which can binds to certain integrins, including the integrin αvβ3[16].

In humans, β-cells represent ~ 60% and α-cells ~ 30% of the islet population[17]. Insulin is secreted proportionally to the glucose concentration present in the blood, mediating the uptake of glucose, fatty acids, and amino acids in insulin-sensitive tissues, such as skeletal muscles or liver. In contrast, glucagon release is activated by low blood glucose concentration, and induces the breakdown of glycogen into glucose in insulin-sensitive tissues[18]. Other cell types, including δ-cells, pancreatic polypeptide (PP)-cells and ε-cells secrete somatostatin, PP, and ghrelin, respectively[5,19–22]. δ-cells represent ~ 5% of the pancreatic islet cells. Somatostatin secretion acts as a local paracrine inhibitor of both insulin and glucagon secretion[23]. PP-cells make up 1-2% of the islet population and their PP secretion has been shown to inhibit glucagon at low glucose concentration[24]. The main role of PP-cells appears to be related to satiety, reducing appetite and food intake in humans[25]. Ghrelin-positive cells account for 1-10% of the islet mass and their role is significantly different between animal models and humans[26]. In the developing mouse, 70-95% of ghrelin-positive cells also co-express glucagon, while in humans, no co-expression of glucagon is observed at any stage of the development[27,28]. In humans, rats and mice, ghrelin is insulinostatic, mediating insulin, glucagon, PP, and somatostatin secretion[29–32].

The control of glucose homeostasis via the hormones secreted in the blood stream results in a tight glucose concentration ranging from 4 to 6 mM in humans (**Figure 2**)[4]. In brief, insulin secretion is stimulated by glucose levels higher than 3.3 mM. Insulin binds via its receptor to liver, muscle, and fat cells[33]. It promotes glucose uptake in muscle adipose tissue, reducing the blood glucose level. In addition, insulin induces glycogenesis, lipogenesis, and incorporation of amino acids into proteins[34]. Glucagon is secreted at low

glucose levels and has a catabolic activity, which is mostly on the liver cells[18]. It enhances the rate of gluconeogenesis in the liver from stored glycogen. In extreme cases, glucagon can promote the release of amino acids from skeletal muscles as a source for gluconeogenic precursors. Moreover, glucagon can promote hepatic fatty acid oxidation which produces the energy required to support gluconeogenesis.

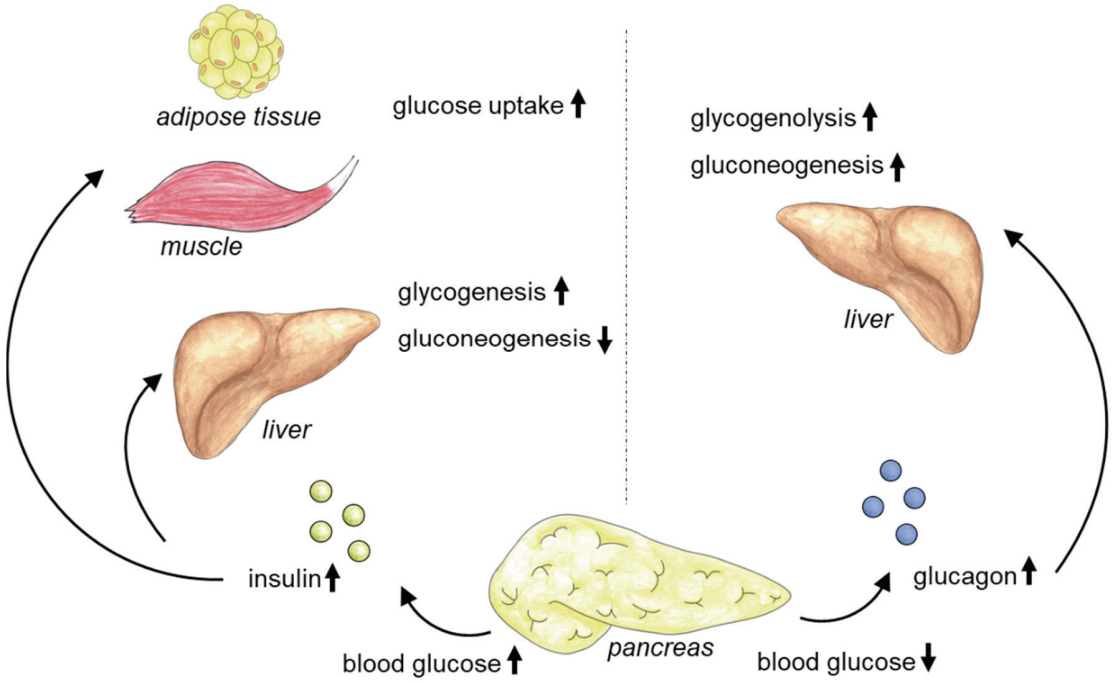

Figure 2: Glucose homeostasis. Illustration representing the main interactions between pancreas and insulin/ glucagon-sensitive organs to maintain glucose homeostasis. Arrowheads upwards indicate an increase; arrowheads downwards indicate a decrease. Illustration adapted from Rogal & Zbinden et al.[35]

1.2. Insulin secretion in β-cells

Insulin secretion in β-cells is triggered by several nutrients, including glucose, some amino acids, as well as non-esterified fatty acids[36]. Glucose is the most potent secretagogue and induces the release of insulin within minutes by a biphasic response[37]. In humans, the first peak of insulin occurs within 5 minutes after the glucose stimulation, where the majority of the insulin is secreted. The second phase occurs at a lower rate, where the remaining insulin is released while new insulin is produced. Glucose is transported via the transporters of the GLUT family (GLUT1 in humans, GLUT2 in rodents) by facilitated diffusion, which is not rate limiting[38]. The primary glucose sensor in mammalians is the glucokinase (GCK) that controls the rate of entry of glucose into glycolysis via glucose phosphorylation[39]. Only phosphorylated glucose can enter the

glycolysis process and downstream metabolic pathways. Therefore, the GCK and GLU1/2 pair is often considered as the glucose-sensor controlling the blood glucose level. Pyruvate, the glycolysis end-product, is transported into the mitochondria via the pyruvate transporter and is decarboxylated to acetyl-CoA, which can enter the Krebs cyle[40]. Nicotinamide adenine dinucleotide (NADH) and flavin adenine dinucleotide ($FADH_2$) are produced by the Krebs cycle and subsequently oxidized in the respiratory chain, producing ATP. The rise in ATP level leads to the inactivation of the K^+_{ATP} channels in the plasma membrane, resulting in the membrane depolarization. This results in the opening of voltage-dependent Na^+ and Ca^{2+} channels in the plasma membrane[41]. Ca^{2+} entry in the cytoplasm triggers insulin granules to fuse with the plasma membrane, resulting in insulin secretion. A simplified graphic describing the mechanisms of insulin secretion is illustrated **in Figure 3**.

The increase in Ca^{2+} is rapidly reversed by Na^+/Ca^{2+} exchangers and Ca^{2+}ATPases activity in the plasma membrane[42,43]. Endoplasmic reticulum (ER) Ca^{2+} pumps also play a critical role in Ca^{2+} homeostasis[44]. At high glucose concentration, oscillatory behaviors in cytosolic Ca^{2+} concentration can be observed in β-cells and in islets[45,46]. As β-cells are electrically coupled, changes in cytosolic Ca^{2+} concentration spread from one cell to another. Subsequently, oscillations can be observed in membrane potential, ATP/ADP ratio, K^+_{ATP} channel conductance, glucose level, oxygen, and insulin secretion. Insulin secretion also involves a complex transcriptional regulation to ensure proper trafficking of intracellular storage insulin granules to the plasma membrane. It requires the remodeling of filamentous actin and the cytoskeletal network at the cell surface and cell-cell junctions via focal adhesion complexes[47]. The formation of focal adhesions recruits and stimulates a number of intracellular signaling proteins, including effectors of the MAPK pathway such as ERK1/2 and MEK1/2[48]. Importantly, a large variety of external stimuli can activate the MAPK pathways, such as integrin stimulation or growth factors[49].

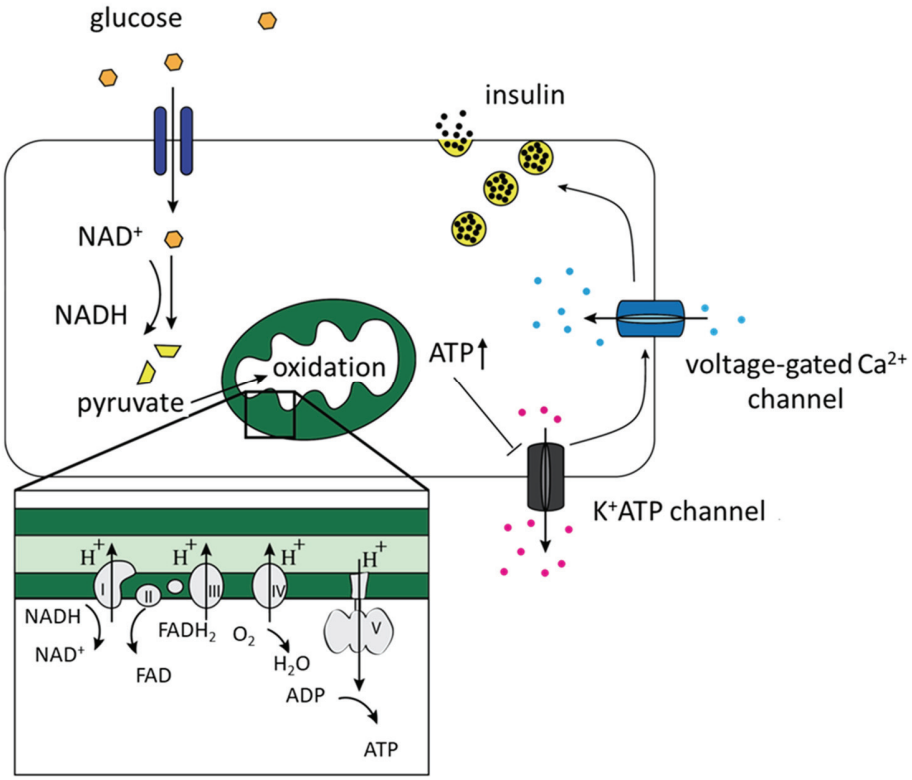

Figure 3: Simplified description of insulin secretion. Glucose enters in the β-cell via the GLUT transporter family and is processed by the glycolysis producing pyruvate and NADH. Pyruvate enters the mitochondria and is processed by the Krebs cycle producing ATP. In this process, bound-NADH is converted into NAD. The increase in ATP leads to the blocking of the of K^{+}_{ATP} channels, influx of Ca^{2+} and exocytosis of insulin granules. NAD: nicotinamide adenine dinucleotide, NAD^{+}: oxidized form, NADH: reduced form; FAD: flavin adenine dinucleotide (oxidized form), $FADH_2$: reduced form. Illustration adapted from Fu et al.[36]

1.3. Diabetes Mellitus

Diabetes Mellitus (DM) is classified as a group of metabolic diseases characterized by chronic hyperglycemia[50]. In 2019, the International Diabetes Federation registered more than 463 million people with DM. The number of DM patients is predicted to rise to 700 million people worldwide by 2045, making DM one of the most important public health challenge of this century[51]. DM disorders are characterized by a chronic disruption of the glucose homeostatic state[52]. In type 1 DM (T1DM), the progressive autoimmune destruction of pancreatic β-cells reduces the insulin secretory capacity to respond to glucose uptake[53]. Type 2 DM (T2DM), which represents the majority of DM patients (~90%), is led by a progressive β-cell dysfunction combined with insulin resistance in glucose sensitive-tissues[54]. Although, dysregulated glucose metabolism leads to hyperglycemic events and in severe cases to death in both DM types, the etiology of T1DM and T2DM is different[55].

In T1DM, there is an important genetic contribution to the development of the pathology[56]. Although the genetic basis of T1DM is not yet fully understood, over 40 locations in the human genome have been identified as risk factors[57]. For instance, alleles of the major histocompatibility locus (HLA) at specific locus account for 40-50% of the familial clustering in T1DM[58,59]. The low incidence suggests that other non-identified genetic and environmental factors contribute to the development of autoimmunity towards β-cells[60]. The scientific community agrees that T1DM is triggered by a set of environmental factors in genetically pre-disposed individuals. The autoimmune attack is initiated by auto-reactive immune cells, such as thymic lymphocytes (T-cells) that have failed the process of negative selection in the thymus[61].

T2DM is a multifactorial disease, with key characteristics such as progressive insulin resistance, β-cell dysfunction, and a chronic state of inflammation[62]. Obesity is considered as the main factor behind insulin resistance[63]. Insulin resistance increases the demand for insulin secretion, which can progressively exhaust β-cells and induce apoptosis. Besides lifestyle and nutrition risk factors, genetic pre-disposition is considered an important factor contributing to the development of the pathology[64]. However, for most of the genes identified as risk factors for T2DM, there is little understanding on how they pre-dispose to T2DM. Researchers have hypothesized that these genes are related to β-cell function, β-cell development or regulation of the β-cell mass[64,65]. The key attributes of T1DM and T2DM are illustrated in **Figure 4**.

1.4. Therapies to treat Diabetes Mellitus

1.4.1. Classical Therapies to Treat Diabetes Mellitus

Banting and Best discovered insulin in 1923[66]. Since then, different humanized insulin analogues have been commercialized, which remain the main treatment for T1DM patients[67]. The current regimen using insulin focuses on the combination of extensive diet and administration of exogenous insulin via manual injections or via insulin pumps[68]. In addition, insulin can be utilized in patients with T2DM when the regulation of blood glucose level is not sufficient with other oral pharmaceuticals[69]. Nonetheless, clinical insights gathered in the past decades have identified important limitations of such insulin replacement therapy. For instance, it was shown that exogenous insulin fails to fully

replicate the biological functions of endogenous insulin[70,71]. Therefore, T1DM patients following a conventional clinical management have nonetheless a high risk of developing a number of vascular complications due, in part, to chronic elevation of blood glucose level[72].

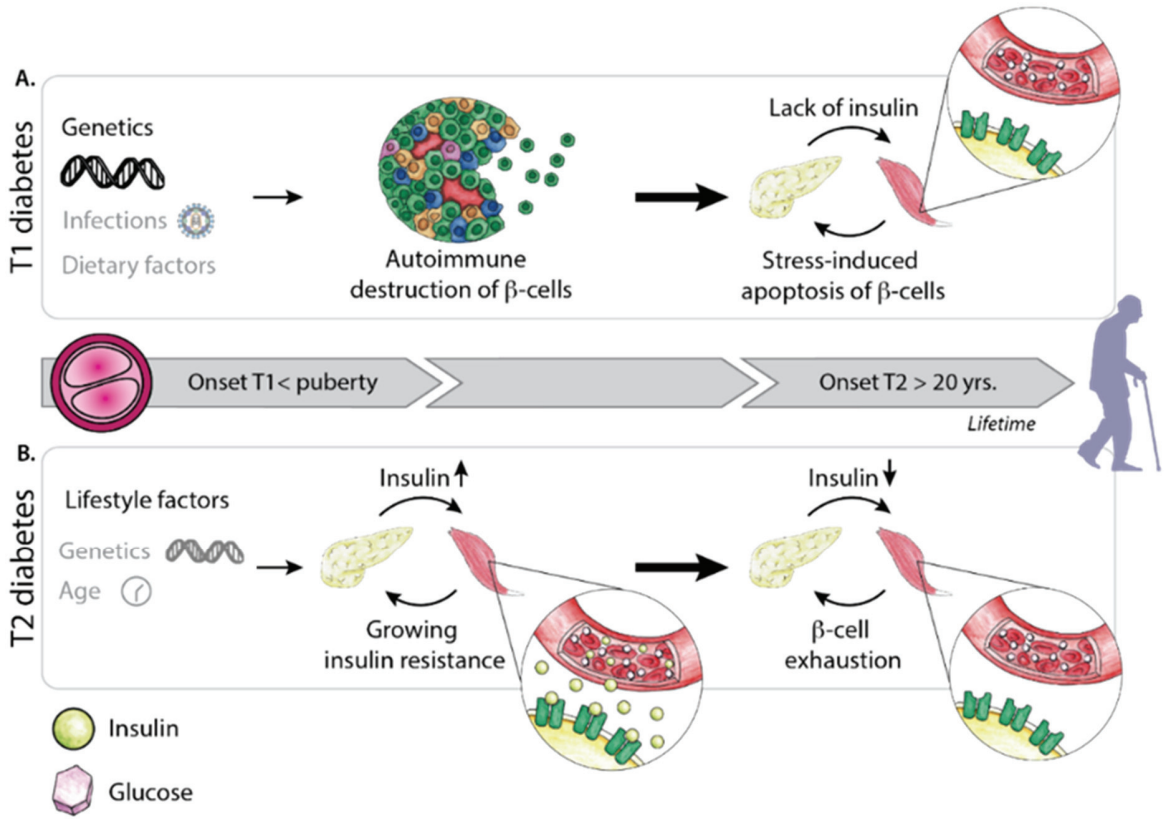

Figure 4: Diabetes mellitus type 1 (T1DM) and type 2 (T2DM). (A) T1DM: Predominantly genetic factors are leading to the autoimmune destruction of β-cells. The increasing workload forced on the remaining β-cells causes cellular stress and stress-induced apoptosis. (B) T2DM: The combination of lifestyle factors, obesity, and genetic predispositions are the main drivers behind the increase insulin resistance in insulin-sensitive tissues and the progressive exhaustion of β-cells. Illustration adapted from Rogal & Zbinden et al.[35]

For T2DM, a number of studies have shown that lifestyle modifications can improve glycemic control[73]. However, changes in lifestyle alone are rarely sufficient to reach normoglycemia and should be combined with a variety of pharmaceutical agents[74,75]. For most T2DM patients, a combination of pharmaceutical agents is required, which is adapted over time to the progressive β-cell decline[76]. There are different classes of antidiabetic agents with defined mechanisms. For instance, the primary first-line drug metformin acts by decreasing insulin resistance[77]. Dipeptidyl peptidase-4 (DPP4) inhibitors, glucagon like peptide-1 (GLP-1) receptor agonists and amylin analogs are known to suppress glucagon secretion by a glucose-dependent mechanism[78,79]. Sulfonylureas and meglitinides increase

β-cell insulin secretion[80,81]. Despite the availability of such antidiabetic drugs, the majority of T2DM patients do not achieve the target goal regarding normoglycemia, blood pressure and lipid levels[82,83]. Similar to T1DM, T2DM patients suffer from diabetic complications arising from damaged blood vessels due to chronic hyperglycemia[72]. Altogether, this indicates that further research is required in the field of DM regarding the biological understanding of the pathology at a cellular, tissue and organ level. There is a need to find alternative strategies to insulin replacement therapy for T1DM patients, as well as to decipher the complex interactions and effects of current and novel antidiabetic drugs in T2DM patients.

1.4.2. Langerhans Islets Transplantation

Pancreatic islet transplantation emerged in the early 1970's as a method to reestablish glucose homeostasis in DM patients[84,85]. In 2000, the Edmonton group reported the first consistent achievement of insulin independency in seven DM patients that were infused with isolated pancreatic islets via the portal vein (**Figure 5**)[86,87]. However, the insulin independent rate remained low. For instance in 2006, only 58% of patients were insulin independent one year after transplantation[88]. The five-year follow up showed that only up to 15% of patients were still insulin independent[89].

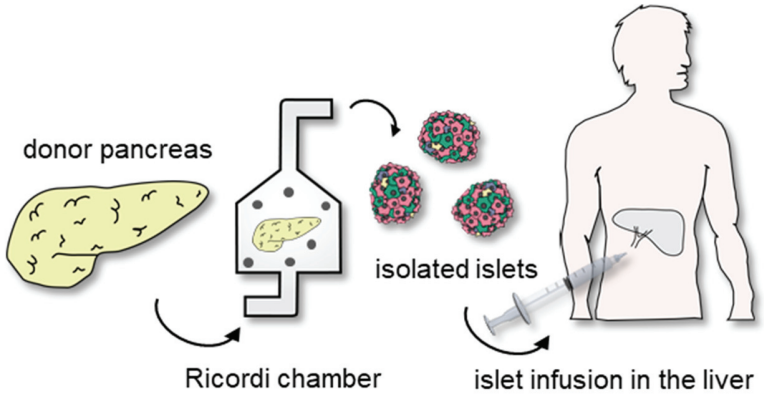

Figure 5: Islet transplantation procedure. The first step includes the enzymatic and mechanical digestion of donor pancreas using a Ricordi chamber. Isolated and purified islets are then infused in via hepatic portal vein into the liver of the recipient. Illustration adapted from Naftanel et al.[90]

The isolation of islets from donor pancreas separates endocrine from exocrine tissue, disrupting the BM components and disconnecting blood vessels and oxygen supply[91]. The blend of collagenases injected into the donor pancreas digests the ECM of the interstitial matrix, releasing islets from the exocrine tissue. After a purification step that separates

acinar cells and fat tissue from islets, islet quality and functionality are assessed following specific guidelines provided by regulatory bodies, such as the Food and Drug Administration[92]. Regarding safety, islet batches must meet specific characteristics in terms of sterility, mycoplasma and endotoxin testing. In addition, regulatory bodies mandate the assessment of key batch properties including, islet count, purity, viability, and islet potency (i.e. via glucose stimulated insulin secretion (GSIS) assays).

Several factors have been identified as contributors to the poor long-term clinical efficacy of islet transplantation (**Figure 6**). For instance, the isolation process is known to significantly damage islets, increasing their susceptibility to posttransplant stresses. Precisely, the enzymatic and mechanical digestions of the exocrine tissue can release proteolytic enzymes which further damage the isolated endocrine cells[93]. After isolation, islet quality is assessed and islet batches containing hypoxia or apoptotic islets may be identified and discarded prior to transplantation. However, quality assessments are performed on a small islet population, which do not reflect the heterogeneity of large islet batches. Consequently, batches approved for transplantation may still contain damaged, hypoxic, or apoptotic islets, ultimately contributing to the poor engraftment and functionality of the transplant.

The hepatic portal vasculature is a hostile environment which limits the capacity of islets to engraft and function properly post-transplantation. The initial loss of islets has been estimated to be between 50-70%[94,95]. It is caused by the pre-transplant factors mentioned, and by post-transplant key events within the liver microenvironment, such as the instant blood-mediates inflammatory reaction (IBMIR), hypoxia and immune cell activation[96]. The IBMIR is triggered by the negatively charged surface of the infused islets and is initiated by a strong activation of the coagulation cascade. The consequence is a non-specific immune reaction of the innate immune system aggravating islet damage. Cytotoxic immune cells secrete cytokines and infiltrate islets, inducing their death[97,98]. Moreover, the IBMIR has an amplifying effect on the adaptive immune responses, negatively impacting transplant outcome[99,100].

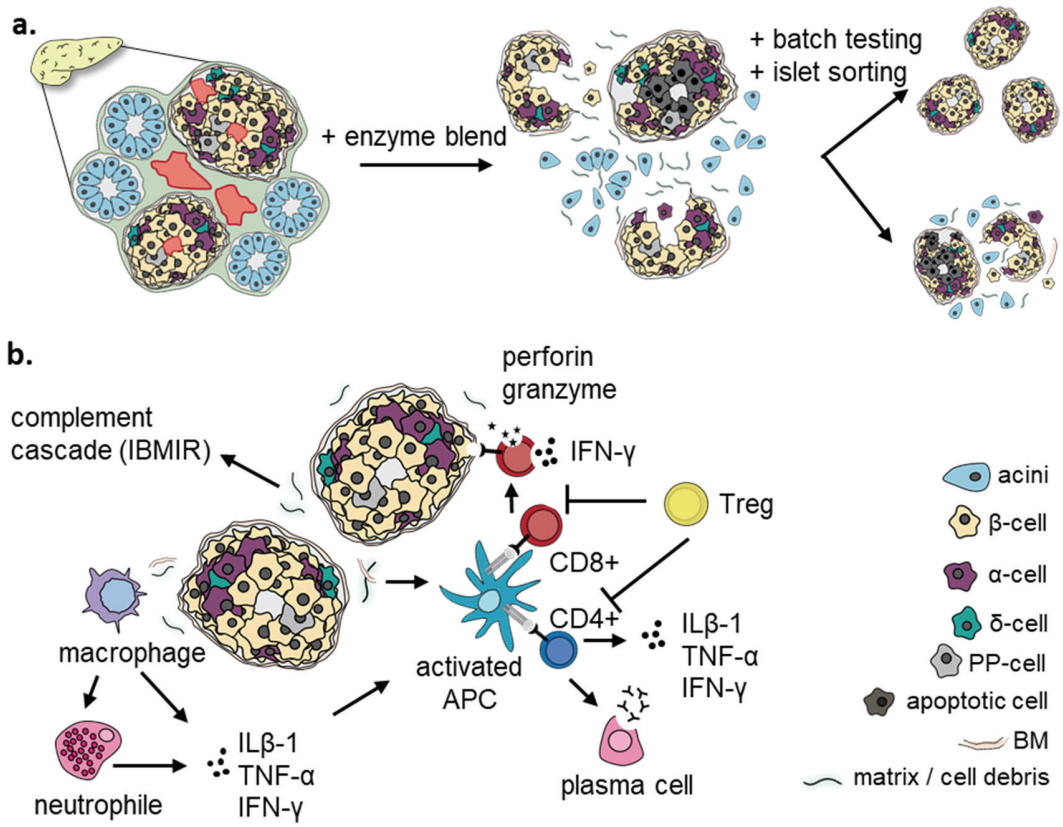

Figure 6: Factors contributing to poor clinical outcome in islet transplantation. (a) Islet isolation disrupts the exocrine tissue, liberating islets. **(b)** Immune responses after the islet transplantation. IBMIR indues the infiltration of various type of leukocytes. Macrophages /neutrophiles are activated by cell debris antigens released by the islets, leading to the release of inflammatory cytokines, ROS and infiltration of additional immune cells into the graft. This cascade activates APCs, which then interact with CD4+ and CD8+ T-cells, destroying the islet via the release of perforin and granzyme. CD4+ T-cell releases inflammatory cytokines activating plasma cells which release antibodies. Treg cells maintain CD4+ T-cell and APCs in an inactive state, which can prevent the islet destruction. IBMIR: instant blood-mediates inflammatory reaction; APC: antigen presenting cell; Treg: regulatory T-cells. ROS: reactive oxygen species. Illustration adapted from Rogal & Zbinden et al.[35]

1.5. Strategies to Improve Islet Function

1.5.1. Procedural Alternatives

Since the first islet transplantation, research has focused on improving the poor clinical outcome[101]. Refinement of the islet isolation process centers on issues related to islet damage caused by enzymatic digestion, increasing the islet yield, and optimizing the pre-transplant culture conditions, storage and shipping of islets[102,103]. Studies have compared enzyme blends for tissue digestion, aiming to find the composition of collagenases and proteases that digest exocrine tissue minimizing peri-islet BM and endocrine cell

damage[104–107]. Others have attempted to refine the sorting of isolated islets based on viability and functionality[108,109].

A number of breakthroughs to combat inflammatory responses after islet infusion led to significant advances in the field. For instance, heparin is now widely used to reduce the blood clotting process[110]. The functionalization of islet surface with heparin mimics the protective features of endothelial cell (EC) lining on the native vascular wall and therefore reduced the coagulation and complement activation in an adult porcine model. Similarly, the use of low molecular weight dextran sulfate and activated protein C have shown to respectively inhibit coagulation and complement cascade, therefore reducing IBIMR in vivo[111,112]. Further investigation and evaluation are required to translate these techniques into a routine clinical setting.

Autoimmune and alloimmune responses are major contributors to the loss of islet mass and function of the transplant. Correlation between the presence of autoantibodies and early graft loss was demonstrated in the late 90' by the Bretzel group[113]. The autoreactive T-cells from T1DM patients are re-activated by the islet transplant and their immune memory triggers an attack on transplanted β-cells[114]. In addition, T-cell mediated immune reactions constitute the major component in islet allotransplantation, which is initiated in part by the genetic differences between donors and recipients[115]. To date, the most wildly used strategy to combat T-cell reactivity is a global immunosuppressive therapy, targeting the production of autoantibodies and the proliferation of memory B-cells[116]. The maintenance of immunosuppression is essential for long-term survival of the transplant; however, most of the immunosuppressive therapies induce liver and kidney toxicity, as well as β-cell toxicity[117–119]. Efforts have been made to find alternative blockades inducing immune tolerance with lower toxicity on other organs, by bocking specific receptors on antigen presenting cells and regulatory T-cells in animal models[120,121]. The liver's hostile microenvironment and IBMIR have pushed researchers to evaluate alternative transplant sites, such as the bone marrow[122,123], subcutaneous sites[124,125] or the omentum[126,127]. Nevertheless, collective efforts are required to validate those strategies in human-based in vitro models and into a clinical setting.

1.5.2. Biomaterials & Biofunctionalization

Encapsulation and biofunctionalization of cell-based therapeutics are a promising strategy not only alleviating the immune response, but also providing a microenvironment supporting cell survival and function[128]. Research groups have focus on the development of devices that prevent the entry of immune cells, complements and antibodies while allowing diffusion of oxygen, nutriments, metabolites, hormones and waste products[129]. For instance, the device Cell Pouch™ developed by Sernova corporation was developed to be transplanted subcutaneously and allow pre-vascularization for 4-5 weeks before human islets are infused by a port into the device. The first clinical trial demonstrated safety of the device[130]. The PEC-direct™ device from ViaCyte, Inc. has a different approach to reduce hypoxia-induce injury subcutaneously by allowing direct contact of the pre-vascularization with the encapsulated β-cells. However, this strategy requires an immunosuppressive therapy as the membrane allows the entry of host cells. This device is currently the only one in trials that uses stem cell-derived β-cells, addressing the issue of islet shortage[131]. The Company Beta-O_2 Technologies Ltd. developed the β-Air device, which is subcutaneous and provides a replenishable gas chamber to oxygenate the implant until vascularization is completed. A preliminary study in 2012 reported a successful transplantation into a 63-year old patient without requiring immunosuppression[132].

Although encapsulation strategies for cell-based therapy have shown great clinical potential, islet function and survival decrease over time. Importantly, the loss of function observed in vitro and in vivo hampers both the development of cell-based therapy and the development of in vitro models to study DM. Therefore, researchers are focusing on strategies to support β-cell survival and function in vitro and in vivo. Pancreatic ECM and BM have been shown to be essential for tissue and organ development and homeostasis[133]. β-cell survival and function depend on their microenvironment, which provides mechanical and biological cues which can influence cell fate[8]. Natural polymers are physiological components derived from the native ECM, which contain specific adhesive sequences and binding sites have shown to support islet function and survival[134]. Different strategies have been explored during the last few years to modulate β-cell function using ECM[135]. Strategies from the tissue engineering field have explored the supplementation of ECM proteins as soluble forms and as supporting scaffolds or coatings[136–138]. For instance, ECM from decellularized organs have been of interests, as it resembles the native structure[139]. Several

studies showed the beneficial effect of decellularized ECM to maintain β-cell function and survival[140–144]. Donor shortage and chemical alterations of ECM present in decellularized materials are two factors that limit the application of decellularized scaffolds in a clinical setting. Therefore, researchers have investigated the effect of single ECM protein or as combinations[134,145]. To re-create the native pancreatic niche, different research groups have incorporated various ECM components into 3D constructs. For instance, collagen-based hydrogels (COL1, COL4), LAM and FN have been extensively used in this context[146–150], as well as microenvironments combing different ECM proteins, such as COL1, COL4 and FN[151]. Stepwise approaches demonstrated that not all ECM proteins are beneficial for islet function, and that different ECM protein concentrations may have opposite effects[152,153]. For example, high concentrations of COL4 decreased islet survival[152]. Similarly, only specific LAM sequences had a beneficial effect on β-cells, while others were ineffective[153]. Additionally, biofunctionalization of hydrogels can be performed using bioactive molecules such as the vascular endothelial growth factor (VEGF) or the glucagon like peptide-1 (GLP-1) to enhance neovascularization or protect β-cells from apoptosis[154,155]. Another interesting research area is the combination of other cell types to pancreatic β-cells or islets. Incorporation of fibroblasts with islets increased islet survival and preserved ECM expression[156]. Similarly, the secretion of FN and LAM from mesenchymal stromal cells (MSCs) had a beneficial effect on islets[157,158]. Although a large number of studies have shown the potential of biological cues to support β-cell and islet function, further research is required for the understanding of the exact underlying mechanisms.

1.6. In vitro Models for Diabetes Mellitus Research

1.6.1. Species-Specific Mechanisms in β-Cells

Significant advances have been made in the past decades in the field of DM research that have relied on human cohort studies and animal models. For instance, cohort studies have contributed to decipher the genetic component linking certain genotypes to a DM-phenotypes, or to correlate distinct lifestyles to different manifestations of DM[55,159]. DM animal models ranging from fruit flies to non-human primates have been developed to study DM in great mechanistic details from a cellular to an organ level[160]. However, the translation

from animals to humans, as in many other research areas, is challenging and often difficult[161,162]. Animal models are mostly developed to study only few aspects of the pathogenesis and do not represent the complexity and multifactorial characteristics of DM[160]. Moreover, identification and prediction of human pathogenic pathways based on animal studies are hampered by species-specific mechanisms at the gene, protein, cellular, organ, and organism level. For instance, glucose regulation varies between humans and rodents. Humans have a single copy of the glucose-regulated insulin gene, while rodents express two functional forms of insulin[163–165]. The regulation and expression of pancreatic duodenal homeobox 1 (Pdx-1), v-maf musculoaponeurotic fibrosarcoma oncogene homologue (MAF) protein A and MAF protein B, which are central transcription factors, are differentially stimulated by glucose based the species specificity of the islets[166]. Species-specific differences have been reported regarding GLUT4 trafficking pathways, insulin secretion profile and responsiveness, Krebs cycle and other critical glucose metabolic pathways[167]. Similarly, the immune responses, which are key players in the development of the autoimmunity toward pancreatic β-cells and in graft immune tolerance, exhibit important species-specific mechanisms[168]. This highlights the need to develop novel in vitro DM models with a human genetic background that recapitulate the complex physiology of the human body to bridge pre-clinical and clinical studies.

1.6.2. Cell Source and Model Architecture

In contrast to animal models, in vitro models allow a considerable control over environmental conditions, enabling the study of specific cellular in molecular pathways under defined conditions[169]. The low costs of in vitro models facilitate the implementation of high throughput studies, which are of interest in the drug discovery setting[170]. The development of relevant in vitro models relies, in part, on a source of cells with a human genetic origin. Primary human tissues, islets and cells obtained from cadaveric donors have already provided considerable knowledge of islet function and mechanistic pathways, interplay between the different islet cell types or effect of various drugs and compounds[171,172]. However, it is important to consider that the rare accessibility of human primary material hinders the possibility to perform high-throughput and large in vitro studies[173]. Long-term culture of primary isolated islets is also limited by the loss of function rapidly occurring within two weeks of continuous culture[174]. In addition, it was reported that

human islet preparations are highly heterogenous and exhibit patient-specific variations[175,176]. Although intrinsic variability between islet preparations is scientifically interesting and worth exploring, the establishment of an in vitro system relies on reliable source of cells exhibiting enough human physiological characteristics with reduced variability and high reproducibility.

As an alternative, collective efforts were made to derive immortalized cell lines from primary cells by introducing specific genetic modifications. Until recently, only glucose-responsive β-cell lines from animal origin were available, such as the rodent-derived insulinoma cell lines INS-1E and MIN-6[177]. In 2011, Ravassard et al. were the first group to overcome the replicative senescence of human β-cells while preserving glucose-stimulated insulin secretory capacity[178]. Human fetal pancreases were transduced with a lentiviral vector expressing SV40 large T antigen (SV40LT) and human telomerase reverse transcriptase (hTERT). Then, insulinomas were grafted onto SCID mice to further amplify the proliferation of β-cells. The resulting cell lines, endoC-βH1 expressed specific β-cell markers and was glucose-responsive. In 2014 and 2015, the Ravassard group presented two additional cell lines: endoC-βH2[179] and endoC-βH3[180], which were both conditionally immortalized β-cell lines based on the endoC-βH1 cell line. The endoC-βH3 cell lines used a drug-activated excision strategy based on tamoxifen coupled with antibiotic selection to allow the removal of the proliferative transgenes. The resulting excised β-cells are non-proliferative and glucose-responsive, and are a promising alternative to human primary islets[180–185].

Since their commercialization, the endoC-βH cell lines have been used as 2-dimentional (2D) in vitro models in a number of studies, which have revealed a number of β-cell specific mechanistic pathways[181–185]. For instance, in the study from Akerman et al., they investigated the regulation of β-cell function by long non-coding RNAs using the endoC-βH1 cell line[181]. They identified PLUTO as a regulator of chromatin structure affecting the expression of Pdx-1. Interestingly, PLUTO was downregulated in isolated islets from T2DM patients and patients with impaired glucose tolerance.

The main criticism over such in vitro models is the poor physiological complexity[186]. Consequently, researchers have aggregated β-cells in so-called pseudo-islets and showed that they had a superior secretory capacity compared to 2D monolayer cultures of these same cell types[187]. This indicates that providing cell-cell contact in a 3-dimentional (3D)

manner increases β-cell response to physiological signals[188,189]. As a further step to increase physiological relevance, ECM proteins can be used as soluble factors or scaffolds to support β-cell function in a similar manner than as done for tissue engineering approaches[134]. To gain control of the microenvironment, 3D culture systems can be integrated into microfluidic devices, a novel field known as organ-on-a-chip (OoC)[190]. Using a similar approach than the computer microchip fabrication, OoC enables the in vitro reconstruction of tissue-level and organ-level structures that resemble tissues and organs in vivo. In addition, their microfluidic integrated platforms are low-shear and can mimic the vasculature perfusion, allowing the analysis of in vitro biochemical, genetic, and metabolic activities in a time-dependent manner. Such read-outs require the implementation of non-invasive label-free techniques to monitor in situ their functions[191].

1.7. Non-Invasive Imaging Tools for in Vitro Models

1.7.1. Mechanisms of Light Scattering

An incoming photon from a light source can interact with a molecule, resulting in elastic and inelastic scattering (**Figure 7**)[192]. The total kinetic energy of the system is conserved in elastic scattering (also called Rayleigh). In contrast, in inelastic scattering, the momentum is conserved but not the kinetic energy of the system. Raman microspectroscopy and fluorescence lifetime imaging microscopy (FLIM), both rely on inelastic scattering processes. Raman scattering involves virtual states, where the interactions of the incoming photon and its re-emission occur almost simultaneously (picosecond range)[193]. When the energy of the scattered photon is lower than the incoming photon, the process is referred as Stokes Raman scattering, while the opposite is termed anti-Stokes Raman scattering. In addition, both processes leave the molecule in a rotation-vibrational modified state. The result is a measurable frequency shift, which is specific to molecular bonds. In contrast, when the incoming photon has enough energy to allow the transition to a higher excited electronic state, the molecule absorbs it. During the relaxation from the higher excited state to the ground electronic state, (auto-) fluorescence is generated[194]. FLIM measures the lifetime of the (auto-) fluorescence process, which is in the nanosecond range and specific to the molecular structure of the excited compound.

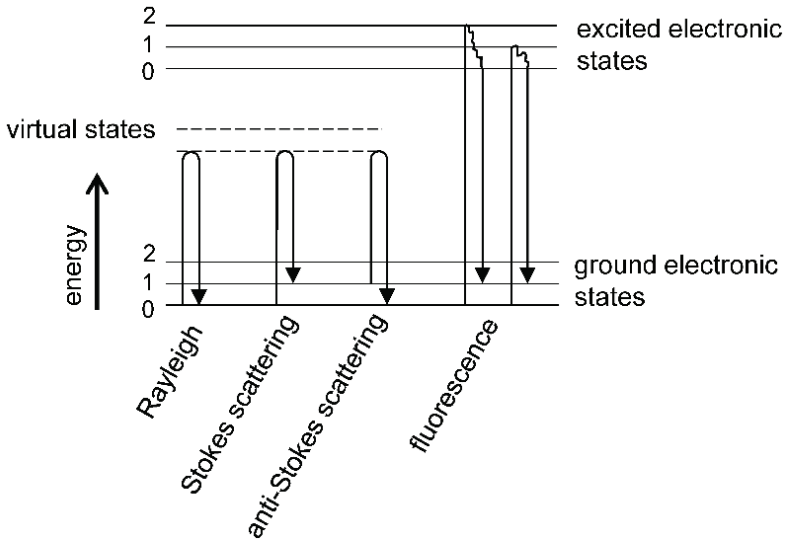

Figure 7: Mechanisms of light scattering processes. Incoming photon excites molecules at different energy levels. Raman microspectroscopy can rely on Stokes and anti-Stokes scattering, while FLIM relies on the lifetime of the fluorescence process. Illustration adapted from Mitsutake et al[192].

1.7.2. Raman Microspectroscopy & Fluorescence Lifetime Imaging Microscopy for Biomedical Research

Raman techniques are well-established and routinely used in the pharmaceutical and material fields[195]. Early studies used Raman microspectroscopy to characterize molecular orientations in polymers and proteins[196]. More recently, a number of research groups have reported the use of Raman microspectroscopy of biological tissues[197]. Raman microspectroscopy has the ability to determine the underlying chemical structures that compose tissues and cells, such as proteins, lipids, and DNA[198]. In addition, a large number of studies used Raman microspectroscopy to identify diseased tissues and cancer cells[199–205]. Raman microspectroscopy was also employed to assess the different stages in stem cell differentiation, including chondrocytes[206], neurons[207], cardiomyocytes[208,209], osteoblasts[210] and polyhormonal pancreatic progenitors[211].

FLIM is a well-established tool to assess the metabolic state in live cells and tissues in situ[194]. The process relies on probing the autofluorescence lifetime of two coenzymes, NADH and FAD, that are involved in different metabolic pathways that generate energy for the cells[212]. The fluorescence lifetimes of NADH and FAD are depending on their configuration, protein-bound NADH has a longer lifetime (τ2: 1000-6500 ps) than its free form (τ1: 300-800 ps). Conversely, protein-bound FAD has a shorter lifetime (τ1: 300- 455

ps) compared to its free form (τ2 :2300- 2900 ps). Free form NADH is mostly found in the cytoplasm and produced by glycolysis, while protein-bound NADH is present in the mitochondria in the oxidative phosphorylation chain[213]. Free form FAD and protein-bound FAD are both mainly in the mitochondria, where it can form complexes with lipoamide dehydrogenases or the electron transfer flavoproteins[214]. Therefore, the metabolic equilibrium between glycolysis and oxidative phosphorylation can be evaluated based on the respective contribution of τ1 (α1) and the optical oxidative ratio, defined as FAD/(FAD + NADH). Moreover, lifetimes are highly sensitive to microenvironmental changes such as pH or temperature[215,216].

Raman measurements can give insights into the molecular compositions and structures of cells, while FLIM can assesses the metabolic state of cells. Such methods have the potential the monitor in a non-destructive manner the function of in vitro models over a long period of time.

Chapter 2

Objective of the Thesis

2. Objective of the Thesis

This thesis aims to develop advanced in vitro models to assess pancreatic β-cell function for the field of diabetes mellitus research. The first step was to mimic the insulin secretory capacity and glucose responsiveness of primary β-cells in vitro. Conventional in vitro assays using Langerhans islets isolated from cadaveric pancreases are limited by their low accessibility and rapid loss of function. Thus, we explored the use of the rat INS1-E insulinoma cell line and human conditionally immortalized endoC-βH3 cell line as alternatives. To increase the physiological relevance of the in vitro models, aggregates of β-cells, so-called pseudo-islets, were produced in a controlled and reproducible manner.

Sever hypoxia post-transplantation contributes to islet loss and clinical failure of islet transplant. Therefore, we develop a post-transplantation in vitro model to evaluate the damage caused by sever hypoxia on pseudo-islets. Cellular and extracellular hypoxia-induced events were evaluated over time. We used the post-transplantation in vitro model to investigate whether extracellular matrix (ECM) protein collagen type 1 and endothelial cells could mitigate the hypoxia-induce damage on pseudo-islets in vitro.

Native islets are highly vascularized in vivo. Therefore, we further improved the in vitro models by providing a vasculature-like flow based on the organ-on-a-chip technology. Insulin secretory capacity from pseudo-islets was assessed via multisampling. To facilitate the non-invasive label-free read-outs in situ, we explored the use of Raman microspectroscopy and Fluorescence Lifetime Imaging (FLIM) microscopy as tool to monitor pseudo-islet function. The goal was to identify Raman fingerprints and FLIM metabolic profiles of pseudo-islets during glucose stimulation. Moreover, the potential of FLIM to discriminate between hypoxic and normoxic pseudo-islets was evaluated.

Finally, the in vitro models developed in this thesis were used to investigate the role of the basement membrane protein nidogen-1 in β-cells. Precisely, the stimulatory and protective effect of nidogen-1 on pseudo-islets, as well as the mechanistic pathways were evaluated in vitro.

Chapter 3

Results & Discussion

The content is based on:

Zbinden A.[§], Urbanczyk M.[§], Layland S.L., Becker L., Marzi J., Bosch M., Loskill P., Duffy G.P. & Schenke-Layland K.; *Collagen and endothelial cell co-culture improves β-cell functionality and rescues pancreatic ECM*, Tissue Engineering Part A; accepted on Sept 22nd, 2020.

Zbinden A., Marzi J., Schlünder K., Probst C., Urbanczyk M., Black S., Brauchle E.M., Layland S.L., Kraushaar U., Duffy G.P., Schenke-Layland K., & Loskill P.; *Non-invasive high content Raman analysis of a microphysiological human pancreas-on-a-chip model*, Matrix Biology, 2020; 85: 205-220.

Zbinden A.[§], Carvajal D.A.[§], Urbanczyk M., Layland S.L., Bosch M., Fliri S., Lu C., Jeyagaran A., Loskill P., Duffy G.P. & Schenke-Layland K.; *Fluorescence lifetime metabolic mapping of hypoxia-induced damage in pancreatic pseudo-islets*, Journal of Biophotonics, 2020; e202000375.

Zbinden A.[§], Layland S.L.[§], Urbanczyk M., Carvajal D.A., Marzi J., Zauner M., Hammerschmidt A., Brauchle E.M., Sudrow K., Fink S., Templin M., Liebscher S., Klein G., Deb A., Duffy G.P., Crooks G.M., Eble J.A., Mikkola H.K.A., Seifert M. and Schenke-Layland K.; *Nidogen-1 Mitigates Ischemia and Promotes Tissue Survival and Regeneration*, Advanced Science, 2021; 8(4): 2170016.

3. Results & Discussion

3.1. Pancreatic β-Cell Containing Pseudo-Islets as an in Vitro Model to Assess Insulin Secretion

The establishment of in vitro models for DM research that are representative of human physiology requires the use of an adequate source of cells and model architectures. 2D cultures have provided considerable information over decades of research, however, they often fail to predict behaviors and responses in vivo[217]. The underlaying reason is that cells in 2D culture have been isolated from their native environment, therefore lacking ECM interactions, native 3D architecture and blood perfusion[218].

In an attempt to re-create the 3D configuration of native islets, we used the rat INS1E cell line to form aggregates of pancreatic β-cells, so called pseudo-islets, of different sizes in vitro (Zbinden & Urbanczyk et al., **Appendix I**, Figure 1). Pseudo-islet size had a direct impact on viability and functionality, which was monitored over a period of 8 days in culture. Small size pseudo-islets (500 cells/pseudo-islets, average diameter of 206 µm) had the highest GSIS index (~2) and viability after 8 days in culture. This is in agreement with other studies showing that pseudo-islets seeded with less than 1000 cells/pseudo-islets are the most performant[219,220]. The superiority of pseudo-islets over standard 2D culture has been demonstrated in several studies. For instance, primary human pseudo-islets showed an increased GSIS response compared to native isolated islets[221–223]. Pseudo-islets could also be maintained in culture for a longer period of time, while retaining their function[222]. Transplanted in mice, human primary pseudo-islets reversed DM[223].

There are important differences that are species-specific between rodent and human cells[167]. Therefore, in this thesis, we adapted our pseudo-islet protocol using INS1E cells to the human endoC-βH3 cell line as shown in **Figure 8** (Zbinden et al., **Appendix II**, Zbinden & Carvajal Berrio et al., **Appendix III**, Zbinden & Layland et al., **Appendix IV**). The success of the excision process was monitored over time to ensure the removal of the proliferative transgenes and subsequent stop in proliferation (Zbinden & Layland et al., **Appendix IV**, Figure S6A-C). Pseudo-islets of different sizes were tested for insulin secretion, indicating that 1000 cells/pseudo-islets led to the highest insulin secretion per cell (Zbinden & Layland et al., **Appendix IV**, Figure S6D). The resulting optimized human pseudo-islets were viable

and expressed insulin homogeneously throughout the pseudo-islets (Zbinden et al., **Appendix II**, Figure 1). The endoC-βH3 pseudo-islets responded to glucose stimulation with a GSIS index of ~2.5 after 5 days in culture (Zbinden et al., **Appendix II**, Figure 2G).

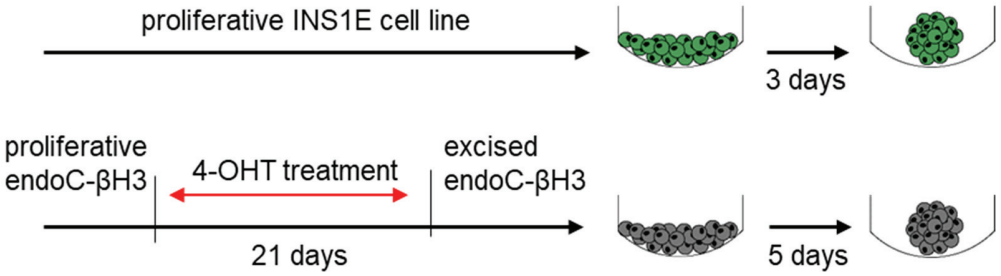

Figure 8: INS1E and endoC-βH3 cell lines. INS1E cells are proliferative and can be seeded in low adherent wells forming pseudo-islets in 3 days. The endoC-βH3 are conditionally immortalized and proliferate in absence of 4-hydroxytamoxifen (4-OHT) treatment. In presence of 4-OHT for 21 days, the proliferative genes are excised. The endoC-βH3 cells form pseudo-islets within 5 days. Illustration adapted from Zbinden et al.[224]

We showed that both, the INS1E and the endoC-βH3 cell lines are glucose-responsive by secreting differential amounts of insulin based on the glucose concentration. In addition, the GSIS indexes of both cell lines are of the same order of magnitude. However, the endoC-βH3 pseudo-islet secretion is in the picogram range (10^{-12} g/mL insulin), while the INS1E pseudo-islet secretion is in the nanogram range (10^{-9} g/mL insulin). In addition, native β-cells ex-vivo can secrete insulin with a GSIS index up to 13[222]. This suggests that the endoC-βH3 pseudo-islets have partially conserved a “fetal phenotype”, although having matured in vivo. However, the endoC-βH3 pseudo-islets have the significant advantage of being from human origin and non-proliferative. EndoC-βH3 pseudo-islets can maintain size and function over 14 days, while INS1E pseudo-islets proliferate, which lead to the formation of large apoptotic cores within pseudo-islets, starting after 8 days in culture. Finally, the methodology to form pseudo-islets generated pseudo-islets with a reproducible size and function. The use of 96-well plates allows the manipulation of hundreds to thousands of pseudo-islets in one experiment.

3.2. Biofunctionalization with Collagen Type 1 and Endothelial Cells Improves Pseudo-Islet Function in a Hypoxia Model

3.2.1. Modelling hypoxia in vitro

Modelling a hypoxic environment in vitro is highly interesting, as it is prevalent in many human physiological processes and diseases[225]. For instance, during the process of transplantation, hypoxic conditions and ischemic injuries are present during the organ procurement, processing, preservation, and subsequent transplantation[226]. In regard to islet transplantation, their oxygen supply is drastically reduced when the islets are separated from their vasculature network, leading to hypoxia[227]. Exposure to sever hypoxia (≤ 1% oxygen) leads to β-cell dysfunction, which compromises their GSIS[228]. Prolongated hypoxia induces non-reversible cellular changes that result in ER stress and ultimately leads to programmed cell death[229]. Transplanted islets are relying on diffusion of oxygen until revascularization is completed, which can last for 10-24 days post-transplantation[230]. In this thesis, we generated a post-transplantation in vitro model using 1% oxygen (Zbinden & Urbanczyk et al., **Appendix I**, Zbinden & Carvajal Berrio et al., **Appendix III**, Zbinden & Layland et al., **Appendix IV**). The overall impact of sever hypoxia was assessed in vitro for 72 hours on the INS1E pseudo-islets and showed an increase in apoptotic markers and a decrease in proliferation, cell-cell contact marker, insulin content and loss of GSIS response (Zbinden & Urbanczyk et al., **Appendix I**, Figure 2A-F). Using the human endoC-βH3 pseudo-islets, time-depended expressions of hypoxic and apoptotic markers were assessed (Zbinden & Carvajal Berrio et al., **Appendix III**, Figure 2A-D). The hypoxia-induced factor 1α (HIF-1α) major expression peak was observed after 6 hours under sever hypoxia, while caspase-3 expression significantly increased after 12 hours (**Figure 9**). Depending on the severity of hypoxia, HIF-1α can act as a pro- or anti-apoptotic transcription factor[231]. Here, the hypoxic conditions were stringent enough to lead to the downstream activation from HIF-1α to caspase-3, leading to a non-reversible pro-apoptotic cascade in both INS1E and endoC-βH3 pseudo-islets[232]. Combined, these two studies give a global insight on the timeline of hypoxia-induced cellular events in vitro. A post-transplantation in vitro model is highly relevant when it comes to bioengineer solutions that aim to counter the damaging effects of a hypoxic microenvironment in vitro and in vivo.

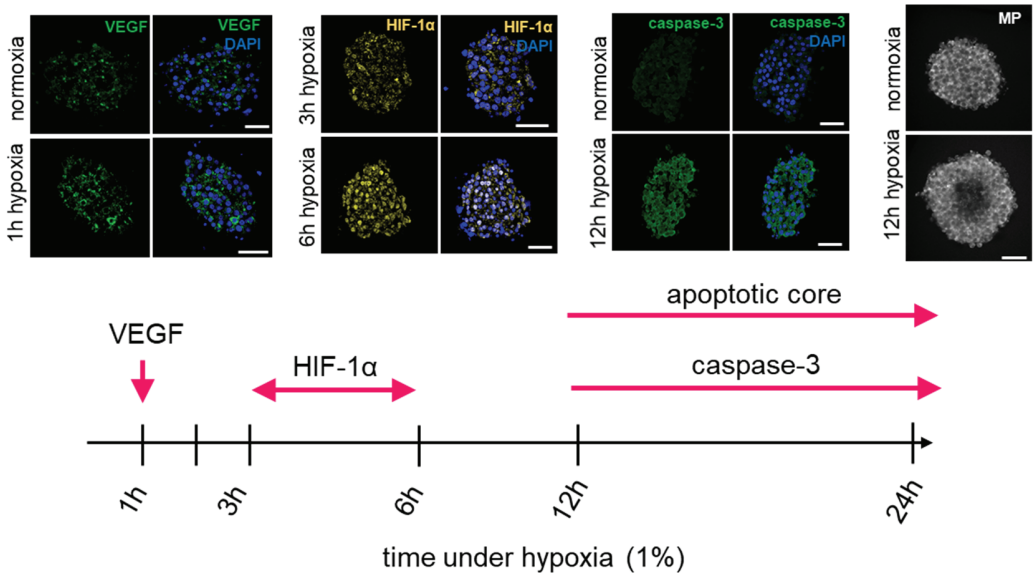

Figure 9: Timeline of hypoxia-induced cellular events in endoC-βH3 pseudo-islets. Expression of VEGF increases after 1 hour under hypoxia. Between 3 and 6 hours under hypoxia, HIF-1α expression significantly increases and is followed by an increase in caspase-3 after 12 hours under hypoxia. The completion of the apoptotic pathways leads to the formation of an apoptotic core that can be detected using multiphoton (MP) imaging. Illustration adapted from Zbinden & Carvajal Berrio et al.[233]

3.2.2. Biofunctionalization using collagen type 1 and endothelial cells

Hypoxia significantly reduced ECM expression of INS1E pseudo-islets, as shown by Raman microspectroscopy (Zbinden & Urbanczyk et al., **Appendix I**, Figure 2G-K). The expression of BM proteins, such as LAM, COL4 and NID1 were significantly altered under hypoxia for 48 hours (Zbinden & Urbanczyk et al., **Appendix I**, Figure 3). It is well established that interstitial ECM and BM are essential for tissue and organ development and homeostasis[133]. Islet survival and function depend on the surrounding microenvironment, which provides mechanical and biological cues that can influence cell fate[234]. To re-create the native pancreatic niche, we used COL1, which is natural polymer derived from the native ECM to encapsulate INS1E pseudo-islets (Zbinden & Urbanczyk et al., **Appendix I**, Figure 4). COL1 contains specific adhesive sequences and binding sites that can initiate signaling cascades, therefore influencing the encapsulated cells[235]. ECM, such as collagens (COL1 and COL4), have been widely used as scaffolds or supplements to promote cell survival and improve insulin secretion in pancreatic islets[236,237]. The combination of LAM and COL4 in an alginate hydrogel reduced cytokine-mediated cell death in human pancreatic islets[153]. Weber et al. biofunctionalized polyethylene glycol with

ECM such as COL1, COL4, LAM, fibrinogen, FN and vitronectin and assed their effects on pancreatic mouse β-cells and mouse islets[145,235]. Interestingly, by blocking specific integrin receptors, the effects could be reversed, highlighting the importance of cell-matrix inteactions[145]. In our study, we showed similar beneficial effects on cell survival and functionality of INS1E pseudo-islets encapsulated in COL1 gel under sever hypoxic conditions for 48 hours (Zbinden & Urbanczyk et al., **Appendix I**, Figure 5). More importantly, we showed that COL1 encapsulation could rescue the expression of the glycoproteins NID1 and DCN in hypoxic INS1E pseudo-islets. However, the expression of BM protein LAM and COL4 remained altered.

Incorporation of pancreatic microvasculature cells, such as pancreatic ECs, with β-cells have been of interest as there is a crosstalk between ECs and β-cells in term of glucose-sensing and regulation[238]. In addition, ECs are the main producers of ECM in the pancreas[239]. Therefore, we asked whether INS1E pseudo-islets could be stimulated by a co-culture with ECs (Zbinden & Urbanczyk et al., **Appendix I**, Figure 6). Co-cultures encapsulated in COL1 had improved functionality, which correlate to several studies where the natural crosstalk between ECs and β-cells has been exploited[240–242]. The beneficial crosstalk between ECs and β-cells was demonstrated in a study from the Schenke-Layland laboratory, where Urbanczyk et al. incorporated human umbilical vein endothelial cells (HUVECs) and endoC-βH3 cells into pseudo-islets using magnetic levitation[241]. The spatial distribution of the two cell types could be controlled and showed that β-cell pseudo-islets surrounded by layers of HUVECs had the highest increase in GSIS and e-cadherin expression, while apoptosis was significantly reduced in vitro**.** Here, we also showed that the incorporation of ECs significantly increased the expression of the BM proteins LAM, COL4 and NID1 in vitro.

A summary of the main results and proposed mechanisms of action are provided in **Figure 10**. We hypothesized that (1) COL1 interacts with receptors present on the cell surface, which lead to signal transduction. In addition, it is possible that the ECM produced by the pseudo-islets positively feedbacks and/or interacts as well with the COL1 gel. (2) The crosstalk between ECs and β-cells occurs by cell-cell contact and by paracrine secretion. It is known that ECs produces TGF-β1, which may positively impact the β-cells[238,243]. Similarly, β-cells secrete VEGF when responding to hypoxia, which may positively impact ECs[8]. Our work highlights the beneficial effect of stimulating β-cells via

cell-ECM and cell-cell interactions, which in turn, improves functionality, viability, and ECM expression of encapsulated cells under sever hypoxia.

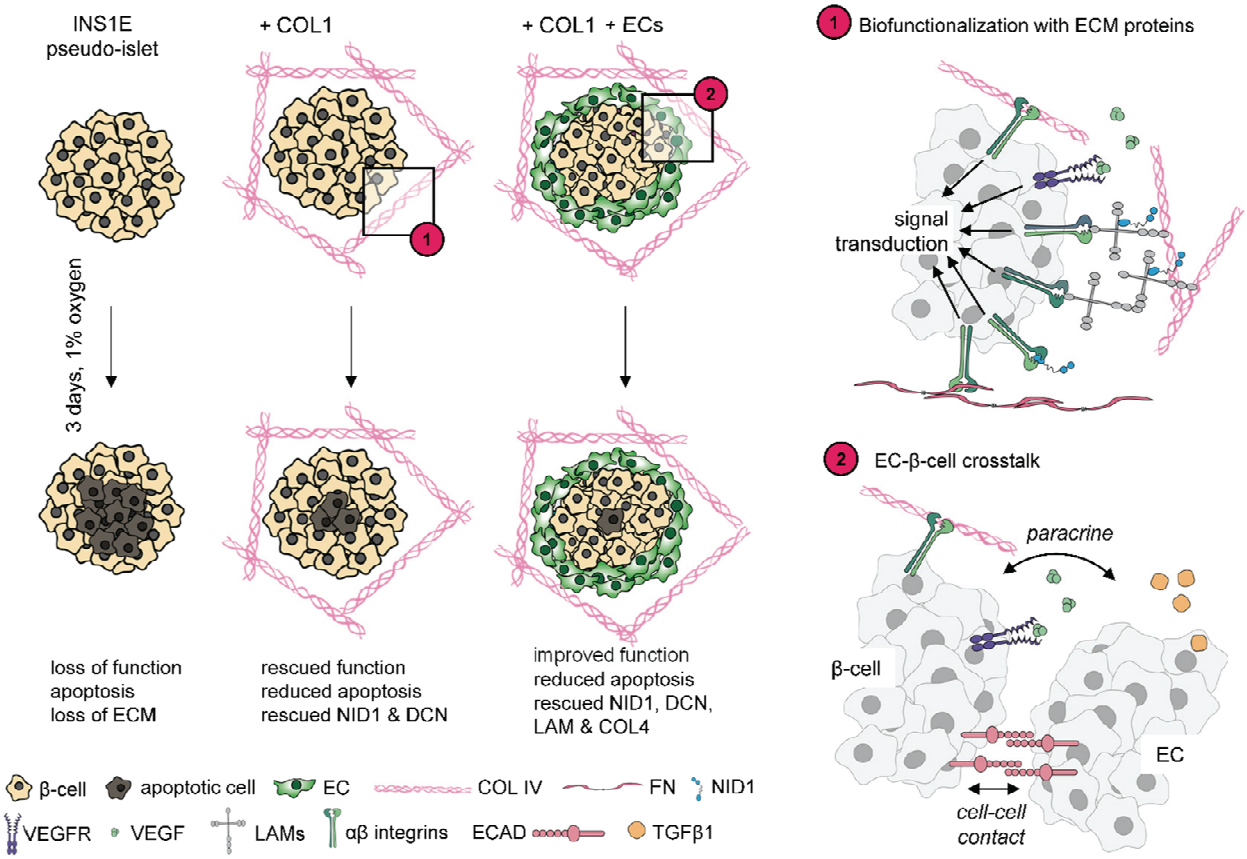

Figure 10: Schematic summarizing the main outcome of the biofunctionalization with COL1 and endothelial cells. INS1E pseudo-islets under hypoxic conditions lose function, become apoptotic and lose ECM expression. COL1 biofunctionalization and endothelial cells promote survival and function of β-cells under hypoxia.

The findings and knowledge generated from our post-transplantation models are valuable and can contribute to the design encapsulation strategies of cell-based therapeutics to treat DM[128]. The goal is to physically separate transplanted islets from the host immune system by a permselective membrane, while providing a microenvironment supporting cell survival and function. Physiochemical and surface properties of the materials are determinant factors to prevent the entry of immune cells, complements and antibodies while allowing diffusion of oxygen, nutriments, metabolites, hormones and waste products[129]. Studies have demonstrated that encapsulation strategies can successfully protect islets from the host immune system[244]. In addition, encapsulation showed promising

results using xenogeneic islets as a safe alternative to cadaveric islets without inducing adverse immune rejection[245].

3.3. Non-Invasive Monitoring of β-Cell Function in a Pancreas-on-a-Chip

3.3.1. Pancreas-on-a-chip to model the pancreatic endocrine function

One important factor that has been overlooked in the presented in vitro models is the lack of vasculature-like perfusion. Our systems are relying on traditional static culture conditions with passive diffusion of compounds, such as oxygen, nutrients or hormones[217]. The organ-on-a-chip (OoC) technology has the potential to overcome some of the limitations of 2D and 3D cultures by combining microphysiological tissue environment together with vasculature-like perfusion[246]. The OoC technology combines the advantages of cell culture (human genetic) with the advantage of animal models (physiological complexity)[35]. The laminar flow of the perfusion allows the spatiotemporal delivery of nutrients, oxygen or other supplements to the microphysiological tissue chamber, while the waste products or released metabolites are transported away either to be discarded or to be sampled for further analysis. In this thesis, we developed a pancreas-on-a-chip system that entraps single human endoC-βH3 pseudo-islets, while providing a continuous vasculature-like low-shear perfusion (Zbinden et al., **Appendix II**, Figure 2A,B). EndoC-βH3 pseudo-islets in the pancreas-on-a-chip maintained viability, insulin expression and GSIS (Zbinden et al., **Appendix II**, Figure 2D-G). Real-time monitoring and assessment of organ-on-a-chips are essential for evaluating the dynamics of various cellular processes. Here, multisampling of the pancreas-on-a-chip efflux was employed in a real-time manner during the glucose stimulation (Zbinden et al., **Appendix II**, Figure 5A). The pancreas-on-a-chip insulin secretion patterns closely mimicked the first and second phase of insulin secretion from human islets[247]. The main characteristics of the pancreas-on-a-chip are illustrated in **Figure 11**.

In the past decade, promising proof-of-principle studies have shown the benefit of OoC technology in mimicking in vivo-like functional responses. For instance, Nguyen et al. used the INS-1 pseudo-islets into a perfused endocrine platform and compared the insulin secretory capacity between INS-1 2D culture, perfused culture, and co-cultures with the intestinal L-cell lines[248]. The Rocheleau group used a similar perfused chamber to assess

the effect of different flow rates on ECs present on isolated mouse islets, which are known to lose density and morphology in culture[249]. More complex platforms were designed by Jun et al. and Lee et al. allowing on-chip aggregation of isolated mouse islet cells and mouse β-cell line into pseudo-islets respectively[250,251]. As a proof-of-concept study for in vitro drug-testing, Jun et al. used two know antidiabetic drugs GLP-1 and tolbutamide to stimulate islets on-chip[251]. In 2020, Walker et al. used primary isolated human islet cells to formed human pseudo-islets in vitro. In addition, the cells were transduced with a biosensor, allowing to visualized changes in calcium concentration on-chip[252]. However, so far, most of the OoC platforms developed used cells from animal origin or primary islets. With the development and recent commercialization of human β-cell lines, the OoC field is expecting to gain momentum, generating physiologically relevant platforms with human genetic background.

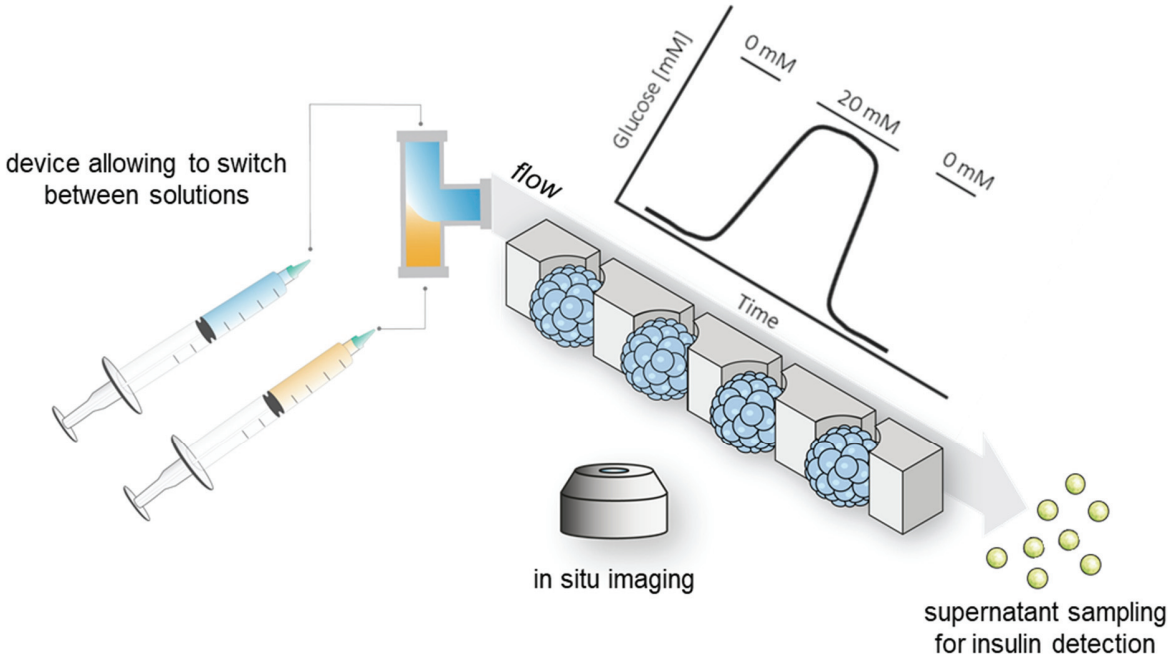

Figure 11: Schematic illustrating the main characteristics of the pancreas-on-a-chip system. The pancreas-on-a-chip can be perfused by different media solutions (i.e., 0 mM glucose or 20 mM glucose) creating a gradient. The supernatant can be collected over time and processed to measure insulin. The pancreas-on-a-chip is bound to thin glass which allow to perform in situ imaging, for instance with Raman microspectroscopy or FLIM.

3.3.2. Non-invasive tools to assess β-cells function

Traditional laboratory techniques that evaluate pancreatic islet viability and function, such as histological sectioning and live/dead staining, are destructive and require the

addition of exogenous dyes[253]. In addition, the use of fluorescence dyes in live staining and imaging is currently debatable, as they may influence the overall cell metabolism. Therefore, the development of novel physiologically relevant in vitro systems requires the integration of non-invasive, marker-free imaging tools to monitor the in vitro systems in real-time. We introduced two studies exploring the use of Raman microspectroscopy and FLIM as promising tools for assessing β-cell function as illustrated in **Figure 12** (Zbinden et al., **Appendix II**, Zbinden & Carvajal Berrio et al., **Appendix III**).

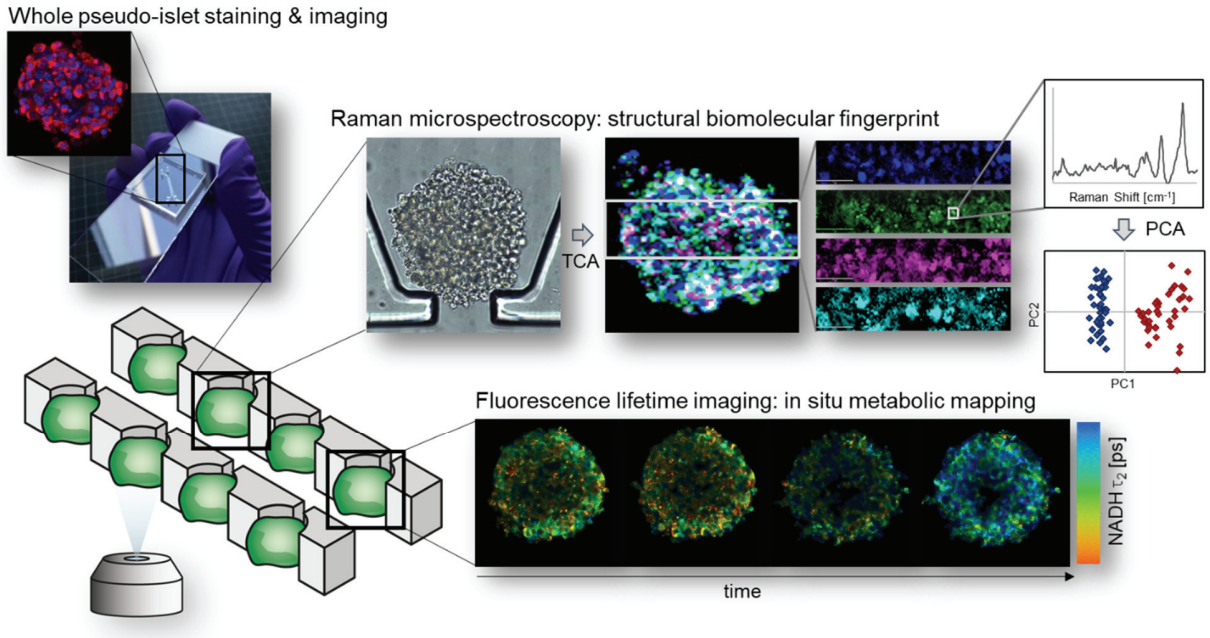

Figure 12: Schematic illustrating the different non-invasive methods used to characterize the pancreas-on-a-chip in situ. The pancreas-on-a-chip is sealed on a thin glass, allowing imaging by confocal microscopy of 3D immunofluorescence staining, Raman microspectroscopy and FLIM. PCA: principal component analysis; TCA: true component analysis. Illustration adapted from Zbinden & Carvajal Berrio et al. and Zbinden et al.[224,233]

Raman microspectroscopy combined with True Component Analysis (TCA) enabled the identification of 3 major structures in human endoC-βH3 pseudo-islets within the pancreas-on-a-chip: lipids, mitochondrial and nuclei (Zbinden et al., **Appendix II**, Figure 3). We showed that the distribution of the TCA mitochondrial component increased from pseudo-islets under Krebs buffer (0 mM glucose) to 20 mM glucose. In addition, using Principal Component Analysis (PCA), in-depth spectral analysis of the TCA lipid component revealed changes in lipid composition during glucose stimulation based on the increase in phosphatidylinositol (Zbinden et al., **Appendix II**, Figure 4). These changes correlate with

the β-cell machinery employed during glucose stimulation to release insulin, where the overall metabolism is increased to process glucose through glycolysis and oxidative phosphorylation[254]. Then, insulin is produced and packed into secreting vesicles, whose lipid compositions were reported to change upon glucose stimulation[255]. By reducing the pixel resolution, real-time monitoring could be achieved by Raman microspectroscopy. These data demonstrate that Raman fingerprints can be used as biomarkers for glucose-induced cellular changes in a pancreas-on-a-chip in vitro model.

Although we showed that pancreatic β-cell response to glucose leads to an overall increase in metabolism, the glucose response in pancreatic β-cells is a highly dynamic process that oscillates in a time-dependent manner[46]. The glucose enters β-cells by passive diffusion through transporters of the GLUT family and is processed in the cytoplasm during glycolysis, which generates, for instance, the coenzyme NADH. The metabolic machinery proceeds within the mitochondria by oxidative phosphorylation, generating NADH and FAD[256]. The ATP concentration increases and leads to the closing of K^+ channels and influx of Ca^{2+}, ultimately resulting in the exocytosis of insulin granules[257].

The metabolism machinery is not only involved in insulin secretion of β-cells, but also in other important cellular processes, such as proliferation, differentiation, metabolic switching in tumor cells, apoptosis, and necrosis [258–260]. Deciphering the dynamism of the metabolic processes such as the time-dependent switch between glycolysis and oxidative phosphorylation would be highly beneficial to evaluate the metabolic state of cells. Importantly, due to the dynamic process, such characterizations should be performed in a non-invasive manner and in real-time. In this thesis, we hypothesized that FLIM could provide valuable insights into the metabolic state of pseudo-islets in a spatial and time-dependent manner. Here, we demonstrated the FLIM can detect metabolic changes due to hypoxic conditions at an early on-set, before the activation of caspase-3 or formation of an apoptotic core (Zbinden & Carvajal Berrio et al., **Appendix III**, Figure 2). In addition, we showed that there is a metabolic spatial distribution within a pseudo-islet characterized by a highly metabolic active outer cell layer (Zbinden & Carvajal Berrio et al., **Appendix III**, Figure 3).

Similar to Raman microspectroscopy, we showed that FLIM can monitor the glucose-response in pseudo-islets (Zbinden & Carvajal Berrio et al., **Appendix III**, Figure 4). FLIM provided complementary information to Raman microspectroscopy on the metabolic state

during glucose stimulation. For instance, glucose stimulation instantaneously altered the lifetimes of cytosolic and mitochondrial NADH, indicating cellular microenvironmental changes, such as pH. In addition, glucose stimulation induced oscillations in NADH α_1 over time and a drop in optical oxidative ratio. These findings indicate an abrupt increase in glycolytic flux, generated by the breaking down of the newly transported glucose in the cytoplasm. The oscillatory behavior of NADH α_1 correlates with the dynamic process of the metabolic machinery during insulin secretion[261]. Importantly, we assessed the metabolic state during glucose stimulation on pseudo-islets subjected to hypoxia for 6 hours and compared their FLIM response to normoxic pseudo-islets (Zbinden & Carvajal Berrio et al., **Appendix III**, Figure 5). Our data indicated that hypoxic pseudo-islets still respond to glucose based on the optical oxidative ratio which decreased during glucose stimulation. However, other parameters such as NADH α_1 did not show any oscillatory behavior. The metabolism machinery in hypoxic β-cells is focused on combatting reactive oxygen species and other hypoxia-induced damage and therefore, it is overloaded when β-cells have to response to glucose. Importantly, FLIM could detect alteration in the metabolic response of hypoxic pseudo-islets which were subjected to hypoxia for 6 hours, while traditional methods such as enzyme-linked immunosorbent assay (ELISA) could not (Zbinden & Carvajal Berrio et al., **Appendix III**, Figure S3).

These two studies (Zbinden et al., **Appendix II** & Zbinden & Carvajal Berrio et al., **Appendix III**) showed how Raman microspectroscopy and FLIM can be used to track pseudo-islet function and survival under different culture conditions in a non-invasive marker-free manner. Combined with the pancreas-on-a-chip system, dynamic cellular processes, such as insulin secretion, can be measured. Although both methods are based on inelastic scattering, their outputs provide distinct information that are complementary. Raman microspectroscopy revealed detailed structural information of the pseudo-islet composition, including proteins, lipids, and nucleic acids. The unique insight into the structure and compositions of tissues by Raman microscopy have been shown by a number of studies, where a high degree of biomolecular specificity and intensities correlated with molecular content[262,263]. In the field of DM, Raman microspectroscopy was used to discriminate between insulin and glucagon within pancreatic islets[264]. In a study from the Liu group, Raman microspectroscopy was used to discriminate between living pancreatic α, β, δ and PP cells[265]. Similarly, Raman microspectroscopy was used to discriminate

between native pancreatic rat islets and the rat INS1 cell line[266]. A clear separation was made based on a higher DNA content and lower protein amount in the cell line. In addition, secretion from human pancreatic islets under different glucose concentrations could be detected in the surrounding medium by surface-enhanced Raman microspectroscopy[267]. Although these studies using Raman microspectroscopy in the DM field have allowed to discriminate between hormones or pancreatic cell type, only few have assessed β-cell function or dysfunction.

While Raman microspectroscopy can detect a large spectrum of molecules and molecular structures, FLIM relies on the autofluorescence lifetimes of two district coenzymes: NADH and FAD, which are involved in different metabolic pathways that generate energy for the cells[212]. FLIM has been used to characterized metabolic processes, such as apoptosis and necrosis, various differentiation of stem cells or metabolic switching in tumors[268–272]. In the DM field, to date, one interesting study from Gregg and associates investigated mouse pancreatic islets using FLIM, where a metabolic decline was observed in an age-dependent manner correlating with a loss of insulin secretion[273]. However, studies utilizing FLIM as a tool to probe β-cell function or dysfunction, so far, remains infrequent.

3.4. The Basement Membrane Protein Nidogen-1 Supports β-Cell Function and Survival in a Hypoxia In Vitro Model

ECM proteins offer important biochemical and mechanical cues influencing cell homeostasis and differentiation[274]. The pancreatic BM is a marker for islet integrity: its disruption contributes to reduced islet yield, viability, and functionality post-isolation[275]. In this thesis, we demonstrated that sever hypoxia not only impaired insulin secretion, but also ECM expression of BM proteins in a post-transplantation in vitro model (Zbinden & Urbanczyk et al., **Appendix I**).

The most predominant component of the BM proteins are collagens, LAM, FN and the nidogens (NID1 and NID2)[9]. LAM have been associated to islet survival and β-cell proliferation in vitro[153]. COL1 and COL4 are essential for a proper BM morphology[9]. In this thesis, we showed the beneficial effect of COL1 gel in a post-transplantation in vitro model (Zbinden & Urbanczyk et al., **Appendix I**). LAM and COL4 are copolymerized into a dense network that are connected by NID1, also known as entactin-1[276–278].

NID1 was identified as a candidate for cardiovascular regenerative approaches by colleagues at the Schenke-Layland laboratory (Zbinden & Layland et al., **Appendix IV**, Figure 1). Briefly, in a myocardial infraction and reperfusion (MI/R) mouse model, injections of the infract border zone with human recombinant NID1 in a hyaluronic acid (HA) carrier improved heart function compared to injection with only the HA carrier (Zbinden & Layland et al., **Appendix IV**, Figure 2). Investigation of the scar tissue quality of the infarct zone indicated a protective effect from NID1 of the cardiovascular cells subjected to an ischemic environment. The protective effect of NID1 was demonstrated in vitro under sever hypoxia on human induced pluripotent stem cells (hiPSC)-cardiomyocytes, where expressions of caspase-3 and $TUNEL^+$ cells were significantly reduced using NID1 as supplement in the media (Zbinden & Layland et al., **Appendix IV**, Figure 3). In addition, NID1 mitigated the hypoxia-induced effects on fibroblasts, reducing the expression of α-smooth muscle actin (αSMA). We also demonstrated that NID1 is pro-angiogenic by increasing tube formation of endothelial cells in vitro. Moreover, NID1 induced the migration of blood monocytes and influenced its polarization towards a phenotype with characteristics of both the M0 and the M2 regenerative subtypes. Importantly, NID1 did not induced a pro-inflammatory phenotype (Zbinden & Layland et al., **Appendix IV**, Figure 5). Altogether, these findings indicate a protective effect of NID1 under hypoxia which is not restricted to a single cell type (**Figure 13**).

Therefore, we asked whether the protective and antifibrotic effects of NID1 under sever hypoxia would benefit in noncardiac therapeutic areas, where ischemia is also present, for instance for islet transplantation. Investigation of the spatial distribution of NID1 in human fetal and adult pancreas showed that NID1 is co-localized with insulin at higher degree compared to COL4, LAM and NID2 (Zbinden & Layland et al., **Appendix IV**, Figure 4A-C). These results suggest that NID1 may have a specific function in β-cells. We showed that insulin secretion could be increased using NID1 at 30 µg/mL for 72 hours as supplement using the human endoC-βH3 pseudo-islets in vitro model (Zbinden & Layland et al., **Appendix IV**, Figure 4D-F). In addition, expression of e-cadherin significantly increased using NID1, indicating that NID1 enhanced cell-cell contact. To model the ischemic conditions present post-transplantation, we subjected the pseudo-islets to sever hypoxia for 72 hours (Zbinden & Layland et al., **Appendix IV**, Figure 4G-I). Under these conditions, NID1 increased the insulin secretion, e-cadherin expression and reduced the expression of

caspase-3 and TUNEL$^+$ cells. Using the pancreas-on-a-chip, the impact on NID1 on hypoxia pseudo-islets was evaluated by Raman microspectroscopy (Zbinden & Layland et al., **Appendix IV**, Figure S6J-O). TCA analysis could identify four major structures: nucleic acids, vesicular lipids, mitochondria and cellular lipids and proteins. Quantifications revealed an increase in TCA vesicular lipid and TCA mitochondria components in pseudo-islets with NID1.

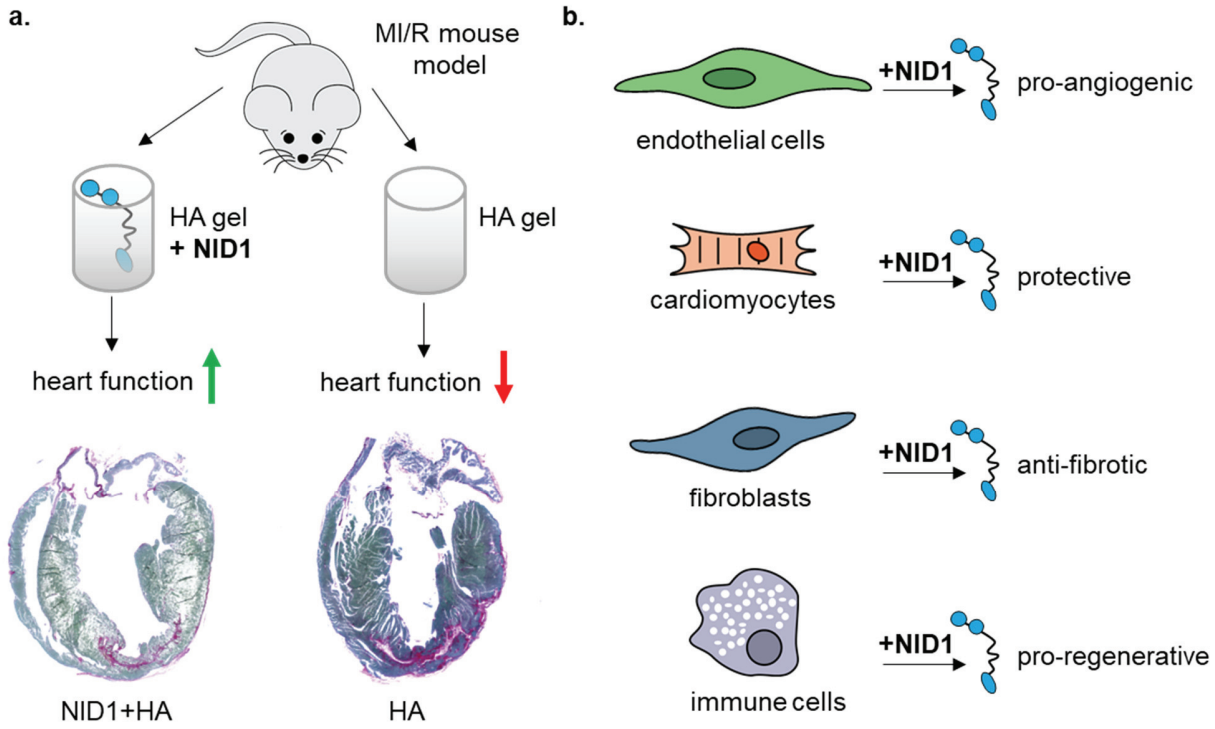

Figure 13: Illustration of the effects of NID1 on cardiovascular cells in vivo and in vitro. (a) In a MI/R mouse model NID1 improved heart function. Histological analysis of heart tissue showed reduced scarring (in pink, picrosirius) in hearts treated with NID1 in the HA carrier compared to the HA carrier only condition. (b) In vitro studies showed a pro-angiogenic effect of NID1 on endothelial cells, a protective effect on cardiomyocytes, an anti-fibrotic effect on fibroblasts and a pro-regenerative effect on immune cells. Illustration adapted from Zbinden & Layland et al.[279]

Translation into clinical trials of therapeutic candidates, such as NID1, requires the understanding of the mechanistic pathways involved. Here, we showed how NID1 binds to the integrin αvβ3 in vitro (Zbinden & Layland et al., **Appendix IV**, Figure 6A). Blocking this integrin on β-cells could reverse the beneficial effect of NID1 on insulin secretion, indicating that the integrin αvβ3 mediated the action of NID1 on β-cells in vitro (Zbinden & Layland et al., **Appendix IV**, Figure 6B). Moreover, specific biological pathways that are activated by NID1 could be identified using a high-throughput digital western blot platform (DigiWest)

(Zbinden & Layland et al., **Appendix IV**, Figure 6E-F)[280]. NID1 binds the integrin αvβ3 and activates the downstream signaling via the MAPK pathway. Downstream effectors such as ERK1/2 are known to be expressed following oxidative stress and can lead to the transcription of anti-apoptotic genes[281,282]. The MAPK pathways is also involved in the GSIS response of β-cells[47]. Here, we also showed an increase of p21, Wnt3 and EpCAM in pseudo-islets treated with NID1. Interestingly, the cell-cycle regulator p21 is among the effectors of the MAPK pathway and can protect different cell types against apoptosis, including myoblasts, hematopoietic stem cells and macrophages[283–287]. Wnt3 increase may arise through a crosstalk with αvβ3 downstream signaling[288–290]. Wnt signaling is involved in β-cell insulin secretion mechanisms on the nuclear transcription level, as well as cell survival[291,292]. The upregulation of Wnt3 is coherent with increased survival and increased insulin secretion of β-cells. Summary of the mechanistic pathways of NID1 is illustrated in **Figure 14**.

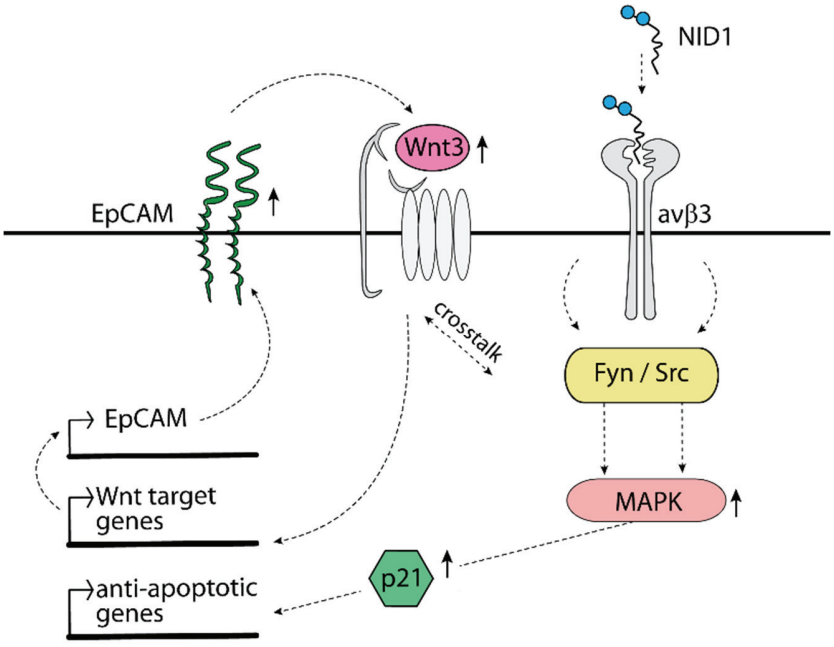

Figure 14: Proposed mechanisms of action of NID1 in β-cells in vitro. NID1 ligation with the integrin αvβ3 upregulating Fyn/Src, which stimulates Wnt3 and the MAPK pathway. Fyn/Src activates the MAPK pathway, upregulating p21, which can be antiapoptotic. Fyn/Src can crosstalk with Wnt3 and EpCAM, enhancing insulin secretion. Illustration adapted from Zbinden & Layland et al.[279]

DigiWest data showed a significant upregulation in EpCAM in NID1-treated β-cells. NID1 and EpCAM have a high sequence homology[293], suggesting that NID1 might bind to

EpCAM. This was confirmed here, for the first time to our knowledge, by a NID1-EpCAM binding assay (**Figure 15A**). We also performed an immunofluorescence staining of EpCAM expression in hypoxic pseudo-islets with NID1 (**Figure 15B**). Semi-quantification showed an increase in EpCAM expression, which corroborate the DigiWest data. Potential pathways and crosstalk between NID1 and EpCAM in illustrated in **Figure 15C**. Increase in EpCAM expression can lead to an increase in Wnt canonical signaling, as the extracellular domain of EpCAM has been shown to cooperate with Wnt signaling by sequestering Kremen1[294,295]. In addition, increase in Wnt might feedback on EpCAM itself, as EpCAM is a target gene of Wnt signaling[296]. This mechanism might contribute to the increase Wnt arising from αvβ3. In addition, the homotypic junction formed by EpCAM can stimulate its own expression[293]. Here, NID1 may have a similar stimulatory role.

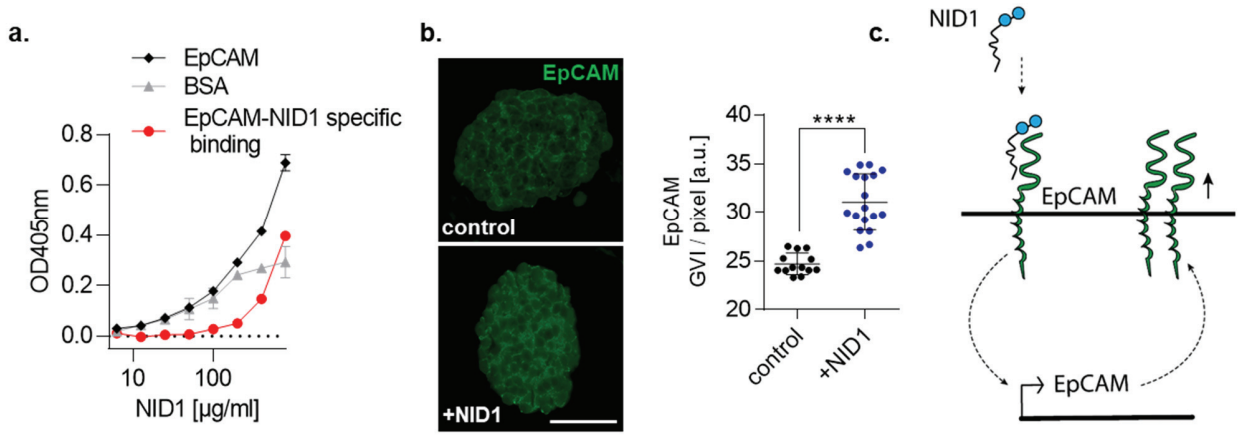

Figure 15: NID1 binds to EpCAM and may stimulate EpCAM expression. (a) Dose-dependent binding assay between immobilized EpCAM and NID1. Specific binding is shown in red. NID1 binds to EpCAM in a dose-depending manner and with a relatively low affinity (< 100 µg/ml). **(b)** Immunofluorescence staining of EpCAM (green) in hypoxic pseudo-islets with and without NID1. Corresponding quantification of the mean grey value intensity per pixel (GVI/pixel) is shown on the right. Unpaired t-test, **** p<0.0001, n=13-18. **(c)** Illustration shows the potential feedback look, where NID1 binds to EpCAM leading to the translation of the EpCAM gene in the nucleus. Scale bar equals 50 µm.

So far NID1 was mostly recognized as a linker protein present in most BMs in the human body. NID1 and have been suggested to play a role in angiogenesis[297], hepatic regeneration[298] and regenerative axon growth and guidance[299,300]. Until now, it was unknown whether the nidogen family is involved in β-cell survival, proliferation, or function. Our results indicates that NID1 enhanced β-cell function in hypoxia by increasing the mitochondrial function, insulin, and insulin-transporting lipid vesicles. For the first time, we demonstrated the protective effect of NID1 on β-cells under normoxic and hypoxic

conditions. Moreover, we identified several mechanistic biological pathways induced by NID1 in vitro. These findings indicate that NID1 have multiple clinical applications not only in the cardiovascular field, but for islet transplantation as well.

Chapter 4

Conclusion

4. Conclusion

The establishment of in vitro models for DM is essential to bridge the gap between pre-clinical studies and human clinical trials. Although animal models have provided considerable knowledge over the past decades, there are important species-specific mechanisms that hinder the clinical translation of target drugs or biological compounds. However, the available in vitro platforms using human biological materials lack physiological relevance and fail to mimic an in vivo-like human responses to drugs or biological compounds. Therefore, there is an urgent need to develop in vitro models that mimic some of the physiological complexity seen in vivo.

In this thesis, we developed aggregates of pancreatic β-cells, so called pseudo-islets, that responded to glucose stimulation by secreting insulin. Pseudo-islets mimicked the 3D spherical structure of human pancreatic islets. The rat insulinoma INS1E cell line was used to optimize pseudo-islet size and culture conditions. The expertise developed was then transferred to form human pseudo-islets based on the conditionally immortalized endoC-βH3 cell line, forming glucose-responsive human pseudo-islets. In addition, we created a post-transplantation in vitro model, where sever hypoxia was induced, mimicking the microenvironment present after islet transplantation. With this model, we evaluated the impact of sever hypoxia on INS1E pseudo-islets and showed how β-cell function, structure and ECM expression were significantly altered. Using biological cues such as COL1 gel and endothelial cells, hypoxia-induced damage could be diminished. COL1 binding to β-cells, as well as cell-cell contact and paracrine signals from the endothelial cells, likely activated downstream protective signaling pathways.

Native islets are highly vascularized, allowing the rapid exchange of nutrients, oxygen, and release of insulin. To mimic these physiological conditions, we developed a pancreas-on-a-chip system which entrapped single endoC-βH3 pseudo-islets in a microfluidic device. The vasculature-like flow allowed for the dynamic glucose stimulation of pseudo-islets. Multisampling of the pancreas-on-a-chip efflux and analysis of the insulin secretion revealed a first and second phase of insulin secretion, an important characteristic of native pancreatic islets in vivo. To non-invasively monitor the function of the pancreas-on-a-chip, we integrated two non-invasive label-free microscopy techniques: Raman microspectroscopy and FLIM. The insulin secretion from pseudo-islets could be assessed in situ by Raman

microspectroscopy based on Raman spectra describing overall mitochondrial function and phospholipid compositions. Using FLIM, we could assess in more detail the metabolic dynamic switches between glycolysis and oxidative phosphorylation. In addition, we used FLIM to identify hypoxia-induced damage in pseudo-islets over time. FLIM could detect at an early onset the metabolic switches occurring in β-cells that activate an adaptive response to hypoxia. Importantly, the high sensitivity of FLIM could identify defects in glucose response, while traditional methods such as ELISA could not.

Using the in vitro models developed in this thesis, we investigated the potential therapeutic effect NID1 on β-cells. NID1 co-localized with insulin in native pancreatic tissue, suggesting a specific role in β-cells. Using recombinant human NID1, we demonstrated the stimulatory effect of NID1 on insulin secretion, and its protective effect on β-cells under hypoxia. Raman microspectroscopy corroborated these findings by showing an increase in insulin-containing vesicular lipids and mitochondrial TCA components in pseudo-islets treated with NID1. Finally, we identified a mechanism of action of NID1 via the integrin αvβ3 and MAPK pathway. We also showed that NID1 binds to EpCAM contributing to the overall beneficial downstream signaling pathways. These findings indicate NID1 as a potential therapeutic candidate to support β-cell function and survival post-transplantation.

Chapter 5

Outlook

5. Outlook

The establishment of physiologically relevant in vitro models for DM remains challenging. With the significant recent technological advances in tissue engineering, microfabrication and cellular engineering, a number of tools are now accessible to researchers, facilitating the future development of in vitro models in the field of DM[35]. The main components to consider designing an in vitro system are illustrated in **Figure 16**. The first choice to make is a relevant source of cells with a human genetic background. This includes primary cells, such as isolated islets, pancreatic cell lines or human embryonic stem cells (hESCs) or iPSC-derived cells. Primary cells are currently the most widely used, however their rare availability and short-term culture limit their application in large screening studies[173]. Pancreatic cell lines, such as the endoC-βH cell lines, can be expanded in large quantity in vitro and provide valuable insights as we and others have shown[178,301,302]. However, their less mature phenotype can be debated. Therefore, the use of human hESCs or hiPSCs to derive the different pancreatic cell types have been of growing interests for in vitro models, disease modelling and cell-based therapy[303,304]. Substantial effort were made to push forwards the differentiation protocols to derived β-cell fully in vitro[305–307]. Recently, Nair et al., developed a protocol of the in vitro differentiation and maturation of hESCs-derived β-cell in 3D which closely recapitulate organogenesis[308]. Immature β-like cells were sorted by FACS based on a GFP insulin reporter gene, and re-aggregated into spheroids. The hESCs-derived β-cell aggregates exhibited functional characteristics that were a step closer to human islets in vitro.

Although pancreatic β-cells play a central role in DM research, collective efforts have been made to include other cell types to mimic the multifactorial characteristics of DM. For instance, primary islets were disaggregated and cell types such as α-cells, δ-cells (, PP-cells and ECs were used in combination with β-cells[222,309,310]. Currently, there are only few alternatives to primary pancreatic isolated cells, including the use of a mouse α-cell line or hESC-derived α-cells, which was recently published by the Melton group[311,312]. Other cell types such as δ-cells, PP-cells or ε-cells, to date, can only be obtained by transplanting hESC- or hiPSC-derived pancreatic progenitor cells into animal models to spontaneously mature in vivo[313]. A number of groups have attempted to differentiate hESCs or hiPSCs into ECs with relevant functional properties in immune, transport, hematological and mechanical

response[314]. So far, there is no method available to differentiate hESCs or hiPSCs into organ- or tissue-specific EC subtypes. Although the differentiation towards hiPSCs-derived pancreatic cell types remains challenging, the use of pancreatic cells derived from hiPSCs will significantly impact the DM field. For instance, hiPSCs-derived pancreatic cell types have the potential to generate patient-specific in vitro models for personalized medicine applications.

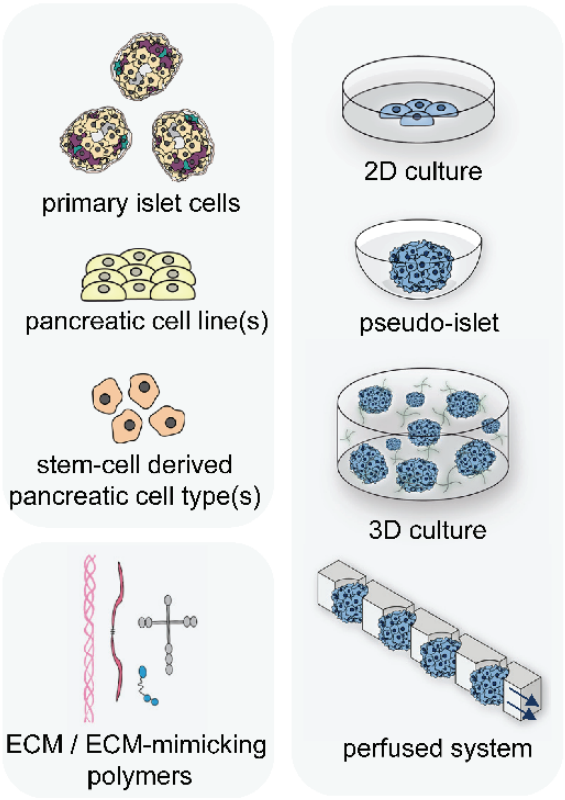

Figure 16: Main components to establish an in vitro system with a human genetic background. The first element to determined is the cell source that will be used in the in vitro systems: primary islets cells, pancreatic cell lines or stem-cell derived pancreatic cells. The second components that can be incorporated into in vitro systems are ECM or ECM-mimicking hydrogels, which will stimulate through integrin/receptor-binding the cells. The last component to determined is the model architecture of the in vitro systems: standard 2D culture, culturing cells as pseudo-islets, incorporating cells into hydrogel and/or using a vasculature-like perfusion system.

The second component relevant to build an in vitro system are pancreatic ECM proteins, which provide biological and mechanical cues to β-cells to promote function and survival[134]. Here, we showed the protective effect of two ECM proteins, COL1 and NID1, on β-cells. In future studies, one should consider the incorporation of other ECM proteins and biomolecules to further improve our system. The combination of different cell types, ECMs and biomolecules has the potential to further improve in vitro models for DM research.

The third component to consider when designing in vitro models, is the model architecture, including traditional 2D monolayer culture, pseudo-islets culture, 3D hydrogel-based culture and perfused systems. Future in vitro models should incorporate the physiological complexity seen in vivo, including ECM-based hydrogels in a 3D manner with a vasculature-like perfusion provided by microfluidics. For instance, combining the COL1 gel with NID1 into the pancreas-on-a-chip would significantly improve the physiological relevance of our model. Physiologically relevant in vitro models require the development of non-invasive label-free imaging tool to monitor and assess in real-time the functionality of the model. We showed the potential of Raman microspectroscopy and FLIM to assess pancreatic β-cell function. In future studies, one could combine these two technologies in a multimodal approach. Although it represents a technological challenge, such multimodal approach could allow the correlation between Raman fingerprint with the oxidative state of the model.

The understanding and knowledge acquired through the development of vitro models are transferable to the design of implant for islet transplantation. Encapsulation and biofunctionalization of cell-based therapeutics are a promising strategy not only alleviating the immune response, but also providing a microenvironment supporting cell survival and function post-transplantation[128]. However, there are important limitations that further need to be explored before achieving long-term survival and functionality of islet transplant (**Figure 17**). These includes: (1) incorporation of biological and mechanical cues to support islets, (2) engineered solutions promoting enhanced vascularization or providing oxygen supply, and (3) biofunctionalization of the islet using other cell types. For instance, hydrogel biofunctionalized with IL-4 and dexamethasone induced the polarization of anti-inflammatory M2 macrophage, thereby modulating the immune response[315]. Similarly, biofunctionalization with Fas ligands induced ligand-mediated apoptosis in T-cell effectors[316]. Xenotransplantation outcome from a rat-to-mice model were significantly improved by the co-transplantation of autologous regulatory IL-10 murine dendritic cells in absence of any additional immunosuppressive therapy[317]. In addition, several studies have reported the benefit of transplanting MSCs with islets in term of graft efficacy in animal models[318–322]. In the future, our work may contribute beneficially to the outcome of islet transplantation. Incorporation of NID1 and COL1 with encapsulated cells could increase the

survival rate and function of transplanted islets. Similarly, providing endothelial cells, which secrete VEGF, may improve the neovascularization of transplanted islets.

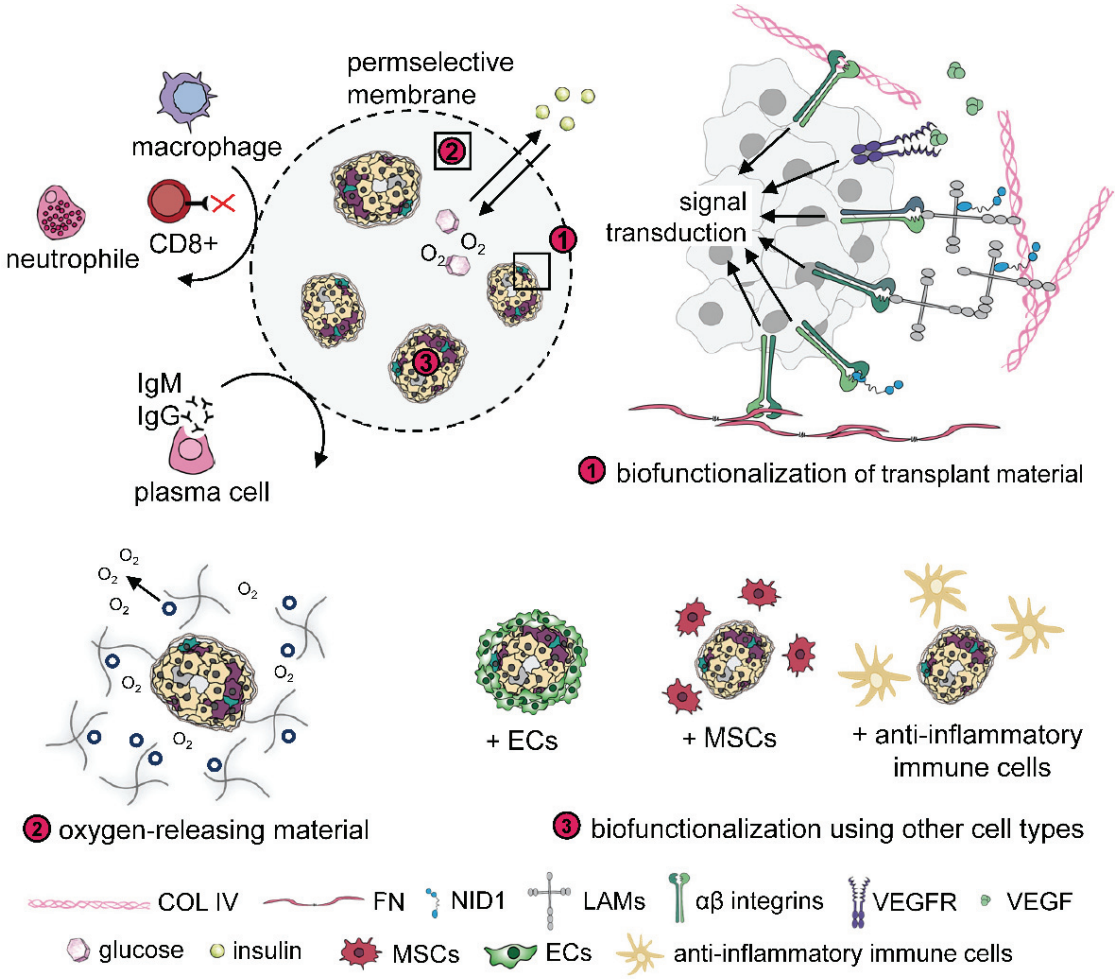

Figure 17: Encapsulation and biofunctionalization for islet transplant. Encapsulation strategies of islets aim to physically separate host immune cells from the transplant, while allowing diffusion of small molecules, such as glucose, insulin or oxygen and blocking the entry of larger proteins such as IgM or IgG. Key research areas focus on: ❶ biofunctionalization of the transplant material, using pancreatic ECM proteins such as COL4, FN, LAM and/or biomolecules such as VEGF to promote vascularization;❷ developing oxygen-releasing materials, alleviating the hypoxic conditions; ❸ co-transplantation of islet cells with other cell types.

References

1. Jouvet, N. & Estall, J. L. The pancreas: Bandmaster of glucose homeostasis. *Exp. Cell Res.* **360,** 19–23 (2017).
2. Keller, J. Human pancreatic exocrine response to nutrients in health and disease. *Gut* **54,** 1–28 (2005).
3. Efrat, S. & Russ, H. A. Making β cells from adult tissues. *Trends Endocrinol. Metab.* **23,** 278–285 (2012).
4. Röder, P. V., Wu, B., Liu, Y. & Han, W. Pancreatic regulation of glucose homeostasis. *Exp. Mol. Med.* **48,** e219 (2016).
5. Ionescu-Tirgoviste, C., Gagniuc, P. A., Gubceac, E., Mardare, L., Popescu, I., Dima, S. & Militaru, M. A 3D map of the islet routes throughout the healthy human pancreas. *Sci. Rep.* **5,** 14634 (2015).
6. Saito, K., Iwama, N. & Takahashi, T. Morphometrical analysis on topographical difference in size distribution, number and volume of islets in the human pancreas. *Tohoku J. Exp. Med.* **124,** 177–86 (1978).
7. Steiner, D. J., Kim, A., Miller, K. & Hara, M. Pancreatic islet plasticity: Interspecies comparison of islet architecture and composition. *Islets* **2,** 135 (2010).
8. Townsend, S. E. & Gannon, M. Extracellular Matrix–Associated Factors Play Critical Roles in Regulating Pancreatic β-Cell Proliferation and Survival. *Endocrinology* **160,** 1885–1894 (2019).
9. Lammert, E. & Kragl, M. in *Islets of Langerhans* **654,** 39–58 (Springer Netherlands, 2015).
10. Otonkoski, T., Banerjee, M., Korsgren, O., Thornell, L.-E. & Virtanen, I. Unique basement membrane structure of human pancreatic islets: implications for β-cell growth and differentiation. *Diabetes, Obes. Metab.* **10,** 119–127 (2008).
11. Arous, C. & Wehrle-Haller, B. Role and impact of the extracellular matrix on integrin-mediated pancreatic β-cell functions. *Biol. Cell* **109,** 223–237 (2017).
12. Bosco, D., Meda, P., Halban, P. A. & Rouiller, D. G. Importance of cell-matrix interactions in rat islet beta-cell secretion in vitro: role of alpha6beta1 integrin. *Diabetes* **49,** 233–243 (2000).
13. Hammar, E. B., Irminger, J.-C., Rickenbach, K., Parnaud, G., Ribaux, P., Bosco, D., Rouiller, D. G. & Halban, P. A. Activation of NF-κB by Extracellular Matrix Is Involved in Spreading and Glucose-stimulated Insulin Secretion of Pancreatic Beta Cells. *J. Biol. Chem.* **280,** 30630–30637 (2005).
14. Hammar, E., Tomas, A., Bosco, D. & Halban, P. A. Role of the Rho-ROCK (Rho-Associated Kinase) Signaling Pathway in the Regulation of Pancreatic β-Cell Function. *Endocrinology* **150,** 2072–2079 (2009).
15. Humphries, J. D., Byron, A. & Humphries, M. J. Integrin ligands at a glance. *J. Cell Sci.* **119,** 3901–3903 (2006).
16. Takada, Y., Ye, X. & Simon, S. The integrins. *Genome Biol.* **8,** 215 (2007).
17. Petersen, M. C. & Shulman, G. I. Mechanisms of insulin action and insulin resistance. *Physiol. Rev.* **98,** 2133–2223 (2018).
18. Adeva-Andany, M. M., Funcasta-Calderón, R., Fernández-Fernández, C., Castro-Quintela, E. & Carneiro-Freire, N. Metabolic effects of glucagon in humans. *J. Clin. Transl. Endocrinol.* **15,** 45–53 (2019).
19. Cabrera, O., Berman, D. M., Kenyon, N. S., Ricordi, C., Berggren, P.-O. & Caicedo, A. The unique cytoarchitecture of human pancreatic islets has implications for islet cell function. *Proc. Natl. Acad. Sci.* **103,** 2334–2339 (2006).
20. Brissova, M., Fowler, M. J., Nicholson, W. E., Chu, A., Hirshberg, B., Harlan, D. M. & Powers, A. C. Assessment of Human Pancreatic Islet Architecture and Composition by Laser Scanning Confocal Microscopy. *J. Histochem. Cytochem.* **53,** 1087–1097 (2005).

21. Orci, L., Baetens, D., Ravazzola, M., Stefan, Y. & Malaisse-Lagae, F. Pancreatic polypeptide and glucagon: Non-random distribution in pancreatic islets. *Life Sci.* **19,** 1811–1816 (1976).
22. Ichii, H., Inverardi, L., Pileggi, A., Molano, R. D., Cabrera, O., Caicedo, A., Messinger, S., Kuroda, Y., Berggren, P.-O. & Ricordi, C. A Novel Method for the Assessment of Cellular Composition and Beta-Cell Viability in Human Islet Preparations. *Am. J. Transplant.* **5,** 1635–1645 (2005).
23. Rorsman, P. & Huising, M. O. The somatostatin-secreting pancreatic δ-cell in health and disease. *Nat. Rev. Endocrinol.* **14,** 404–414 (2018).
24. Aragón, F., Karaca, M., Novials, A., Maldonado, R., Maechler, P. & Rubí, B. Pancreatic polypeptide regulates glucagon release through PPYR1 receptors expressed in mouse and human alpha-cells. *Biochim. Biophys. Acta - Gen. Subj.* **1850,** 343–351 (2015).
25. Batterham, R. L., Le Roux, C. W., Cohen, M. A., Park, A. J., Ellis, S. M., Patterson, M., Frost, G. S., Ghatei, M. A. & Bloom, S. R. Pancreatic polypeptide reduces appetite and food intake in humans. *J. Clin. Endocrinol. Metab.* **88,** 3989–3992 (2003).
26. Wierup, N., Sundler, F. & Heller, R. S. The islet ghrelin cell. *J. Mol. Endocrinol.* **52,** R35–R49 (2014).
27. Heller, R. S., Jenny, M., Collombat, P., Mansouri, A., Tomasetto, C., Madsen, O. D., Mellitzer, G., Gradwohl, G. & Serup, P. Genetic determinants of pancreatic ε-cell development. *Dev. Biol.* **286,** 217–224 (2005).
28. Wierup, N., Svensson, H., Mulder, H. & Sundler, F. The ghrelin cell: a novel developmentally regulated islet cell in the human pancreas. *Regul. Pept.* **107,** 63–69 (2002).
29. Egido, E. M., Rodriguez-Gallardo, J., Silvestre, R. A. & Marco, J. Inhibitory effect of ghrelin on insulin and pancreatic somatostatin secretion. *Eur. J. Endocrinol.* **146,** 241–4 (2002).
30. Broglio, F., Gottero, C., Benso, A., Prodam, F., Destefanis, S., Gauna, C., Maccario, M., Deghenghi, R., van der Lely, A. J. & Ghigo, E. Effects of Ghrelin on the Insulin and Glycemic Responses to Glucose, Arginine, or Free Fatty Acids Load in Humans. *J. Clin. Endocrinol. Metab.* **88,** 4268–4272 (2003).
31. Salehi, A. Effects of ghrelin on insulin and glucagon secretion: a study of isolated pancreatic islets and intact mice. *Regul. Pept.* **118,** 143–150 (2004).
32. Arosio, M., Ronchi, C. L., Gebbia, C., Cappiello, V., Beck-Peccoz, P. & Peracchi, M. Stimulatory Effects of Ghrelin on Circulating Somatostatin and Pancreatic Polypeptide Levels. *J. Clin. Endocrinol. Metab.* **88,** 701–704 (2003).
33. Saltiel, A. R. in *Handb. Exp. Pharmacol.* **233,** 51–71 (Springer New York LLC, 2015).
34. Rui, L. Energy metabolism in the liver. *Compr. Physiol.* **4,** 177–197 (2014).
35. Rogal, J., Zbinden, A., Schenke-Layland, K. & Loskill, P. Stem-cell based organ-on-a-chip models for diabetes research. *Adv. Drug Deliv. Rev.* **140,** (2018).
36. Fu, Z., R. Gilbert, E. & Liu, D. Regulation of Insulin Synthesis and Secretion and Pancreatic Beta-Cell Dysfunction in Diabetes. *Curr. Diabetes Rev.* **9,** 25–53 (2012).
37. Henquin, J.-C., Ishiyama, N., Nenquin, M., Ravier, M. A. & Jonas, J.-C. Signals and Pools Underlying Biphasic Insulin Secretion. *Diabetes* **51,** S60–S67 (2002).
38. McCulloch, L. J., van de Bunt, M., Braun, M., Frayn, K. N., Clark, A. & Gloyn, A. L. GLUT2 (SLC2A2) is not the principal glucose transporter in human pancreatic beta cells: Implications for understanding genetic association signals at this locus. *Mol. Genet. Metab.* **104,** 648–653 (2011).
39. Matschinsky, F. M. & Wilson, D. F. The central role of glucokinase in glucose homeostasis: A perspective 50 years after demonstrating the presence of the enzyme in islets of Langerhans. *Front. Physiol.* **10,** 148 (2019).
40. Jitrapakdee, S., Wutthisathapornchai, A., Wallace, J. C. & MacDonald, M. J. Regulation of insulin secretion: Role of mitochondrial signalling. *Diabetologia* **53,** 1019–1032 (2010).
41. Klec, C., Ziomek, G., Pichler, M., Malli, R. & Graier, W. F. Calcium signaling in ß-cell physiology and pathology: A revisit. *Int. J. Mol. Sci.* **20,** (2019).
42. Strehler, E. & Treiman, M. Calcium Pumps of Plasma Membrane and Cell Interior. *Curr. Mol.*

Med. **4,** 323–335 (2005).
43. Blaustein, M. P. & Lederer, W. J. Sodium/Calcium Exchange: Its Physiological Implications. *Physiol. Rev.* **79,** 763–854 (1999).
44. Prasad, V., Okunade, G. W., Miller, M. L. & Shull, G. E. Phenotypes of SERCA and PMCA knockout mice. *Biochem. Biophys. Res. Commun.* **322,** 1192–1203 (2004).
45. Gilon, P., Ravier, M. A., Jonas, J. C. & Henquin, J. C. Control mechanisms of the oscillations of insulin secretion in vitro and in vivo. in *Diabetes* **51,** S144–S151 (American Diabetes Association Inc., 2002).
46. Kennedy, R. T., Kauri, L. M., Dahlgren, G. M. & Jung, S. K. Metabolic oscillations in β-cells. in *Diabetes* **51,** S152–S161 (American Diabetes Association, 2002).
47. Kalwat, M. A. & Thurmond, D. C. Signaling mechanisms of glucose-induced F-actin remodeling in pancreatic islet β cells. *Exp. Mol. Med.* **45,** e37 (2013).
48. Zhang, W., Thompson, B. J., Hietakangas, V. & Cohen, S. M. MAPK/ERK signaling regulates insulin sensitivity to control glucose metabolism in Drosophila. *PLoS Genet.* **7,** 1–10 (2011).
49. Sidarala, V. & Kowluru, A. The Regulatory Roles of Mitogen-Activated Protein Kinase (MAPK) Pathways in Health and Diabetes: Lessons Learned from the Pancreatic β-Cell. *Recent Pat. Endocr. Metab. Immune Drug Discov.* **10,** 76–84 (2016).
50. Diagnosis and Classification of Diabetes Mellitus. *Diabetes Care* **37,** S81–S90 (2014).
51. International Diabetes Federation. *IDF Diabetes Atlas, 9th edn.* (2019). at <http://www.diabetesatlas.org>
52. Kharroubi, A. T. Diabetes mellitus: The epidemic of the century. *World J. Diabetes* **6,** 850 (2015).
53. Katsarou, A., Gudbjörnsdottir, S., Rawshani, A., Dabelea, D., Bonifacio, E., Anderson, B. J., Jacobsen, L. M., Schatz, D. A. & Lernmark, A. Type 1 diabetes mellitus. *Nat. Rev. Dis. Prim.* **3,** 1–17 (2017).
54. DeFronzo, R. A., Ferrannini, E., Groop, L., Henry, R. R., Herman, W. H., Holst, J. J., Hu, F. B., Kahn, C. R., Raz, I., Shulman, G. I., Simonson, D. C., Testa, M. A. & Weiss, R. Type 2 diabetes mellitus. *Nat Rev Dis Prim.* **1,** 15019 (2015).
55. Permutt, M. A., Wasson, J. & Cox, N. Genetic epidemiology of diabetes. *J. Clin. Invest.* **115,** 1431–1439 (2005).
56. McDevitt, H. O. Characteristics of autoimmunity in type 1 diabetes and type 1.5 overlap with type 2 diabetes. *Diabetes* **54,** S4–S10 (2005).
57. Polychronakos, C. & Li, Q. Understanding type 1 diabetes through genetics: advances and prospects. *Nat. Rev. Genet.* **12,** 781–792 (2011).
58. Hyttinen, V., Kaprio, J., Kinnunen, L., Koskenvuo, M. & Tuomilehto, J. Genetic Liability of Type 1 Diabetes and the Onset Age Among 22,650 Young Finnish Twin Pairs: A Nationwide Follow-Up Study. *Diabetes* **52,** 1052–1055 (2003).
59. Nejentsev, S., Howson, J. M. M., Walker, N. M., Szeszko, J., Field, S. F., Stevens, H. E., Reynolds, P., Hardy, M., King, E., Masters, J., Hulme, J., Maier, L. M., Smyth, D., Bailey, R., Cooper, J. D., Ribas, G., Campbell, R. D., Clayton, D. G. & Todd, J. A. Localization of type 1 diabetes susceptibility to the MHC class I genes HLA-B and HLA-A. *Nature* **450,** 887–892 (2007).
60. Knip, M., Veijola, R., Virtanen, S. M., Hyoty, H., Vaarala, O. & Akerblom, H. K. Environmental Triggers and Determinants of Type 1 Diabetes. *Diabetes* **54,** S125–S136 (2005).
61. Jeker, L. T., Bour-Jordan, H. & Bluestone, J. A. Breakdown in peripheral tolerance in type 1 diabetes in mice and humans. *Cold Spring Harb. Perspect. Med.* **2,** (2012).
62. Kahn, S. E., Hull, R. L. & Utzschneider, K. M. Mechanisms linking obesity to insulin resistance and type 2 diabetes. *Nature* **444,** 840–846 (2006).
63. Yaturu, S. Obesity and type 2 diabetes. *J. Diabetes Mellit.* **01,** 79–95 (2011).
64. McCarthy, M. I. Genomics, Type 2 Diabetes, and Obesity. *N. Engl. J. Med.* **363,** 2339–2350 (2010).
65. Bonnefond, A., Froguel, P. & Vaxillaire, M. The emerging genetics of type 2 diabetes. *Trends*

Mol. Med. **16,** 407–416 (2010).
66. Karamitsos, D. T. The story of insulin discovery. *Diabetes Res. Clin. Pract.* **93,** S2 (2011).
67. Ahmad, K. Insulin sources and types: a review of insulin in terms of its mode on diabetes mellitus. *J. Tradit. Chinese Med.* **34,** 234–237 (2014).
68. Janež, A., Guja, C., Mitrakou, A., Lalic, N., Tankova, T., Czupryniak, L., Tabák, A. G., Prazny, M., Martinka, E. & Smircic-Duvnjak, L. Insulin Therapy in Adults with Type 1 Diabetes Mellitus: a Narrative Review. *Diabetes Ther.* **11,** 387–409 (2020).
69. Hanefeld, M. Use of insulin in type 2 diabetes: What we learned from recent clinical trials on the benefits of early insulin initiation. *Diabetes Metab.* **40,** 391–399 (2014).
70. Cohen, O., Filetti, S., Castañeda, J., Maranghi, M. & Glandt, M. When Intensive Insulin Therapy (MDI) Fails in Patients With Type 2 Diabetes: Switching to GLP-1 Receptor Agonist Versus Insulin Pump. *Diabetes Care* **39,** S180–S186 (2016).
71. Grunberger, G. The need for better insulin therapy. *Diabetes, Obes. Metab.* **15,** 1–5 (2013).
72. Forbes, J. M. & Cooper, M. E. Mechanisms of diabetic complications. *Physiol Rev* **93,** 137–188 (2013).
73. Tuomilehto, J., Lindström, J., Eriksson, J. G., Valle, T. T., Hämäläinen, H., Ilanne-Parikka, P., Keinänen-Kiukaanniemi, S., Laakso, M., Louheranta, A., Rastas, M., Salminen, V., Aunola, S., Cepaitis, Z., Moltchanov, V., Hakumäki, M., Mannelin, M., Martikkala, V., Sundvall, J. & Uusitupa, M. Prevention of Type 2 Diabetes Mellitus by Changes in Lifestyle among Subjects with Impaired Glucose Tolerance. *N. Engl. J. Med.* **344,** 1343–1350 (2001).
74. Turner, R. C. Glycemic Control With Diet, Sulfonylurea, Metformin, or Insulin in Patients With Type 2 Diabetes Mellitus:Progressive Requirement for Multiple Therapies (UKPDS 49). UK Prospective Diabetes Study (UKPDS) Group. *JAMA* **281,** 2005 (1999).
75. Nathan, D. M., Buse, J. B., Davidson, M. B., Ferrannini, E., Holman, R. R., Sherwin, R. & Zinman, B. Medical Management of Hyperglycemia in Type 2 Diabetes: A Consensus Algorithm for the Initiation and Adjustment of Therapy: A consensus statement of the American Diabetes Association and the European Association for the Study of Diabetes. *Clin. Diabetes* **27,** 4–16 (2009).
76. Lebovitz, H. E. Type 2 diabetes mellitus-current therapies and the emergence of surgical options. *Nat. Rev. Endocrinol.* **7,** 408–419 (2011).
77. Hundal, R. S. & Inzucchi, S. E. Metformin. *Drugs* **63,** 1879–1894 (2003).
78. Drucker, D. J. Dipeptidyl Peptidase-4 Inhibition and the Treatment of Type 2 Diabetes: Preclinical biology and mechanisms of action. *Diabetes Care* **30,** 1335–1343 (2007).
79. Holst, J. J. The Physiology of Glucagon-like Peptide 1. *Physiol. Rev.* **87,** 1409–1439 (2007).
80. Proks, P., Reimann, F., Green, N., Gribble, F. & Ashcroft, F. Sulfonylurea Stimulation of Insulin Secretion. *Diabetes* **51,** S368–S376 (2002).
81. Lamos, E. L., Stein, S. A. & Davis, S. N. Sulfonylureas and meglitinides: historical and contemporary issues. *Panminerva Med.* **55,** 239–51 (2013).
82. Hoerger, T. J., Zhang, P., Segel, J. E., Gregg, E. W., Narayan, K. M. V. & Hicks, K. A. Improvements in risk factor control among persons with diabetes in the United States: Evidence and implications for remaining life expectancy. *Diabetes Res. Clin. Pract.* **86,** 225–232 (2009).
83. Hoerger, T. J., Segel, J. E., Gregg, E. W. & Saaddine, J. B. Is Glycemic Control Improving in U.S. Adults? *Diabetes Care* **31,** 81–86 (2008).
84. Reckard, C. R. & Barker, C. F. Transplantation of isolated pancreatic islets across strong and weak histocompatibility barriers. *Transplant. Proc.* **5,** 761–3 (1973).
85. Ballinger, W. F. & Lacy, P. E. Transplantation of intact pancreatic islets in rats. *Surgery* **72,** 175–86 (1972).
86. Shapiro, A. M. J., Lakey, J. R. T., Ryan, E. A., Korbutt, G. S., Toth, E., Warnock, G. L., Kneteman, N. M. & Rajotte, R. V. Islet Transplantation in Seven Patients with Type 1 Diabetes Mellitus Using a Glucocorticoid-Free Immunosuppressive Regimen. *N. Engl. J. Med.* **343,** 230–238 (2000).

87. Ryan, E. A., Lakey, J. R. T., Paty, B. W., Imes, S., Korbutt, G. S., Kneteman, N. M., Bigam, D., Rajotte, R. V. & Shapiro, A. M. J. Successful Islet Transplantation: Continued Insulin Reserve Provides Long-Term Glycemic Control. *Diabetes* **51,** 2148–2157 (2002).
88. Shapiro, A. M. J., Ricordi, C., Hering, B. J., Auchincloss, H., Lindblad, R., Robertson, R. P., Secchi, A., Brendel, M. D., Berney, T., Brennan, D. C., Cagliero, E., Alejandro, R., Ryan, E. A., DiMercurio, B., Morel, P., Polonsky, K. S., Reems, J.-A., Bretzel, R. G., Bertuzzi, F., Froud, T., Kandaswamy, R., Sutherland, D. E. R., Eisenbarth, G., Segal, M., Preiksaitis, J., Korbutt, G. S., Barton, F. B., Viviano, L., Seyfert-Margolis, V., Bluestone, J. & Lakey, J. R. T. International Trial of the Edmonton Protocol for Islet Transplantation. *N. Engl. J. Med.* **355,** 1318–1330 (2006).
89. Ryan, E. A., Paty, B. W., Senior, P. A., Bigam, D., Alfadhli, E., Kneteman, N. M., Lakey, J. R. T. & Shapiro, A. M. J. Five-Year Follow-Up After Clinical Islet Transplantation. *Diabetes* **54,** 2060–2069 (2005).
90. Naftanel, M. A. & Harlan, D. M. Pancreatic islet transplantation. *PLoS Med.* **1,** 198–201 (2004).
91. Cross, S. E., Vaughan, R. H., Willcox, A. J., McBride, A. J., Abraham, A. A., Han, B., Johnson, J. D., Maillard, E., Bateman, P. A., Ramracheya, R. D., Rorsman, P., Kadler, K. E., Dunne, M. J., Hughes, S. J. & Johnson, P. R. V. Key Matrix Proteins Within the Pancreatic Islet Basement Membrane Are Differentially Digested During Human Islet Isolation. *Am. J. Transplant.* **17,** 451–461 (2017).
92. Weber, D. J. FDA regulation of allogeneic islets as a biological product. *Cell Biochem. Biophys.* **40,** 19–22 (2004).
93. Loganathan, G., Dawra, R. K., Pugazhenthi, S., Guo, Z., Soltani, S. M., Wiseman, A., Sanders, M. A., Papas, K. K., Velayutham, K., Saluja, A. K., Sutherland, D. E. R., Hering, B. J. & Balamurugan, A. N. Insulin degradation by acinar cell proteases creates a dysfunctional environment for human islets before/after transplantation: Benefits of α-1 antitrypsin treatment. *Transplantation* **92,** 1222–1230 (2011).
94. Toso, C., Zaidi, H., Morel, P., Armanet, M., Andres, A., Pernin, N., Baertschiger, R., Slosman, D., Bühler, L. H., Bosco, D. & Berney, T. Positron-Emission Tomography Imaging of Early Events after Transplantation of Islets of Langerhans. *Transplantation* **79,** 353–355 (2005).
95. Eich, T., Eriksson, O., Sundin, A., Estrada, S., Brandhorst, D., Brandhorst, H., Langstrom, B., Nilsson, B., Korsgren, O. & Lundgren, T. Positron Emission Tomography: A Real-Time Tool to Quantify Early Islet Engraftment in a Preclinical Large Animal Model. *Transplantation* **84,** 893–898 (2007).
96. Delaune, V., Berney, T., Lacotte, S. & Toso, C. Intraportal islet transplantation: the impact of the liver microenvironment. *Transpl. Int.* **30,** 227–238 (2017).
97. Rabinovitch, A. & Suarez-Pinzon, W. L. Cytokines and Their Roles in Pancreatic Islet β-Cell Destruction and Insulin-Dependent Diabetes Mellitus. *Biochem. Pharmacol.* **55,** 1139–1149 (1998).
98. Bennet, W., Sundberg, B., Groth, C. G., Brendel, M. D., Brandhorst, D., Brandhorst, H., Bretzel, R. G., Elgue, G., Larsson, R., Nilsson, B. & Korsgren, O. Incompatibility between human blood and isolated islets of langerhans: A finding with implications for clinical intraportal islet transplantation? *Diabetes* **48,** 1907–1914 (1999).
99. Kirchhof, N., Shibata, S., Wijkstrom, M., Kulick, D. M., Salerno, C. T., Clemmings, S. M., Heremans, Y., Galili, U., Sutherland, D. E. R., Dalmasso, A. P. & Hering, B. J. Reversal of diabetes in non-immunosuppressed rhesus macaques by intraportal porcine islet xenografts precedes acute cellular rejection. *Xenotransplantation* **11,** 396–407 (2004).
100. Badet, L., Titus, T., Metzen, E., Handa, A., McShane, P., Chang, L.-W., Giangrande, P. & Gray, D. W. R. The interaction between primate blood and mouse islets induces accelerated clotting with islet destruction. *Xenotransplantation* **9,** 91–96 (2002).
101. Anazawa, T., Okajima, H., Masui, T. & Uemoto, S. Current state and future evolution of pancreatic islet transplantation. *Ann. Gastroenterol. Surg.* **3,** 34–42 (2019).

102. Matsumoto, S., Noguchi, H., Naziruddin, B., Onaca, N., Jackson, A., Hatanaka, N., Okitsu, T., Kobayashi, N., Klintmalm, G. & Levy, M. Improvement of Pancreatic Islet Cell Isolation for Transplantation. *Baylor Univ. Med. Cent. Proc.* **20,** 357–362 (2007).
103. Brandhorst, D., Brandhorst, H. & Johnson, P. R. V. Enzyme Development for Human Islet Isolation: Five Decades of Progress or Stagnation? *Rev. Diabet. Stud.* **14,** 22–38 (2017).
104. Caballero-Corbalán, J., Friberg, A. S., Brandhorst, H., Nilsson, B., Korsgren, O., Brandhorst, D., Andersson, H. H., Felldin, M., Foss, A., Salmela, K., Tibell, A. & Tufveson, G. Vitacyte collagenase HA: A novel enzyme blend for efficient human islet isolation. *Transplantation* **88,** 1400–1402 (2009).
105. Shimoda, M., Noguchi, H., Naziruddin, B., Fujita, Y., Chujo, D., Takita, M., Peng, H., Tamura, Y., Olsen, G. S., Sugimoto, K., Itoh, T., Onaca, N., Levy, M. F., Grayburn, P. A. & Matsumoto, S. Assessment of human islet isolation with four different collagenases. in *Transplant. Proc.* **42,** 2049–2051 (Elsevier, 2010).
106. Bucher, P., Mathe, Z., Morel, P., Bosco, D., Andres, A., Kurfuest, M., Friedrich, O., Raemsch-Guenther, N., Buhler, L. H. & Berney, T. Assessment of a novel two-component enzyme preparation for human islet isolation and transplantation. *Transplantation* **79,** 91–97 (2005).
107. Brandhorst, H., Kurfürst, M., Johnson, P. R., Korsgren, O. & Brandhorst, D. Comparison of Neutral Proteases and Collagenase Class I as Essential Enzymes for Human Islet Isolation. *Transplant. Direct* **2,** e47 (2016).
108. Steffen, A., Ludwig, B., Krautz, C., Bornstein, S. & Solimena, M. Functional assessment of automatically sorted pancreatic islets using large particle flow cytometry. *Islets* **3,** 267–270 (2011).
109. Weegman, B. P., Kumar Sajja, V. S., Suszynski, T. M., Rizzari, M. D., Scott, W. E., Kitzmann, J. P., Mueller, K. R., Hanley, T. R., Kennedy, D. J., Todd, P. W., Balamurugan, A. N., Hering, B. J. & Papas, K. K. Continuous Quadrupole Magnetic Separation of Islets during Digestion Improves Purified Porcine Islet Viability. *J. Diabetes Res.* **2016,** (2016).
110. Cabric, S., Sanchez, J., Lundgren, T., Foss, A., Felldin, M., Källen, R., Salmela, K., Tibell, A., Tufveson, G., Larsson, R., Korsgren, O. & Nilsson, B. Islet surface heparinization prevents the instant blood-mediated inflammatory reaction in islet transplantation. *Diabetes* **56,** 2008–2015 (2007).
111. Goto, M., Johansson, H., Maeda, A., Elgue, G., Korsgren, O. & Nilsson, B. Low molecular weight dextran sulfate prevents the instant blood-mediated inflammatory reaction induced by adult porcine islets. *Transplantation* **77,** 741–747 (2004).
112. Contreras, J. L., Eckstein, C., Smyth, C. A., Bilbao, G., Vilatoba, M., Ringland, S. E., Young, C., Thompson, J. A., Fernandez, J. A., Griffin, J. H. & Eckhoff, D. E. Activated Protein C Preserves Functional Islet Mass After Intraportal Transplantation: A Novel Link Between Endothelial Cell Activation, Thrombosis, Inflammation, and Islet Cell Death. *Diabetes* **53,** 2804–2814 (2004).
113. Jaeger, C., Brendel, M. D., Hering, B. J., Eckhard, M. & Bretzel, R. G. Progressive islet graft failure occurs significantly earlier in autoantibody-positive than in autoantibody-negative IDDM recipients of intrahepatic islet allografts. *Diabetes* **46,** 1907–1910 (1997).
114. Sutherland, D. E., Sibley, R., Xu, X. Z., Michael, A., Srikanta, A. M., Taub, F., Najarian, J. & Goetz, F. C. Twin-to-twin pancreas transplantation: reversal and reenactment of the pathogenesis of type I diabetes. *Trans. Assoc. Am. Physicians* **97,** 80–7 (1984).
115. Burrack, A. L., Martinov, T. & Fife, B. T. T cell-mediated beta cell destruction: Autoimmunity and alloimmunity in the context of type 1 diabetes. *Front. Endocrinol. (Lausanne).* **8,** 1 (2017).
116. Li, X., Meng, Q. & Zhang, L. The fate of allogeneic pancreatic islets following intraportal transplantation: Challenges and solutions. *J. Immunol. Res.* **2018,** (2018).
117. Barlow, A. D., Nicholson, M. L. & Herbert, T. P. Evidence for rapamycin toxicity in pancreatic β-Cells and a review of the underlying molecular mechanisms. *Diabetes* **62,** 2674–2682 (2013).
118. Ricordi, C., Zeng, Y., Alejandro, R., Tzakis, A., Venkataramanan, R., Fung, J., Bereiter, D.,

Mintz, D. H. & Starzl, T. E. In vivo effect of FK506 on human pancreatic islets. *Transplantation* **52,** 519–522 (1991).
119. Paty, B. W., Harmon, J. S., Marsh, C. L. & Robertson, R. P. Inhibitory effects of immunosuppressive drugs on insulin secretion from HIT-T15 cells and Wistar rat islets. *Transplantation* **73,** 353–357 (2002).
120. Adams, A. B., Shirasugi, N., Jones, T. R., Durham, M. M., Strobert, E. A., Cowan, S., Rees, P., Hendrix, R., Price, K., Kenyon, N. S., Hagerty, D., Townsend, R., Hollenbaugh, D., Pearson, T. C. & Larsen, C. P. Development of a Chimeric Anti-CD40 Monoclonal Antibody That Synergizes with LEA29Y to Prolong Islet Allograft Survival. *J. Immunol.* **174,** 542–550 (2005).
121. El Khatib, M. M., Sakuma, T., Tonne, J. M., Mohamed, M. S., Holditch, S. J., Lu, B., Kudva, Y. C. & Ikeda, Y. β-cell-targeted blockage of PD1 and CTLA4 pathways prevents development of autoimmune diabetes and acute allogeneic islets rejection. *Gene Ther.* **22,** 430–438 (2015).
122. Maffi, P., Balzano, G., Ponzoni, M., Nano, R., Sordi, V., Melzi, R., Mercalli, A., Scavini, M., Esposito, A., Peccatori, J., Cantarelli, E., Messina, C., Bernardi, M., Del Maschio, A., Staudacher, C., Doglioni, C., Ciceri, F., Secchi, A. & Piemonti, L. Autologous pancreatic islet transplantation in human bone marrow. *Diabetes* **62,** 3523–3531 (2013).
123. Cantarelli, E., Citro, A., Pellegrini, S., Mercalli, A., Melzi, R., Dugnani, E., Jofra, T., Fousteri, G., Mondino, A. & Piemonti, L. Transplant Site Influences the Immune Response After Islet Transplantation. *Transplantation* **101,** 1046–1055 (2017).
124. Lacy, P., Hegre, O., Gerasimidi-Vazeou, A., Gentile, F. & Dionne, K. Maintenance of normoglycemia in diabetic mice by subcutaneous xenografts of encapsulated islets. *Science (80-.).* **254,** 1782–1784 (1991).
125. Pepper, A. R., Gala-Lopez, B., Pawlick, R., Merani, S., Kin, T. & Shapiro, A. M. J. A prevascularized subcutaneous device-less site for islet and cellular transplantation. *Nat. Biotechnol.* **33,** 518–523 (2015).
126. Berman, D. M., O'Neil, J. J., Coffey, L. C. K., Chaffanjon, P. C. J., Kenyon, N. M., Ruiz, P., Pileggi, A., Ricordi, C. & Kenyon, N. S. Long-Term Survival of Nonhuman Primate Islets Implanted in an Omental Pouch on a Biodegradable Scaffold. *Am. J. Transplant.* **9,** 91–104 (2008).
127. Berman, D. M., Molano, R. D., Fotino, C., Ulissi, U., Gimeno, J., Mendez, A. J., Kenyon, N. M., Kenyon, N. S., Andrews, D. M., Ricordi, C. & Pileggi, A. Bioengineering the Endocrine Pancreas: Intraomental Islet Transplantation Within a Biologic Resorbable Scaffold. *Diabetes* **65,** 1350–1361 (2016).
128. Ashammakhi, N., Darabi, M. A., Kehr, N. S., Erdem, A., Hu, S. K., Dokmeci, M. R., Nasr, A. S. & Khademhosseini, A. Advances in Controlled Oxygen Generating Biomaterials for Tissue Engineering and Regenerative Therapy. *Biomacromolecules* **21,** 56–72 (2020).
129. Barkai, U., Rotem, A. & de Vos, P. Survival of encapsulated islets: More than a membrane story. *World J. Transplant.* **6,** 69 (2016).
130. MACGILLIVARY, A. S., TOLEIKIS, P. M. & MAZZUCA, D. M. 205-LB: Clinical Validation of the Implanted Prevascularized Cell Pouch as a Viable, Safe Site for Diabetes Cell Therapy. *Diabetes* **69,** 205-LB (2020).
131. Pullen, L. C. Stem Cell-Derived Pancreatic Progenitor Cells Have Now Been Transplanted into Patients: Report from IPITA 2018. *Am. J. Transplant.* **18,** 1581–1582 (2018).
132. Carlsson, P. O., Espes, D., Sedigh, A., Rotem, A., Zimerman, B., Grinberg, H., Goldman, T., Barkai, U., Avni, Y., Westermark, G. T., Carlbom, L., Ahlström, H., Eriksson, O., Olerud, J. & Korsgren, O. Transplantation of macroencapsulated human islets within the bioartificial pancreas βAir to patients with type 1 diabetes mellitus. *Am. J. Transplant.* **18,** 1735–1744 (2018).
133. Bonnans, C., Chou, J. & Werb, Z. Remodelling the extracellular matrix in development and disease. *Nat. Rev. Mol. Cell Biol.* **15,** 786–801 (2014).

134. Llacua, L. A., Faas, M. M. & de Vos, P. Extracellular matrix molecules and their potential contribution to the function of transplanted pancreatic islets. *Diabetologia* **61,** 1261–1272 (2018).
135. Immunology, T., Sordi, A. R. M. (I P. A. V, Editors, S., Smink, A. M. & de Vos, P. Therapeutic Strategies for Modulating the Extracellular Matrix to Improve Pancreatic Islet Function and Survival After Transplantation. *Curr. Diab. Rep.* **18,** 39 (2018).
136. Yap, W. T., Salvay, D. M., Silliman, M. A., Zhang, X., Bannon, Z. G., Kaufman, D. B., Lowe, W. L. & Shea, L. D. Collagen IV-Modified Scaffolds Improve Islet Survival and Function and Reduce Time to Euglycemia. *Tissue Eng. Part A* **19,** 2361–2372 (2013).
137. Yamashita, S., Ohashi, K., Utoh, R., Okano, T. & Yamamoto, M. Human Laminin Isotype Coating for Creating Islet Cell Sheets. *Cell Med.* **8,** 39–46 (2015).
138. Beenken-Rothkopf, L. N., Karfeld-Sulzer, L. S., Davis, N. E., Forster, R., Barron, A. E. & Fontaine, M. J. The incorporation of extracellular matrix proteins in protein polymer hydrogels to improve encapsulated beta-cell function. *Ann. Clin. Lab. Sci.* **43,** 111–21 (2013).
139. Mayorca-Guiliani, A. E., Willacy, O., Madsen, C. D., Rafaeva, M., Elisabeth Heumüller, S., Bock, F., Sengle, G., Koch, M., Imhof, T., Zaucke, F., Wagener, R., Sasaki, T., Erler, J. T. & Reuten, R. Decellularization and antibody staining of mouse tissues to map native extracellular matrix structures in 3D. *Nat. Protoc.* **14,** 3395–3425 (2019).
140. Katsuki, Y., Yagi, H., Okitsu, T., Kitago, M., Tajima, K., Kadota, Y., Hibi, T., Abe, Y., Shinoda, M., Itano, O., Takeuchi, S. & Kitagawa, Y. Endocrine pancreas engineered using porcine islets and partial pancreatic scaffolds. *Pancreatology* **16,** 922–930 (2016).
141. Peloso, A., Urbani, L., Cravedi, P., Katari, R., Maghsoudlou, P., Fallas, M. E. A., Sordi, V., Citro, A., Purroy, C., Niu, G., McQuilling, J. P., Sittadjody, S., Farney, A. C., Iskandar, S. S., Zambon, J. P., Rogers, J., Stratta, R. J., Opara, E. C., Piemonti, L., Furdui, C. M., Soker, S., De Coppi, P. & Orlando, G. The Human Pancreas as a Source of Protolerogenic Extracellular Matrix Scaffold for a New-generation Bioartificial Endocrine Pancreas. *Ann. Surg.* **264,** 169–179 (2016).
142. Mirmalek-Sani, S.-H., Orlando, G., McQuilling, J. P., Pareta, R., Mack, D. L., Salvatori, M., Farney, A. C., Stratta, R. J., Atala, A., Opara, E. C. & Soker, S. Porcine pancreas extracellular matrix as a platform for endocrine pancreas bioengineering. *Biomaterials* **34,** 5488–5495 (2013).
143. Guruswamy Damodaran, R. & Vermette, P. Decellularized pancreas as a native extracellular matrix scaffold for pancreatic islet seeding and culture. *J. Tissue Eng. Regen. Med.* **12,** 1230–1237 (2018).
144. Fernández-Pérez, J. & Ahearne, M. The impact of decellularization methods on extracellular matrix derived hydrogels. *Sci. Rep.* **9,** 1–12 (2019).
145. Weber, L. M. & Anseth, K. S. Hydrogel encapsulation environments functionalized with extracellular matrix interactions increase islet insulin secretion. *Matrix Biol.* **27,** 667–673 (2008).
146. Szebeni, G. J., Tancos, Z., Feher, L. Z., Alfoldi, R., Kobolak, J., Dinnyes, A. & Puskas, L. G. Real architecture For 3D Tissue (RAFT^{TM}) culture system improves viability and maintains insulin and glucagon production of mouse pancreatic islet cells. *Cytotechnology* **69,** 359–369 (2017).
147. Riopel, M. & Wang, R. *Collagen matrix support of pancreatic islet survival and function*. *Front. Biosci. - Landmark* **19,** 77–90 (Frontiers in Bioscience, 2014).
148. Seo, H., Son, J. & Park, J. K. Controlled 3D co-culture of beta cells and endothelial cells in a micropatterned collagen sheet for reproducible construction of an improved pancreatic pseudo-tissue. *APL Bioeng.* **4,** 046103 (2020).
149. Vlahos, A. E., Kinney, S. M., Kingston, B. R., Keshavjee, S., Won, S. Y., Martyts, A., Chan, W. W. C. & Sefton, M. V. Endothelialized collagen based pseudo-islets enables tuneable subcutaneous diabetes therapy. *Biomaterials* **232,** 119710 (2020).
150. Krishnamurthy, M., Li, J., Al-Masri, M. & Wang, R. Expression and function of αβ1 integrins

in pancretic beta (INS-1) cells. *J. Cell Commun. Signal.* **2,** 67–79 (2008).
151. Daoud, J. T., Petropavlovskaia, M. S., Patapas, J. M., Degrandpré, C. E., DiRaddo, R. W., Rosenberg, L. & Tabrizian, M. Long-term in vitro human pancreatic islet culture using three-dimensional microfabricated scaffolds. *Biomaterials* **32,** 1536–1542 (2011).
152. Llacua, A., de Haan, B. J., Smink, S. A. & de Vos, P. Extracellular matrix components supporting human islet function in alginate-based immunoprotective microcapsules for treatment of diabetes. *J. Biomed. Mater. Res. Part A* **104,** 1788–1796 (2016).
153. Llacua, L. A., Haan, B. J. & Vos, P. Laminin and collagen IV inclusion in immunoisolating microcapsules reduces cytokine-mediated cell death in human pancreatic islets. *J. Tissue Eng. Regen. Med.* **12,** 460–467 (2018).
154. Crisóstomo, J., Araújo, F., Granja, P., Barrias, C., Sarmento, B. & Seiça, R. Increasing levels of insulin secretion in bioartificial pancreas technology: co-encapsulation of beta cells and nanoparticles containing GLP-1 in alginate hydrogels. *Health Technol. (Berl).* **10,** 885–890 (2020).
155. Weaver, J. D., Headen, D. M., Aquart, J., Johnson, C. T., Shea, L. D., Shirwan, H. & García, A. J. Vasculogenic hydrogel enhances islet survival, engraftment, and function in leading extrahepatic sites. *Sci. Adv.* **3,** e1700184 (2017).
156. Matsushima, H., Kuroki, T., Adachi, T., Kitasato, A., Ono, S., Tanaka, T., Hirabaru, M., Kuroshima, N., Hirayama, T., Sakai, Y., Soyama, A., Hidaka, M., Takatsuki, M., Kin, T., Shapiro, J. & Eguchi, S. Human Fibroblast Sheet Promotes Human Pancreatic Islet Survival and Function in Vitro. *Cell Transplant.* **25,** 1525–1537 (2016).
157. Borg, D. J., Welzel, P. B., Grimmer, M., Friedrichs, J., Weigelt, M., Wilhelm, C., Prewitz, M., Stißel, A., Hommel, A., Kurth, T., Freudenberg, U., Bonifacio, E. & Werner, C. Macroporous biohybrid cryogels for co-housing pancreatic islets with mesenchymal stromal cells. *Acta Biomater.* **44,** 178–187 (2016).
158. Arzouni, A. A., Vargas-Seymour, A., Rackham, C. L., Dhadda, P., Huang, G.-C., Choudhary, P., Nardi, N., King, A. J. F. & Jones, P. M. Mesenchymal stromal cells improve human islet function through released products and extracellular matrix. *Clin. Sci.* **131,** 2835–2845 (2017).
159. Zhang, Y., Pan, X. F., Chen, J., Xia, L., Cao, A., Zhang, Y., Wang, J., Li, H., Yang, K., Guo, K., He, M. & Pan, A. Combined lifestyle factors and risk of incident type 2 diabetes and prognosis among individuals with type 2 diabetes: a systematic review and meta-analysis of prospective cohort studies. *Diabetologia* **63,** 21–33 (2020).
160. King, A. J. F. The use of animal models in diabetes research. *Br. J. Pharmacol.* **166,** 877–894 (2012).
161. Ali, Z., Charukeshi Chandrasekera, P. & Pippin, J. J. Animal research for type 2 diabetes mellitus, its limited translation for clinical benefit, and the way forward. *ATLA Altern. to Lab. Anim.* **46,** 13–22 (2018).
162. von Herrath, M. & Nepom, G. T. Animal models of human type 1 diabetes. *Nat. Immunol.* **10,** 129–132 (2009).
163. Owerbach, D., Bell, G. I., Rutter, W. J. & Shows, T. B. The insulin gene is located on chromosome 11 in humans. *Nature* **286,** 82–84 (1980).
164. Lomedico, P., Rosenthal, N., Efstratiadis, A., Gilbert, W., Kolodner, R. & Tizard, R. The structure and evolution of the two nonallelic rat preproinsulin genes. *Cell* **18,** 545–558 (1979).
165. Wentworth, B. M., Schaefer, I. M., Villa-Komaroff, L. & Chirgwin, J. M. Characterization of the two nonallelic genes encoding mouse preproinsulin. *J. Mol. Evol.* **23,** 305–312 (1986).
166. Dai, C., Brissova, M., Hang, Y., Thompson, C., Poffenberger, G., Shostak, A., Chen, Z., Stein, R. & Powers, A. C. Islet-enriched gene expression and glucose-induced insulin secretion in human and mouse islets. *Diabetologia* **55,** 707–718 (2012).
167. Chandrasekera, P. C. & Pippin, J. J. Of rodents and men: Species-specific glucose regulation and type 2 diabetes research. *ALTEX* **31,** 157–176 (2014).
168. Mestas, J. & Hughes, C. C. W. Of Mice and Not Men: Differences between Mouse and Human

Immunology. *J. Immunol.* **172,** 2731–2738 (2004).
169. Astashkina, A., Mann, B. & Grainger, D. W. A critical evaluation of in vitro cell culture models for high-throughput drug screening and toxicity. *Pharmacol. Ther.* **134,** 82–106 (2012).
170. Zhang, H., Whalley, R. D., Ferreira, A. M. & Dalgarno, K. High throughput physiological micro-models for in vitro pre-clinical drug testing: a review of engineering systems approaches . *Prog. Biomed. Eng.* **2,** 022001 (2020).
171. Hart, N. J. & Powers, A. C. Use of human islets to understand islet biology and diabetes: progress, challenges and suggestions. *Diabetologia* **62,** 212–222 (2019).
172. Kaddis, J. S., Olack, B. J., Sowinski, J., Cravens, J., Contreras, J. L. & Niland, J. C. Human pancreatic islets and diabetes research. *JAMA - J. Am. Med. Assoc.* **301,** 1580–1587 (2009).
173. Chakradhar, S. Diabetes researchers fear worsening access to human islets. *Nat. Med.* **20,** 567 (2014).
174. Schmied, B. M., Ulrich, A., Matsuzaki, H., Ding, X., Ricordi, C., Moyer, M. P., Batra, S. K., Adrian, T. E. & Pour, P. M. Maintenance of human islets in long term culture. *Differentiation* **66,** 173–180 (2000).
175. Henquin, J.-C. Influence of organ donor attributes and preparation characteristics on the dynamics of insulin secretion in isolated human islets. *Physiol. Rep.* **6,** e13646 (2018).
176. Dominguez-Gutierrez, G., Xin, Y. & Gromada, J. Heterogeneity of human pancreatic β-cells. *Mol. Metab.* **27,** S7–S14 (2019).
177. Skelin, M., Rupnik, M. & Cencic, A. Pancreatic beta cell lines and their applications in diabetes mellitus research. *ALTEX* **27,** 105–113 (2010).
178. Ravassard, P., Hazhouz, Y., Pechberty, S., Bricout-Neveu, E., Armanet, M., Czernichow, P. & Scharfmann, R. A genetically engineered human pancreatic β cell line exhibiting glucose-inducible insulin secretion. *J. Clin. Invest.* **121,** 3589–3597 (2011).
179. Scharfmann, R., Pechberty, S., Hazhouz, Y., Von Bülow, M., Bricout-Neveu, E., Grenier-Godard, M., Guez, F., Rachdi, L., Lohmann, M., Czernichow, P. & Ravassard, P. Development of a conditionally immortalized human pancreatic β cell line. *J. Clin. Invest.* **124,** 2087–2098 (2014).
180. Benazra, M., Lecomte, M.-J., Colace, C., Müller, A., Machado, C., Pechberty, S., Bricout-Neveu, E., Grenier-Godard, M., Solimena, M., Scharfmann, R., Czernichow, P. & Ravassard, P. A human beta cell line with drug inducible excision of immortalizing transgenes. *Mol. Metab.* **4,** 916–925 (2015).
181. Akerman, I., Tu, Z., Beucher, A., Rolando, D. M. Y., Sauty-Colace, C., Benazra, M., Nakic, N., Yang, J., Wang, H., Pasquali, L., Moran, I., Garcia-Hurtado, J., Castro, N., Gonzalez-Franco, R., Stewart, A. F., Bonner, C., Piemonti, L., Berney, T., Groop, L., Kerr-Conte, J., Pattou, F., Argmann, C., Schadt, E., Ravassard, P. & Ferrer, J. Human Pancreatic β Cell lncRNAs Control Cell-Specific Regulatory Networks. *Cell Metab.* **25,** 400–411 (2017).
182. Miguel-Escalada, I., Bonàs-Guarch, S., Cebola, I., Ponsa-Cobas, J., Mendieta-Esteban, J., Atla, G., Javierre, B. M., Rolando, D. M. Y., Farabella, I., Morgan, C. C., García-Hurtado, J., Beucher, A., Morán, I., Pasquali, L., Ramos-Rodríguez, M., Appel, E. V. R., Linneberg, A., Gjesing, A. P., Witte, D. R., Pedersen, O., Grarup, N., Ravassard, P., Torrents, D., Mercader, J. M., Piemonti, L., Berney, T., de Koning, E. J. P., Kerr-Conte, J., Pattou, F., Fedko, I. O., Groop, L., Prokopenko, I., Hansen, T., Marti-Renom, M. A., Fraser, P. & Ferrer, J. Human pancreatic islet three-dimensional chromatin architecture provides insights into the genetics of type 2 diabetes. *Nat. Genet.* **51,** 1137–1148 (2019).
183. Hakonen, E., Chandra, V., Fogarty, C. L., Yu, N. Y. L., Ustinov, J., Katayama, S., Galli, E., Danilova, T., Lindholm, P., Vartiainen, A., Einarsdottir, E., Krjutškov, K., Kere, J., Saarma, M., Lindahl, M. & Otonkoski, T. MANF protects human pancreatic beta cells against stress-induced cell death. *Diabetologia* **61,** 2202–2214 (2018).
184. Staels, W., Verdonck, Y., Heremans, Y., Leuckx, G., De Groef, S., Heirman, C., de Koning, E., Gysemans, C., Thielemans, K., Baeyens, L., Heimberg, H. & De Leu, N. Vegf-A mRNA transfection as a novel approach to improve mouse and human islet graft revascularisation.

Diabetologia **61,** 1804–1810 (2018).
185. Lagundžin, D., Hu, W.-F., Law, H. C. H., Krieger, K. L., Qiao, F., Clement, E. J., Drincic, A. T., Nedić, O., Naldrett, M. J., Alvarez, S. & Woods, N. T. Delineating the role of FANCA in glucose-stimulated insulin secretion in β cells through its protein interactome. *PLoS One* **14,** e0220568 (2019).
186. Jensen, C. & Teng, Y. Is It Time to Start Transitioning From 2D to 3D Cell Culture? *Front. Mol. Biosci.* **7,** 33 (2020).
187. Chowdhury, A., Dyachok, O., Tengholm, A., Sandler, S. & Bergsten, P. Functional differences between aggregated and dispersed insulin-producing cells. *Diabetologia* **56,** 1557–1568 (2013).
188. Hauge-Evans, A. C., Squires, P. E., Persaud, S. J. & Jones, P. M. Pancreatic beta-cell-to-beta-cell interactions are required for integrated responses to nutrient stimuli: enhanced Ca2+ and insulin secretory responses of MIN6 pseudoislets. *Diabetes* **48,** 1402–1408 (1999).
189. Luther, M. J., Hauge-Evans, A., Souza, K. L. A., Jörns, A., Lenzen, S., Persaud, S. J. & Jones, P. M. MIN6 β-cell–β-cell interactions influence insulin secretory responses to nutrients and non-nutrients. *Biochem. Biophys. Res. Commun.* **343,** 99–104 (2006).
190. Low, L. A., Mummery, C., Berridge, B. R., Austin, C. P. & Tagle, D. A. Organs-on-chips: into the next decade. *Nat. Rev. Drug Discov.* 1–17 (2020). doi:10.1038/s41573-020-0079-3
191. Kilic, T., Navaee, F., Stradolini, F., Renaud, P. & Carrara, S. Organs-on-chip monitoring: sensors and other strategies. *Microphysiological Syst.* **1,** 1–1 (2018).
192. Mitsutake, H., Poppi, R. J. & Breitkreitz, M. C. Raman Imaging Spectroscopy: History, Fundamentals and Current Scenario of the Technique. *J. Braz. Chem. Soc* **30,** (2243).
193. Jones, R. R., Hooper, D. C., Zhang, L., Wolverson, D. & Valev, V. K. Raman Techniques: Fundamentals and Frontiers. *Nanoscale Res. Lett.* **14,** 1–34 (2019).
194. Datta, R., Heaster, T. M., Sharick, J. T., Gillette, A. A. & Skala, M. C. Fluorescence lifetime imaging microscopy: fundamentals and advances in instrumentation, analysis, and applications. *J. Biomed. Opt.* **25,** 1 (2020).
195. Esmonde-White, K. A., Cuellar, M., Uerpmann, C., Lenain, B. & Lewis, I. R. Raman spectroscopy as a process analytical technology for pharmaceutical manufacturing and bioprocessing. *Anal. Bioanal. Chem.* **409,** 637–649 (2017).
196. Rygula, A., Majzner, K., Marzec, K. M., Kaczor, A., Pilarczyk, M. & Baranska, M. Raman spectroscopy of proteins: a review. *J. Raman Spectrosc.* **44,** 1061–1076 (2013).
197. Movasaghi, Z., Rehman, S. & Rehman, I. U. Raman spectroscopy of biological tissues. *Appl. Spectrosc. Rev.* **42,** 493–541 (2007).
198. Smith, R., Wright, K. L. & Ashton, L. Raman spectroscopy: an evolving technique for live cell studies. *Analyst* **141,** 3590–3600 (2016).
199. Brauchle, E., Kasper, J., Daum, R., Schierbaum, N., Falch, C., Kirschniak, A., Schäffer, T. E. & Schenke-Layland, K. Biomechanical and biomolecular characterization of extracellular matrix structures in human colon carcinomas. *Matrix Biol.* **68–69,** 180–193 (2018).
200. Brauchle, E., Bauer, H., Fernes, P., Zuk, A., Schenke-Layland, K. & Sengle, G. Raman microspectroscopy as a diagnostic tool for the non-invasive analysis of fibrillin-1 deficiency in the skin and in the in vitro skin models. *Acta Biomater.* **52,** 41–48 (2017).
201. Sugiyama, K., Marzi, J., Brauchle, E. M., Ando, M., Yamashiro, Y., Ramkhelawon, B., Schenke-Layland, K. & Yanagisawa, H. Raman Microspectroscopy and Imaging Reveal Novel Biomarkers Specific for Thoracic Aortic Aneurysms. *SSRN Electron. J.* (2020). doi:10.2139/ssrn.3606775
202. Morais, C. L. M., Martin-Hirsch, P. L. & Martin, F. L. A three-dimensional principal component analysis approach for exploratory analysis of hyperspectral data: Identification of ovarian cancer samples based on Raman microspectroscopy imaging of blood plasma. *Analyst* **144,** 2312–2319 (2019).
203. O'Malley, J., Kumar, R., Kuzmin, A. N., Pliss, A., Yadav, N., Balachandar, S., Wang, J., Attwood, K., Prasad, P. N. & Chandra, D. Lipid quantification by Raman microspectroscopy

as a potential biomarker in prostate cancer. *Cancer Lett.* **397,** 52–60 (2017).
204. Liu, W., Wang, H., Du, J. & Jing, C. Raman microspectroscopy of nucleus and cytoplasm for human colon cancer diagnosis. *Biosens. Bioelectron.* **97,** 70–74 (2017).
205. Moradi, H., Ahmad, A., Shepherdson, D., Vuong, N. H., Niedbala, G., Eapen, L., Vanderhyden, B., Nyiri, B. & Murugkar, S. Raman micro-spectroscopy applied to treatment resistant and sensitive human ovarian cancer cells. *J. Biophotonics* **10,** 1327–1334 (2017).
206. Ravera, F., Efeoglu, E. & Byrne, H. J. Monitoring stem cell differentiation using Raman microspectroscopy: chondrogenic differentiation, towards cartilage formation. *Analyst* **146,** 322–337 (2021).
207. Hsu, C. C., Xu, J., Brinkhof, B., Wang, H., Cui, Z., Huang, W. E. & Ye, H. A single-cell Raman-based platform to identify developmental stages of human pluripotent stem cell-derived neurons. *Proc. Natl. Acad. Sci. U. S. A.* **117,** 18412–18423 (2020).
208. Chan, J. W., Lieu, D. K., Huser, T. & Li, R. A. Label-free separation of human embryonic stem cells and their cardiac derivatives using Raman spectroscopy. *Anal. Chem.* **81,** 1324–1331 (2009).
209. Brauchle, E., Knopf, A., Bauer, H., Shen, N., Linder, S., Monaghan, M. G., Ellwanger, K., Layland, S. L., Brucker, S. Y., Nsair, A. & Schenke-Layland, K. Non-invasive Chamber-Specific Identification of Cardiomyocytes in Differentiating Pluripotent Stem Cells. *Stem cell reports* **6,** 188–99 (2016).
210. Chiang, H. K., Peng, F.-Y., Hung, S.-C. & Feng, Y.-C. *In situ* Raman spectroscopic monitoring of hydroxyapatite as human mesenchymal stem cells differentiate into osteoblasts. *J. Raman Spectrosc.* **40,** 546–549 (2009).
211. Konorov, S. O., Schulze, H. G., Gage, B. K., Kieffer, T. J., Piret, J. M., Blades, M. W. & Turner, R. F. B. Process Analytical Utility of Raman Microspectroscopy in the Directed Differentiation of Human Pancreatic Insulin-Positive Cells. *Anal. Chem.* **87,** 10762–10769 (2015).
212. Georgakoudi, I. & Quinn, K. P. Optical Imaging Using Endogenous Contrast to Assess Metabolic State. *Annu. Rev. Biomed. Eng.* **14,** 351–367 (2012).
213. Schaefer, P. M., Kalinina, S., Rueck, A., von Arnim, C. A. F. & von Einem, B. NADH Autofluorescence-A Marker on its Way to Boost Bioenergetic Research. *Cytom. Part A* **95,** 34–46 (2019).
214. Kolenc, O. I. & Quinn, K. P. Evaluating cell metabolism through autofluorescence imaging of NAD(P)H and FAD. *Antioxidants Redox Signal.* **30,** 875–889 (2019).
215. Zelent, B., Troxler, T. & Vanderkooi, J. M. Temperature dependence for fluorescence of β-NADH in glycerol/water solution and in trehalose/sucrose glass. *J. Fluoresc.* **17,** 37–42 (2007).
216. Ogikubo, S., Nakabayashi, T., Adachi, T., Islam, M. S., Yoshizawa, T., Kinjo, M. & Ohta, N. Intracellular pH Sensing Using Autofluorescence Lifetime Microscopy. *J. Phys. Chem. B* **115,** 10385–10390 (2011).
217. Anton, D., Burckel, H., Josset, E. & Noel, G. Three-dimensional cell culture: A breakthrough in vivo. *Int. J. Mol. Sci.* **16,** 5517–5527 (2015).
218. Abbott, R. D. & Kaplan, D. L. Strategies for improving the physiological relevance of human engineered tissues. *Trends Biotechnol.* **33,** 401–407 (2015).
219. Hilderink, J., Spijker, S., Carlotti, F., Lange, L., Engelse, M., van Blitterswijk, C., de Koning, E., Karperien, M. & Van Apeldoorn, A. Controlled aggregation of primary human pancreatic islet cells leads to glucose-responsive pseudoislets comparable to native islets. *J. Cell. Mol. Med.* **19,** 1836–1846 (2015).
220. Ichihara, Y., Utoh, R., Yamada, M., Shimizu, T. & Uchigata, Y. Size effect of engineered islets prepared using microfabricated wells on islet cell function and arrangement. *Heliyon* **2,** e00129 (2016).
221. Zuellig, R. A., Cavallari, G., Gerber, P., Tschopp, O., Spinas, G. A., Moritz, W. & Lehmann, R. Improved physiological properties of gravity-enforced reassembled rat and human pancreatic pseudo-islets. *J. Tissue Eng. Regen. Med.* **11,** 109–120 (2017).

222. Lorza-Gil, E., Gerst, F., Oquendo, M. B., Deschl, U., Häring, H.-U., Beilmann, M. & Ullrich, S. Glucose, adrenaline and palmitate antagonistically regulate insulin and glucagon secretion in human pseudoislets. *Sci. Rep.* **9,** 10261 (2019).
223. Yu, Y., Gamble, A., Pawlick, R., Pepper, A. R., Salama, B., Toms, D., Razian, G., Ellis, C., Bruni, A., Gala-Lopez, B., Lu, J. (Lulu), Vovko, H., Chiu, C., Abdo, S., Kin, T., Korbutt, G., Shapiro, A. M. J. & Ungrin, M. Bioengineered human pseudoislets form efficiently from donated tissue, compare favourably with native islets in vitro and restore normoglycaemia in mice. *Diabetologia* **61,** 2016–2029 (2018).
224. Zbinden, A., Marzi, J., Schlünder, K., Probst, C., Urbanczyk, M., Black, S., Brauchle, E. M., Layland, S. L., Kraushaar, U., Duffy, G., Schenke-Layland, K. & Loskill, P. Non-invasive marker-independent high content analysis of a microphysiological human pancreas-on-a-chip model. *Matrix Biol.* **85–86,** (2020).
225. Solaini, G., Baracca, A., Lenaz, G. & Sgarbi, G. Hypoxia and mitochondrial oxidative metabolism. *Biochim. Biophys. Acta - Bioenerg.* **1797,** 1171–1177 (2010).
226. Cantley, J., Grey, S. T., Maxwell, P. H. & Withers, D. J. The hypoxia response pathway and β-cell function. *Diabetes, Obes. Metab.* **12,** 159–167 (2010).
227. Komatsu, H., Kandeel, F. & Mullen, Y. Impact of Oxygen on Pancreatic Islet Survival. *Pancreas* **47,** 533–543 (2018).
228. Garcia-Contreras, M., Tamayo-Garcia, A., Pappan, K. L., Michelotti, G. A., Stabler, C. L., Ricordi, C. & Buchwald, P. Metabolomics Study of the Effects of Inflammation, Hypoxia, and High Glucose on Isolated Human Pancreatic Islets. *J. Proteome Res.* **16,** 2294–2306 (2017).
229. Zheng, X., Zheng, X., Wang, X., Ma, Z., Gupta Sunkari, V., Botusan, I., Takeda, T., Björklund, A., Inoue, M., Catrina, S. B., Brismar, K., Poellinger, L. & Pereira, T. S. Acute hypoxia induces apoptosis of pancreatic β-cell by activation of the unfolded protein response and upregulation of CHOP. *Cell Death Dis.* **3,** e322–e322 (2012).
230. Menger, M. D., Yamauchi, J. & Vollmar, B. Revascularization and Microcirculation of Freely Grafted Islets of Langerhans. *World J. Surg.* **25,** 509–515 (2001).
231. Piret, J. P., Mottet, D., Raes, M. & Michiels, C. Is HIF-1α a pro- or an anti-apoptotic protein? *Biochem. Pharmacol.* **64,** 889–892 (2002).
232. Greijer, A. E. & Van Der Wall, E. The role of hypoxia inducible factor 1 (HIF-1) in hypoxia induced apoptosis. *J. Clin. Pathol.* **57,** 1009–1014 (2004).
233. Zbinden, A., Carvajal Berrio, D. A., Urbanczyk, M., Layland, S. L., Bosch, M., Fliri, S., Lu, C., Jeyagaran, A., Loskill, P., Duffy, G. P. & Schenke-Layland, K. Fluorescence lifetime metabolic mapping of hypoxia-induced damage in pancreatic pseudo-islets. *J. Biophotonics* **13,** (2020).
234. Shrestha, P., Regmi, S. & Jeong, J. H. Injectable hydrogels for islet transplantation: a concise review. *J. Pharm. Investig.* **50,** 29–45 (2020).
235. Weber, L. M., Hayda, K. N. & Anseth, K. S. Cell–Matrix Interactions Improve β-Cell Survival and Insulin Secretion in Three-Dimensional Culture. *Tissue Eng. Part A* **14,** 1959–1968 (2008).
236. Stephens, C. H., Orr, K. S., Acton, A. J., Tersey, S. A., Mirmira, R. G., Considine, R. V. & Voytik-Harbin, S. L. In situ type I oligomeric collagen macroencapsulation promotes islet longevity and function in vitro and in vivo. *Am. J. Physiol. - Endocrinol. Metab.* **315,** E650–E661 (2018).
237. Razavi, M., Primavera, R., Kevadiya, B. D., Wang, J., Buchwald, P. & Thakor, A. S. A Collagen Based Cryogel Bioscaffold that Generates Oxygen for Islet Transplantation. *Adv. Funct. Mater.* **30,** 1902463 (2020).
238. Narayanan, S., Loganathan, G., Dhanasekaran, M., Tucker, W., Patel, A., Subhashree, V., Mokshagundam, S., Hughes, M. G., Williams, S. K. & Balamurugan, A. N. Intra-islet endothelial cell and β-cell crosstalk: Implication for islet cell transplantation. *World J. Transplant.* **7,** 117 (2017).
239. Nikolova, G., Strilic, B. & Lammert, E. The vascular niche and its basement membrane.

Trends Cell Biol. **17,** 19–25 (2007).
240. Hospodiuk, M., Dey, M., Ayan, B., Sosnoski, D., Moncal, K. K., Wu, Y. & Ozbolat, I. T. Sprouting angiogenesis in engineered pseudo islets. *Biofabrication* **10,** 035003 (2018).
241. Urbanczyk, M., Zbinden, A., Layland, S. L., Duffy, G. & Schenke-Layland, K. Controlled Heterotypic Pseudo-Islet Assembly of Human β-Cells and Human Umbilical Vein Endothelial Cells Using Magnetic Levitation. *Tissue Eng. Part A* **26,** 387–399 (2020).
242. Nalbach, L., Roma, L. P., Schmitt, B. M., Becker, V., Körbel, C., Wrublewsky, S., Pack, M., Später, T., Metzger, W., Menger, M. M., Frueh, F. S., Götz, C., Lin, H., Manning Fox, J. E., MacDonald, P. E., Menger, M. D., Laschke, M. W. & Ampofo, E. Improvement of islet transplantation by the fusion of islet cells with functional blood vessels. *EMBO Mol. Med.* **13,** (2021).
243. van Meeteren, L. A. & ten Dijke, P. Regulation of endothelial cell plasticity by TGF-β. *Cell Tissue Res.* **347,** 177–186 (2012).
244. Farina, M., Alexander, J. F., Thekkedath, U., Ferrari, M. & Grattoni, A. Cell encapsulation: Overcoming barriers in cell transplantation in diabetes and beyond. *Adv. Drug Deliv. Rev.* **139,** 92–115 (2019).
245. Elliott, R. B., Escobar, L., Tan, P. L. J., Muzina, M., Zwain, S. & Buchanan, C. Live encapsulated porcine islets from a type 1 diabetic patient 9.5 yr after xenotransplantation. *Xenotransplantation* **14,** 157–161 (2007).
246. Kimura, H., Sakai, Y. & Fujii, T. Organ/body-on-a-chip based on microfluidic technology for drug discovery. *Drug Metab. Pharmacokinet.* **33,** 43–48 (2018).
247. Henquin, J.-C., Dufrane, D., Kerr-Conte, J. & Nenquin, M. Dynamics of glucose-induced insulin secretion in normal human islets. *Am. J. Physiol. Metab.* **309,** E640–E650 (2015).
248. Nguyen, D. T. T., Van Noort, D., Jeong, I. K. & Park, S. Endocrine system on chip for a diabetes treatment model. *Biofabrication* **9,** 015021 (2017).
249. Sankar, K. S., Green, B. J., Crocker, A. R., Verity, J. E., Altamentova, S. M. & Rocheleau, J. V. Culturing Pancreatic Islets in Microfluidic Flow Enhances Morphology of the Associated Endothelial Cells. *PLoS One* **6,** e24904 (2011).
250. Lee, S. H., Hong, S., Song, J., Cho, B., Han, E. J., Kondapavulur, S., Kim, D. & Lee, L. P. Microphysiological Analysis Platform of Pancreatic Islet β-Cell Spheroids. *Adv. Healthc. Mater.* **7,** 1701111 (2018).
251. Jun, Y., Lee, J., Choi, S., Yang, J. H., Sander, M., Chung, S. & Lee, S.-H. In vivo–mimicking microfluidic perfusion culture of pancreatic islet spheroids. *Sci. Adv.* **5,** eaax4520 (2019).
252. Walker, J. T., Haliyur, R., Nelson, H. A., Ishahak, M., Poffenberger, G., Aramandla, R., Reihsmann, C., Luchsinger, J. R., Saunders, D. C., Wang, P., Garcia-Ocaña, A., Bottino, R., Agarwal, A., Powers, A. C. & Brissova, M. Integrated human pseudoislet system and microfluidic platform demonstrate differences in GPCR signaling in islet cells. *JCI Insight* **5,** (2020).
253. Papas, K. K., Suszynski, T. M. & Colton, C. K. Islet assessment for transplantation. *Curr. Opin. Organ Transplant.* **14,** 674–682 (2009).
254. MacDonald, P. E., Joseph, J. W. & Rorsman, P. Glucose-sensing mechanisms in pancreatic β-cells. *Philos. Trans. R. Soc. B Biol. Sci.* **360,** 2211–2225 (2005).
255. MacDonald, M. J., Ade, L., Ntambi, J. M., Ansari, I.-U. H. & Stoker, S. W. Characterization of Phospholipids in Insulin Secretory Granules and Mitochondria in Pancreatic Beta Cells and Their Changes with Glucose Stimulation. *J. Biol. Chem.* **290,** 11075–11092 (2015).
256. Stein, L. R. & Imai, S. The dynamic regulation of NAD metabolism in mitochondria. *Trends Endocrinol. Metab.* **23,** 420–428 (2012).
257. Idevall-Hagren, O. & Tengholm, A. Metabolic regulation of calcium signaling in beta cells. *Semin. Cell Dev. Biol.* **103,** 20–30 (2020).
258. Ito, K. & Ito, K. Metabolism and the Control of Cell Fate Decisions and Stem Cell Renewal. *Annu. Rev. Cell Dev. Biol.* **32,** 399–409 (2016).
259. Covarrubias, A. J., Perrone, R., Grozio, A. & Verdin, E. NAD+ metabolism and its roles in

cellular processes during ageing. *Nat. Rev. Mol. Cell Biol.* **22,** 119–141 (2021).
260. Green, D. R., Galluzzi, L. & Kroemer, G. Metabolic control of cell death. *Science (80-.).* **345,** 1250256 (2014).
261. Tengholm, A. & Gylfe, E. Oscillatory control of insulin secretion. *Mol. Cell. Endocrinol.* **297,** 58–72 (2009).
262. Bergholt, M. S., Serio, A. & Albro, M. B. Raman Spectroscopy: Guiding Light for the Extracellular Matrix. *Front. Bioeng. Biotechnol.* **7,** 303 (2019).
263. Spiers, R. M., Marzi, J., Brauchle, E. M., Cross, S. E., Vaughan, R. H., Bateman, P. A., Hughes, S. J., Schenke-Layland, K. & Johnson, P. R. V. Donor age significantly influences the Raman spectroscopic biomolecular fingerprint of human pancreatic extracellular matrix proteins following collagenase-based digestion. *Acta Biomater.* **99,** 269–283 (2019).
264. Hilderink, J., Otto, C., Slump, C., Lenferink, A., Engelse, M., van Blitterswijk, C., de Koning, E., Karperien, M. & van Apeldoorn, A. Label-Free Detection of Insulin and Glucagon within Human Islets of Langerhans Using Raman Spectroscopy. *PLoS One* **8,** e78148 (2013).
265. Yin, D., Wei, F., Liu, H., Kuang, Q., Luo, R., Huang, S., Rong, X., Yuan, X., Jiang, Y., Wei, F., Luo, R., Yuan, X., Kuang, Q., Yin, D., Huang, S., Jiang, Y. & Liu, H. Discrimination of Single Living Rat Pancreatic α, β, δ, and Pancreatic Polypeptide (PP) Cells Using Raman Spectroscopy. *Appl. Spectrosc.* **72,** 706–714 (2018).
266. Zhou, Q.-L., Rong, X., Wei, F., Luo, R.-Q. & Liu, H. Different Raman spectral patterns of primary rat pancreatic β cells and insulinoma cells. *J. Biomed. Opt.* **20,** 047001 (2015).
267. Cho, H., Kumar, S., Yang, D., Vaidyanathan, S., Woo, K., Garcia, I., Shue, H. J., Yoon, Y., Ferreri, K. & Choo, H. Surface-Enhanced Raman Spectroscopy-Based Label-Free Insulin Detection at Physiological Concentrations for Analysis of Islet Performance. *ACS Sensors* **3,** 65–71 (2018).
268. Okkelman, I. A., Papkovsky, D. B. & Dmitriev, R. I. Estimation of the Mitochondrial Membrane Potential Using Fluorescence Lifetime Imaging Microscopy. *Cytom. Part A* **97,** 471–482 (2020).
269. Meleshina, A. V., Dudenkova, V. V., Bystrova, A. S., Kuznetsova, D. S., Shirmanova, M. V. & Zagaynova, E. V. Two-photon FLIM of NAD(P)H and FAD in mesenchymal stem cells undergoing either osteogenic or chondrogenic differentiation. *Stem Cell Res. Ther.* **8,** 15 (2017).
270. Wang, M., Tang, F., Pan, X., Yao, L., Wang, X., Jing, Y., Ma, J., Wang, G. & Mi, L. Rapid diagnosis and intraoperative margin assessment of human lung cancer with fluorescence lifetime imaging microscopy. *BBA Clin.* **8,** 7–13 (2017).
271. Bower, A. J., Marjanovic, M., Zhao, Y., Li, J., Chaney, E. J. & Boppart, S. A. Label-free in vivo cellular-level detection and imaging of apoptosis. *J. Biophotonics* **10,** 143–150 (2017).
272. Lakner, P. H., Monaghan, M. G., Möller, Y., Olayioye, M. A. & Schenke-Layland, K. Applying phasor approach analysis of multiphoton FLIM measurements to probe the metabolic activity of three-dimensional in vitro cell culture models. *Sci. Rep.* **7,** 1–11 (2017).
273. Gregg, T., Poudel, C., Schmidt, B. A., Dhillon, R. S., Sdao, S. M., Truchan, N. A., Baar, E. L., Fernandez, L. A., Denu, J. M., Eliceiri, K. W., Rogers, J. D., Kimple, M. E., Lamming, D. W. & Merrins, M. J. Pancreatic β-cells from mice offset age-associated mitochondrial deficiency with reduced KATP channel activity. *Diabetes* **65,** 2700–2710 (2016).
274. Frantz, C., Stewart, K. M. & Weaver, V. M. The extracellular matrix at a glance. *J. Cell Sci.* **123,** 4195–4200 (2010).
275. Wang, R. & Rosenberg, L. Maintenance of beta-cell function and survival following islet isolation requires re-establishment of the islet-matrix relationship. *J. Endocrinol.* **163,** 181–190 (1999).
276. Carlin, B., Jaffe, R., Bender, B. & Chung, A. E. Entactin, a novel basal lamina-associated sulfated glycoprotein. *J. Biol. Chem.* **256,** 5209–5214 (1981).
277. Paulsson, M., Aumailley, M., Deutzmann, R., Timpl, R., Beck, K. & Engel, J. Laminin-nidogen complex. Extraction with chelating agents and structural characterization. *Eur. J. Biochem.*

166, 11–19 (1987).
278. Fox, J. W., Mayer, U., Nischt, R., Aumailley, M., Reinhardt, D., Wiedemann, H., Mann, K., Timpl, R., Krieg, T. & Engel, J. Recombinant nidogen consists of three globular domains and mediates binding of laminin to collagen type IV. *EMBO J.* **10,** 3137–3146 (1991).
279. Zbinden, A., Layland, S. L., Urbanczyk, M., Carvajal Berrio, D. A., Marzi, J., Zauner, M., Hammerschmidt, A., Brauchle, E. M., Sudrow, K., Fink, S., Templin, M., Liebscher, S., Klein, G., Deb, A., Duffy, G. P., Crooks, G. M., Eble, J. A., Mikkola, H. K. A., Nsair, A., Seifert, M. & Schenke-Layland, K. Nidogen-1 Mitigates Ischemia and Promotes Tissue Survival and Regeneration. *Adv. Sci.* 2002500 (2020). doi:10.1002/advs.202002500
280. Treindl, F., Ruprecht, B., Beiter, Y., Schultz, S., Döttinger, A., Staebler, A., Joos, T. O., Kling, S., Poetz, O., Fehm, T., Neubauer, H., Kuster, B. & Templin, M. F. A bead-based western for high-throughput cellular signal transduction analyses. *Nat. Commun.* **7,** 12852 (2016).
281. Adderley, S. R. & Fitzgerald, D. J. Oxidative damage of cardiomyocytes is limited by extracellular regulated kinases 1/2-mediate induction of cyclooxygenase-2. *J. Biol. Chem.* **274,** 5038–5046 (1999).
282. Juan-Zhang, Bian, H. J., Li, X. X., Liu, X. B., Sun, J. P., Na-Li, Yun-Zhang & Ji, X. P. ERK-MAPK signaling opposes rho-kinase to reduce cardiomyocyte apoptosis in heart ischemic preconditioning. *Mol. Med.* **16,** 307–315 (2010).
283. Mihailidou, C., Chatzistamou, I., Papavassiliou, A. G. & Kiaris, H. Modulation of pancreatic islets' function and survival during aging involves the differential regulation of endoplasmic reticulum stress by p21 and CHOP. *Antioxid. Redox Signal.* **27,** 185–200 (2017).
284. Inoue, Y., Kawachi, S., Ohkubo, T., Nagasaka, M., Ito, S., Fukuura, K., Itoh, Y., Ohoka, N., Morishita, D. & Hayashi, H. The CDK inhibitor p21 is a novel target gene of ATF4 and contributes to cell survival under ER stress. *FEBS Lett.* **591,** 3682–3691 (2017).
285. Bottazzi, M. E., Zhu, X., Böhmer, R. M. & Assoian, R. K. Regulation of p21(cip1) expression by growth factors and the extracellular matrix reveals a role for transient ERK activity in G1 phase. *J. Cell Biol.* **146,** 1255–1264 (1999).
286. Cheng, T., Rodrigues, N., Shen, H., Yang, Y. G., Dombkowski, D., Sykes, M. & Scadden, D. T. Hematopoietic stem cell quiescence maintained by p21(cip1/waf1). *Science (80-.).* **287,** 1804–1809 (2000).
287. Asada, M. Apoptosis inhibitory activity of cytoplasmic p21Cip1/WAF1 in monocytic differentiation. *EMBO J.* **18,** 1223–1234 (1999).
288. Rallis, C., Pinchin, S. M. & Ish-Horowicz, D. Cell-autonomous integrin control of Wnt and Notch signalling during somitogenesis. *Development* **137,** 3591–3601 (2010).
289. Renner, G., Noulet, F., Mercier, M. C., Choulier, L., Etienne-Selloum, N., Gies, J. P., Lehmann, M., Lelong-Rebel, I., Martin, S. & Dontenwill, M. Expression/activation of α5β1 integrin is linked to the β-catenin signaling pathway to drive migration in glioma cells. *Oncotarget* **7,** 62194–62207 (2016).
290. Piva, M. B. R., Jakubzig, B. & Bendas, G. Integrin activation contributes to lower cisplatin sensitivity in MV3 melanoma cells by inducing the Wnt signalling pathway. *Cancers (Basel).* **9,** 125 (2017).
291. Welters, H. J. & Kulkarni, R. N. Wnt signaling: relevance to β-cell biology and diabetes. *Trends Endocrinol. Metab.* **19,** 349–355 (2008).
292. Li, F., Chong, Z. Z. & Maiese, K. Winding through the WNT pathway during cellular development and demise. *Histol. Histopathol.* **21,** 103–124 (2006).
293. Balzar, M., Briaire-de Bruijn, I. H., Rees-Bakker, H. A. M., Prins, F. A., Helfrich, W., de Leij, L., Riethmuller, G., Alberti, S., Warnaar, S. O., Fleuren, G. J. & Litvinov, S. V. Epidermal growth factor-like repeats mediate lateral and reciprocal interactions of Ep-CAM molecules in homophilic adhesions. *Mol. Cell. Biol.* **21,** 2570–2580 (2001).
294. Yang, Y., Liu, S., Lei, Z., Chen, G., Huang, L., Yang, F., Lei, Y., Liu, Y., Yang, L., Liu, W., Lai, L., Guo, J., Lei, Y., Lei, Y., Liu, Y., Liu, Y., Yang, L., Yang, L., Liu, W., Liu, W., Lai, L., Lai, L., Guo, J. & Guo, J. Circular RNA profile in liver tissue of EpCAM knockout mice. *Int. J. Mol.*

Med. **44,** 1063–1077 (2019).
295. Lu, H., Ma, J., Yang, Y., Shi, W. & Luo, L. EpCAM is an endoderm-specific Wnt derepressor that licenses hepatic development. *Dev. Cell* **24,** 543–553 (2013).
296. Yamashita, T., Budhu, A., Forgues, M. & Wang, X. W. Activation of Hepatic Stem Cell Marker EpCAM by Wnt–β-Catenin Signaling in Hepatocellular Carcinoma. *Cancer Res.* **67,** 10831–10839 (2007).
297. Nicosia, R. F., Bonanno, E., Smith, M. & Yurchenco, P. Modulation of angiogenesis in vitro by laminin-entactin complex. *Dev. Biol.* **164,** 197–206 (1994).
298. Martinez-Hernandez, A. & Amenta, P. S. The extracellular matrix in hepatic regeneration. *FASEB J.* **9,** 1401–1410 (1995).
299. Lee, H. K., Seo, I. A., Suh, D. J. & Park, H. T. Nidogen plays a role in the regenerative axon growth of adult sensory neurons through Schwann cells. *J. Korean Med. Sci.* **24,** 654–659 (2009).
300. Wolfstetter, G., Dahlitz, I., Pfeifer, K., Töpfer, U., Alt, J. A., Pfeifer, D. C., Lakes-Harlan, R., Baumgartner, S., Palmer, R. H. & Holz, A. Characterization of *Drosophila Nidogen* / *entactin* reveals roles in basement membrane stability, barrier function and nervous system patterning. *Development* **146,** dev168948 (2019).
301. Tsonkova, V. G., Sand, F. W., Wolf, X. A., Grunnet, L. G., Kirstine Ringgaard, A., Ingvorsen, C., Winkel, L., Kalisz, M., Dalgaard, K., Bruun, C., Fels, J. J., Helgstrand, C., Hastrup, S., Öberg, F. K., Vernet, E., Sandrini, M. P. B., Shaw, A. C., Jessen, C., Grønborg, M., Hald, J., Willenbrock, H., Madsen, D., Wernersson, R., Hansson, L., Jensen, J. N., Plesner, A., Alanentalo, T., Petersen, M. B. K., Grapin-Botton, A., Honoré, C., Ahnfelt-Rønne, J., Hecksher-Sørensen, J., Ravassard, P., Madsen, O. D., Rescan, C. & Frogne, T. The EndoC-βH1 cell line is a valid model of human beta cells and applicable for screenings to identify novel drug target candidates. *Mol. Metab.* **8,** 144–157 (2018).
302. Hastoy, B., Godazgar, M., Clark, A., Nylander, V., Spiliotis, I., van de Bunt, M., Chibalina, M. V., Barrett, A., Burrows, C., Tarasov, A. I., Scharfmann, R., Gloyn, A. L. & Rorsman, P. Electrophysiological properties of human beta-cell lines EndoC-βH1 and -βH2 conform with human beta-cells. *Sci. Rep.* **8,** 16994 (2018).
303. Assady, S., Maor, G., Amit, M., Itskovitz-Eldor, J., Skorecki, K. L. & Tzukerman, M. Insulin Production by Human Embryonic Stem Cells. *Diabetes* **50,** 1691–1697 (2001).
304. Zhou, Z., Ma, X. & Zhu, S. Recent advances and potential applications of human pluripotent stem cell-derived pancreatic β cells. *Acta Biochim. Biophys. Sin. (Shanghai).* **52,** 708–715 (2020).
305. Rezania, A., Bruin, J. E., Arora, P., Rubin, A., Batushansky, I., Asadi, A., O'Dwyer, S., Quiskamp, N., Mojibian, M., Albrecht, T., Yang, Y. H. C., Johnson, J. D. & Kieffer, T. J. Reversal of diabetes with insulin-producing cells derived in vitro from human pluripotent stem cells. *Nat. Biotechnol.* **32,** 1121–1133 (2014).
306. Pagliuca, F. W., Millman, J. R., Gürtler, M., Segel, M., Van Dervort, A., Ryu, J. H., Peterson, Q. P., Greiner, D. & Melton, D. A. Generation of functional human pancreatic β cells in vitro. *Cell* **159,** 428–39 (2014).
307. Russ, H. A., Parent, A. V., Ringler, J. J., Hennings, T. G., Nair, G. G., Shveygert, M., Guo, T., Puri, S., Haataja, L., Cirulli, V., Blelloch, R., Szot, G. L., Arvan, P. & Hebrok, M. Controlled induction of human pancreatic progenitors produces functional beta-like cells in vitro. *EMBO J.* **34,** 1759–1772 (2015).
308. Nair, G. G., Liu, J. S., Russ, H. A., Tran, S., Saxton, M. S., Chen, R., Juang, C., Li, M., Nguyen, V. Q., Giacometti, S., Puri, S., Xing, Y., Wang, Y., Szot, G. L., Oberholzer, J., Bhushan, A. & Hebrok, M. Recapitulating endocrine cell clustering in culture promotes maturation of human stem-cell-derived β cells. *Nat. Cell Biol.* **21,** 263–274 (2019).
309. Ramachandran, K., Peng, X., Bokvist, K. & Stehno-Bittel, L. Assessment of re-aggregated human pancreatic islets for secondary drug screening. *Br. J. Pharmacol.* **171,** 3010–3022 (2014).

310. Wassmer, C.-H., Bellofatto, K., Perez, L., Lavallard, V., Cottet-Dumoulin, D., Ljubicic, S., Parnaud, G., Bosco, D., Berishvili, E. & Lebreton, F. Engineering of Primary Pancreatic Islet Cell Spheroids for Three-dimensional Culture or Transplantation: A Methodological Comparative Study. *Cell Transplant.* **29,** 096368972093729 (2020).
311. Piro, S., Mascali, L. G., Urbano, F., Filippello, A., Malaguarnera, R., Calanna, S., Rabuazzo, A. M. & Purrello, F. Chronic Exposure to GLP-1 Increases GLP-1 Synthesis and Release in a Pancreatic Alpha Cell Line (α-TC1): Evidence of a Direct Effect of GLP-1 on Pancreatic Alpha Cells. *PLoS One* **9,** e90093 (2014).
312. Peterson, Q. P., Veres, A., Chen, L., Slama, M. Q., Kenty, J. H. R., Hassoun, S., Brown, M. R., Dou, H., Duffy, C. D., Zhou, Q., Matveyenko, A. V., Tyrberg, B., Sörhede-Winzell, M., Rorsman, P. & Melton, D. A. A method for the generation of human stem cell-derived alpha cells. *Nat. Commun.* **11,** 2241 (2020).
313. Gaertner, B., Carrano, A. C. & Sander, M. Human stem cell models: lessons for pancreatic development and disease. *Genes Dev.* **33,** 1475–1490 (2019).
314. Jang, S., Collin de l'Hortet, A. & Soto-Gutierrez, A. Induced Pluripotent Stem Cell–Derived Endothelial Cells: Overview, Current Advances, Applications, and Future Directions. *Am. J. Pathol.* **189,** 502–512 (2019).
315. Kumar, M., Gupta, P., Bhattacharjee, S., Nandi, S. K. & Mandal, B. B. Immunomodulatory injectable silk hydrogels maintaining functional islets and promoting anti-inflammatory M2 macrophage polarization. *Biomaterials* **187,** 1–17 (2018).
316. Headen, D. M., Woodward, K. B., Coronel, M. M., Shrestha, P., Weaver, J. D., Zhao, H., Tan, M., Hunckler, M. D., Bowen, W. S., Johnson, C. T., Shea, L., Yolcu, E. S., García, A. J. & Shirwan, H. Local immunomodulation with Fas ligand-engineered biomaterials achieves allogeneic islet graft acceptance. *Nat. Mater.* **17,** 732–739 (2018).
317. Madelon, N., Montanari, E., Gruaz, L., Pimenta, J., Muller, Y. D., Bühler, L. H., Puga Yung, G. L. & Seebach, J. D. Prolongation of rat-to-mouse islets xenograft survival by co-transplantation of autologous IL-10 differentiated murine tolerogenic dendritic cells. *Xenotransplantation* **27,** (2020).
318. Rackham, C. L., Chagastelles, P. C., Nardi, N. B., Hauge-Evans, A. C., Jones, P. M. & King, A. J. F. Co-transplantation of mesenchymal stem cells maintains islet organisation and morphology in mice. *Diabetologia* **54,** 1127–1135 (2011).
319. Berman, D. M., Willman, M. A., Han, D., Kleiner, G., Kenyon, N. M., Cabrera, O., Karl, J. A., Wiseman, R. W., O'Connor, D. H., Bartholomew, A. M. & Kenyon, N. S. Mesenchymal Stem Cells Enhance Allogeneic Islet Engraftment in Nonhuman Primates. *Diabetes* **59,** 2558–2568 (2010).
320. Yoshimatsu, G., Sakata, N., Tsuchiya, H., Minowa, T., Takemura, T., Morita, H., Hata, T., Fukase, M., Aoki, T., Ishida, M., Motoi, F., Naitoh, T., Katayose, Y., Egawa, S. & Unno, M. The Co-Transplantation of Bone Marrow Derived Mesenchymal Stem Cells Reduced Inflammation in Intramuscular Islet Transplantation. *PLoS One* **10,** e0117561 (2015).
321. Kerby, A., Jones, E. S., Jones, P. M. & King, A. J. Co-transplantation of islets with mesenchymal stem cells in microcapsules demonstrates graft outcome can be improved in an isolated-graft model of islet transplantation in mice. *Cytotherapy* **15,** 192–200 (2013).
322. Navaei-Nigjeh, M., Moloudizargari, M., Baeeri, M., Gholami, M., Lotfibakhshaiesh, N., Soleimani, M., Vasheghani-farahani, E., Al, J. & Abdollahi, M. Reduction of marginal mass required for successful islet transplantation in a diabetic rat model using adipose tissue–derived mesenchymal stromal cells. *Cytotherapy* **20,** 1124–1142 (2018).

Acknowledgements

I would like to express my sincere gratitude to my advisor Prof. Dr. Katja Schenke-Layland for the continuous support during my PhD study, for her patience, motivation, and dedication. I could not have imagined having a better advisor and mentor for my PhD study. I would also like to thank Prof. Dr. Garry Duffy for his support as my second advisor and for the great collaboration during the DRIVE EU project.

I would like to thank Prof. Dr. Peter Loskill for his support during my PhD, for providing the pancreas-on-a-chip device and for his scientific input during our collaboration. I would like to thank Prof. Dr. Johannes Eble for welcoming me in his lab and his valuable input regarding protein binding assays. I would like to thank Prof. Dr. Hanna K. A. Mikkola for her support during the redaction of the Nidogen manuscript.

A special thank goes to Max Urbanczyk, who has been a great science partner, for his precious help and input during our collaborative projects. I would like to also thank Daniel Carvajal Berrio for his support with fluorescence lifetime imaging microscopy, Dr. Julia Marzi for her support regarding Raman microspectroscopy and Simone Liebscher for her help with histological procedures. Furthermore, I would like to thank Shannon Lee Layland for his support, his time for everlasting scientific discussions and for his help during the publication process.

To all the Schenke-Layland laboratory members, a special thank for providing a friendly working environment, valuable scientific suggestion, motivation and help during my time in Tübingen.

I would like to thank my friends and colleagues, Julia, Silke, Lisa, Isabel, Katharina, and Elena you for their unlimited support, motivation and stimulating discussion. Finally, I would like to thank my family for the continuous support and encouragement.

Declaration

Ich erkläre hiermit, dass ich die zur Promotion eingereichte Arbeit mit dem Titel *"Three-Dimensional In Vitro Models To Assess Pancreatic β-Cell Function*" selbstständig verfasst, nur die angegebenen Quellen und Hilfsmittel benutzt und wörtlich oder inhaltlich übernommene Zitate also solche gekennzeichnet habe. Ich erkläre, dass die Richtlinien zur Sicherung guter wissenschaftlicher Praxis der Universität Tübingen beachtet wurden. Ich versichere an Eides statt, dass diese Angaben wahr sind und dass ich nichts verschwiegen habe. Mir ist bekannt, dass die falsche Angabe einer Versicherung an Eides statt mit Freiheitsstrafe bis zu drei Jahren oder mit Geldstrafe bestraft wird.

Tübingen, 16.02.2021

Aline Zbinden

Curriculum Vitae

Aline Zbinden

Tübinger Straße 72	aline.zbinden@uni-tuebingen.de	21.04.1991
70178 Stuttgart, Germany	+49 176 21233146	Swiss

EDUCATION

Since 10.2015	**Dr. rer. nat. candidate in Biology, University of Tübingen** AG Schenke-Layland Department of Women's Health Research Institute for Women's Health
09.2012 – 02.2015	**Master in Bioengineering and Biotechnology (Life Science, EPFL)** *Semester Project*: "Fabrication of "smart" multiwell plate by hydrogel microfluidics" at the Laboratory of Stem Cell Bioengineering at EPFL, (Prof. Lütolf) *Master Project*: "Multivalency of bFGF Conjugated to Hyaluronic Acid » at the Laboratory of Tissue Engineering and Biomaterials, UC Berkeley (02.2014 – 02.2015) (Prof. Healy & Prof. Lütolf (EPFL))
09.2009 – 07.2012	**Bachelor in Life Sciences and Technology (Life Science, EPFL)** *Bachelor Project:* Plasmids design, at the Swiss Institute for Experimental Cancer Research (EPFL)

WORK EXPERIENCE

Since 10.2015	**Department of Women's Health, University of Tübingen** Research Assistant (Dr. rer. nat Candidate) Advisor: Prof. K. Schenke-Layland
02.2015 – 08.2015	**Department of Bioengineering, UC Berkeley** *Junior specialist,* Laboratory of Kevin Healy.
09.2013- 12.2013	**University Hospital, Lausanne, Switzerland** Intern, Diagnostic Laboratory of the Immunology and Allergy Division, Prof. Giuseppe Pantaleo.
02.2012 – 09.2013	**School of Life Science, (EPFL)** *Teaching Assistant for Physiology Lab* (09.2012 – 09.2013), responsible for the preparation and supervision of 3rd year BSc lab sessions *Teaching Assistant for Molecular Biology Course* (02.2012 – 07.2012), responsible for preparation and teaching of 1st year BSc exercise session

PUBLICATIONS

Zbinden A.#, Layland S.L.#, Urbanczyk M., Carvajal D.A., Marzi J., Zauner M., Hammerschmidt A., Brauchle E.M., Sudrow K., Fink S., Templin M., Liebscher S., Klein G., Deb A., Duffy G.P., Crooks G.M., Eble J.A., Mikkola H.K.A., Seifert M. and Schenke-Layland K.; *Nidogen-1 Mitigates Ischemia and Promotes Tissue Survival and Regeneration*, Advanced Science, 2021; 8(4): 2170016. https://doi.org/10.1002/advs.202002500.

Zbinden A.[#], Carvajal D.A.[#], Urbanczyk M., Layland S.L., Bosch M., Fliri S., Lu C., Jeyagaran A., Loskill P., Duffy G.P. & Schenke-Layland K.; *Fluorescence lifetime metabolic mapping of hypoxia-induced damage in pancreatic pseudo-islets*, Journal of Biophotonics, 2020; 13(12): e202000375. https://doi.org/10.1002/jbio.202000375

Zbinden A.[#], Urbanczyk M.[#], Layland S.L., Becker L., Marzi J., Bosch M., Loskill P., Duffy G.P. & Schenke-Layland K.; *Collagen and endothelial cell co-culture improves β-cell functionality and rescues pancreatic ECM*, Tissue Engineering Part A, 2020; accepted on Sept. 22nd, 2020. https://doi.org/10.1089/ten.tea.2020.0250

Zbinden A., Marzi J., Schlünder K., Probst C., Urbanczyk M., Black S., Brauchle E.M., Layland S.L., Kraushaar U., Duffy G.P., Schenke-Layland K., & Loskill P.; *Non-invasive high content Raman analysis of a microphysiological human pancreas-on-a-chip model,* Matrix Biology, 2020; 85: 205-220. https://doi.org/10.1016/j.matbio.2019.06.008

Urbanczyk M., **Zbinden A.**, Layland S. L., Duffy G., & Schenke-Layland K.; Controlled Heterotypic *Pseudo-Islet Assembly of Human β-Cells and Human Umbilical Vein Endothelial Cells Using Magnetic Levitation*, Tissue Engineering Part A, 2019; 26(7-8): 387-399. https://doi.org/10.1089/ten.tea.2019.0158

Rogal J.[#], **Zbinden A.**[#], Schenke-Layland K., & Loskill P., *Stem-cell based organ-on-a-chip models for diabetes research*, Advanced Drug Delivery Reviews, 2019; 140: 101-128. https://doi.org/10.1016/j.addr.2018.10.010

Zbinden A.[#], Browne S.[#], Altiok E. I., Svedlund F. L., Jackson W. M., & Healy K. E. (2018). *Multivalent conjugates of basic fibroblast growth factor enhance in vitro proliferation and migration of endothelial cells.* Biomaterials science, 6(5): 1076-1083. http://www.dx.doi.org/10.1039/C7BM01052D

Zbinden A., Hinderer S., Layland S.L., and Schenke-Layland K., *Real-Time Analysis of Biomaterials Function*, Elsevier, Oxford, Paul Ducheyne, 2017; 85-100.

Altiok E. I., Santiago-Ortiz J. L., Svedlund F. L., **Zbinden A.**, Jha A. K., Bhatnagar D., Loskill P., Jackson W. M., Schaffer D. V. & Healy, K. E. (2016). *Multivalent hyaluronic acid bioconjugates improve sFlt-1 activity in vitro.* Biomaterials, 93: 95-105. http://www.dx.doi.org/10.1016/j.biomaterials.2016.03.017

CONFERENCES

Zbinden A., Loskill P. & Schenke-Layland K. *Organ-on-a-chip for Diabetes Research.* Invited speaker at the Annual Rachmiel Levine-Arthur Riggs Diabetes Research Symposium, Pasadena, USA, 2019.

Zbinden, A. Urbanczyk M., Hinderer S., Layland S., and Schenke-Layland K. *ECM and Pancreatic β-cell Interaction Influence β-cell Insulin Production In Vitro.* Talk at the Joint Meeting of the German and Swiss Societies for Matrix Biology (DGMB), Stuttgart, Germany, 2018.

Zbinden A., Hinderer S., Layland S. L. & Schenke-Layland K. *Pancreatic Niche Molecules As Support for Rat Insulinoma pseudo-islets in Vitro.* Talk at the Annual Meeting of the German Society for Matrix Biology (DGMB), Cologne, Germany, 2017.

Zbinden A., Carvaja-Berrio D., and Schenke-Layland K. *Evaluation of the metabolic contribution of cytosolic and mitochondrial NAD(P)H during insulin secretion.* Poster at the Microscopy Conference, EPFL, Lausanne, Switzerland, 2017.

Zbinden A., Hinderer S., Layland S. L. & Schenke-Layland K. *Pancreatic Niche Molecules As Support for Rat Insulinoma pseudo-islets in Vitro.* Poster at the Gordon Research Conference & Seminar: Pancreatic Disease, Waterville Valley, NH, USA, 2017.

Zbinden A., Layland S. L., Holeiter M., Hinderer S. & Schenke-Layland K. *Diabetes-reversing implants for enhanced viability and long-term efficacy*. Poster at the Gordon Research Conference & Seminar: Signal Transduction by Engineered Extracellular Matrices, University of New England, Biddeford, ME, USA, 2016.

Zbinden A., Layland S. L., Nsair A., & Schenke-Layland K. *ECM analyses of Islet-1+ neuronal clusters innervating the developing human heart.* Poster at the Annual Meeting of the German Society for Matrix Biology (DGMB), Freiburg, Germany, 2016.

AWARDS & FELLOWSHIPS

11.2020	International Foundation for Ethical Research (IFER) Graduate Student Fellowship, Chicago, USA. - $12'500
11.2019	International Foundation for Ethical Research (IFER) Graduate Student Fellowship, Chicago, USA. - $12'500
08.2019	Exzellenzoffensive Lehre PROFIL, University Hospital Tübingen, Germany – €30'000
02.2019	Deutsche Gesellschaft für Matrixbiologie (DGMB) travel grant, Regensburg, Germany.

Appendices

Appendix I: Zbinden A.§, Urbanczyk M.§, Layland S.L., Becker L., Marzi J., Bosch M., Loskill P., Duffy G.P. & Schenke-Layland K.; *Collagen and endothelial cell co-culture improves β-cell functionality and rescues pancreatic ECM*, Tissue Engineering Part A; accepted on Sept 22nd, 2020.

TISSUE ENGINEERING: Part A
Volume 00, Number 00, 2020
Mary Ann Liebert, Inc.
DOI: 10.1089/ten.tea.2020.0250

termis
Tissue Engineering
& Regenerative Medicine
International Society

Collagen and Endothelial Cell Coculture Improves β-Cell Functionality and Rescues Pancreatic Extracellular Matrix

Aline Zbinden, MSc,[1,2,*] Max Urbanczyk, MSc,[1,2,*] Shannon L. Layland, MBA,[1,2]
Lucas Becker, MSc,[1–3] Julia Marzi, PhD,[1–4] Mariella Bosch, BSc,[1,2] Peter Loskill, PhD,[1,2,5]
Garry P. Duffy, PhD,[6] and Katja Schenke-Layland, MSc, PhD[1–4,6,7]

The use of biomaterials and biomaterial functionalization is a promising approach to support pancreatic islet viability posttransplantation in an effort to reduce insulin dependence for patients afflicted with diabetes mellitus type 1. Extracellular matrix (ECM) proteins are known to impact numerous reparative functions in the body. Assessing how endogenously expressed pancreatic ECM proteins are affected by posttransplant-like hypoxic conditions may provide significant insights toward the development of tissue-engineered therapeutic strategies to positively influence β-cell survival, proliferation, and functionality. Here, we investigated the expression of three relevant groups of pancreatic ECM proteins in human native tissue, including basement membrane (BM) proteins (collagen type 4 [COL4], laminins [LAM]), proteoglycans (decorin [DCN], nidogen-1 [NID1]), and fibril-forming proteins (fibronectin [FN], collagen type 1 [COL1]). In an *in vitro* hypoxia model, we identified that ECM proteins were differently affected by hypoxic conditions, contributing to an overall loss of β-cell functionality. The use of a COL1 hydrogel as carrier material demonstrated a protective effect on β-cells mitigating the effect of hypoxia on proteoglycans as well as fibril-forming protein expression, supporting β-cell functionality in hypoxia. We further showed that providing endothelial cells (ECs) into the COL1 hydrogel improves β-cell response as well as the expression of relevant BM proteins. Our data show that β-cells benefit from a microenvironment composed of structure-providing COL1 with the incorporation of ECs to withstand the harsh conditions of hypoxia. Such hydrogels support β-cell survival and can serve as an initial source of ECM proteins to allow cell engraftment while preserving cell functionality posttransplantation.

Keywords: β-cells, diabetes, hypoxia, extracellular matrix, collagen type 1

Impact Statement

Expression analysis identifies hypoxia-induced pathological changes in extracellular matrix (ECM) homeostasis as potential targets to support β-cell transplants by encapsulation in biomaterials for the treatment of diabetes mellitus. A collagen-1 hydrogel is shown to attenuate the effect of hypoxia on β-cells and their ECM expression. The functionalization of the hydrogel with endothelial cells increases the β-cell response to glucose and rescues essential basement membrane proteins.

[1]Department of Bioengineering, Eberhard Karls University Tübingen, Tübingen, Germany.
[2]Department of Women's Health, Research Institute for Women's Health, Eberhard Karls University Tübingen, Tübingen, Germany.
[3]Cluster of Excellence iFIT (EXC 2180) "Image-Guided and Functionally Instructed Tumor Therapies," Eberhard Karls University Tübingen, Tübingen, Germany.
[4]NMI Natural and Medical Sciences Institute at the University of Tübingen, Reutlingen, Germany.
[5]Fraunhofer IGB, Stuttgart, Germany.
[6]Anatomy & Regenerative Medicine Institute, School of Medicine, College of Medicine Nursing and Health Sciences, National University of Ireland Galway, Galway, Ireland.
[7]Cardiovascular Research Laboratories, Department of Medicine/Cardiology, David Geffen School of Medicine at UCLA, Los Angeles, California, USA.
*These two authors contributed equally to this work.

Introduction

THE EXTRACELLULAR MATRIX (ECM) physically and biochemically supports tissues and organs. It consists of large fibrillar proteins, glycoproteins, and proteoglycans, as well as water, growth factors, enzymes, and other biomolecules.[1] The ECM is vital for cell survival and function as it provides biological, chemical, and mechanical cues to cells, which in turn, remodel the ECM to control tissue homeostasis.[1]

Alterations and disruptions of the ECM homeostatic state adversely affect cells resulting in structural tissue damages, diseases, and potentially organ failure.[2] Mechanical disruption of the ECM that occurs during injury or is induced during transplant surgery can severely compromise cell survival and function, ultimately hindering cell engraftment.[1] This is a major issue in cell and tissue transplantation due to a number of underlying factors, including the hypoxic environment at the transplant site, the implant/transplant-triggered immune response, and pathological ECM remodeling posttransplantation.

The transplantation of Islets of Langerhans or isolated pancreatic β-cells is a promising therapy to treat type 1 diabetes mellitus. However, poor engraftment combined with hypoxic conditions of posttransplantation are responsible for the loss of more than 60% of the transplanted cells within 1 month, leading to the loss of insulin-independency and severe hypoglycemic events.[3,4] Therefore, strategies to improve transplant survival and efficacy should include tissue-engineered methods to support the transplants' survival under hypoxic conditions and improve the ECM homeostasis of the transplant itself.

The isolation of the Islets of Langerhans from donor pancreases severs the vasculature connection between the islets and pancreas. During this process, collagenases are infused into the tissues, disrupting the interstitial matrix of fibrillar proteins, such as collagen type 1 (COL1).[4–6] The process partially digests the double basement membrane (BM) surrounding the islets, which is composed of collagen type 4 (COL4), laminins (LAM), fibronectin (FN), and proteoglycans.[6,7] BM proteins were reported to be differentially affected by the isolation procedure; perlecan and laminin α5 are completely lost, while COL4 and other LAM are still present after the process.[7] The resulting loss in ECM structure has been previously shown to negatively impact islet survival and function of posttransplantation.[8]

Endothelial cells (ECs) are the main source of BM proteins in the native pancreas.[9] Most transplantation sites lack ECs. The reestablishment of EC presence via revascularization requires several days of posttransplantation.[10] During that time, β-cells experience severe hypoxic conditions leading to improper ECM remodeling. Hence, β-cells initially rely on their intrinsic ECM protein expression to survive in a hypoxic posttransplantation environment or on external support, for example, carrier materials such as collagen-based hydrogels.[11,12]

Although many studies have shown the importance of the ECM and how it affects β-cell function, there have been very few investigations on how hypoxia regulates the expression and homeostasis of endogenous ECM in pancreatic islets.[13] Therefore, we developed an *in vitro* hypoxia model to investigate the ECM expression of β-cell composed of pseudoislets and to monitor pathological ECM changes under hypoxic conditions (Supplementary Fig. S1). We showed that hypoxia differentially affects the expression of BM proteins, proteoglycans, and fibril-forming ECM proteins. The use of a clinically approved COL1 hydrogel as carrier material allowed the rescue of the proteoglycans and fibril-forming ECM proteins. Coculturing ECs with β-cell pseudoislets in the COL1 hydrogel improved the endogenous expression of BM proteins. The combination of biological cues together with ECs is a promising strategy to prevent or reduce hypoxia-related apoptosis and loss of β-cell functionality.

Materials and Methods

INS1E cell culture and pseudoislet assembly

The insulin producing rat insulinoma cell line INS1E was a kind gift from Prof. Maechler from the University of Geneva, Switzerland. INS1E cells were cultured in adapted RPMI 1640 (Gibco) containing 10 mM HEPES (Gibco), 50 μM 2-mercapto-ethanol (Sigma-Aldrich), 1 mM pyruvate (Gibco), 5% fetal bovine serum (Sigma-Aldrich), 100 iU/mL penicillin, and 100 μg/mL streptomycin, under standard humidified normoxic conditions (37°C, 5% CO_2, 20% O_2), and passaged at 80% confluency. To assemble pseudoislets, nonadherent 96-well U-bottom plates (Thermo Fisher Scientific) were used at a density ranging from 500 to 10,000 cells per well in a working volume of 100 μL/well and placed under normoxic conditions for 48 h before any experiment. Hypoxia experiments were performed under the following conditions: 37°C, 5% CO_2 and 1% O_2, which were chosen according to literature.[14–16] In detail, pseudoislets were seeded in overnight preincubated hypoxia medium. Media was changed every other day. Every 24 h, images of the pseudoislets were obtained using a brightfield microscope (Zeiss), and the pseudoislet size was analyzed using ImageJ V 1.52p. The growth speed was assessed by applying a linear regression curve for each pseudoislet size from day 2 to 8, resulting in the average growth in micrometers per day.

Viability assay

Fluorescein diacetate (FDA)/propidium iodide (PI) (Sigma-Aldrich) staining was performed according to the manufacturer's protocol. In brief, pseudoislets were washed once with phosphate-buffered saline (PBS), incubated with 33 μL FDA and 300 μL PI per 1 mL RPMI 1640 for 15 min at normoxic conditions. After incubation, pseudoislets were washed three times with PBS before recording the fluorescence using a laser scanning microscope 710 (Zeiss). The fluorescence was recorded in the z-stack mode using maximum intensity projection. Images were evaluated by Zen Blue (Zeiss) and ImageJ V 1.52p software. The number of PI^+ cells was normalized by the diameter of each pseudoislet.

Human umbilical vein endothelial cell culture and coculture pseudoislet assembly

Human umbilical vein endothelial cell (HUVEC) culture and coculture pseudoislet assembly was performed as recently reported.[17] The magnetizing of HUVEC and INS1E allows the proper and reproducible aggregation of pseudoislets by placing the HUVECs around the INS1E β-cells. In brief, HUVECs (PromoCell) were cultured in corresponding

EC growth medium (PromoCell), passaged at a confluency between 80% and 90%, and used between passage 2 and 6. For coculture pseudoislets assembly, INS1E cells and HUVECs were magnetized overnight before seeding, using NanoShuttle™-PL (Greiner) at a concentration of 40 µL/mL according to the manufacturer's protocol. To obtain optimal glucose-stimulated insulin secretion (GSIS) functionality of the cocultured pseudoislets, INS1E cells were seeded first at a density of 500 cells per well in 50 µL INS1E media to ensure proper pseudoislet formation. HUVECs were added 24 h later at a density of 500 cells per well in 50 µL HUVEC media, resulting in a media ratio of 1:1, and placed atop the magnetic levitation plate for 30 min under standard culture conditions for another 24 h.

COL1 pseudoislet encapsulation

An average number of 48 pseudoislets or coculture pseudoislets were encapsulated in COL1 with a concentration of 6.0 mg/mL with a total volume of 250 µL following the manufacturer's instructions (Fraunhofer IGB, Stuttgart[18]).

GSIS assay

Ninety-six hours after seeding, pseudoislets with 500 and 1000 cells per pseudoislet were grouped by 4 per well in 50 µL medium. Pseudoislets were washed twice using KREBS 1×buffer containing 0.1% bovine serum albumin (Sigma-Aldrich) and 25 mM HEPES (Gibco). Then, pseudoislets were incubated for 30 min in KREBS 1×buffer under normoxic conditions. Subsequently, KREBS 1×buffer containing 3.3 mM glucose (Gibco) was added and the pseudoislets were incubated for 1.5 h. The pseudoislets were washed again twice and incubated with KREBS 1×buffer containing 16.7 mM glucose for another 1.5 h. The supernatants were collected and stored at −20°C for further insulin detection using enzyme-linked immunosorbent assay (Mercodia). The GSIS index represents the fold increase in insulin secretion from 3.3 to 16.7 mM glucose. For the GSIS assay in COL1 hydrogel, all incubation times were doubled with regard to diffusion properties.

Histological analysis

Pseudoislets were washed with PBS (Gibco), fixed with 4% paraformaldehyde, embedded in HistoGel® (Thermo Fisher Scientific), and processed for paraffin embedding using a Shandon Citadel 1000 (Thermo Fisher Scientific) according to the manufacturer's protocol. Sections were cut with a thickness of 3 µm (Microtome RM2145; Leica), deparaffinized using xylene, and rehydrated by graded ethanol (100–50%) in VE-water. Adult human pancreatic tissues were commercially obtained from Novus biologicals (NBP2-30191; Novus Biological, Bio-Techne GmbH, Wiesbaden, Germany).

Immunofluorescence staining

TRIS-EDTA (pH9) and citrate (pH6) buffer were used for antigen retrieval. The antibodies were used according to the manufacturer's specifications and are shown in Supplementary Table S1. Sections were incubated for 10 min with 4′,6-diamidino-2-phenylindole (DAPI, 2 µg/mL in PBS; Sigma-Aldrich) prior mounting with Molecular Probes ProLong Gold Antifade solution (Invitrogen). Immunofluorescence (IF) staining images of pseudoislets and pancreatic tissues were obtained using an Axio Observer Z1 microscope (Zeiss) as well as laser scanning microscopes 710 (Zeiss) and 780 (Zeiss). The images were analyzed using Zeiss Zen Blue software and ImageJ V1.52p.

Terminal deoxynucleotidyl transferase-mediated nick-end labeling assay

Click-iT TUNEL Alexa Fluor Imaging Assay Kit (Thermo Fisher Scientific) was used according to the manufacturer's specifications and used as previously described.[17] In brief, the sections were deparaffinized and permeabilized with 0.25% Triton-X for 20 min. Terminal deoxynucleotidyl transferase reaction buffer was added to the slides for 60 min at 60°C. Subsequently, sections were incubated with Click-iT reaction buffer for 30 min at room temperature. The counterstaining was performed using DAPI.

Image analysis

PI^+ cells were counted using an automated macro in ImageJ V 1.52p and normalized by the size of the pseudoislet. Blinded terminal deoxynucleotidyl transferase-mediated nick-end labeling (TUNEL)- and Ki67-stained images were quantified by two independent, unbiased observers. Cells were counted as $TUNEL^+$ and $Ki67^+$ when exhibiting a green (TUNEL or Ki67) and blue (DAPI) double staining. Ratios of $TUNEL^+$ and $Ki67^+$ cells were calculated by dividing the number of $TUNEL^+$ and $Ki67^+$ cells, respectively, by the number of total $DAPI^+$ cells. Staining intensities were evaluated via the mean gray value (MGV) per pixel within the region of interest (ROI). Pseudoislet ROI was selected as $DAPI^+$ area and for human pancreatic sections as $insulin^+$ region. Fold changes were calculated by dividing the MGV of the hypoxia samples by the MGV of the normoxia samples. The standard deviation was calculated using the formula for the propagation of error.

Nuclear expression of FN was quantified by a custom-written macro using Microsoft Excel (Microsoft Corporation, 2018). The program validates, whether the single pixel values of the blue channel (DAPI) and the green channel (FN) exceed a set threshold value. If both thresholds were exceeded, this pixel was counted as nuclear FN expression. The pixel was counted as nonnuclear FN expression only when the green threshold was exceeded. The percentage of nuclear FN expression was calculated using the following formula: percentage of nuclear fibronectin expression = (number of pixels with nuclear fibronectin expression)/(number of pixels with nuclear fibronectin expression + number of pixels with nonnuclear fibronectin expression).

Overall fold changes for ECM protein expression between normoxic COL1 hydrogel and hypoxic COL1 hydrogel+HUVECs were calculated by multiplying the fold changes of (hypoxic COL1 hydrogel/normoxic COL1 hydrogel)*(hypoxic COL1 hydrogel + HUVECs/hypoxic COL1 hydrogel).

Raman imaging of pseudoislets

INS1E pseudoislets were prepared for Raman imaging as previously described.[19] In brief, hypoxic and control

pseudoislets were placed in a microfluidic chip for noninvasive *in situ* Raman imaging. The microfluidic device stabilizes the pseudoislets during measurements, while supplementing nutrients via media perfusion. Spectral mapping was performed on a customized inverted WITec alpha300 R Raman system (WITec GmbH) equipped with a green laser (532 nm) and a CCD spectrograph with a grating of 600 g/mm. An incubation chamber (Okolab S.R.L.) was integrated in the setup to keep the pseudoislets constantly at 37°C. Images were acquired as triplicates at a laser power of 58 mW, an integration time per spectrum of 0.5 s and a pixel resolution of 1×1 µm.

Multivariate data analysis

Image analysis of the spectral map was performed with the Project Five 5.2 software (WITec GmbH). Raman data were pretreated whereby each scan was subjected to cosmic ray removal, polynomial baseline correction (to remove the glass background), and intensity normalization. True component analysis (TCA) was performed at the spectral range of 600–1800 cm^{-1}. In brief, TCA is a nonnegative matrix factorization-based multivariate data analysis tool elaborating spectral components, which predominantly occur in the data set allowing to identify the localization of these components by false color intensity distribution heatmaps. Gray value intensities per pixel (MGV) were determined in ImageJ V 1.52p to semiquantify the distribution of the spectral components in normoxic and hypoxic conditions. Furthermore, TCA allowed to preselect ROI with similar spectral information representing nuclei, ECM, and mitochondria, which was extracted for further in-depth analysis of the molecular composition by principal component analysis (PCA) using Unscrambler X10.5 (Camo). PCA is a multivariate data analysis tool reducing the dimensionality of a set of spectral data on a vector-based approach. Each vector, the so-called principal component (PC), describes a variation in the spectra. Plotting PC values against each other visualizes a correlation or separation of two or more data sets.

Statistical analysis

Statistical analysis was performed using Origin 2019b (OriginLab) and GraphPad Prism version 6.00 for Windows (GraphPad Software). Results are shown throughout the entire article as mean ± standard deviation. All data sets are tested for normal distribution using Kolmogorov–Smirnov test; outliers were removed using Grubb's test with a confidence interval of 0.05. All *n*-numbers, applied tests, and corresponding significances for each result are listed in the figure legends.

Results

Assembly of pancreatic β-cells into glucose-responsive pseudoislets

To assess the ECM-related changes induced by hypoxic conditions on pancreatic islets, we established an *in vitro* model composed of INS1E β-cells that were assembled into pseudoislets to mimic the insulin-secreting endocrine function of the native Islets of Langerhans. The native pancreatic islets range is from 50 to 400 µm in diameter with an average size of 150 µm.[20,21] Therefore, pseudoislets were formed by spontaneous aggregation with 500 to 10,000 cells per pseudoislets (Fig. 1). The proliferative nature of the INS1E β-cells lead to an overall increase in their size over time, monitored for a period of 8 days (Fig. 1A). The growth speed was impacted by the number of initially seeded cells: pseudoislets of 2000 (2k), 4000 (4k), and 10,000 (10k) cells per pseudoislet grew significantly faster than pseudoislets of 500 (0.5k) and 1000 (1k) cells per pseudoislet (Fig. 1B).

Diffusion of nutrients and oxygen are essential for the survival and physiological function of three-dimensional (3D) cell constructs.[22,23] The lack of diffusion that occurs in large cell aggregates results in the formation of a hypoxic core.[24] Therefore, we assessed the influence of pseudoislet size on pseudoislet viability (Fig. 1C). We observed a hypoxic core depicted by PI-stained cells in large pseudoislets (4k and 10k pseudoislets) after 8 days in culture, which was not observed in smaller pseudoislets (0.5k, 1k, and 2k pseudoislets). The quantification of PI^+ cells in 0.5k, 1k, and 2k pseudoislets showed a significantly higher dead cell ratio in 2k pseudoislets compared with 0.5k and 1k pseudoislets after 3 and 8 days (0.5k: 0.038 ± 0.026 [3 days] vs. 0.082 ± 0.04 [8 days], $p < 0.0001$; 1k: 0.0656 ± 0.024 [3 days] vs. 0.163 ± 0.006 [8 days], $p < 0.01$; 2k: 0.163 ± 0.022 [3 days] vs. 0.0164 ± 0.040, $p < 0.0001$). These data suggest that 0.5k and 1k pseudoislets allowed for proper nutrient and oxygen diffusion overtime, which is in line with previous studies showing that pseudoislets above 1000 cells per islet lead to an unstable aggregation (Fig. 1D).[24,25]

The major function of β-cells is to secrete insulin in response to glucose, which is also influenced by the pseudoislet size.[26,27] Therefore, GSIS assays were performed to assess potential functional differences between 0.5k and 1k pseudoislets (Fig. 1E, F). The GSIS index revealed that 0.5k pseudoislets had a significantly higher glucose response compared with the 1k pseudoislets (Fig. 1E; 0.5k GSIS of 2.024 ± 0.51 compared with 1k GSIS 1.232 ± 0.340; $p < 0.05$). We showed that 0.5k pseudoislets were highly viable and glucose-responsive with an average basal insulin secretion of 0.0427 ± 0.0077 and 0.0839 ± 0.0134 µg/L per islet when stimulated with 16.7 mM glucose (Fig. 1F). The 0.5k pseudoislets were chosen for all further experiments, as they offer high reproducibility and stability over time to study the effects of hypoxia on endogenous β-cell ECM expression.

Hypoxia induces apoptosis and impairs pseudoislet functionality in vitro

Pseudoislets were subjected for a period of 48 h to hypoxic conditions (1% oxygen). B-cell death, proliferation, and functionality were evaluated to validate the hypoxic effect in the *in vitro* model (Fig. 2). The expression of caspase-3, which is a downstream activator of the apoptotic pathway, significantly increased under hypoxic conditions (Fig. 2A).[28] To verify that the activation of caspase-3 signaled to its final target, we looked at the number of cells positive for TUNEL, which identifies DNA fragmentation in nuclei that occurs during late-stage apoptosis.[28] We identified a significant increase of $TUNEL^+$ cells in the hypoxia *in vitro* model (Fig. 2B; 0.54% ± 0.76% normoxia vs. 10.45% ± 0.764% hypoxia; $p < 0.0001$), confirming the completion of apoptotic pathways. The proliferative

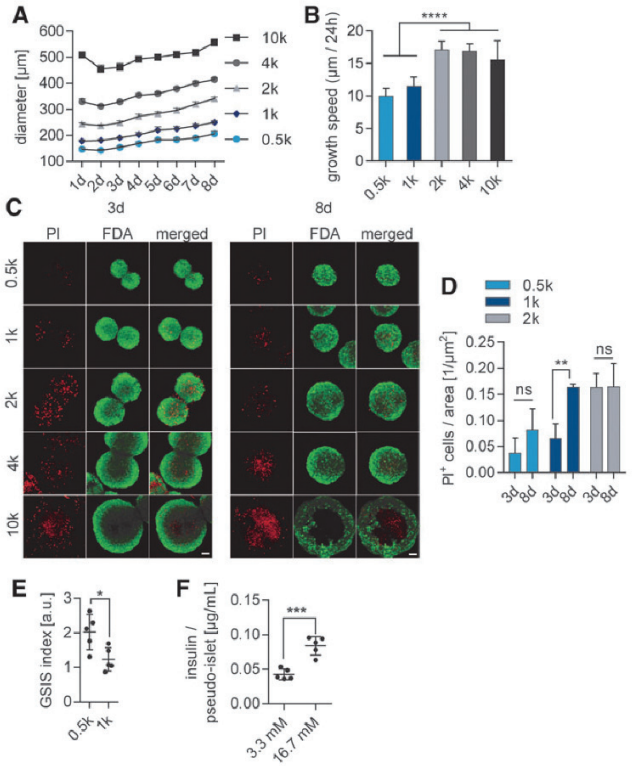

FIG. 1. Pseudoislet size affects survival, growth, and functionality *in vitro*. **(A)** Pseudoislet size assessment over a period of 8 days. Different cell concentrations were tested: 10,000 cells per pseudoislet (10k), 4000 cells per pseudoislet (4k), 2000 cells per pseudoislet (2k), 1000 cells per pseudoislet (1k), and 500 cells per pseudoislets. **(B)** Evaluation of growth speed of pseudoislets depending on the initial number of seeded cells. **(C)** Cell viability at 3 days after seeding and 8 days after seeding. FDA indicates live cells (*green*) and PI indicates dead cells (*red*). **(D)** Quantification of FDA/PI ratio of 0.5k, 1k, and 2k pseudoislets after 3 and 8 days, $n \geq 3$, two-way ANOVA with Tukey's multiple comparisons test. **(E)** GSIS index of 0.5k pseudoislets compared to 1k pseudoislets, $n = 5$, unpaired *t*-test. **(F)** Insulin secretion of 0.5k pseudoislets under 3.3 mM glucose and 16.7 mM glucose, $n = 5$, unpaired *t*-test. $*p < 0.05$, $**p < 0.01$, $***p < 0.001$, $****p < 0.0001$. Scale bars = 50 µm. FDA, fluorescein diacetate; GSIS, glucose-stimulated insulin secretion; PI, propidium iodide.

capacity of INS1E β-cells was impaired by the hypoxic culture condition, demonstrated by a significant loss of Ki67 expression (Fig. 2C; 79.27% ± 7.89% normoxia vs. 43.3% ± 11.34% hypoxia; $p < 0.001$).

We assessed GSIS, insulin expression, and E-cadherin expression, which is an important cell–cell contact protein contributing to pseudoislet integrity and functionality under hypoxic conditions.[29] We showed that pseudoislets cultured under hypoxic conditions expressed significantly lower amounts of E-cadherin (Fig. 2D; 6321 ± 1086 gray value intensities (GVI)/pixel normoxia vs. 1940 ± 209 GVI/pixel hypoxia; $p < 0.0001$) and also expressed significantly less insulin (Fig. 2E; 14223 ± 2491 GVI/pixel normoxia vs. 4583 ± 1204 GVI/pixel hypoxia; $p < 0.0001$), contributing to a lack of response when stimulated by glucose (Fig. 2F).

To identify hypoxia-specific biochemical changes *in situ* within the living cells and cell-derived ECM in pseudoislets, Raman microspectroscopy and Raman imaging were used as noninvasive marker-independent techniques on living pseudoislets (Fig. 2G–K).[19] Raman imaging and TCA identified three main components in the pseudoislets that were previously assigned to nuclei, mitochondria, and ECM (Fig. 2G, H). Major peaks related to nuclei were identified as 785 cm^{-1} (DNA) and 826 and 1090 cm^{-1} (PO_2 backbone). Mitochondria TCA was defined by intense peaks located at 747, 1125, and 1583 cm^{-1} describing heme vibrations in cytochrome C complexes.[30,31] The ECM TCA was highly impacted by changes in collagens (1173, 1310, and 1340 cm^{-1}).[30,32,33] TCA quantification further revealed a significant decrease in the distribution of the nuclei component, indicating changes and/or loss of the nuclear biochemical spectral fingerprint, while there was no impact on the mitochondrial component (Fig. 2I).

For in-depth analysis of the TCA patterns within the mitochondrial component, Raman spectra were subjected to PCA. The multivariate data analysis of single spectra showed a separation according to the first principal component (PC1) (Fig. 2J). The loading of PC1 revealed that the major molecular differences responsible for the separation were 751 and 1125 cm^{-1}, indicating that mitochondria of pseudoislets are more active under normoxic conditions (Fig. 2K). The negative range showed an overall higher protein signal in hypoxic pseudoislets, which may be the results of mitochondrial damage followed by the infiltration of cytoplasmic proteins.

Raman TCA quantification identified a significant alteration of the ECM proteins in hypoxic pseudoislets. This impact on crucial pancreatic ECM structures most likely contributes to the loss of β-cell function, as it has been previously shown that intraislet ECM interactions can modulate β-cell proliferation and survival.[34]

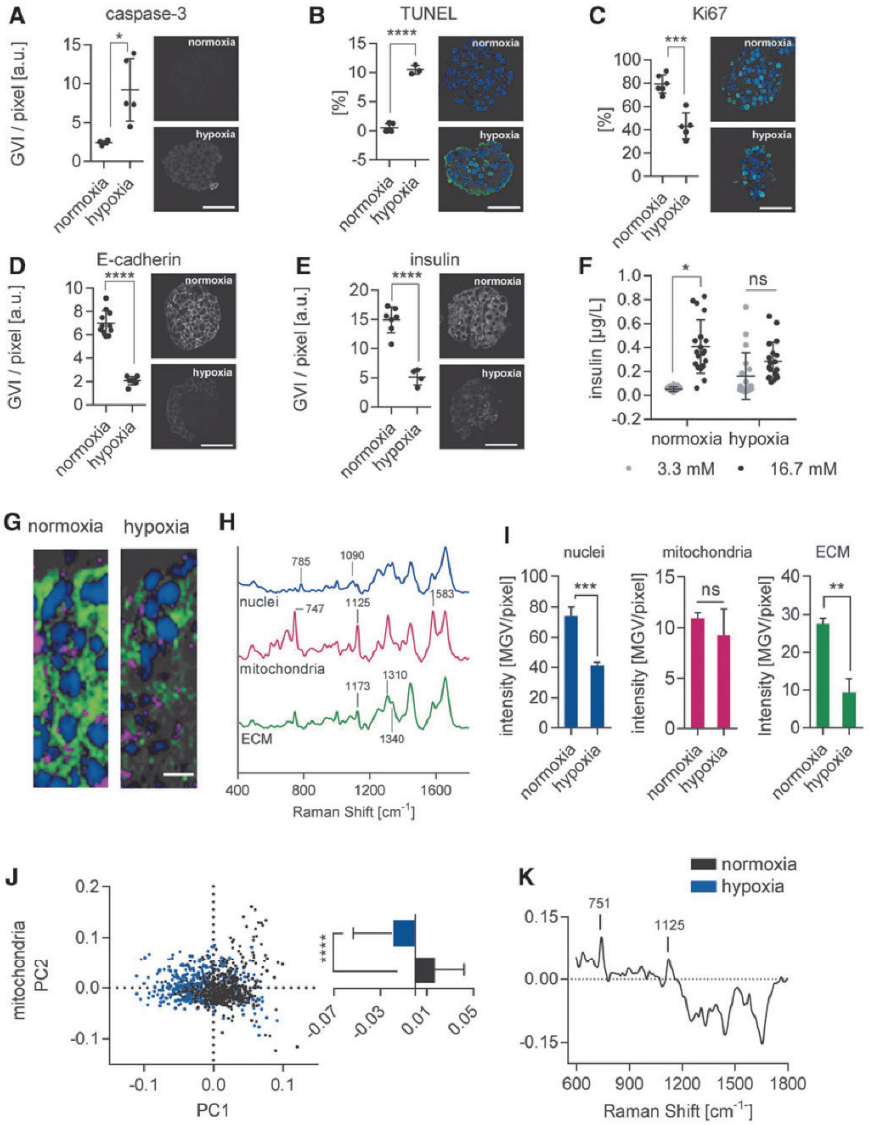

FIG. 2. Hypoxia induces apoptosis and impairs pseudoislet functionality *in vitro*. **(A, B)** Cell death assessment under normoxic and hypoxic conditions is quantified via **(A)** expression of cleaved caspase-3 ($n \geq 4$) and **(B)** number of TUNEL$^+$ cells ($n \geq 3$) (TUNEL$^+$ in *green*, DAPI in *blue*), **(C)** Ki67 ($n \geq 5$) (Ki67$^+$ in *green*, DAPI in *blue*), **(D)** E-cadherin expression ($n \geq 6$), **(E)** insulin expression ($n \geq 6$); unpaired *t*-test. Scale bars = 50 µm. **(F)** GSIS response of pseudoislets ($n = 19$); two-way ANOVA with Tukey's multiple comparisons test. **(G–K)** *In situ* characterization of hypoxic pseudoislets by Raman imaging. **(G)** Identification and location of the three major components: nuclei (*blue*), mitochondria (*pink*), and ECM (*green*). Scale bar = 10 µm. **(H)** Corresponding Raman spectra of the three major TCA components. **(I)** Semiquantification of component intensities ($n \geq 3$); unpaired *t*-tests. **(J)** Separation of normoxic and hypoxic samples by mitochondrial spectra component by PCA and difference of spectral mean values ($n = 600$); unpaired *t*-test. **(K)** Loadings plot of PC1 with peak marking responsible for sample separation. $^*p < 0.05$, $^{**}p < 0.01$, $^{***}p < 0.001$, $^{****}p < 0.0001$. DAPI, 4′,6-diamidino-2-phenylindole; ECM, extracellular matrix; PC, principal component; PCA, principal component analysis; TCA, true component analysis; TUNEL, terminal deoxynucleotidyl transferase-mediated nick-end labeling.

Hypoxia differentially impairs the ECM protein expression in pseudoislets

To assess the effects of hypoxia on endogenous ECM expression in β-cells, we focused on three different groups of ECM proteins: BM proteins (LAM and COL4), the proteoglycans decorin (DCN) and nidogen-1 (NID1), and the fibril-forming proteins FN and COL1 (Fig. 3 and Supplementary Fig. S2). Comparative immunofluorescence staining verified the presence of the selected ECM proteins in both native human pancreatic tissue and pseudoislets cultured under normoxic conditions. However, semiquantification showed that hypoxia differentially regulated ECM expression. The expression of BM proteins LAM (Fig. 3A, B) and COL4 (Fig. 3C, D) was homogenous throughout pseudoislets cultured under normoxic conditions and significantly decreased in the hypoxia *in vitro* model (LAM: 12259 ± 985 GVI/pixel normoxia vs. 7628 ± 1241 GVI/pixel hypoxia, $p < 0.001$; COL4: 5980 ± 336 GVI/pixel normoxia vs. 3928 ± 900.97 hypoxia, $p < 0.001$).

Similar to the BM proteins, the expression patterns of DCN (Fig. 3E, F; 8619 ± 436 GVI/pixel normoxia vs. 5464 ± 504 GVI/pixel hypoxia; $p < 0.001$) and NID1 (Fig. 3G, H; 12267 ± 1656 GVI/pixel normoxia vs. 7568 ± 1675 GVI/pixel hypoxia; $p < 0.01$) were homogeneous under normoxic conditions, but significantly decreased in the hypoxia *in vitro* model.

In contrast to BM proteins and proteoglycans, the expression levels of fibril-forming proteins (Fig. 3I–M) were not significantly impacted (FN: 7820 ± 2499 GVI/pixel normoxic conditions vs. 8454 ± 1840 GVI/pixel hypoxic conditions, $p = 0.68$; COL1: 5527 ± 1353 GVI/pixel normoxia vs. 5915 ± 1617 GVI/pixel hypoxia, $p = 0.70$). Although FN expression did not significantly decrease ($p = 0.68$), its cellular location shifted from cytoplasmic to nuclear after being subjected to hypoxia (Fig. 3I).

Changes in ECM composition have been described to promote transcriptional changes in the nucleus, potentially hinting toward cellular stress.[35] Therefore, we investigated whether cytoplasmic and nuclear expression of FN was present under hypoxic conditions (Fig. 3K). When normalized to the normoxia pseudoislet controls (1.0 ± 0.26), native human tissue did not show a significant fold change (0.91 ± 0.19, $p = 0.75$). In contrast, under hypoxic conditions, pseudoislets expressed significantly more nuclear FN (1.0 ± 0.26 normoxia vs. 1.46 ± 0.29 hypoxia; $p < 0.01$), reflecting increased cellular stress under hypoxic conditions.

Our data show that β-cells have the ability to express relevant pancreatic ECM proteins under normoxic conditions.[34,36] However, hypoxia significantly impacted pancreatic BM proteins, glycoproteins, and FN, while COL1 expression remained stable.

COL1 hydrogel mimics native pancreatic tissue and attenuates hypoxic impact on pseudoislet functionality

To prevent ECM loss with concomitant loss of functionality under hypoxic conditions, we investigated the effect of encapsulating the pseudoislets in a COL1 hydrogel that is commercially available as an FDA-approved GMP-product and has been used to support β-cell function in normoxic conditions.[37,38] Pseudoislets were encapsulated in a COL1 hydrogel, exhibiting similar COL1 expression patterns to native human adult pancreatic tissue (Fig. 4).

The impact of COL1 hydrogel on pseudoislets under hypoxic conditions was investigated by comparing changes in apoptosis, proliferative capacity, basic β-cell functionality and ECM protein expression patterns with pseudoislets cultured in suspension under hypoxic conditions (Fig. 5A–F). The expression of the hypoxia-induced apoptosis marker caspase-3 (Fig. 5A; 4.41 ± 1.44 suspension vs. 1.77 ± 0.68 COL1 hydrogel; $p < 0.05$) as well as the number of $TUNEL^+$ cells (Fig. 5B; 5.88 ± 1.67 suspension vs. 3.27 ± 0.76 COL1 hydrogel; $p < 0.05$) were significantly decreased in pseudoislets cultured in the 3D COL1 hydrogel when compared with pseudoislets grown in suspension cultures. Although the proliferative capacity between pseudoislets in suspension and COL1 hydrogel was comparable (Fig. 5C; 0.55 ± 0.14 suspension vs. 0.49 ± 0.15 COL1 hydrogel; $p = 0.55$), the expression of E-cadherin (0.31 ± 0.06 suspension vs. 0.75 ± 0.25 COL1 hydrogel; $p < 0.01$) and insulin (0.32 ± 0.09 suspension vs. 0.59 ± 0.12 COL1 hydrogel; $p < 0.01$) was significantly higher in pseudoislets in COL1 hydrogel (Fig. 5D, E). While hypoxia significantly decreased the overall insulin content of the pseudoislets in COL1 hydrogel, E-cadherin did not change significantly (Supplementary Fig. S3). Pseudoislets in COL1 hydrogel under normoxic and hypoxic conditions secreted significantly more insulin with 16.7 mM glucose stimulation than in the basal state (3.3 mM) (Fig. 5F; normoxia: 0.08 ± 0.03 basal state vs. 0.144 ± 0.04 16.7 mM glucose, $p < 0.05$; hypoxia: 0.09 ± 0.02 basal state vs. 0.16 ± 0.06 16.7 mM glucose, $p < 0.05$). These data demonstrate the beneficial effect of the COL1 hydrogel on pseudoislet functionality when comparing glucose diffusion and insulin release under hypoxic conditions.

Exogenous biomechanical cues are known to impact cellular behavior.[1] Therefore, we investigated whether providing an external COL1 hydrogel changes the ECM protein secretion patterns in the pseudoislet cultures (Fig. 5G–M). Interestingly, only the secretion of LAM (6577 ± 1360 GVI/pixel normoxia vs. 4007 ± 594 hypoxia; $p < 0.05$) and COL4 (8553 ± 223 GVI/pixel normoxia vs. 7306 ± 708 GVI/pixel hypoxia; $p < 0.05$) significantly decreased, whereas the expression of DCN (9117 ± 2877 GVI/pixel normoxia vs. 6418 ± 1824 GVI/pixel hypoxia; $p = 0.14$) and NID1 (4451 ± 1488 GVI/pixel normoxia vs. 3996 ± 96 GVI/pixel hypoxia; $p = 0.60$), as well as fibril-associated (FN: 6655 ± 936 GVI/pixel normoxia vs. 7129 ± 1360 GVI/pixel hypoxia; $p = 0.58$) and fibrillar proteins (COL1: 9396 ± 2297 GVI/pixel normoxia vs. 6751 ± 2022 GVI/pixel hypoxia; $p = 0.18$) were not significantly impaired. In contrast to pseudoislets cultured in suspension, no change in nuclear FN expression was observed under hypoxia in pseudoislets encapsulated in the 3D COL1 hydrogel (Fig. 5L; 1.0 ± 0.09 normoxia vs. 0.90 ± 0.24 hypoxia; $p = 0.46$).

COL1 hydrogel functionalized with HUVECs supports endogenous pseudoislet BM protein expression

The encapsulation of pseudoislets in a COL1 hydrogel attenuated the hypoxic effect and preserved the expression of the glycoproteins DCN and NID1. However, the expression of BM proteins LAM and COL4 remained impaired. ECs are an important producers of BM protein in the pancreas.[9] Therefore, we established a co-culture of 1000 INS1E β-cells with 1000 HUVECs using magnetic levitation with HUVECs surrounding the β-cells as previously described.[17] After culturing control β-cell only pseudoislets and coculture pseudoislets in a

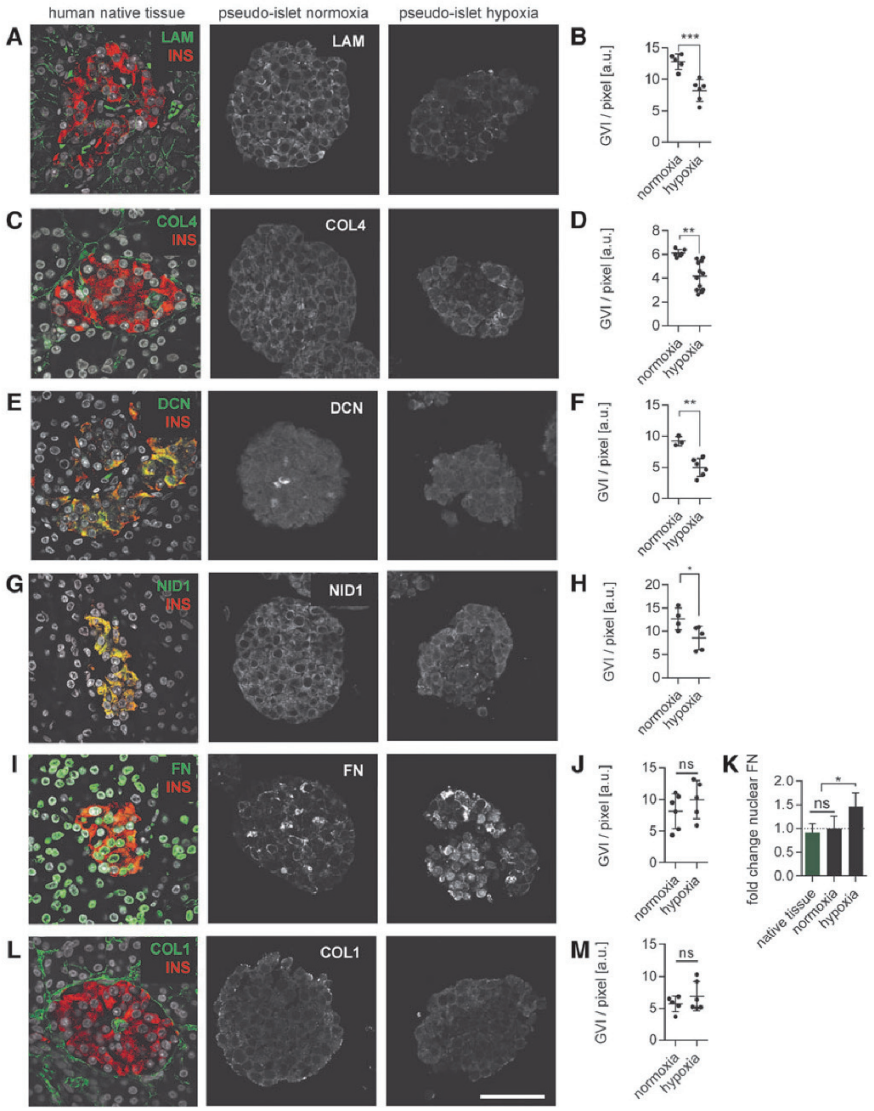

FIG. 3. Hypoxia differentially impacts the expression patterns of BM proteins, glycoproteins, fibrillar, and fibril-associated ECM proteins. IF staining and quantification of different ECM proteins in human native tissue and in pseudoislets under normoxic and hypoxic culture conditions. **(A–D)** BM proteins are represented by **(A, B)** LAM ($n \geq 5$) and **(C, D)** COL4 ($n \geq 6$). **(E–H)** Glycoproteins are represented by **(E, F)** DCN ($n \geq 3$) and **(G, H)** NID1 ($n \geq 4$). **(I–M)** Fibril-associated and fibrillar ECM proteins are represented by **(I, J)** FN ($n \geq 5$) and **(L, M)** COL1 ($n \geq 5$). **(K)** Quantification of nuclear FN in native pancreatic tissue, and in pseudoislets cultured under normoxic and hypoxic conditions ($n \geq 5$); one-way ANOVA. Unpaired t-test. $^{*}p < 0.05$, $^{**}p < 0.01$, $^{***}p < 0.001$. Scale bar = 50 µm. BM, basement membrane; COL1, collagen type 1; COL4, collagen type 4; DCN, decorin; FN, fibronectin; IF, immunofluorescence; LAM, laminins; NID1, nidogen-1.

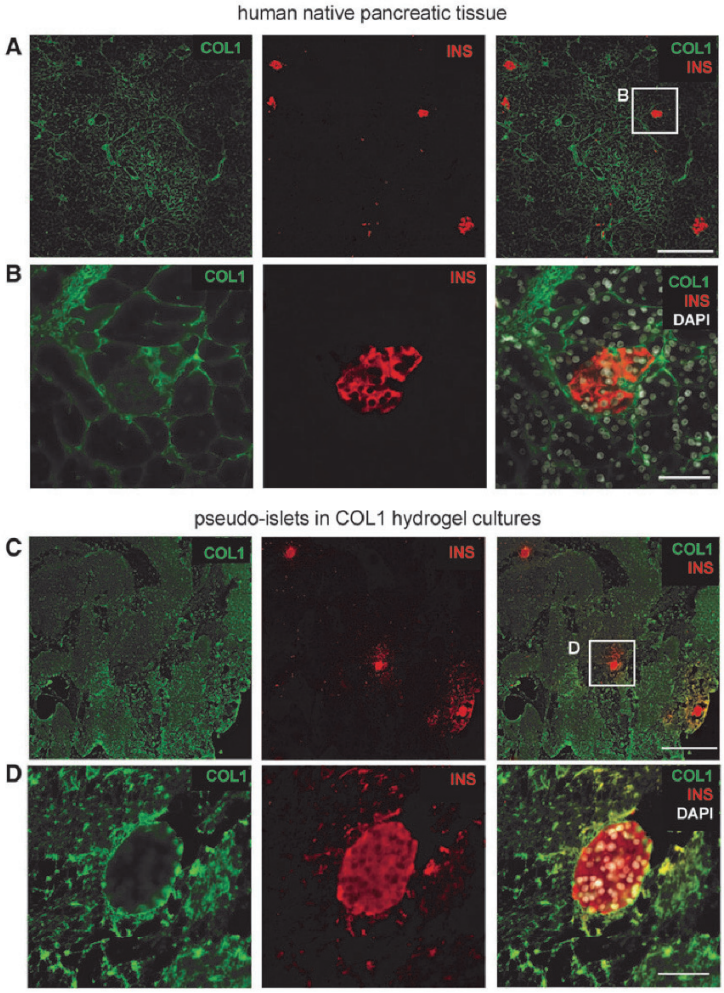

FIG. 4. COL1 hydrogel mimics native pancreatic tissue. **(A, B)** IF staining of adult pancreatic tissue showing COL1 (*green*), insulin (*red*), and nuclei (DAPI, *white*). Scale bars equal **(A)** 200 μm and **(B)** 50 μm. **(C, D)** IF staining of COL1-encapsulated pseudoislets with COL1 (*green*), insulin (*red*), and nuclei (DAPI, *white*). Scale bars equal **(C)** 200 μm and **(D)** 50 μm.

COL1 hydrogel for 48h under hypoxic conditions, functionality, and ECM protein expression were assessed (Fig. 6). Coculture pseudoislets grown in the COL1 hydrogel were glucose responsive after 48h in hypoxia (Fig. 6A) and secreted significantly more insulin upon glucose stimulation compared with only β-cell-containing pseudoislets in COL1 hydrogels (Fig. 6B; 0.16±0.06 COL1 hydrogel vs. 0.36±0.24 COL1 hydrogel+HUVECs; $p<0.05$), while the GSIS was not significantly changed (Supplementary Fig. S4A). Furthermore, evaluation of caspase-3, TUNEL, Ki67, E-cadherin, and insulin expression using IF staining did not show significant differences between the two groups (Supplementary

FIG. 5. COL1 hydrogel improved pseudoislet functionality and minimized ECM changes due to hypoxia. **(A–F)** Relative fold change in expression due to hypoxic conditions of pseudoislets in suspension or encapsulated in COL1 gel; **(A)** cleaved caspase-3 ($n\geq3$), **(B)** number of TUNEL$^+$ cells ($n\geq3$), **(C)** Ki67, ($n\geq4$), **(D)** E-cadherin ($n\geq5$) and **(E)** insulin ($n\geq4$), unpaired *t*-tests. **(F)** GSIS response of encapsulated normoxic and hypoxic pseudoislets ($n=7$); two-way ANOVA with Tukey's multiple comparisons test. **(G–M)** Quantification of the expression under normoxic or hypoxic conditions of relevant pancreatic ECM proteins, including **(G)** LAM ($n=4$), **(H)** COL4 ($n\geq3$), **(I)** DCN ($n\geq3$), **(J)** NID1 ($n\geq4$), **(K)** FN ($n\geq4$), and **(M)** COL1 ($n=4$). **(L)** Quantification of nuclear FN in encapsulated normoxic and hypoxic pseudoislets ($n=4$) with corresponding representative IF images are shown on the *right*. Unpaired *t*-tests. **(A–E, G–K, M)** Scale bars = 50 μm. **(L)** Scale bar = 5 μm $^*p<0.05$, $^{**}p<0.01$.

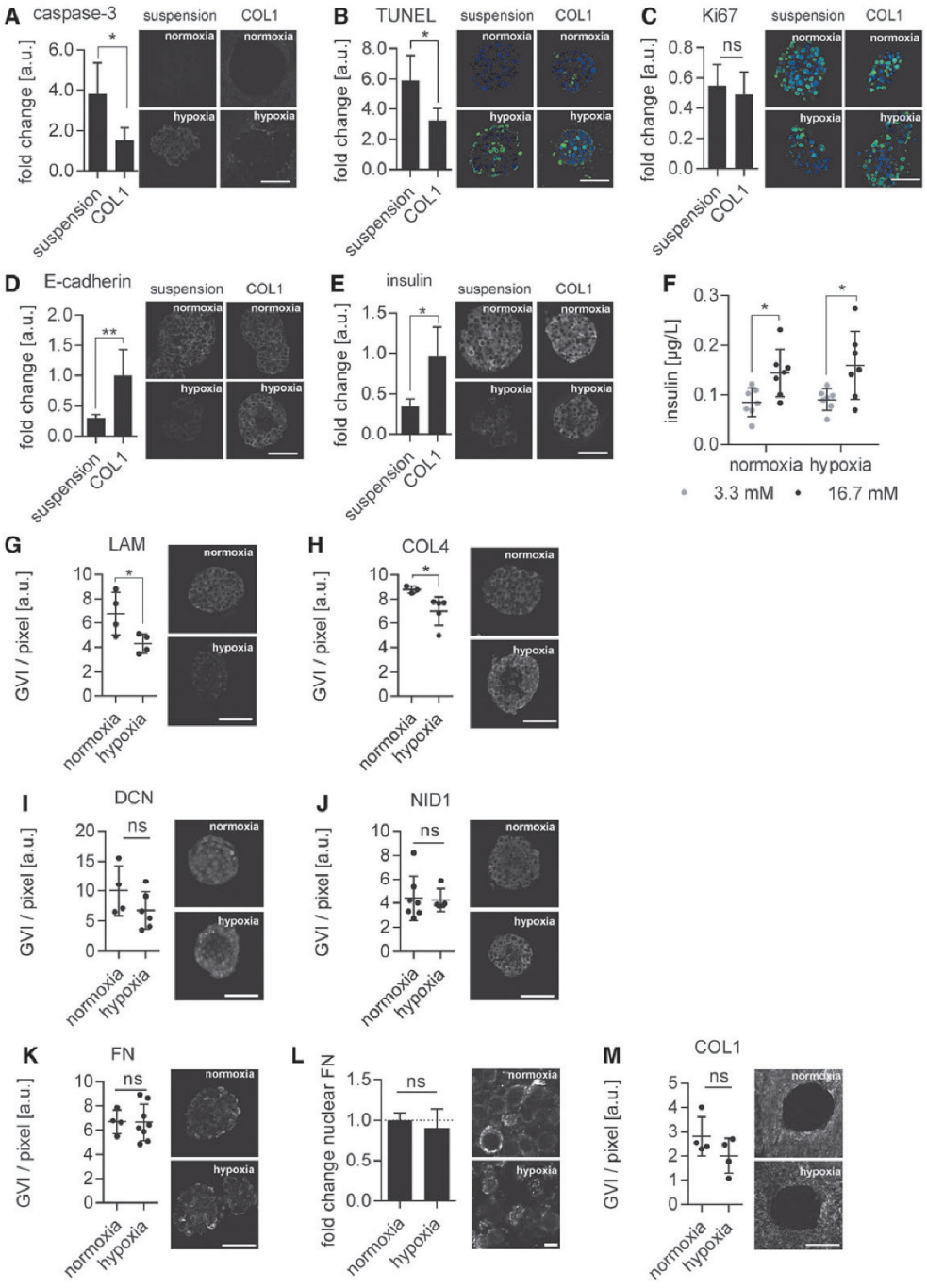
A caspase-3
suspension
COL1
normoxia
hypoxia
fold change [a.u.]
B TUNEL
C Ki67
ns
D E-cadherin
E insulin
F
insulin [µg/L]
normoxia hypoxia
3.3 mM
16.7 mM
G LAM
H COL4
GVI / pixel [a.u.]
I DCN
J NID1
K FN
L
fold change nuclear FN
M COL1

10

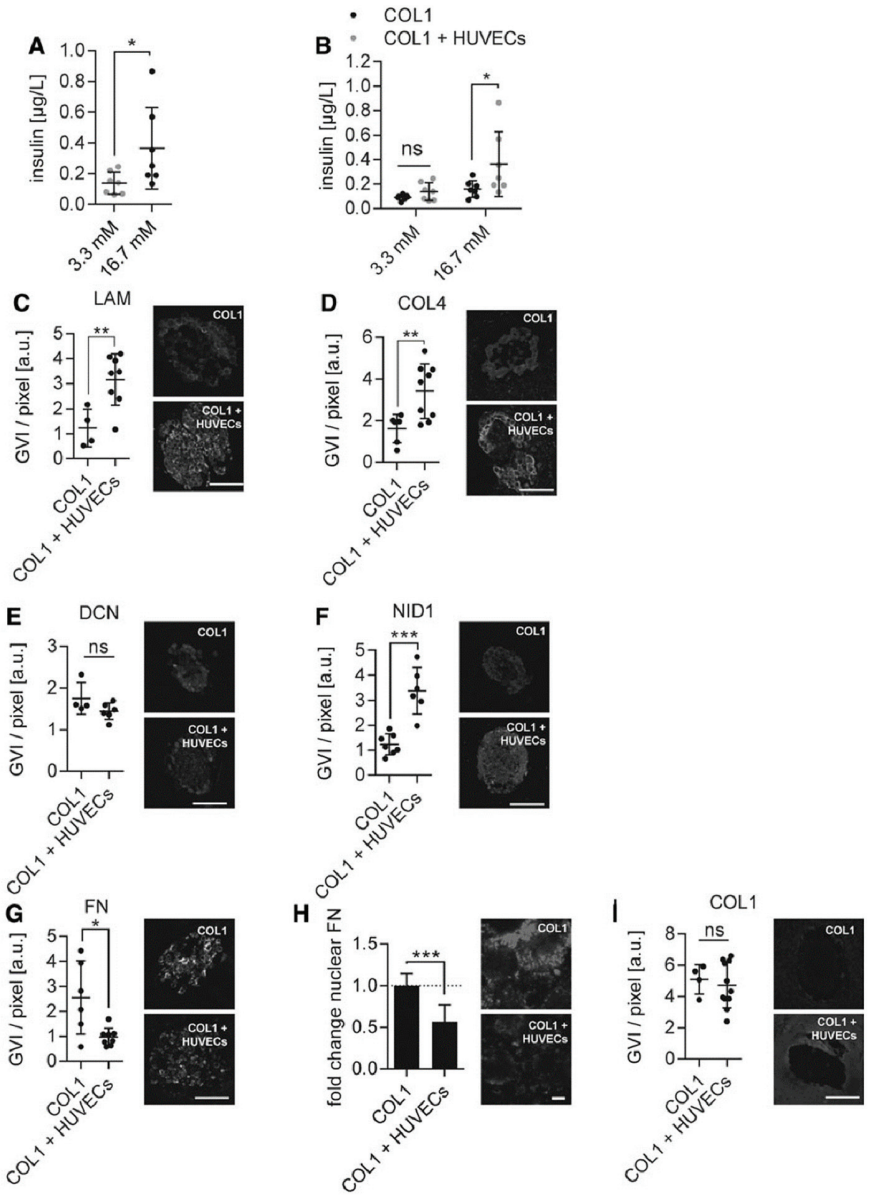

FIG. 6. COL1 hydrogel with incorporated HUVECs stimulates insulin and BM protein secretion in β-cell-containing pseudoislets. **(A)** Insulin expression in β-cells encapsulated in COL1 hydrogel with HUVECs ($n=7$). **(B)** β-cell-containing pseudoislets in COL1 hydrogel with HUVECs secrete significantly more insulin upon glucose stimulation compared with β-cell-containing pseudoislets cultured in COL1 hydrogels alone ($n=7$); two-way ANOVA with Sidak's multiple comparisons test. **(C–I)** Quantification of pancreatic ECM protein expression under hypoxic conditions in cultures with or without incorporation of HUVECs: **(C)** LAM ($n\geq4$), **(D)** COL4 ($n\geq6$), **(E)** DCN ($n\geq4$), **(F)** NID1 ($n\geq6$), **(G)** FN ($n\geq6$), and **(I)** COL1 ($n\geq4$). **(H)** Quantification of nuclear FN in pseudoislets with or without HUVECs ($n\geq6$). Unpaired *t*-tests. **(C–G, I)** Scale bars = 50 µm. **(H)** Scale bar = 5 µm. $^{*}p<0.05$, $^{**}p<0.01$, $^{***}p<0.001$. HUVEC, human umbilical vein endothelial cell.

Fig. S4B–F). The successful integration of HUVECs into the hydrogel was shown by significantly more CD31$^+$ cells (Supplementary Fig. S4G; 0.07 ± 0.03 GVI/pixel COL1 hydrogel vs. 0.26 ± 0.11 GVI/pixel COL1 hydrogel+HUVECS; $p < 0.01$). The evaluation of the ECM protein expression in β-cell only pseudoislets and coculture pseudoislets in the COL1 hydrogel after 48h (Fig. 6C–I) revealed a significant increase in both LAM (1.24 ± 0.66 GVI/pixel COL1 hydrogel vs. 3.16 ± 0.96 GVI/pixel COL1 hydrogel+HUVECs; $p < 0.01$) and COL4 (1.62 ± 0.62 GVI/pixel COL1 hydrogel vs. 3.42 ± 1.24 GVI/pixel COL1 hydrogel+HUVECs; $p < 0.01$) as well as NID1 (1.23 ± 0.39 GVI/pixel COL1 hydrogel vs. 3.38 ± 0.85 GVI/pixel COL1 hydrogel+HUVECs; $p < 0.001$). Interestingly, both the overall expression of FN (2.55 ± 1.34 GVI/pixel COL1 hydrogel vs. 0.97 ± 0.33 GVI/pixel COL1 hydrogel+HUVECs; $p < 0.05$) and the normalized nuclear expression of FN (1.0 ± 0.15 COL1 hydrogel vs. 0.57 ± 0.20 COL1 hydrogel+HUVEC; $p < 0.001$) decreased significantly, while DCN (1.75 ± 0.33 GVI/pixel COL1 hydrogel vs. 1.44 ± 0.18 COL1 hydrogel+HUVECs; $p = 0.12$) and COL1 (5.10 ± 0.81 GVI/pixel COL1 hydrogel vs. 4.72 ± 1.37 GVI/pixel COL1 hydrogel+HUVECs; $p = 0.64$) were not affected by the HUVEC coculture. These data demonstrate the stimulative capacity of HUVECs on β-cells regarding functionality, BM protein expression, and decrease in hypoxia-induced cellular stress markers.

Discussion

In healthy native pancreatic tissue, pancreatic β-cell functionality is supported by a highly specialized composition of ECM proteins produced by various cell types, including fibroblasts and ECs.[9,39] A dense vascularization of the pancreas further ensures highly oxygenated blood and nutrient delivery.[40] Using current protocols, during the Islets of Langerhans isolation procedure, the majority of the ECM and vascular access are destroyed, resulting in decreased islet survival and functionality.[8,41] Posttransplantation, the Islets of Langerhans are subjected to an ischemic period leading to severe hypoxia, with a partial oxygen pressure ranging from 5 to 10 mmHg, corresponding to 1% oxygen.[42] The removal of the pancreatic ECM, which is accelerated by hypoxic conditions, accentuates the importance for β-cells to produce their own microenvironment. However, the role of β-cell ECM production in hypoxia had not been investigated yet.

In this study, we asked whether β-cells have the ability to secrete ECM proteins and how their production is impacted by a hypoxic environment that mimics the initial phase posttransplantation where no vascularization is present. We developed a functional rat-based model to successfully mimic hypoxic conditions to study the direct effect of hypoxia on β-cells. In line with previously reported studies, β-cell glucose responsiveness was lost under hypoxic conditions accompanied by increased apoptosis and necrosis markers, especially in the core region of the islets.[16,43] Here, marker-free Raman imaging on living pseudoislets identified a significant hypoxia-induced alteration in ECM homeostasis. This impact on pancreatic ECM structures may contribute to the loss of β-cell function, as it had been previously shown that intraislet ECM interactions can modulate β-cell proliferation and survival.[34] The overall decrease in ECM signal within pseudoislets supports our hypothesis that hypoxia negatively impacts the ECM expression of β-cells.

The specific roles of the different types of ECM regarding Islets of Langerhans transplant survival and function are not fully understood.[44] Hence, we assessed the hypoxia-induced disruption of ECM homeostasis on six different ECM proteins. DCN is an important binding partner of collagens (mainly types I and III) that regulates collagen fibrillogenesis. The loss of DCN can lead to uncontrolled collagen fiber formation, which then results in pathological ECM development such as fibrosis and ultimately graft failure.[45] The hypoxia-induced decrease of DCN in the pseudoislets after 48 h expression can be a driver for early graft failure as a controlled fibrillogenesis of COL1 and COL3 may be impaired. Furthermore, DCN has been shown to positively affect angiogenesis and modulate the immune response,[46,47] which are both highly important processes to achieve proper transplant engraftment.

The main purpose of COL1 and other parts of the exocrine interstitial matrix is the preservation of structural stability[48] as well as assuring β-cell survival and insulin expression by stimulating a variety of surface receptors.[49] Although COL1 overall expression remained stable, the quality or maturity of COL1 fibers might be impaired by the decreased DCN expression. Immature COL1 has not been described yet to act via the same integrins as fully formed COL1, potentially contributing to the loss of glucose responsiveness.[50]

FN is another component of the interstitial matrix.[51] The impact of FN on β-cells is currently controversially discussed. Freshly isolated human Islets of Langerhans showed an improved glucose response on surfaces coated with FN.[37] Hadavi *et al.* recently published the positive effect of FN in combination with COL4 and LAM to stimulate β-cell functionality *in vitro*.[52] In contrast, Navarro-Alvarez *et al.* demonstrated that isolated human Islets of Langerhans, which were attached to FN-coated dishes, showed a clear tendency toward disintegration and loss of spherical structure.[53] Here, FN expression patterns exhibited a hypoxia-induced shift from cytoplasmic to nuclear expression, especially in the central region of the pseudoislets. Since FN is present in tissues to repair damaged cells, the increase in nuclear FN expression may be the first indicator for a hypoxia-induced cell damage.[54] Nuclear FN has been shown to be present in some tumor cells; however, the precise role of nuclear FN remains unclear.[55]

In contrast to proteins of the interstitial matrix, the expression of ECM proteins associated with the BM were highly affected by hypoxic conditions. In the pancreas, Islets of Langerhans are located in the BM, a dense network of copolymerized LAM and COL4. These proteins are connected by NID1, which acts as key bridging protein between LAM and COL4 in native tissues.[56] Laminin α5 and COL4 have been reported to modulate β-cell differentiation and maturation from stem cells into mature β-cells and stimulate insulin expression in pseudoislet systems,[57,58] highlighting the relevance of BM proteins for β-functionality *in vitro*. Since the expression of all proteins of the BM was reduced in our study under hypoxic conditions, this lack of BM proteins may be associated with functionality loss. Hence, the rescue of BM proteins may support β-cell function under hypoxic conditions posttransplantation.[59,60]

One approach to reduce hypoxia-induced damage and altered ECM expression is to provide exogenous ECM to the cellular transplant. The addition of a protective COL1 hydrogel surrounding the β-cell pseudoislets significantly

TABLE 1. OVERVIEW OF EXTRACELLULAR MATRIX PROTEIN EXPRESSION CHANGES IN COLLAGEN TYPE 1 HYDROGEL OF β-CELL PSEUDOISLETS AND COCULTURE PSEUDOISLETS AFTER 48 H UNDER HYPOXIC CULTURE CONDITIONS (NORMALIZATION TO PSEUDOISLETS CULTURED UNDER NORMOXIC CULTURE CONDITIONS)

ECM protein	*LAM*	*COL4*	*DCN*	*NID1*	*FN*	*COL1*
COL1 gel normoxia	1	1	1	1	1	1
COL1 gel hypoxia	0.63 ↓	0.80 ↓	n.s.	n.s.	n.s.	n.s.
COL1 gel+HUVECs hypoxia	1.61 ↑	1.69 ↑	n.s.	2.63 ↑	0.38 ↓	n.s.

The *up arrow* indicates significant upregulation ($p < 0.05$) and the *down arrow* indicates significant downregulation ($p < 0.05$).
COL1, collagen type 1; COL4, collagen type 4; DCN, decorin; EC, endothelial cell; ECM, extracellular matrix; FN, fibronectin; HUVECs, human umbilical vein endothelial cells; LAM, laminins; NID1, nidogen-1; n.s., not significant.

reduced the negative impact of hypoxia. While apoptotic and necrotic cell numbers decreased, functionality markers increased, and glucose responsiveness was restored. The results of previous studies on the effect of COL1 as well as the reduced number of apoptotic markers and dead cells in this study point toward a combination of biological and mechanophysical support by the COL1 hydrogel.[61–63]

Assessment of the endogenously expressed ECM proteins showed that DCN and NID1 could be restored. DCN binds COL1 via the leucine-rich repeats five to six to regulate its assembly, structure, and biomechanical properties.[64] The rescue of DCN might therefore be facilitated by the supply of the COL1 hydrogel, which offers possible binding sites. However, an interaction between COL1 and NID1 has not been reported yet. Interestingly, the translocation of FN into the nucleus was prevented, supporting the observation that the COL1 hydrogel attenuates the cellular stress levels of the hypoxic environment.

Although the levels of NID1 could be restored, the LAM and COL4 did not show any signs of rescue. The persistent lack of BM proteins suggests that providing β-cells with only COL1 is not enough for a long-term restoration of glucose-responsiveness. Therefore, we hypothesized that stimulation of β-cells by ECs might enhance the expression of BM proteins, as ECs are the main producers of BM proteins in pancreatic tissues.[9] We encapsulated both β-cells and HUVECs into the pseudoislets and cultured them in COL1 hydrogels. We identified that upon encapsulation of β-cells together with HUVECs, we could both stimulate functionality of β-cells as well as rescue BM protein expression of LAM, COL4, and the linker protein NID1 (Table 1). In addition, overall FN expression was reduced, which might be precipitated by the highly significant decrease in nuclear FN, an indicator for reduced hypoxia-induced cellular stress.[29] Furthermore, FN regulates the fibrotic response along with COL1,[49] which is unfavorable for engraftment of the transplant. Consequently, a drop in FN content may have a beneficial long-term effect.

In summary, our data demonstrate the supportive effect of the COL1 hydrogel protecting β-cell-composed pseudoislets under hypoxic conditions by reducing apoptotic effects and cell death, attenuating a loss of ECM protein secretion while rescuing the glucose responsiveness. We further showed how the combination of biological cues from ECs in a coculture system with COL1 hydrogel rescued BM protein expression and improved the glucose responsiveness. Importantly, COL1 is a bioactive base hydrogel that can be further modified and functionalized using growth factors, other ECM proteins or cell types to meet specific requirements, for example to improve transplant function,[5,24,37,61–63,65] or to create a more robust *in vitro* model. Future studies could include the addition of α and δ cells into the pseudoislets. Also, the investigation of reoxygenation posthypoxia would be of interest as it may elucidate key biomolecules influencing the transplantation and healing process; however, it may be difficult to mimic the exact time response and oxygen percentages *in vitro* that are found during the healing processes *in vivo*. In addition, the addition of immune cells would be of high interest as the foreign body response to islet transplantation is a major issue requiring the use of immune suppressants posttransplantation. Many groups are working on the addition of immune cells into *in vitro* test systems in general, which has been difficult in the past due to the complexity of the immune system. Any addition to *in vitro* model complexity must be weighed against its increase in cost and the ability to determine valid readouts that can answer the scientific question being asked.

Conclusion

In this study, we developed an *in vitro* model mimicking the hypoxic posttransplantation environment of pancreatic islets for the purpose of investigating and mitigating the pathological effects of hypoxia on ECM homeostasis with a functionalized material. We identified a significantly reduced production of important ECM proteins such as COL4, LAM, DCN, and NID1 within β-cells accompanied with increased cellular death and loss in functionality. Furthermore, we evaluated a clinically approved COL1 hydrogel and demonstrated its protective effect on β-cells in hypoxia. We further functionalized the hydrogel with HUVECs, which prevented ECM loss and stimulated β-cell functionality. By establishing a COL1 hydrogel, including ECs, we created a carrier matrix that attenuates the hypoxia-induced disruption of ECM homeostasis in β-cells to support them during the first phase of ECM reestablishment of post-transplantation and therefore potentially increase the efficacy of the Edmonton protocol for diabetic patients.

Disclosure Statement

No competing financial interests exist.

Funding Information

This work was financially supported by the European Union (H2020-NMP10-2014-645991-2, DRIVE to Katja Schenke-Layland and Garry Duffy), the International Foundation for Ethical Research (to Aline Zbinden), Germany's Excellence Strategy (EXC 2180-390900677 to Katja Schenke-Layland), as well as the Ministry of Science,

Research and the Arts of Baden-Württemberg (33-729.55-3/214 and SI-BW 01222-91 to Katja Schenke-Layland), and the Deutsche Forschungsgemeinschaft (INST 2388/33-1 and GRK 2543/1 to Katja Schenke-Layland).

Supplementary Material

Supplementary Table S1
Supplementary Figure S1
Supplementary Figure S2
Supplementary Figure S3
Supplementary Figure S4

References

1. Urbanczyk, M., Layland, S.L., and Schenke-Layland, K. The role of extracellular matrix in biomechanics and its impact on bioengineering of cells and 3D tissues. Matrix Biol **85–86,** 1, 2020.
2. Lukashev, M. ECM signalling: orchestrating cell behaviour and misbehaviour. Trends Cell Biol **8,** 437, 1998.
3. Thomas, F.T., Contreras, J.L., Bilbao, G., Ricordi, C., Curiel, D., and Thomas, J.M. Anoikis, extracellular matrix, and apoptosis factors in isolated cell transplantation. Surgery **126,** 299, 1999.
4. Shapiro, A.M.J., Lakey, J.R.T., Ryan, E.A., *et al.* Islet transplantation in seven patients with type 1 diabetes mellitus using a glucocorticoid-free immunosuppressive regimen. N Engl J Med **343,** 230, 2000.
5. Weber, L.M., and Anseth, K.S. Hydrogel encapsulation environments functionalized with extracellular matrix interactions increase islet insulin secretion. Matrix Biol **27,** 667, 2008.
6. Spiers, R.M., Marzi, J., Brauchle, E.M., *et al.* Donor age significantly influences the Raman spectroscopic biomolecular fingerprint of human pancreatic extracellular matrix proteins following collagenase-based digestion. Acta Biomater **99,** 269, 2019.
7. Cross, S.E., Vaughan, R.H., Willcox, A.J., *et al.* Key matrix proteins within the pancreatic islet basement membrane are differentially digested during human islet isolation. Am J Transplant **17,** 451, 2017.
8. Delaune, V., Berney, T., Lacotte, S., and Toso, C. Intraportal islet transplantation: the impact of the liver microenvironment. Transpl Int **30,** 227, 2017.
9. Nikolova, G., Strilic, B., and Lammert, E. The vascular niche and its basement membrane. Trends Cell Biol **17,** 19, 2007.
10. Rambøl, M.H., Han, E., and Niklason, L.E. Microvessel network formation and interactions with pancreatic islets in three-dimensional chip cultures. Tissue Eng Part A **26,** 556, 2020.
11. Cen, L., Liu, W.E.I., Cui, L.E.I., *et al.* Collagen tissue engineering: development of novel biomaterials. Pediatr Res **63,** 492, 2008.
12. Zhu, H., Li, W., Liu, Z., *et al.* Selection of implantation sites for transplantation of encapsulated pancreatic islets. Tissue Eng Part B Rev **24,** 191, 2017.
13. Irving-Rodgers, H.F., Choong, F.J., Hummitzsch, K., Parish, C.R., Rodgers, R.J., and Simeonovic, C.J. Pancreatic islet basement membrane loss and remodeling after mouse islet isolation and transplantation: impact for allograft rejection. Cell Transplant **23,** 59, 2014.
14. Mouré, A., Bacou, E., Bosch, S., *et al.* Extracellular hemoglobin combined with an O_2-generating material overcomes O_2 limitation in the bioartificial pancreas. Biotechnol Bioeng **116,** 1176, 2019.
15. Emamaullee, J.A., Shapiro, A.M.J., Rajotte R V., Korbutt, G., and Elliott, J.F. Neonatal porcine islets exhibit natural resistance to hypoxia-induced apoptosis. Transplantation **82,** 945, 2006.
16. Lehmann, R., Zuellig, R.A., Kugelmeier, P., *et al.* Superiority of small islets in human islet transplantation. Diabetes **56,** 594, 2007.
17. Urbanczyk, M., Zbinden, A., Layland, S.L., Duffy, G., and Schenke-Layland, K. Controlled heterotypic pseudo-islet assembly of human β-cells and human umbilical vein endothelial cells using magnetic levitation. Tissue Eng Part A **26,** 387, 2020.
18. Xiong, X., Ghosh, R., Hiller, E., *et al.* A new procedure for rapid, high yield purification of Type I collagen for tissue engineering. Process Biochem **44,** 1200, 2009.
19. Zbinden, A., Marzi, J., Schlünder, K., *et al.* Non-invasive marker-independent high content analysis of a microphysiological human pancreas-on-a-chip model. Matrix Biol **85–86,** 205, 2020.
20. Vlahos, A.E., Kinney, S.M., Kingston, B.R., *et al.* Endothelialized collagen based pseudo-islets enables tuneable subcutaneous diabetes therapy. Biomaterials **232,** 119710, 2020.
21. Hellman, B., and Angervall, L. The frequency distribution of the number and volume of the Islets of Langerhans in man. Acta Pathol Microbiol Scand **53,** 230, 2009.
22. Jun, Y., Lee, J., Choi, S., *et al.* In vivo–mimicking microfluidic perfusion culture of pancreatic islet spheroids. Sci Adv **5,** eaax4520, 2019.
23. Yuan, Q., Arkudas, A., Horch, R.E., *et al.* Vascularization of the arteriovenous loop in a rat isolation chamber model—quantification of hypoxia and evaluation of its effects. Tissue Eng Part A **24,** 719, 2018.
24. Ichihara, Y., Utoh, R., Yamada, M., Shimizu, T., and Uchigata, Y. Size effect of engineered islets prepared using microfabricated wells on islet cell function and arrangement. Heliyon **2,** e00129, 2016.
25. Hilderink, J., Spijker, S., Carlotti, F., *et al.* Controlled aggregation of primary human pancreatic islet cells leads to glucose-responsive pseudoislets comparable to native islets. J Cell Mol Med **19,** 1836, 2015.
26. Chen, Z., Wang, J., Sun, W., *et al.* Synthetic beta cells for fusion-mediated dynamic insulin secretion. Nat Chem Biol **14,** 86, 2018.
27. Rogal, J., Zbinden, A., Schenke-Layland, K., and Loskill, P. Stem-cell based organ-on-a-chip models for diabetes research. Adv Drug Deliv Rev **140,** 101, 2019.
28. Majtnerová, P., and Roušar, T. An overview of apoptosis assays detecting DNA fragmentation. Mol Biol Rep **45,** 1469, 2018.
29. Stendahl, J.C., Kaufman, D.B., and Stupp, S.I. Extracellular matrix in pancreatic islets: relevance to scaffold design and transplantation. Cell Transplant **18,** 1, 2009.
30. Dukor, R.K. Vibrational spectroscopy in the detection of cancer. In: Griffiths, P.R., edr. Handbook of Vibrational Spectroscopy. Chichester, UK: John Wiley & Sons, Ltd., 2006.
31. Brazhe, N.A., Treiman, M., Brazhe, A.R., Find, N.L., Maksimov, G.V., and Sosnovtseva, O.V. Mapping of redox state of mitochondrial cytochromes in live cardiomyocytes using raman microspectroscopy. PLoS One **7,** e41990, 2012.
32. Zhang, X., Yu, F., Li, J., *et al.* Investigation on the cancer invasion and metastasis of skin squamous cell carcinoma by Raman spectroscopy. Molecules **24,** 2059, 2019.
33. Cheng, W-T., Liu, M-T., Liu, H-N., and Lin, S-Y. Micro-Raman spectroscopy used to identify and grade human skin pilomatrixoma. Microsc Res Tech **68,** 75, 2005.

34. Townsend, S.E., and Gannon, M. Extracellular matrix–associated factors play critical roles in regulating pancreatic β-cell proliferation and survival. Endocrinology **160,** 1885, 2019.
35. Spencer, V.A., Xu, R., and Bissell, M.J. Extracellular matrix, nuclear and chromatin structure, and gene expression in normal tissues and malignant tumors: a work in progress. Adv Cancer Res **97,** 275, 2007.
36. Smink, A.M., and de Vos, P. Therapeutic strategies for modulating the extracellular matrix to improve pancreatic islet function and survival after transplantation. Curr Diab Rep **18,** 39, 2018.
37. Daoud, J., Petropavlovskaia, M., Rosenberg, L., and Tabrizian, M. The effect of extracellular matrix components on the preservation of human islet function in vitro. Biomaterials **31,** 1676, 2010.
38. Wang, Z.Z., and Sakiyama-Elbert, S.E. Matrices, scaffolds & carriers for cell delivery in nerve regeneration. Exp Neurol **319,** 1, 2019.
39. Topalovski, M., and Brekken, R.A. Matrix control of pancreatic cancer: new insights into fibronectin signaling. Cancer Lett **381,** 252, 2016.
40. Emamaullee, J.A., Rajotte R V, Liston, P., *et al.* XIAP overexpression in human islets prevents early post-transplant apoptosis and reduces the islet mass needed to treat diabetes. Diabetes **54,** 2541, 2005.
41. Dionne, K.E., Colton, C.K., and Yarmush, M.L. Effect of hypoxia on insulin secretion by isolated rat and canine islets of Langerhans. Diabetes **42,** 12, 1993.
42. Wu, H., Panakanti, R., Li, F., and Mahato, R.I. XIAP gene expression protects β-cells and human islets from apoptotic cell death. Mol Pharm **7,** 1655, 2010.
43. Zheng, X., Zheng, X., Wang, X., *et al.* Acute hypoxia induces apoptosis of pancreatic β-cell by activation of the unfolded protein response and upregulation of CHOP. Cell Death Dis **3,** 1, 2012.
44. Llacua, L.A., Faas, M.M., and de Vos, P. Extracellular matrix molecules and their potential contribution to the function of transplanted pancreatic islets. Diabetologia **61,** 1261, 2018.
45. Gubbiotti, M.A., Vallet, S.D., Ricard-Blum, S., and Iozzo R V. Decorin interacting network: a comprehensive analysis of decorin-binding partners and their versatile functions. Matrix Biol **55,** 7, 2016.
46. Järveläinen, H., Sainio, A., and Wight, T.N. Pivotal role for decorin in angiogenesis. Matrix Biol **43,** 15, 2015.
47. Hildebrand, A., Romaris, M., Rasmussen, M., *et al.* Interaction of the small interstitial proteoglycans biglycan, decorin and fibromodulin with transforming growth factor β. Biochem J **302(Pt 2),** 527, 1994.
48. Nagata, N., Iwanaga, A., Inoue, K., and Tabata, Y. Co-culture of extracellular matrix suppresses the cell death of rat pancreatic islets. J Biomater Sci Polym Ed **13,** 579, 2002.
49. Mouw, J.K., Ou, G., and Weaver, V.M. Extracellular matrix assembly: a multiscale deconstruction. Nat Rev Mol Cell Biol **15,** 771, 2014.
50. Boraschi-Diaz, I., Wang, J., Mort, J.S., and Komarova, S.V. Collagen type I as a ligand for receptor-mediated signaling. Front Phys **5,** 12, 2017.
51. Ignotz, R.A., and Massague, J. Transforming growth factor-β stimulates the expression of fibronectin and collagen and their incorporation into the extracellular matrix. J Biol Chem **261,** 4337, 1986.
52. Hadavi, E., Leijten, J., Engelse, M., *et al.* Microwell scaffolds using collagen-IV and laminin-111 lead to improved insulin secretion of human islets. Tissue Eng Part C Methods **25,** 71, 2019.
53. Navarro-Alvarez, N., Rivas-Carrillo, J.D., Soto-gutierrez A, and Yuasa, T. Reestablishment of microenvironment is necessary to maintain in vitro and in vivo human islet function. Cell Transplant **17,** 111, 2016.
54. To, W.S., and Midwood, K.S. Plasma and cellular fibronectin: distinct and independent functions during tissue repair. Fibrogenesis Tissue Repair **4,** 1, 2011.
55. Zerlauth, G., Wesierska-Gadek, J., and Sauermann, G. Fibronectin observed in the nuclear matrix of HeLa tumour cells. J Cell Sci **89 (Pt 3),** 415, 1988.
56. Jiang, F., Naselli, G., and Harrison, L.C. Distinct distribution of laminin and its integrin receptors in the pancreas. J Histochem Cytochem **50,** 1625, 2002.
57. Spenlé, C., Simon-Assmann, P., Orend, G., and Miner, J.H. Laminin α5 guides tissue patterning and organogenesis. Cell Adh Migr **7,** 90, 2013.
58. Maillard, E., Sencier M-C, Langlois, A., *et al.* Extracellular matrix proteins involved in pseudoislets formation. Islets **1,** 232, 2009.
59. Mokkapati, S., Nischt, R., Smyth, N., Ho, M.S.P., and Bo, K. Nidogens—extracellular matrix linker molecules **395,** 387, 2008.
60. Kaido, T., Yebra, M., Cirulli, V., and Montgomery, A.M. Regulation of human β-cell adhesion, motility, and insulin secretion by collagen IV and its receptor α1β1. J Biol Chem **279,** 53762, 2004.
61. Bernhardt, A., Österreich, V., and Gelinsky, M. Three-dimensional co-culture of primary human osteocytes and mature human osteoclasts in collagen gels. Tissue Eng Part A **26,** 647, 2020.
62. Schuh, C.M.A.P., Day, A.G.E., Redl, H., and Phillips, J. An optimized collagen-fibrin blend engineered neural tissue promotes peripheral nerve repair. Tissue Eng Part A **24,** 1332, 2018.
63. Aloy-Reverté, C., Moreno-Amador, J.L., Nacher, M., Montanya, E., and Semino, C.E. Use of RGD-functionalized sandwich cultures to promote redifferentiation of human pancreatic beta cells after in vitro expansion. Tissue Eng Part A **24,** 394, 2017.
64. Kalamajski, S., Aspberg, A., and Oldberg, Å. The decorin sequence SYIRIADTNIT binds collagen type I. J Biol Chem **282,** 16062, 2007.
65. Riopel, M., and Wang, R. Collagen matrix support of pancreatic islet survival and function. Front Biosci **19,** 77, 2014.

Address correspondence to:
Katja Schenke-Layland, MSc, PhD
Department of Women's Health
Research Institute for Women's Health
Eberhard Karls University Tübingen
Silcherstr. 7/1
Tübingen 72076
Germany

E-mail: katja.schenke-layland@uni-tuebingen.de;
katja.schenke-layland@nmi.de

Received: August 26, 2020
Accepted: September 22, 2020
Online Publication Date: November 6, 2020

1 **Supplemental data**

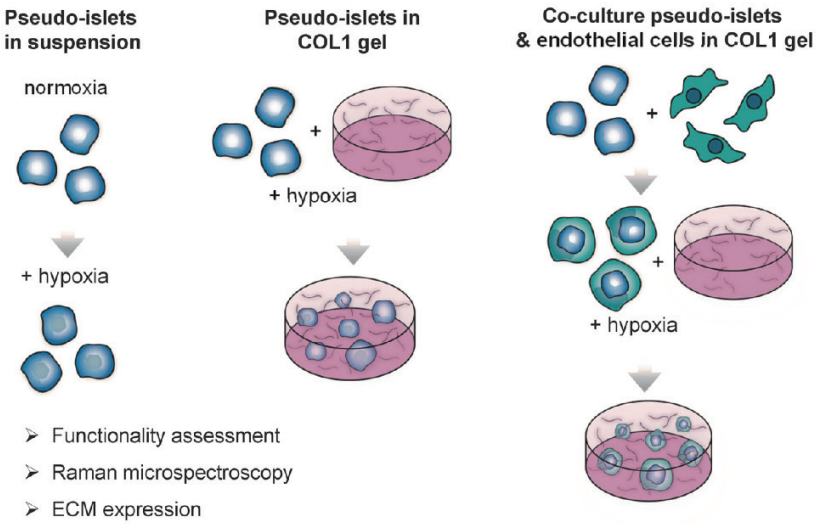

2

3 **Figure S1:** Illustration of the experimental set-up using pseudo-islets, pseudo-islets encapsulated into

4 a COL1 gel, and co-culture pseudo-islets with endothelial cells encapsulated into a COL1 gel.

Zbinden & Urbanczyk et al. Supplemental Data
Collagen and endothelial cell co-culture improves β-cell functionality and rescues pancreatic ECM

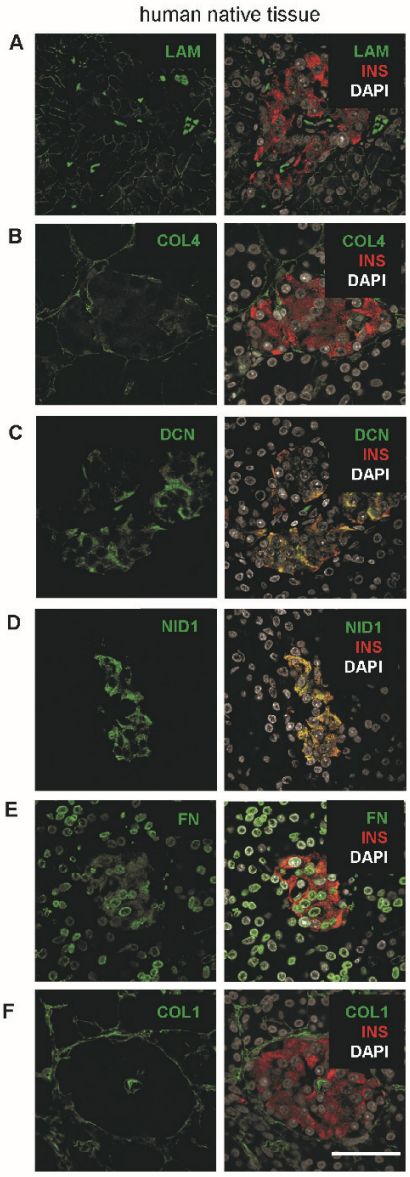

Figure S2: Immunofluorescence staining expression patterns of relevant ECM proteins (in green) in adult human pancreatic tissue. **(A)** LAM, **(B)** COL4, **(C)** DCN, **(D)** NID1, **(E)** FN and **(F)** COL1 with insulin (INS) in red and nuclei (DAPI) in white. Scale bar equals 50 µm.

Zbinden & Urbanczyk et al. Supplemental Data
Collagen and endothelial cell co-culture improves β-cell functionality and rescues pancreatic ECM

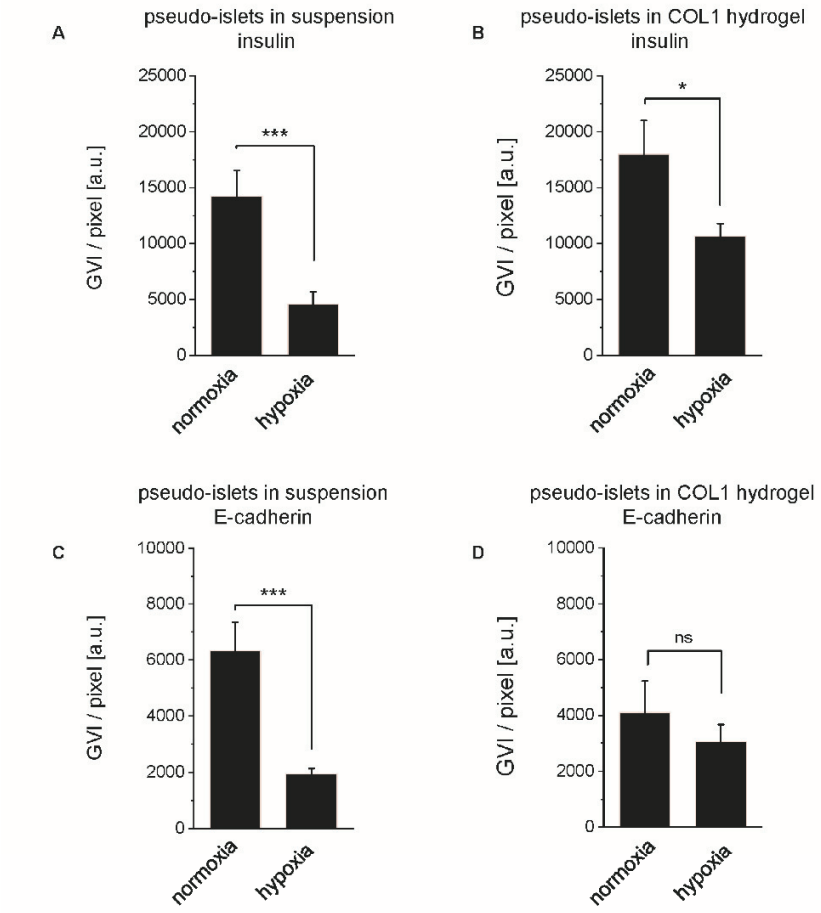

Figure S3: Expression of E-cadherin and insulin in suspension and COL1 hydrogel cultures under normoxic and hypoxic conditions. (**A,B**) Semi-quantification of IF staining of insulin in (**A**) suspension ($n \geq 6$) and (**B**) COL1 hydrogel cultures ($n \geq 4$) shows a significant decrease in insulin expression under hypoxic conditions. (**C,D**) E-cadherin staining in pseudo-islets in (**C**) suspension ($n \geq 6$) and (**D**) COL-1 hydrogel ($n \geq 5$). Unpaired t-test, *$p<0.05$, ***$p<0.001$.

Zbinden & Urbanczyk et al. Supplemental Data
Collagen and endothelial cell co-culture improves β-cell functionality and rescues pancreatic ECM

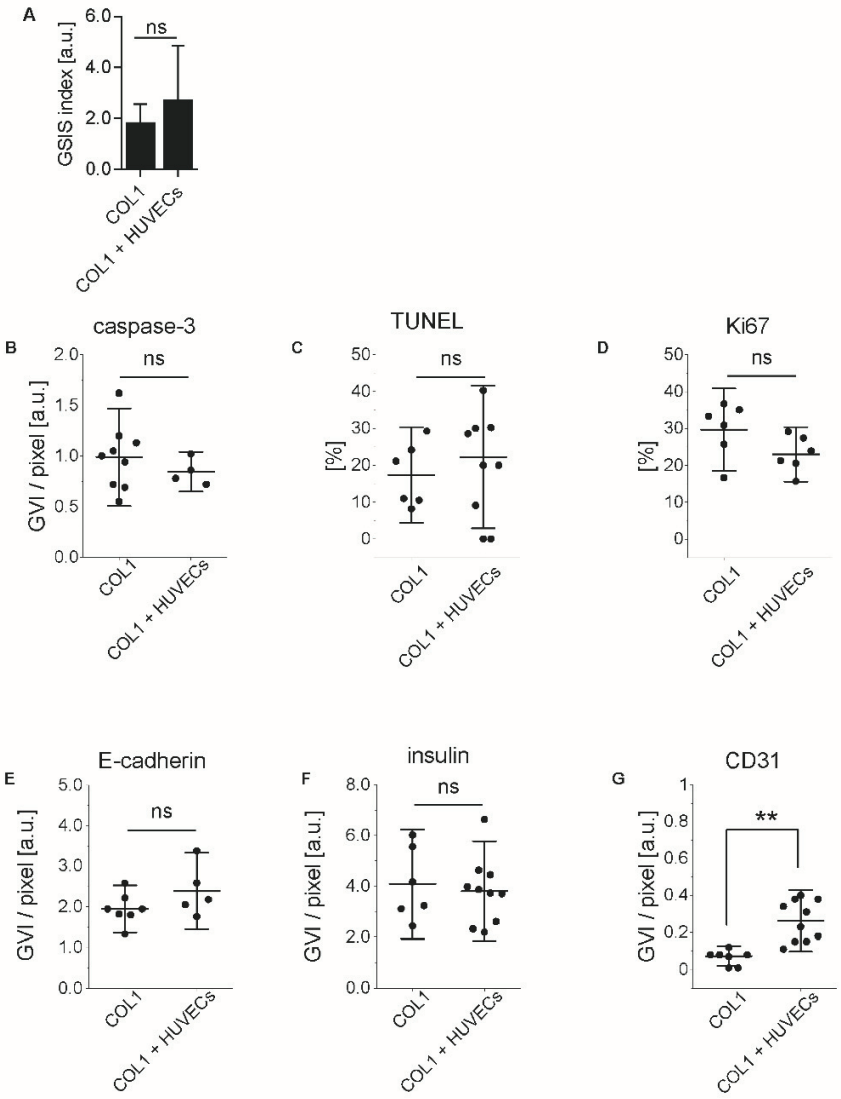

Figure S4: Comparison of β-cell pseudo-islets and co-culture β-cell pseudo-islets with HUVECs in COL1 hydrogel under hypoxic conditions for 48h. (**A**) No difference in GSIS response was observed. No differences were seen in the expression of (**B**) caspase-3 ($n \geq 4$), (**C**) $TUNEL^+$ cells ($n \geq 6$), (**D**) KI67 ($n = 6$), (**E**) E-cadherin ($n \geq 5$) and (**F**) insulin ($n \geq 6$). (**G**) Co-culture β-cell pseudo-islets express significantly more CD31 ($n \geq 6$). Unpaired t-test, **$p<0.01$.

Table S1: List of primary and secondary antibodies used for immunofluorescence staining

antibodies	0.1% Triton-X treatment	dilution
primary antibodies		
caspase-3 (ab13847)	30 min	1:100
collagen type 1 (ab138492)		1:75
collagen type 1 (R1038)		1:250
collagen type 4 (ab6586)		1:250
decorin (sc-73896)		1:200
E-cadherin (ab76055)		1:250
fibronectin (ab2413)		1:100
insulin (ab181547)	30 min	1:200
KI67 (ab15580)	30 min	1:1000
laminin (ab11575)		1:50
nidogen-1 (sc-33141)		1:100
secondary antibodies		
Alexa Fluor 488 anti-rabbit IgG(ab150077)		1:250
Alexa Fluor 488 anti-mouse IgG 1 (ab150117)		1:250
Alexa Fluor 594 anti-rabbit IgG(ab150080)		1:250

Appendix II: Zbinden A., Marzi J., Schlünder K., Probst C., Urbanczyk M., Black S., Brauchle E.M., Layland S.L., Kraushaar U., Duffy G.P., Schenke-Layland K., & Loskill P.; *Non-invasive high content Raman analysis of a microphysiological human pancreas-on-a-chip model*, Matrix Biology, 2020; 85: 205-220.

ARTICLE IN PRESS

Article

MATBIO-1576; No. of pages: 16; 4C:

Non-invasive marker-independent high content analysis of a microphysiological human pancreas-on-a-chip model

Aline Zbinden[a], Julia Marzi[a,b], Katharina Schlünder[c], Christopher Probst[c], Max Urbanczyk[a], Scott Black[b], Eva M. Brauchle[a,b], Shannon L. Layland[a], Udo Kraushaar[b], Garry Duffy[d,e], Katja Schenke-Layland[a,b,f1] and Peter Loskill[a,c1]

***a* - Dept. of Women's Health,** *Research Institute of Women's Health, Eberhard Karls University Tübingen, Germany*
***b* - The Natural and Medical Sciences Institute (NMI) at the University of Tübingen,** *Reutlingen, Germany*
***c* - Fraunhofer Institute for Interfacial Engineering and Biotechnology (IGB),** *Stuttgart, Germany*
***d* - Discipline of Anatomy and the Regenerative Medicine Institute,** *School of Medicine, College of Medicine Nursing and Health Sciences, National University of Ireland Galway, Ireland*
***e* - Science Foundation Ireland (SFI),** *Centre for Research in Advanced Materials for Biomedical Engineering (AMBER), Trinity College Dublin, National University of Ireland Galway, Galway, Ireland*
***f* - Dept. of Medicine/Cardiology,** *University of California Los Angeles (UCLA), Los Angeles, CA, USA*

Correspondence to Katja Schenke-Layland and Peter Loskill: *at: Research Institute for Women's Health, Dept. of Women's Health, Eberhard Karls University Tübingen, Silcherstr. 7/1, 72076 Tübingen, Germany.*
katja.schenke-layland@med.uni-tuebingen.de
https://doi.org/10.1016/j.matbio.2019.06.008

Abstract

The increasing prevalence of diabetes, its heterogeneity, and the limited number of treatment options drive the need for physiologically relevant assay platforms with human genetic background that have the potential to improve mechanistic understanding and e\xpedite diabetes-related research and treatment. In this study, we developed an endocrine pancreas-on-a-chip model based on a tailored microfluidic platform, which enables self-guided trapping of single human pseudo-islets. Continuous, low-shear perfusion provides a physiologically relevant microenvironment especially important for modeling and monitoring of the endocrine function as well as sufficient supply with nutrients and oxygen. Human pseudo-islets, generated from the conditionally immortalized EndoC-βH3 cell line, were successfully injected by hydrostatic pressure-driven flow without altered viability. To track insulin secretion kinetics in response to glucose stimulation in a time-resolved manner, dynamic sampling of the supernatant as well as non-invasive real-time monitoring using Raman microspectroscopy was established on-chip. Dynamic sampling indicated a biphasic glucose-stimulated insulin response. Raman microspectroscopy allowed to trace glucose responsiveness in situ and to visualize different molecular structures such as lipids, mitochondria and nuclei. In-depth spectral analyses demonstrated a glucose stimulation-dependent, increased mitochondrial activity, and a switch in lipid composition of insulin secreting vesicles, supporting the high performance of our pancreas-on-a-chip model.

Introduction

Diabetes mellitus (DM) is a group of metabolic disorders characterized by a dysregulated glucose metabolism, which is the result of a progressive autoimmune destruction of pancreatic β-cells (type 1) or a combination of β-cell dysfunction and systemic insulin resistance (type 2) [1]. In 2017, over 450 million adults were diagnosed, representing a global cost of 727 billion USD for the health care expenses [2]. A wide range of chronic and acute complications are associated with DM, mainly caused by sustained elevated blood glucose levels [3,4]. Injection of insulin and transplantation of the

pancreas or pancreatic islet are the most prominent treatment options for type 1 DM, while for type 2 DM lifestyle changes and metformin administration are the recommended clinical approaches [5]. To date, no robust cure for DM has been developed and patient's life quality is continuously challenged physically and psychologically by the high-maintenance management of their disease, as well as the severe risk of hypoglycemic events [6]. Therefore, it is highly urgent to deepen our knowledge of the underlying mechanisms of DM, as well as to provide new tools to facilitate pharmacological drug screening that could support the development of an effective cure reversing the functionality loss of beta-cells or insulin resistance. Unfortunately, the identification and prediction of relevant pathways involved in diabetic patients based on animal models is often inadequate, mainly due to the multifactorial nature of DM, as well as species-differences in mechanisms, for instance in glucose regulatory pathways [7]. Due to the difficultly in creating human DM in animal models, there is a strong need to develop advanced in vitro platforms with human genetic background, physiological relevance as well as integrated non-invasive readouts.

Organ-on-a-Chip (OoC) technologies provides the basis for the recapitulation and monitoring of the endocrine function of the pancreas by generating a physiologically relevant microenvironment with a constant low-sheer perfusion, allowing exchange of nutrients (e.g. glucose) as well as transport of secreted hormones (e.g. insulin). In the last decade, significant efforts have contributed to the development of OoC platforms, allowing microfluidic assessments of rodent and human pancreatic Langerhans islet function by measurement of insulin release, evaluation of mitochondrial potential and intracellular Ca^{2+} changes to glucose stimulation [8–13]. The use of native pancreatic islets for research is hampered by two main limitations; while findings from rodent pancreatic islets have resulted in controversy due to major differences in spatial composition within the islets as well as in insulin secretory pathways, the shortage of cadaveric human pancreatic islets remains the most predominant drawback [14–16]. An alternative is the use of cell lines. Previously, only rodent (INS-1E, MIN-6) cell lines were glucose-responsive and the human cell lines available had a debatable insulin expression and glucose-stimulated insulin secretion [17]. Recently, a new conditionally immortalized cell line was developed (EndoC-βH3), enabling the generation of non-proliferative glucose-sensitive β-cells representative of primary human β-cells [18]. In addition to the generation of physiologically relevant, perfused microenvironments and the establishment of suitable cell and tissue sources, it is of upmost importance for an advanced in vitro platform to integrate non-invasive, marker-independent read-out methods [19–21]. Raman microspectroscopy and Raman imaging provide excellent features for non-destructive in situ monitoring in OoC systems. The laser-based techniques allow the assessment and visualization of molecular information in the form of a spectral fingerprint. Whereas this technique is already well-established in pharmaceutical and material sciences [20–22], it is constantly gaining broader relevance in the biomedical field for applications such as tissue diagnosis, monitoring of drug-delivery or the identification of cells with regard to differentiation state, cell death stage or carcinogenesis [23–27]. Moreover, recent work reported the application of Raman spectroscopy-based technologies to define diabetes biomarkers in body fluids [28–30].

In this study, we developed a microphysiological pancreas-on-a-chip model enabling the self-guided trapping of human conditionally immortalized EndoC-βH3 pseudo-islets. Our platform enables a precisely controllable vasculature-like perfusion, ensuring the constant delivery of nutrients to the pseudo-islets and removal of metabolites and secreted factors. This enabled the time-resolved sampling of the effluent to characterize endocrine functionality. In addition, taking advantage of the optical accessibility of the platform, we established Raman microspectroscopy and Raman imaging as marker-independent, non-invasive, real-time technique to monitor pseudo-islets functionality. Applying this toolbox of non-invasive characterization methods, we were able to monitor dynamic insulin secretion, mitochondrial activation as well as lipid composition of insulin secreting vesicles in situ on-chip.

Methods

Chip design & fabrication

Tailored microfluidic platforms were fabricated using standard PDMS soft lithography. Master molds were generated by spin coating two consecutive layers of SU8 50 (MicroChem Corp, Newton, MA, USA) onto a previously cleaned and dehydrated 4″ wafer. The first layer of SU8 50 was coated onto the substrate at 500 rpm/s (10 s; acceleration 100 rpm/s) and then at 1000 rpm (30 s; acceleration 300 rpm/s), resulting in an overall height of 100 µm. Subsequently, the substrate was baked at 65 °C for 10 min and at 95 °C for 30 min. Prior to spin coating the second layer, the substrate was allowed to cool down to room temperature. Afterwards, SU8 50 was spin coated onto the substrate at 500 rpm (10 s; acceleration 100 rpm/s) and then at 2000 rpm (30 s; acceleration 300 rpm/s) to achieve an overall height of 150 µm. Subsequent to a baking step at 65 °C for 6 min and at 95 °C for 20 min, the wafers were exposed to UV-light for 16 s at 25 mW/cm^2 (400 mJ/cm^2). A post-exposure bake was then carried out at

Please cite this article as: A. Zbinden, J. Marzi, K. Schlünder, et al., Non-invasive marker-independent high content analysis of a microphysiological human pancreas-on-a-chip model, Matrix Biology, https://doi.org/10.1016/j.matbio.2019.06.008

65 °C for 1 min and at 95 °C for 15 min. Development of the substrate was performed in three consecutive washing steps: The substrate was developed in two baths of SU8 developer (Micro-Chem Corp) for 5 min each followed by a final wash in isopropyl alcohol for 5 min. Afterwards the substrate was blow dried using a nitrogen gun. Master molds were immediately silanized using chlorotrimethylsilane (75–77-4) (Sigma-Aldrich, Schnelldorf, Germany).

PDMS replicas were generated by pouring a 1:10 mixture of PDMS (Sylgard 184, Dow Corning, Midland, MI, USA) onto the silanized master and baking it at 60 °C overnight. PDMS slabs were then released from the master and cut into individual devices. Inlets and outlets were punched using a biopsy punch with a diameter of 0.75 mm (World Precision Instruments, Sarasota, USA). Prior to the experiments, each chip was thoroughly cleaned with acetone, isopropyl alcohol and, after drying, scotch tape. Cleaned chips were bonded onto a cleaned microscopy slide using oxygen plasma exposure in a plasma generator (Diener electronic GmbH & Co KG, Germany).

Computational fluid dynamics simulation

Computational fluid dynamics (CFD)-based analysis was performed using COMSOL multiphysics (COMSOL Multiphysics GmbH, Göttingen, Germany) with the model geometry depicted in Fig. S1. The incompressible stationary flow was modeled by the Navier-Stokes equation with the properties of water (dynamic viscosity $\mu = 1 \times 10^{-3}$ m^2/s, density $\rho = 1000$ kg/m^3) and an inlet pressure of 294 Pa. The transport of diluted species was described by the time dependent convection-diffusion with a diffusion co-efficient 1×10^{-9} m^2/s and an initial concentration of 1 mol/m^3.

Cell culture & pseudo-islet formation

The conditionally immortalized human pancreatic beta-cell line EndoC-ßH3® was cultured as described previously [18]. Briefly, unexcised cells were culture in T25 flasks coated with βCOAT® (Univercell-Biosolutions, Paris, France) at a density of 70,000 cells/cm^2. Cells were passaged every 7 days and cultured with OPTIβ1® (Univercell-Biosolutions) media supplemented with 10 µg/ml puromycin (Invitrogen, Darmstadt, Germany). Excision of the floxed immortalizing transgenes of the EndoC-ßH3® cells was performed according to the manufacturer's instructions (Univercell-Biosolutions) using 4-hydroxy tamoxifen (4-OHT) (Sigma-Aldrich, Germany) treatment. After 21 days of 4-OHT treatment, pseudo-islets were formed under standard culture conditions at a concentration of 1000 cells/aggregate over 96 h in a 96-well plate with a non-adherent round bottom (Greiner, Frickenhausen, Germany). Fully formed pseudo-islets were loaded in the pancreas-on-a-chip model by hydrostatic pressure-driven flow. The starving medium OPTIβ2® (Univercell-Biosolutions) was perfused at a speed of 50 µl/h for 24 h prior to any experiments.

Immunofluorescence staining

Pseudo-islets in static culture conditions and in the pancreas-on-a-chip platform were washed with PBS and fixed with 4% paraformaldehyde (PFA) (Sigma-Aldrich) for 10 min. Pseudo-islets in static culture were encapsulated in HistoGel (Thermo Fisher Scientific, Darmstadt, Germany) and embedded in paraffin. Sections of 3 µm thickness were deparaffinized and antigen retrieval with Citrate and EDTA buffer was performed. Then, the sections were permeabilized with 0.1% Triton-X for 15 min, rinsed with PBS, and blocked for 30 min using 2% goat serum block. The pseudo-islets in the pancreas-on-a-chip were permeabilized with Triton-X 0.1% for 25 min and blocked for 45 min using 2% goat block serum. Afterwards, sections and pseudo-islets on-chip were incubated with an anti-insulin guinea pig antibody (DAKO, Frankfurt, Germany, anti-guinea pig IgG, 1:100) overnight at 4 °C. The next day, sections and pseudo-islets on-chip were washed with PBS, incubated with anti-guinea pig Alexa 594 (abcam, Cambridge, UK, 1:250) for 25 min at room temperature and incubated with DAPI (Sigma-Aldrich) for 10 min. Sections were mounted using with Prolong Gold Anti Fade solution (Thermo Fisher Scientific). Imaging was done with an LSM710 confocal microscope (Zeiss, Jena, Germany).

Live/dead staining

Pseudo-islets in suspension and in the pancreas-on-a-chip were washed with PBS, incubated for 15 min with fluorescein diacetate (FDA) at 5 µg/ml (Thermo Fisher Scientific) and propidium (PI) (Thermo Fisher Scientific) at 1 µg/ml in OPTIβ1® and imaged using a fluorescence microscope (Leica DMi8, Wetzlar, Germany).

Glucose stimulated insulin secretion (GSIS) assays

Static control

Pseudo-islets were grouped by 5 per well, washed twice with KREBS-BSA (Krebs buffer) (Univercell-Biosolution), and incubated for 1 h with KREBS-BSA to induce synchronization, as described previously [18]. Supernatant was discarded and fresh KREBS-BSA was added for 1 h. Pseudo-islets were washed twice with KREBS-BSA and incubated with 20 mM glucose (Gibco, Thermo Fisher Scientific) in

Please cite this article as: A. Zbinden, J. Marzi, K. Schlünder, et al., Non-invasive marker-independent high content analysis of a microphysiological human pancreas-on-a-chip model, Matrix Biology, https://doi.org/10.1016/j.matbio.2019.06.008

KREBS-BSA for 1 h. Supernatant was then collected, and pseudo-islets were washed twice with KREBS-BSA and freshly incubated with KREBS-BSA for 1 h. Subsequently, supernatant was again collected. All supernatant samples were stored at −20 °C for further analysis.

GSIS-in-the-chip

20 human pseudo-islets in OPTIβ2® were loaded in each pancreas-on-a-chip through hydrostatic pressure-driven flow. Low pressure 4-port switching valves (IDEX Heath & Science, Oak Harbor, USA) were incorporated upstream to the chip inlets to allow dynamic switching between the different conditions (KREBS-BSA and 20 mM glucose). A low-shear flow of 50 µl/h was set for all experiments. To enable a comparison to the static GSIS assay, effluent was sampled at respective time points. Switching time points were calculated based on total volume of the tubing, the chip and the switching valves (t_x media transport from the switching valves to the pseudo-islet positions: 8 min; t_y media transport from pseudo-islets to the collecting Eppendorf: 16 min). Prior to assay start ($t = 0$), an incubation of 1 h 24 min with KREBS-BSA was performed in order to exchange the media (24 min) and synchronize the pseudo-islets (1 h). Then at $t =$ 1 h, the supernatant (50 µl) of a second incubation with KREBS-BSA was collected as "Krebs(1)". The switch to high glucose was performed at $t = 2$ h - t_x - t_y. The pseudo-islets were incubated with high glucose for a total of 1 h and effluent was collected as "high glucose" at t = 2 h. The switch back to KREBS-BSA was performed at $t = 3$ h - t_x - t_y with a last effluent sampling at t = 3 h as "Krebs(2)". Experiments were performed in quadruplets.

Dynamic insulin secretion

Pancreas-on-a-chip platforms were prepared as mentioned above. Sampling took place every 15 min (starting at $t = -1$ h), during the first KREBS-BSA incubation/synchronization (1 h), the second KREBS-BSA (1 h) and 4 h of high glucose. Experiment were performed in triplicates. Effluent was sampled straight out of the platform outlets (t_y media transport from pseudo-islets to the outlet: 10 min). All GSIS assays were performed at 37 °C.

Raman microspectroscopy and imaging on-chip

Raman measurements and imaging were performed on a customized WiTec alpha300 R Raman microscope equipped with a charge-coupled device (CCD) camera (WiTec GmbH, Ulm, Germany) [31]. An inverted microscope setup with a 60× air objective (Carl Zeiss GmbH, Jena, Germany), a green laser (532 nm) and a spectrograph with a grating of 600 g/mm were selected for spectral acquisition. In addition, the setup contained an incubation chamber (Okolab S.R.L., Pozzuoli, Italy) to keep the pancreas-on-a-chip at constantly 37 °C. For data acquisition, the pancreas-on-a-chip was loaded with human pseudo-islets as described above for the dynamic GSIS assay and placed in the sample holder of the microscope stage. In situ Raman images were acquired of complete pseudo-islets in KREBS-BSA or 20 mM glucose buffer. A spectral map containing a single spectrum per pixel was generated of an area of 150 × 150 µm, at a pixel resolution of 2 × 2 µm, an acquisition time of 0.5 s per spectrum and a laser power of 50 mW. Furthermore, real-time monitoring of the kinetic of insulin secretion in the pancreas-on-a-chip was performed as described above. A defined area within the islet of 160 × 30 µm was constantly measured every 5 min at an acquisition time of 3 s per spectrum. Measurements were acquired over a total period of 90 min (the last 20 min in KREBS-BSA and 1 h at 20 mM glucose). Experiments were performed at least as triplicates.

Spectral analysis

Image analysis of the spectral map was performed by the Project FIVE 5.1 software (WiTec GmbH). Spectral data were baseline corrected and pretreated by cosmic ray removal. True component analysis (TCA) was applied to generate images of the spectral map data. TCA identified spectral components that were most prevalent in the data set and enabled a visualization by generating intensity distribution images for each identified component [31]. The peaks of the identified components were analyzed to characterize their molecular assignment. Grey value intensities (GVI) were determined in the intensity distribution images for quantitative assessment of each component under different buffer conditions. In very heterogeneous samples only the major spectral components are clearly distinguished by TCA. Thus, principal component analysis (PCA) was performed on extracted spectra of the same TCA component for in-depth analysis of smaller spectral differences. PCA is a multivariate data analysis tool, commonly applied in chemometrics, that has been established as well for the analysis of Raman data [32]. Briefly, spectral data are reduced in their dimensionality on a vector-based approach. Each vector, so-called principal component (PC), describes a variation in the spectra. The first PC represents the highest amount of variation, the subsequent PCs refer to the next highest amount of variation chronologically. PC values can be plotted against each other to visualize a correlation or separation of two or more data sets.

In situ GSIS assay Raman data were evaluated by TCA to identify a time-dependent component.

Please cite this article as: A. Zbinden, J. Marzi, K. Schlünder, et al., Non-invasive marker-independent high content analysis of a microphysiological human pancreas-on-a-chip model, Matrix Biology, https://doi.org/10.1016/j.matbio.2019.06.008

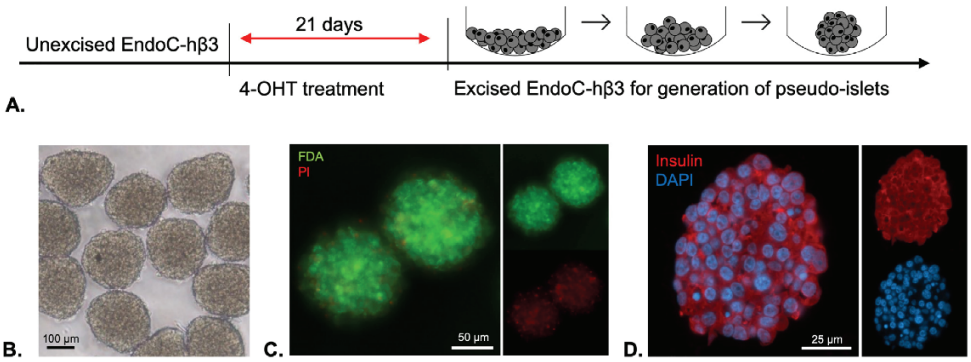

Fig. 1. Generation and static culture of human pancreatic pseudo-islets. **(A)** Schematic timeline of the EndoC-βH3 cell culture and pseudo-islet generation. **(B)** Brightfield image of human pseudo-islets in static culture. **(C)** Live (FDA, green) / dead (PI, red) staining of pseudo-islets. **(D)** Immunofluorescent staining of insulin (red) and nuclei (DAPI) of pseudo-islet. (For interpretation of the references to colour in this figure legend, the reader is referred to the web version of this article.)

Weightings of the CCD counts were extracted from the intensity distribution images of the TCA results and compared.

Statistical analysis

Data are presented as mean ± standard deviation (SD). Data normality was determined by Sharpiro Wilk test. Statistical significance was determined by ANOVA by employing the Kruskal Wallis, with Tukey multiple comparison test. Statistical analyses were performed in Prism 6 (GraphPad Software Inc., La Jolla, CA, USA). Data with p-values $\ll 0.05$ were identified as statistically significant.

Results

Generation of functional human pseudo-islets

Human pseudo-islets were generated using the conditionally immortalized cell line EndoC-βH3, aiming to mimic the endocrine function of Langerhans islets in vitro (Fig. 1A). EndoC-βH3 was cultured in standard conditions as previously described [18]. After excision, non-proliferative cells were harvested and seeded with 1000 cells per well. Within 4–5 days, cells aggregated and formed stable so-called pseudo-islets with a highly reproducible size (Fig. 1B). The aggregation of cells was promoted by the low-adherence feature of the 96-well plate used and occurred in a spontaneous manner in static conditions. Cell viability and insulin expression were maintained by pseudo-islets as demonstrated via live/dead staining (Fig. 1C) and routine immunochemistry, showing a homogenous insulin staining throughout the pseudo-islet (Fig. 1D).

Chip design, fabrication & modeling

A tailored microfluidic PDMS-based system was developed to culture and analyze individual human pseudo-islets, which can hold up to 32 pseudo-islets per chip (Fig. 2A). A microfluidic hydrodynamic trapping principle previously described by Takeuchi et al. was modified to isolate individual pseudo-islets from suspension [33]. A detailed description and calculations of the hydrodynamic entrapment of pseudo-islets in the pancreas-on-a-chip is provided in the Supplemental Data File. The pseudo-islets are sequentially loaded into the traps (Fig. 2B, Supplemental Movie), whereby individual pseudo-islets are guided one after another in the 4 × 8 trapping array until all trapping structures are filled. Trapping is supported by a small interconnecting (60 µm width) channel between each trapping structure and the surrounding so-called loop channel. After the first trap is filled thereby blocking the interconnecting channel, flow through the interconnecting channels of the subsequent trapping structures is increased, guiding the following pseudo-islets to. Channel dimensions were chosen such that a successful loading of human pseudo-islets was achieved leveraging gravitational flow from a 200 µl pipette tip inserted in the inlet port of the pancreas-on-a-chip, resulting in an inlet pressure of approx. 294 Pa.

Structural and functional characterization of human pseudo-islets on-chip

A reproducible loading of pseudo-islets into the pancreas-on-a-chip was successfully achieved via

Please cite this article as: A. Zbinden, J. Marzi, K. Schlünder, et al., Non-invasive marker-independent high content analysis of a microphysiological human pancreas-on-a-chip model, Matrix Biology, https://doi.org/10.1016/j.matbio.2019.06.008

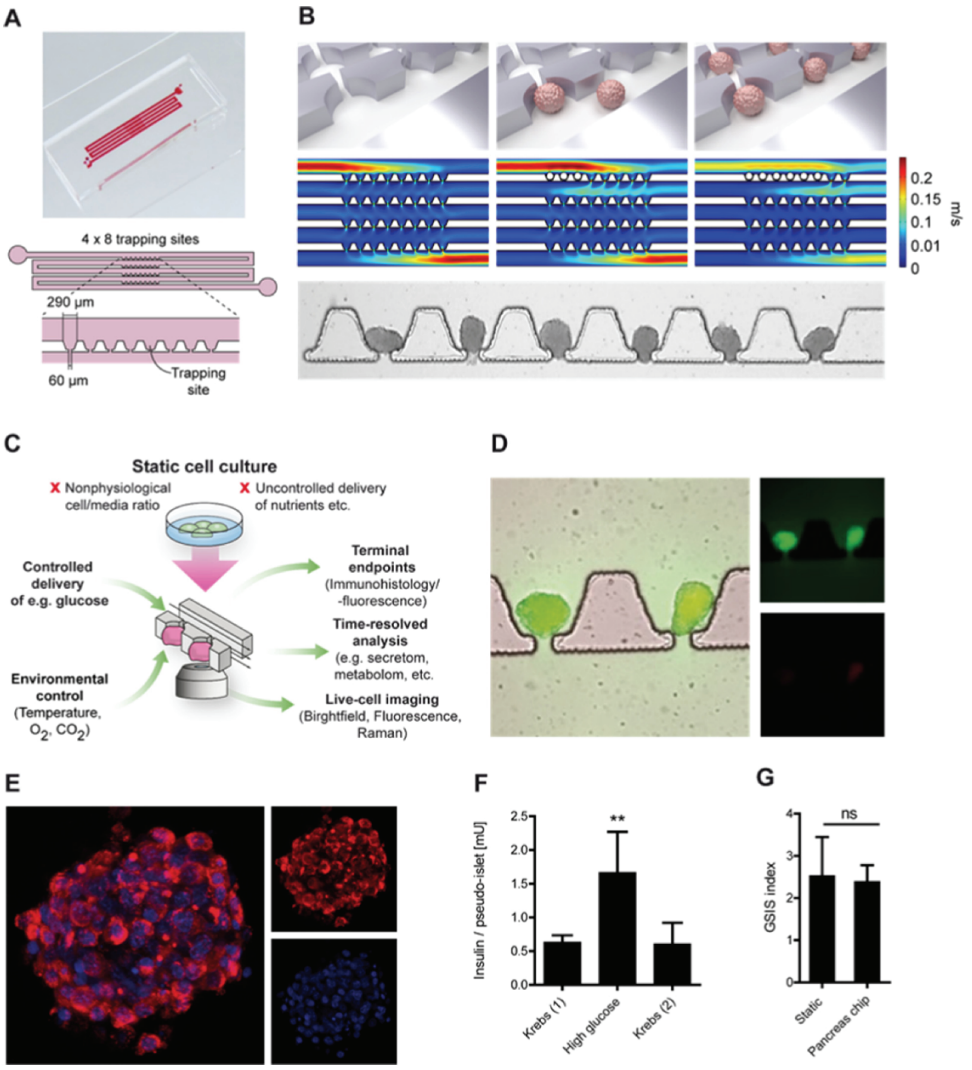

Fig. 2. Human pancreas-on-a-chip. **(A)** Image of pancreas-on-a-chip (visualized using dyed water) and schematic of the fluid channels and trapping geometries. **(B)** 3D illustration depicting the loading procedure of single pseudo-islet into trapping sites with the respective changes in fluid flow, described by computational fluid dynamics based analysis. The hydrodynamic trapping yields a sufficient and stable immobilization of always one individual pseudo-islet per trapping site in the entire device, demonstrated by a brightfield image of human pancreatic pseudo-islets loaded in the pancreas-on-a-chip. **(C)** General key features and benefits of the pancreas-on-a-chip system compared to conventional static cell culture methods. **(D)** Live (FDA, green) /dead (PI, red) staining of pseudo-islets on-chip 24 h after loading. **(E)** Representative immunofluorescent staining of insulin (red) and nuclei (DAPI) of pseudo-islet on-chip. **(F)** Sequential glucose stimulated insulin secretion assay on-chip with Krebs (no glucose) and high glucose (20 mM) buffer. $^{**}p \ll 0.01$; $n = 4$. **(G)** Comparison of the GSIS index between static and dynamic conditions. $n \geq 4$. (For interpretation of the references to colour in this figure legend, the reader is referred to the web version of this article.)

Please cite this article as: A. Zbinden, J. Marzi, K. Schlünder, et al., Non-invasive marker-independent high content analysis of a microphysiological human pancreas-on-a-chip model, Matrix Biology, https://doi.org/10.1016/j.matbio.2019.06.008

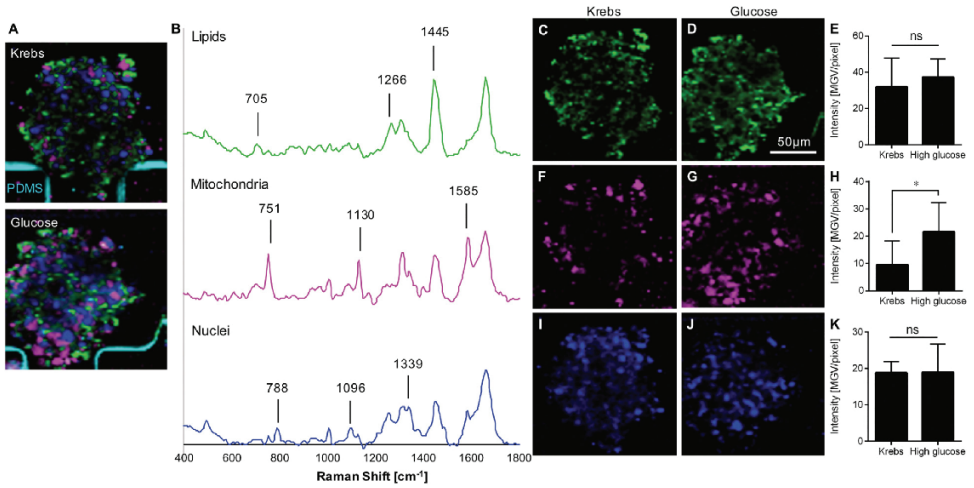

Fig. 3. In situ Raman imaging of human pancreas-on-a-chip in Krebs and high glucose condition. (A) True component analysis identified 3 major spectral components in the pseudo-islets and the PDMS of the chip (light blue). (B) The identified components show peaks assigned to lipids (green), mitochondria (pink) and nuclei (blue). (C-K) Image analysis by grey value intensity determination demonstrated no quantitative difference in lipids (C-E) and nuclei (I-K) between Krebs buffer and glucose condition. A significantly different distribution was observed for the mitochondrial component (F-H). Scale bar equals 50 µm; n = 3, $*p < 0.05$.(For interpretation of the references to colour in this figure legend, the reader is referred to the web version of this article.)

hydrostatic pressure-driven flow. The precisely controllable, low-stress character of the loading process did not impair cell viability in the pseudo-islets as demonstrated via live/dead staining (Fig. 2D). In contrast to static dish culture, the pancreas-on-a-chip platform enabled in situ immunofluorescence staining of individual pseudo-islets. Thereby, we could show that on-chip, insulin is homogeneously distributed throughout the entire pseudo-islet (Fig. 2E). To validate the functionality of the pseudo-islets on-chip, we adapted the conventional static culture Glucose Stimulated Insulin Secretion (GSIS) assay to the perfusion conditions of the pancreas-on-a-chip system by first flushing the media channel with no glucose solution (Krebs buffer) for 1 h, followed by a 1 h perfusion with 20 mM glucose solution and finally a second flushing with Krebs buffer. The perfused effluent was collected for 1 h for each condition resulting in 50 µl samples for further ELISA analysis. The insulin secreted by the pseudo-islets on-chip increased significantly from the first incubation of Krebs buffer (Krebs(1)) to the 20 mM glucose condition (high glucose) and subsequently decrease significantly again when perfused with Krebs buffer (Krebs(2)) (Fig. 2F). The fold increase between Krebs(1) and 20 mM glucose, the GSIS index, corresponded with the results from the gold standard static culture experiments, validating that glucose response from the pseudo-islets was not impaired in the pancreas-on-a-chip model (Fig. 2G).

On-chip Raman analysis for in-situ imaging and characterization of molecular structures

Raman microspectroscopy was established as non-destructive in situ monitoring tool for functional and qualitative assessment of the pancreas-on-a-chip. Raman images of single human pseudo-islets in the pancreas-on-a-chip in Krebs buffer or 20 mM glucose solution were acquired under dynamic flow conditions. Combined with true component analysis (TCA), a non-invasive, marker-independent assessment of three major structures was possible (Fig. 3A). Furthermore, the PDMS mold could be clearly identified due to its strong Raman signal. The peaks were analyzed to characterize the assigned molecular structures (Fig. 3B). The first component (green) showed major peaks at 705, 1266 and 1445 cm^{-1} referring to ring deformation in cholesterol as well as = CH deformation and CH_2/CH_3 scissoring in lipids [34]. The second component (pink) contained peaks at 751, 1130 and 1585 cm^{-1}, described before in relation to mitochondria and mitochondrial activity [35–37]. Peaks at 788, 1096 and 1339 cm^{-1} were found in the third component (blue) and

Please cite this article as: A. Zbinden, J. Marzi, K. Schlünder, et al., Non-invasive marker-independent high content analysis of a microphysiological human pancreas-on-a-chip model, Matrix Biology, https://doi.org/10.1016/j.matbio.2019.06.008

Table 1. Peak assignments of the components identified by Raman imaging and TCA.

Peak [cm^{-1}]	1 - lipid-related	2 - mitochondria-related	3 - DNA-related
415	Phosphatidylinositol [41]		
488	Glycogen [42]		
608	Cholesterol [41]		
704			Cholesterol [34,43]
751	Mitochondria [37]		
755		Symmetric breathing tryptophan [42]	
788		Phosphodiester stretching in DNA [38]	
940	C-C mode [44]		
1006		Phenylalanine (ring-breathing) [44]	
1096		Phosphodioxy groups [39]	
1127			C-N lipids, proteins [42,45]
1130	Cytochrome C [46,47]		
1257		A,T (ring breathing modes) [48]	
1266			C-H lipids, amide III [40]
1307			CH_3 / CH_2 twisting in lipids [49]
1312	CH_3CH_2 twisting [49]		
1342		Nucleic acid mode (DNA/RNA) [40]	
1402	Oxidized cytochrome C [46]		
1445			CH_2 bending in lipids [50]
1455		Deoxyribose [51]	
1585	Mitochondria [46]		
1659			C = O stretching, C=C [39,50]

corresponded to phosphodiester and nucleic acid vibrations in DNA [38–40]. A detailed summary of all peaks and molecular assignments is displayed in Table 1. Quantitative assessment and comparison of the distributions of the three components in the pseudo-islets in Krebs buffer and 20 mM glucose conditions was performed by grey value intensity analysis. There was no significant difference in lipid (Fig. 3C, D, E) and nuclei (Fig. 3I, J, K) expression between both conditions. The mitochondria-related spectral component was significantly higher expressed in glucose-stimulated pseudo-islets (Fig. 3F, G, H).

Whereas the mitochondrial component revealed an increased expression in the pseudo-islets in glucose conditions, no quantitative differences between Krebs buffer and 20 mM glucose conditions were detected for the lipid component. However, the average spectra of all spectra identified as lipids in Krebs or 20 mM glucose conditions demonstrated minor qualitative differences in their Raman fingerprint. The peak at 415 cm^{-1}, referring to phosphatidylinositol (PI3) [41], appeared with a higher intensity in glucose conditions when compared to Krebs buffer condition (Fig. 4A). Thus, a principal component analysis (PCA) was performed on the extracted lipid component spectra for in-depth spectral analysis of differences in the lipid composition. The scores plot of PC-2 against PC-3 demonstrated a separation of the pancreas-on-a-chip lipid spectra in Krebs and 20 mM glucose condition (Fig. 4B). Compared to the lipid data set in Krebs buffer, the spectral data of the glucose conditions were highly significantly shifted to the positive PC-2 range and significantly shifted to the negative PC-3 range (Fig. 4C). The major spectral differences explained by the PCs were demonstrated in the loadings plots (Fig. 4D). Negative peaks in the loadings referred to relevant spectral information of data in the negative PC range, positive loadings peaks indicated spectral assignments of data in the positive PC range. Spectral differences within the groups were linked to PI3 peaks at 415 and 597 cm^{-1} [41,52,53] that were more prevalent in the glucose condition data. Moreover, differences were observed in peaks at 1136 and 1269 cm^{-1} that are assigned to C – C vibrations and = CH deformation in lipids [34]. Data of the lipids in the Krebs condition were dominated by spectral assignments to 1437, 1656 and 1737 cm^{-1}, characterizing CH_2/CH_3 scissoring in sphingomyelin as well as C=C and C=O vibrations in phosphatidylcholines and phosphatidylethanolamines [34]. These data correspond to a previous study that reported changes in the insulin secreting granules' phospholipid composition in correlation to glucose stimulation [54]. Certain phospholipids such as PI3 and phosphatidylserine increased, whereas other phospholipids remained unaffected.

Real-time monitoring of GSIS kinetics

To monitor insulin secretion in a time-resolved manner, we employed both dynamic sampling of the supernatant as well as non-invasive real-time monitoring using Raman microspectroscopy. The continuous, low-shear flow of buffer/solution through the pancreas-on-a-chip allowed the tracking of insulin secretion kinetics by collecting the supernatant every 15 min (Fig. 5A). The first switch from the culture medium to Krebs buffer is known as a synchronization step to equilibrate pseudo-islets to their basal insulin secretion level. The typical decrease of insulin secretion due to this

Please cite this article as: A. Zbinden, J. Marzi, K. Schlünder, et al., Non-invasive marker-independent high content analysis of a microphysiological human pancreas-on-a-chip model, Matrix Biology, https://doi.org/10.1016/j.matbio.2019.06.008

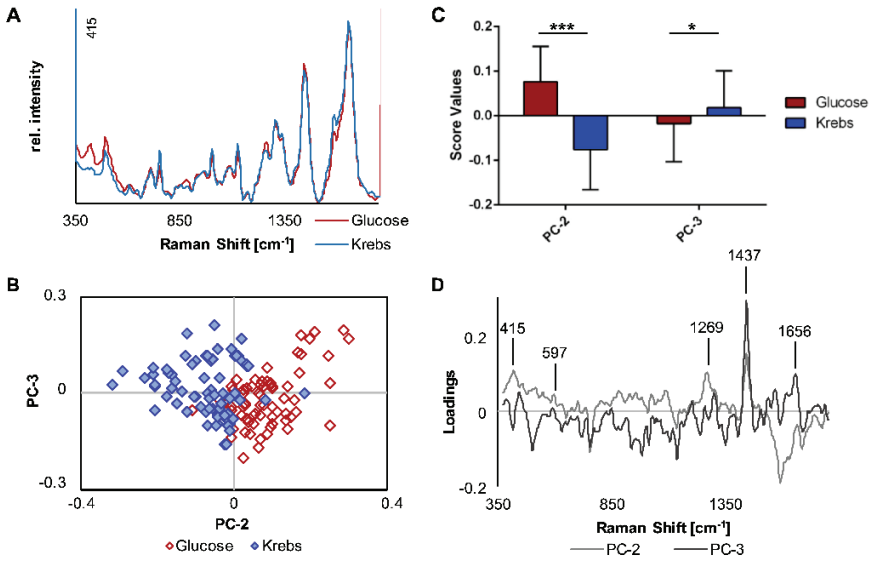

Fig. 4. PCA analysis of the influence of glucose stimulation on the lipid composition in pseudo-islets. (A) Average spectra of the lipid component identified by TCA in Krebs and glucose reveal minor spectral differences. (B) Detailed analysis using a PCA of the lipid spectra highlights the differences in the lipid component. (C) A highly significant separation of lipid composition in glucose and Krebs buffer is visible in PC2 and a significant separation is demonstrated in PC3. (D) The loadings plots were assigned to lipid-related spectral differences. $^{*}p \ll 0.05$, $^{***}p \ll 0.001$.

phenomenon was observed over the first hour of sampling (yellow). During the second incubation with Krebs buffer, the pseudo-islets reached their stable basal insulin secretion (blue). Addition of 20 mM glucose increased insulin release significantly within the first 45 min (red) and stayed higher than the base level for an additional hour. Afterwards, the insulin secretion slowly decreased to its baseline level. Here, the multisampling of the supernatant indicates a biphasic glucose response of our human pseudo-islets, a feature which has been widely used to characterize the functionality of native pancreatic Langerhans islets [55].

In addition, the GSIS response in the pancreas-on-a-chip was monitored in situ by Raman micro-spectroscopy. A transverse section of a pseudo-islet in the chip of an area of 160 × 30 µm was imaged every 5 min over a total period of 90 min. The images were stitched and analyzed by TCA. TCA was able to identify a time-dependent intensity shift in the intensity distribution images (Fig. 5B). The corresponding spectral component indicated an increase in mitochondrial activity and protein synthesis in correlation to the buffer change/glucose stimulation (Fig. 5C). Peaks at 415, 597 and 776 cm^{-1} referred to PI3 [41,52,53]. Mitochondria-related peaks were found at 748 and 1585 cm^{-1} [37,46]. An increased protein synthesis was characterized by peaks at 1123, 1445 and 1656 cm^{-1} corresponding to C−N stretching as well as amide I and amide III vibrations in lipids [42,45,48,56]. Furthermore, an assignment to disulfide-bond vibrations of insulin was detected at 511 cm^{-1} [57,58] as shoulder of the PDMS peak at 498 cm^{-1}. A detailed summary of all peaks and their molecular assignments is provided in Table 2.

The weightings of the CCD counts of the TCA were compared to assess the time point and effect of glucose stimulation on the pancreas-on-a-chip (Fig. 5D). A significant difference was demonstrated between the 35 and 40 min measurement. This time point correlated to the predicted time point of complete replacement of the Krebs buffer after switching to the 20 mM glucose condition. After the stimulating effect, no significant increase or decrease in mitochondrial activity and protein synthesis was detected, the weightings stayed on a constant high level. The baseline of Krebs buffer measurements indicated minor, however not significant, increases of the CCD weightings after the time point of switching to glucose buffer.

Please cite this article as: A. Zbinden, J. Marzi, K. Schlünder, et al., Non-invasive marker-independent high content analysis of a microphysiological human pancreas-on-a-chip model, Matrix Biology, https://doi.org/10.1016/j.matbio.2019.06.008

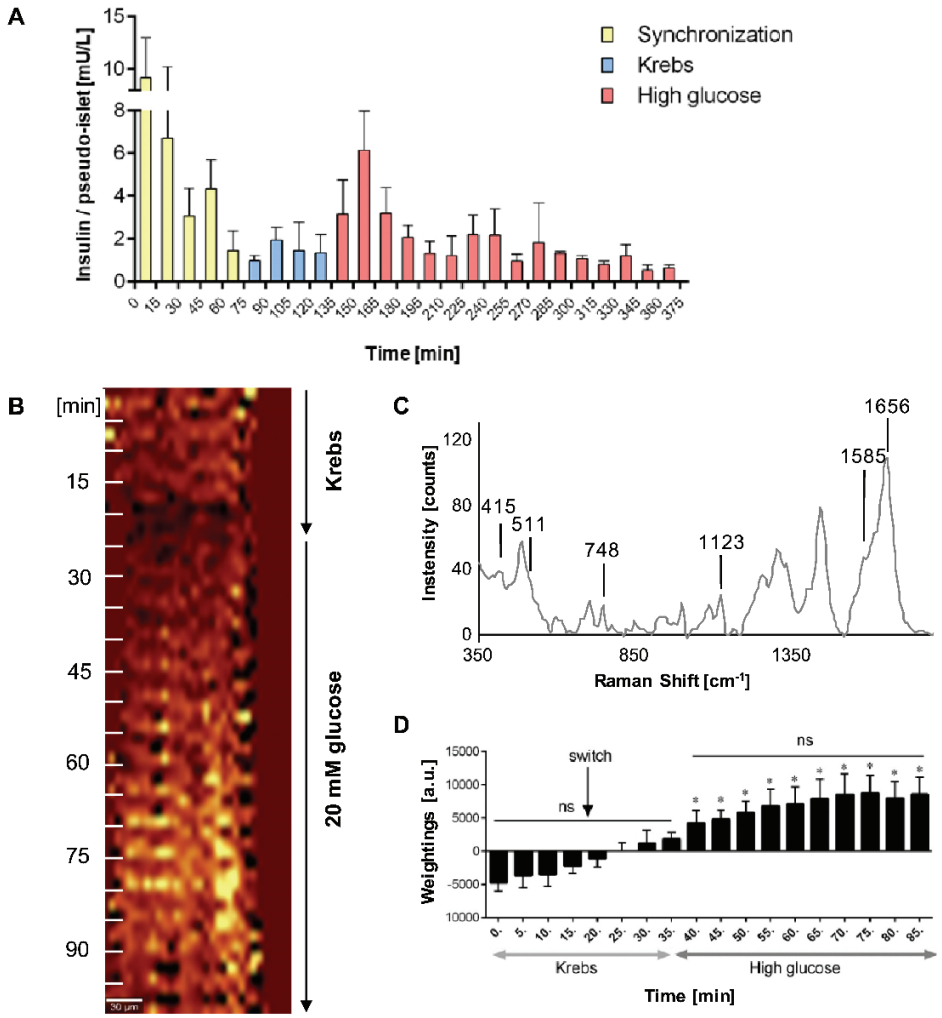

Fig. 5. Real-time monitoring of GSIS assay in human pancreas-on-a-chip. **(A)** Kinetic of insulin secretion by multisampling, $n = 3$. **(B)** Real-time Raman monitoring of glucose stimulation. Each 5 min time step represents a cross section of the pseudo-islet. Scale bar equals 30 µm. **(C)** TCA reveals a time-dependent component that is assigned to metabolic activity and protein production. **(D)** Statistical analysis of the weightings of the TCA shows a significant increase 20 min after the switch from Krebs to glucose buffer, whereas the baseline of Krebs and glucose buffer indicated no significant alteration. $^*p \ll 0.05$; n = 3.

Discussion

Translation from animal models to human clinical trials for the treatment of DM often fails due to the vast differences between animal models and human biology [63]. Current in vitro models often use rodent cells and feature a limited recapitulation of the complex physiological microenvironment found in vivo. Therefore, there is a strong need to develop human-based in vitro platforms with physiological relevance as well as integrated non-invasive read-outs, providing tools to investigate human-specific

Please cite this article as: A. Zbinden, J. Marzi, K. Schlünder, et al., Non-invasive marker-independent high content analysis of a microphysiological human pancreas-on-a-chip model, Matrix Biology, https://doi.org/10.1016/j.matbio.2019.06.008

Table 2. Peak assignments TCA component GSIS assay monitoring.

Peak [cm^{-1}]	Assignment
415	Phosphatidylinositol [41]
511	Insulin S – S bond [57,58]
597	Phosphatidylinositol [52,53]
704	Cholesterol [34,43]
748	Mitochondria [37]
776	Phosphatidylinositol [52,53]
849	Vibration amino acids, polysaccharides, tyrosine [59]
1002	Phenylalanine [60]
1060	C-C stretching (lipids), C – O, C – C stretching (carbohydrate), glucose, proteoglycans [38,61,62]
1123	C-N (proteins), C – C stretching mode lipids & proteins, glucose [42,45]
1257	Amide III (proteins) [48]
1308	CH_3/CH_2 lipids/ proteins [49]
1445	CH_2CH_3 bending modes of proteins, phospholipids [45]
1585	Mitochondria [46]
1656	C=C (lipids), Amide I (protein) [56]

mechanism in DM in vitro and to facilitate pharmaceutical drug testing. The concept of microphysiological systems (OoC platforms) has provided a novel approach with the potential to revolutionize drug development and testing [64,65]. By integrating human tissue in microfluidic systems that provide a physiological microenvironment and a vasculature-like perfusion, OoCs allow the recapitulation of the (patho) physiology and basic features of an organ or tissue in vitro [64].

In this study, we developed a novel integrated pancreas-on-a-chip platform featuring a self-guided trapping of individual human pseudo-islets, a controlled vasculature-like perfusion, and a non-invasive marker-free read-out possibility based on the integration of Raman microspectroscopy and imaging. Human pseudo-islets were generated from the conditionally-immortalized EndoC-βH3 cell line, which is to this date, the commercially available human cell line that most closely mimics functional human primary β-cells. In these cells, the excision of the proliferative transgenes leads to a complete arrest of proliferation, glucose-sensitivity and insulin secretion [18]. In addition, it has been extensively described that β-cells have an increased insulin secretion when cultured as pseudo-islets [66]. Here, we showed the robust and reproducible formation of pseudo-islets of approximately 124 μm diameter in average size, corresponding to what has been previously described in the literature to avoid oxygen and nutrients diffusion issues, while assuring high glucose-responses [57,67]. The pseudo-islets were viable and showed homogenous insulin expression throughout the entire construct.

The tailored microfluidic platform employs a hydrodynamic-based trapping mechanism to stably confine individual pseudo-islets in defined spatial patterns, while ensuring that subsequent pseudo-islets are guided to unoccupied trapping sites. The loading via hydrostatic pressure-driven flow of pseudo-islets, as well as the trapping mechanism did not alter the pseudo-islet viability nor it affected the overall insulin expression. Most importantly, the stable confinement of the individual pseudo-islets allowed the high-resolution analysis of single pseudo-islets. The standard GSIS assay was modified for our pancreas-on-a-chip in order to model the endocrine function of the pancreas, where in vivo, the Langerhans islets are periodically subjected to different glucose concentration and correspondently adjust their insulin secretion. The pancreas-on-a-chip secreted a basal level of insulin under vascular-like flow without glucose. The insulin secretion significantly increased when 20 mM glucose was perfused through the chip, demonstrating the glucose-sensitivity of the pancreas-on-a-chip. Moreover, the subsequent perfusion of Krebs buffer restored the basal insulin secretion level, which is an important feature demonstrating that glucose stimulation is not leading to an impaired response or cell death.

Fully functional Langerhans islets feature a dynamic biphasic glucose-response; therefore the monitoring of insulin kinetics in a time-resolved manner is of upmost importance [55,68]. Using the here presented pancreas-on-a-chip, we tracked the insulin secretion every 15 min via multisampling. A first significant insulin decrease was observed during the synchronization phase from standard media culture to Krebs buffer. Insulin present in the normal culture media may impact the secretory capacity of β-cells [69], which is why Krebs buffer, which does not contain insulin, was used in our study in order to trigger the release of pre-existing insulin vesicles, while inhibiting further insulin translation as no glucose is present. At 20 mM glucose, the pseudo-islets significantly increased their insulin production within the first 30 min and maintained a higher level of insulin secretion for an additional 30 min. This insulin secretion profile is comparable to some extent to isolated human Langerhans islet biphasic glucose response [68]. The major release of insulin occurred in the first phase of 10 min. The second phase of insulin secretion was shown to stay higher than the basal level for 110 min. In this study, the second phase of insulin secretion lasted for half of the time when compared to isolated human Langerhans islets.

Although the EndoC-βH3 cell line represents a considerable advancement for human-based models of pancreatic β-cells, limitations in the secretory capacity, i.e. amplitude and duration of the second phase of insulin secretion should be considered. Future applications of our pancreas-on-a-chip aim to incorporate human pluripotent stem cell-derived β-cells, which so far have been limited in terms of maturation, but for which progressively

Please cite this article as: A. Zbinden, J. Marzi, K. Schlünder, et al., Non-invasive marker-independent high content analysis of a microphysiological human pancreas-on-a-chip model, Matrix Biology, https://doi.org/10.1016/j.matbio.2019.06.008

more advanced differentiation protocols are being developed, resulting in almost mature phenotypes, including dynamic glucose responsivity [70].

Integrating our pancreas-on-a-chip with Raman microspectroscopy provides a powerful tool for non-destructive and marker-independent in situ assessment of pseudo-islet performance. Indeed, addition of fluorescent dyes in many studies (i.e. for calcium imaging) or biologicals is debatable, as it may impact the overall cell metabolism [12,13,71]. Furthermore, any additives to the standard culture methods would prohibit any further use of the biological materials in vivo (i.e. transplantation). Raman imaging allowed for in-depth molecular characterization of pseudo-islet structures under different conditions based on highly specific spectral fingerprints. Moreover, it enabled real-time monitoring of glucose response. Based on high-resolution spectral maps, different molecular structures such as lipids, mitochondria or nuclei, were identified and quantified by TCA, by which a higher mitochondrial activity in glucose-stimulated pseudo-islets was revealed. Mitochondrial activation and metabolism have been reported to play a fundamental role in stimulating insulin secretion [72,73]. In-depth molecular analysis of the lipid composition in Krebs buffer and glucose-treated samples was enabled by PCA. Rapid remodeling of the lipids in the intracellular membrane of insulin secretory vesicles together with an increase in overall metabolism are required during insulin exocytosis [74]. The precise composition and role of lipid changes during glucose stimulation has recently been described by MacDonald et al., who demonstrated that predominantly phosphatidylserine and PI3 increased in insulin secretory vesicles [54]. Our PCA results of the lipids detected in the pancreas-on-a-chip in Krebs buffer and under glucose stimulation are in line with these findings by indicating a higher amount of PI3 in the lipid composition of pseudo-islets in 20 mM glucose solution. High-resolution imaging that enables the visualization and molecular characterization of the structures in the pseudo-islets, is relatively time-consuming (approximately 1 h per pseudo-islet). By limiting the data acquisition to a cross section of the pseudo-islet and a lower pixel resolution of 90 spectra per image, we could achieve a real-time monitoring of the pseudo-islet performance during media switch from Krebs buffer to 20 mM glucose solution. Combined with multivariate analysis, we were able to identify a biomarker that indicates a glucose response in the pancreas-on-a-chip.

The Raman analysis did not focus on direct insulin detection, but rather the definition of an overall Raman fingerprint as biomarker for glucose-induced metabolic effects on the pseudo-islets. In static conditions and tissue sections, it has been shown that Raman microspectroscopy is sensitive enough to image insulin and glucagon in human Langerhans islets [57]. We hypothesize that in our study, insulin detection was limited due to the dynamic conditions in the chip and the physiological wash-out of the secreted insulin. However, one further application of the on-chip Raman could focus on the analysis of the outflow liquid to detect secreted biomarkers. A recent study by Cho et al. applied surface-enhanced Raman microscopy, a signal-enhancing Raman technique, to determine pseudo-islet performance according to the detection of secreted insulin [75]. However, they used the phenylalanine peak at 1001 cm^{-1} as reference peak, which needs to be discussed carefully, because phenylalanine is the most prevalent amino acid, which does not only occur in insulin but in numerous proteins [76]. Moreover, in the future, a PDMS-free chip fabricated out of a less scattering material, such as glass, would be beneficial. The PDMS of the chip caused an intense Raman scattering and predominant peaks. Particularly the strong peak at 498 cm^{-1} overlapped the most characteristic insulin peak at 512 cm^{-1}, which is assigned to the disulfide bonds in insulin and prevented the quantitative assessment of insulin. Biomechanical stress, such as flow, strain and compression has been demonstrated to induce numerous effects on cells and tissues [82–86]. Lock et al. showed an increased MIN6 β-cells response to glucose with pseudo-islets cultured in a stirred suspension culture when compared to static controls [87]. While the role of perfusion in this study was not yet to influence pseudo-islet function via biomechanical flow, the continuous flow in the pancreas-on-a-chip on the one hand allowed trapping of single islets, and the analysis of single pseudo-islets over time and under different media conditions. On the other hand, the flow enabled precisely controllable (constant) media conditions for the islets due to the continuous delivery of fresh nutrients, oxygen and further dissolved molecules as well as the removal of secreted and metabolized products. Moreover, the immobilization of the pseudo-islets offered the capability of long measurements, which were not possible in a standard cell culture dish. The underlying microfluidics and vasculature-like perfusion of the pancreas-on-a-chip provided a further significant benefit: it paves the way for the integration with further organ systems to multi-organ platforms, for instance, by combining the pancreas-chip with adipose, brain, and/or liver, blood-on-a-chip systems [77–81]. These platforms can recapitulate inter-organ crosstalk and systemic effects, thereby providing powerful tools to study complex diseases such as diabetes.

Conclusion

We developed a microfluidic platform and integrated it with a Raman microspectroscope system

Please cite this article as: A. Zbinden, J. Marzi, K. Schlünder, et al., Non-invasive marker-independent high content analysis of a microphysiological human pancreas-on-a-chip model, Matrix Biology, https://doi.org/10.1016/j.matbio.2019.06.008

for the non-invasive monitoring of human pseudo-islets in biomechanical flow conditions. Pseudo-islet glucose response was assessed via multisampling, which demonstrated a beta-cell dynamic biphasic response. Additionally, Raman microspectroscopy analysis identified molecular markers, such as PI3, which were used to assess glucose response in situ. The here presented microfluidic platform with integrated optics demonstrates the advantages of combining interdisciplinary engineering solutions to solve problems such as the quality control of biologics pre-implantation and the online monitoring of biological processes for mechanistic studies. Furthermore, our integrated pancreas-on-a-chip platform is a blueprint for future generations of OoC systems in areas beyond pancreas and diabetes research.

Author contributions

A.Z., J.M., S.L.L., K.S.-L. and P.L. wrote the manuscript. Pancreas-on-a-chip design and fabrication were performed by K.S., C.P. and S.B. Pseudo-islet culture and experiments were conducted by A. Z. and M.U., and Raman microspectroscopy and analysis were performed by A.Z. and J.M.. E.M.B., S. L.L., U.K., G.D., K.S-L. and P.L. provided conceptual input and supervised the research.

Declaration of Competing Interests

The authors declare no competing financial interest.

CRediT authorship contribution statement

Aline Zbinden: Conceptualization, Formal analysis, Investigation, Methodology, Data curation, Writing - review & editing. **Julia Marzi:** Conceptualization, Formal analysis, Investigation, Methodology, Data curation, Writing - review & editing. **Katharina Schlünder:**Investigation, Methodology, Writing - review & editing.**Christopher Probst:**Data curation, Supervision, Writing - review & editing.**Max Urbanczyk:**Investigation, Methodology, Writing - review & editing.**Scott Black:**Investigation, Methodology.**Eva M. Brauchle:**Supervision, Writing - review & editing.**Shannon L. Layland:** Supervision, Writing - review & editing.**Udo Kraushaar:**Supervision, Writing - review & editing. **Garry Duffy:**Supervision, Writing - review & editing.**Katja Schenke-Layland:**Conceptualization, Supervision, Funding acquisition, Writing - review & editing.**Peter Loskill:**Conceptualization, Supervision, Funding acquisition, Writing - review & editing.

Acknowledgements

The research was supported by the European Union's Horizon 2020 research and innovation programme under the grant agreement number 645991-2 (to K.S.-L. & G.P.D) and 766884 (to P. L.), and the Ministry of Science, Research and Art Baden-Württemberg (33-729.55-3/214-8 to K.S.-L. and 7542.2-501-1/13/6 to P.L.).

Appendix A. Supplementary data

Supplementary data to this article can be found online at https://doi.org/10.1016/j.matbio.2019.06.008.

Received 30 March 2019;
Received in revised form 20 June 2019;
Accepted 20 June 2019
Available online xxxx

Keywords:
Organ-on-a-chip;
Raman spectroscopy;
Raman imaging;
Pancreatic islets;
Diabetes;
Insulin secretion

Authors contributed equally.

used:
, .

References

[1] F.M. Ashcroft, P. Rorsman, Diabetes mellitus and the β cell: the last ten years, Cell 148 (6) (2012) 1160–1171.
[2] N. Cho, J. Shaw, S. Karuranga, Y. Huang, J. da Rocha Fernandes, A. Ohlrogge, B. Malanda, IDF diabetes atlas: global estimates of diabetes prevalence for 2017 and projections for 2045, Diabetes Res. Clin. Pract. 138 (2018) 271–281.
[3] K. Sigmundsson, J.R.M. Ojala, M.K. Öhman, A.M. Österholm, A. Moreno-Moral, A. Domogatskaya, L.Y. Chong, Y. Sun, X. Chai, J.A.M. Steele, B. George, M. Patarroyo, A.S. Nilsson, S. Rodin, S. Ghosh, M.M. Stevens, E. Petretto, K. Tryggvason, Culturing functional pancreatic islets on α5-laminins and curative transplantation to diabetic mice, Matrix Biol. 70 (2018) 5–19.
[4] J.M. Forbes, M.E. Cooper, Mechanisms of diabetic complications, Physiol. Rev. 93 (1) (2013) 137–188.
[5] R.A. DeFronzo, E. Ferrannini, L. Groop, R.R. Henry, W.H. Herman, J.J. Holst, F.B. Hu, C.R. Kahn, I. Raz, G.I. Shulman,

Please cite this article as: A. Zbinden, J. Marzi, K. Schlünder, et al., Non-invasive marker-independent high content analysis of a microphysiological human pancreas-on-a-chip model, Matrix Biology, https://doi.org/10.1016/j.matbio.2019.06.008

Type 2 diabetes mellitus, Nat. Rev. Dis. Primers. 1 (2015) 15019.
[6] J.-S. Yun, S.-H. Ko, Risk factors and adverse outcomes of severe hypoglycemia in type 2 diabetes mellitus, Diabetes Metab. J. 40 (6) (2016) 423–432.
[7] P.C. Chandrasekera, J.J. Pippin, Of rodents and men: species-specific glucose regulation and type 2 diabetes research, ALTEX 31 (2) (2014) 157–176.
[8] T. Schulze, K. Mattern, E. Früh, L. Hecht, I. Rustenbeck, A. Dietzel, A 3D microfluidic perfusion system made from glass for multiparametric analysis of stimulus-secretion coupling in pancreatic islets, Biomed. Microdevices 19 (3) (2017) 47.
[9] X. Li, J.C. Brooks, J. Hu, K.I. Ford, C.J. Easley, 3D-templated, fully automated microfluidic input/output multiplexer for endocrine tissue culture and secretion sampling, Lab Chip 17 (2) (2017) 341–349.
[10] J.C. Brooks, K.I. Ford, D.H. Holder, M.D. Holtan, C.J. Easley, Macro-to-micro interfacing to microfluidic channels using 3D-printed templates: application to time-resolved secretion sampling of endocrine tissue, Analyst 141 (20) (2016) 5714–5721.
[11] J.S. Mohammed, Y. Wang, T.A. Harvat, J. Oberholzer, D.T. Eddington, Microfluidic device for multimodal characterization of pancreatic islets, Lab Chip 9 (1) (2009) 97–106.
[12] S.H. Lee, S. Hong, J. Song, B. Cho, E.J. Han, S. Kondapavulur, D. Kim, L.P. Lee, Microphysiological analysis platform of pancreatic islet β-cell spheroids, Adv. Healthc. Mater. 7 (2) (2018) 1701111.
[13] Y. Xing, M. Nourmohammadzadeh, J.E.M. Elias, M. Chan, Z. Chen, J.J. McGarrigle, J. Oberholzer, Y. Wang, A pumpless microfluidic device driven by surface tension for pancreatic islet analysis, Biomed. Microdevices 18 (5) (2016) 80.
[14] M.J. MacDonald, M.J. Longacre, S.W. Stoker, M.A. Kendrick, A. Thonpho, L.J. Brown, N.M. Hasan, S. Jitrapakdee, T. Fukao, M.S. Hanson, Differences between human and rodent pancreatic islets: low pyruvate carboxylase, ATP citrate lyase and pyruvate carboxylation; high glucose-stimulated acetoacetate in human pancreatic islets, Journal of Biological Chemistry 286 (21) (2011) 18383–18396, https://doi.org/10.1074/jbc.M111.241182 (jbc. M111. 241182).
[15] J. Dolenšek, M.S. Rupnik, A. Stožer, Structural similarities and differences between the human and the mouse pancreas, Islets 7 (1) (2015), e1024405.
[16] J.S. Kaddis, B.J. Olack, J. Sowinski, J. Cravens, J.L. Contreras, J.C. Niland, Human pancreatic islets and diabetes research, Jama 301 (15) (2009) 1580–1587.
[17] M. Skelin, M. Rupnik, A. Cencič, Pancreatic beta cell lines and their applications in diabetes mellitus research, ALTEX 27 (2) (2010) 105–113.
[18] M. Benazra, M.-J. Lecomte, C. Colace, A. Müller, C. Machado, S. Pechberty, E. Bricout-Neveu, M. Grenier-Godard, M. Solimena, R. Scharfmann, A human beta cell line with drug inducible excision of immortalizing transgenes, Mol. Metab. 4 (12) (2015) 916–925.
[19] S. Ricard-Blum, G. Baffet, N. Théret, Molecular and tissue alterations of collagens in fibrosis, Matrix Biol. 68-69 (2018) 122–149.
[20] J.W. Ager III, M.D. Drory, Quantitative measurement of residual biaxial stress by Raman spectroscopy in diamond grown on a Ti alloy by chemical vapor deposition, Phys. Rev. B 48 (4) (1993) 2601.
[21] T. De Beer, A. Burggraeve, M. Fonteyne, L. Saerens, J.P. Remon, C. Vervaet, Near infrared and Raman spectroscopy for the in-process monitoring of pharmaceutical production processes, Int. J. Pharm. 417 (1) (2011) 32–47.
[22] Y. Wang, D.C. Alsmeyer, R.L. McCreery, Raman spectroscopy of carbon materials: structural basis of observed spectra, Chem. Mater. 2 (5) (1990) 557–563.
[23] S. Dochow, C. Krafft, U. Neugebauer, T. Bocklitz, T. Henkel, G. Mayer, J. Albert, J. Popp, Tumour cell identification by means of Raman spectroscopy in combination with optical traps and microfluidic environments, Lab Chip 11 (8) (2011) 1484–1490.
[24] C.W. Freudiger, W. Min, B.G. Saar, S. Lu, G.R. Holtom, C. He, J.C. Tsai, J.X. Kang, X.S. Xie, Label-free biomedical imaging with high sensitivity by stimulated Raman scattering microscopy, Science 322 (5909) (2008) 1857–1861.
[25] E. Brauchle, S. Thude, S.Y. Brucker, K. Schenke-Layland, Cell Death Stages in Single Apoptotic and Necrotic Cells Monitored by Raman Microspectroscopy, Scientific Reports 4, 2014.
[26] J. Marzi, A.C. Biermann, E.M. Brauchle, K.G. Brockbank, U. A. Stock, K. Schenke-Layland, Marker-independent in situ quantitative assessment of residual cry-oprotectants in cardiac tissues, Anal. Chem. 91 (3) (2019) 2266–2272, https://doi.org/10.1021/acs.analchem.8b04861.
[27] E. Brauchle, J. Kasper, R. Daum, N. Schierbaum, C. Falch, A. Kirschniak, T.E. Schäffer, K. Schenke-Layland, Biomechanical and biomolecular characterization of extracellular matrix structures in human colon carcinomas, Matrix Biol. 68 (2018) 180–193.
[28] M. Roman, A. Kamińska, A. Drożdż, M. Platt, M. Kuźniewski, M.T. Małecki, W. Kwiatek, C. Paluszkiewicz, E.Ł. Stępień, Raman Spectral Signatures of Urinary Extracellular Vesicles From Diabetic Patients and Hyperglycemic Endothelial Cells as Potential Biomarkers in Diabetes, Nanomedicine, Nanotechnology, Biology and Medicine, 2019.
[29] L. Šťovíčková, M. Tatarkovič, H. Logerová, J. Vavřinec, V. Setnička, Identification of spectral biomarkers for type 1 diabetes mellitus using the combination of chiroptical and vibrational spectroscopy, Analyst 140 (7) (2015) 2266–2272.
[30] Y. Zou, M. Huang, K. Wang, B. Song, Y. Wang, J. Chen, X. Liu, X. Li, L. Lin, G. Huang, Urine surface-enhanced Raman spectroscopy for non-invasive diabetic detection based on a portable Raman spectrometer, Laser Phys. Lett. 13 (6) (2016), 065604.
[31] J. Marzi, E.M. Brauchle, K. Schenke-Layland, M.W. Rolle, Non-invasive functional molecular phenotyping of human smooth muscle cells utilized in cardiovascular tissue engineering, Acta Biomater. 89 (2019) 193–205, https://doi.org/10.1016/j.actbio.2019.03.026.
[32] M. Pudlas, D.A.C. Berrio, M. Votteler, S. Koch, S. Thude, H. Walles, K. Schenke-Layland, Non-contact discrimination of human bone marrow-derived mesenchymal stem cells and fibroblasts using Raman spectroscopy, Med. Laser Appl. 26 (3) (2011) 119–125.
[33] W.-H. Tan, S. Takeuchi, A trap-and-release integrated microfluidic system for dynamic microarray applications, Proc. Natl. Acad. Sci. 104 (4) (2007) 1146–1151.
[34] K. Czamara, K. Majzner, M.Z. Pacia, K. Kochan, A. Kaczor, M. Baranska, Raman spectroscopy of lipids: a review, J. Raman Spectrosc. 46 (1) (2015) 4–20.
[35] C. Matthäus, T. Chernenko, J.A. Newmark, C.M. Warner, M. Diem, Label-free detection of mitochondrial distribution in cells by nonresonant Raman microspectroscopy, Biophys. J. 93 (2) (2007) 668–673.
[36] H. Tang, H. Yao, G. Wang, Y. Wang, Y.-q. Li, M. Feng, NIR Raman spectroscopic investigation of single mitochondria

Please cite this article as: A. Zbinden, J. Marzi, K. Schlünder, et al., Non-invasive marker-independent high content analysis of a microphysiological human pancreas-on-a-chip model, Matrix Biology, https://doi.org/10.1016/j.matbio.2019.06.008

trapped by optical tweezers, Opt. Express 15 (20) (2007) 12708–12716.
[37] K. Klein, A.M. Gigler, T. Aschenbrenner, R. Monetti, W. Bunk, F. Jamitzky, G. Morfill, R.W. Stark, J. Schlegel, Label-free live-cell imaging with confocal Raman microscopy, Biophys. J. 102 (2) (2012) 360–368.
[38] I. Notingher, C. Green, C. Dyer, E. Perkins, N. Hopkins, C. Lindsay, L.L. Hench, Discrimination between ricin and sulphur mustard toxicity in vitro using Raman spectroscopy, J. R. Soc. Interface 1 (1) (2004) 79–90.
[39] R.K. Dukor, Vibrational Spectroscopy in the Detection of Cancer, Handbook of Vibrational Spectroscopy, John Wiley & Sons, Ltd, 2006.
[40] Y. Chen, J. Dai, X. Zhou, Y. Liu, W. Zhang, G. Peng, Raman spectroscopy analysis of the biochemical characteristics of molecules associated with the malignant transformation of gastric mucosa, PLoS One 9 (4) (2014), e93906.
[41] C. Krafft, L. Neudert, T. Simat, R. Salzer, Near infrared Raman spectra of human brain lipids, Spectrochim. Acta A Mol. Biomol. Spectrosc. 61 (7) (2005) 1529–1535.
[42] N. Stone, C. Kendall, J. Smith, P. Crow, H. Barr, Raman spectroscopy for identification of epithelial cancers, Faraday Discuss. 126 (2004) 141–157.
[43] K. Czamara, K. Majzner, A. Selmi, M. Baranska, Y. Ozaki, A. Kaczor, Unsaturated lipid bodies as a hallmark of inflammation studied by Raman 2D and 3D microscopy, Sci. Rep. 7 (2017) 40889.
[44] G. Shetty, C. Kendall, N. Shepherd, N. Stone, H. Barr, Raman spectroscopy: elucidation of biochemical changes in carcinogenesis of oesophagus, Br. J. Cancer 94 (10) (2006) 1460.
[45] Z. Huang, A. McWilliams, H. Lui, D.I. McLean, S. Lam, H. Zeng, Near-infrared Raman spectroscopy for optical diagnosis of lung cancer, Int. J. Cancer 107 (6) (2003) 1047–1052.
[46] N.A. Brazhe, A.B. Evlyukhin, E.A. Goodilin, A.A. Semenova, S.M. Novikov, S.I. Bozhevolnyi, B.N. Chichkov, A.S. Sarycheva, A.A. Baizhumanov, E.I. Nikelshparg, Probing cytochrome c in living mitochondria with surface-enhanced Raman spectroscopy, Sci. Rep. 5 (2015) 13793.
[47] S. Dai, X. Zhang, Z. Du, Y. Huang, H. Dang, Structural properties and Raman spectroscopy of lipid Langmuir monolayers at the air–water interface, Colloids Surf. B: Biointerfaces 42 (1) (2005) 21–28.
[48] J.W. Chan, D.S. Taylor, T. Zwerdling, S.M. Lane, K. Ihara, T. Huser, Micro-Raman spectroscopy detects individual neoplastic and normal hematopoietic cells, Biophys. J. 90 (2) (2006) 648–656.
[49] W.T. Cheng, M.T. Liu, H.N. Liu, S.Y. Lin, Micro-Raman spectroscopy used to identify and grade human skin pilomatrixoma, Microsc. Res. Tech. 68 (2) (2005) 75–79.
[50] E. Hanlon, R. Manoharan, T.W. Koo, K. Shafer, J. Motz, M. Fitzmaurice, J. Kramer, I. Itzkan, R. Dasari, M. Feld, Prospects for in vivo Raman spectroscopy, Phys. Med. Biol. 45 (2) (2000) R1.
[51] J. Wang, K.M. Koo, E.J. Wee, Y. Wang, M. Trau, A nanoplasmonic label-free surface-enhanced Raman scattering strategy for non-invasive cancer genetic subtyping in patient samples, Nanoscale 9 (10) (2017) 3496–3503.
[52] N. Erjavec, G. Pinato, K. Ramser, Raman spectroscopy as a tool for detecting mitochondrial fitness, J. Raman Spectrosc. 47 (8) (2016) 933–939.
[53] A. Gualerzi, S. Niada, C. Giannasi, S. Picciolini, C. Morasso, R. Vanna, V. Rossella, M. Masserini, M. Bedoni, F. Ciceri, Raman spectroscopy uncovers biochemical tissue-related features of extracellular vesicles from mesenchymal stromal cells, Sci. Rep. 7 (1) (2017) 9820.
[54] M.J. MacDonald, L. Ade, J.M. Ntambi, I.-U.H. Ansari, S.W. Stoker, Characterization of phospholipids in insulin secretory granules and mitochondria in pancreatic beta cells and their changes with glucose stimulation, J. Biol. Chem. 290 (17) (2015) 11075–11092.
[55] S.G. Straub, G.W. Sharp, Glucose-stimulated signaling pathways in biphasic insulin secretion, Diabetes Metab. Res. Rev. 18 (6) (2002) 451–463.
[56] R.J. Lakshmi, V. Kartha, C. Murali Krishna, J.R. Solomon, G. Ullas, P. Uma Devi, Tissue Raman spectroscopy for the study of radiation damage: brain irradiation of mice, Radiat. Res. 157 (2) (2002) 175–182.
[57] J. Hilderink, C. Otto, C. Slump, A. Lenferink, M. Engelse, C. van Blitterswijk, E. de Koning, M. Karperien, A. van Apeldoorn, Label-free detection of insulin and glucagon within human islets of Langerhans using Raman spectroscopy, PLoS One 8 (10) (2013), e78148.
[58] N.-T. Yu, C. Liu, D. O'shea, Laser Raman spectroscopy and the conformation of insulin and proinsulin, J. Mol. Biol. 70 (1) (1972) 117–132.
[59] M. Gniadecka, H. Wulf, N. Nymark Mortensen, O. Faurskov Nielsen, D.H. Christensen, Diagnosis of basal cell carcinoma by Raman spectroscopy, J. Raman Spectrosc. 28 (2–3) (1997) 125–129.
[60] V. Sereda, N.M. Ralbovsky, M.C. Vasudev, R.R. Naik, I.K. Lednev, Polarized Raman spectroscopy for determining the orientation of di-d-phenylalanine molecules in a nanotube, J. Raman Spectrosc. 47 (9) (2016) 1056–1062.
[61] J. Shao, M. Lin, Y. Li, X. Li, J. Liu, J. Liang, H. Yao, In vivo blood glucose quantification using Raman spectroscopy, PLoS One 7 (10) (2012), e48127.
[62] S. Gamsjaeger, K. Klaushofer, E.P. Paschalis, Raman analysis of proteoglycans simultaneously in bone and cartilage, J. Raman Spectrosc. 45 (9) (2014) 794–800.
[63] J. Rogal, A. Zbinden, K. Schenke-Layland, P. Loskill, Stem-cell based organ-on-a-chip models for diabetes research, Adv. Drug Deliv. Rev. (2018)https://doi.org/10.1016/j.addr.2018.10.010 (in press).
[64] S.N. Bhatia, D.E. Ingber, Microfluidic organs-on-chips, Nat. Biotechnol. 32 (8) (2014) 760.
[65] Y. Zhao, N. Rafatian, E.Y. Wang, N.T. Feric, B.F. Lai, E.J. Knee-Walden, P.H. Backx, M. Radisic, Engineering microenvironment for human cardiac tissue assembly in heart-on-a-chip platform, Matrix Biol. (2019)https://doi.org/10.1016/j.matbio.2019.04.001 (in press).
[66] N. Kojima, In vitro reconstitution of pancreatic islets, Organogenesis 10 (2) (2014) 225–230.
[67] Y. Ichihara, R. Utoh, M. Yamada, T. Shimizu, Y. Uchigata, Size effect of engineered islets prepared using microfabricated wells on islet cell function and arrangement, Heliyon 2 (6) (2016), e00129.
[68] J.-C. Henquin, D. Dufrane, J. Kerr-Conte, M. Nenquin, Dynamics of glucose-induced insulin secretion in normal human islets, Am. J. Physiol. Endocrinol. Metab. 309 (7) (2015) E640–E650.
[69] I.B. Leibiger, B. Leibiger, P.-O. Berggren, Insulin signaling in the pancreatic β-cell, Annu. Rev. Nutr. 28 (2008) 233–251.
[70] L. Velazco-Cruz, J. Song, K.G. Maxwell, M.M. Goedegebuure, P. Augsornworawat, N.J. Hogrebe, J.R. Millman, Acquisition of dynamic function in human stem cell-derived β cells, Stem Cell Rep. 12 (2) (2019) 351–365, https://doi.org/10.1016/j.stemcr.2018.12.012.

Please cite this article as: A. Zbinden, J. Marzi, K. Schlünder, et al., Non-invasive marker-independent high content analysis of a microphysiological human pancreas-on-a-chip model, Matrix Biology, https://doi.org/10.1016/j.matbio.2019.06.008

[71] M. Nourmohammadzadeh, Y. Xing, J.W. Lee, M.A. Bochenek, J.E. Mendoza-Elias, J.J. McGarrigle, E. Marchese, Y. Chun-Chieh, D.T. Eddington, J. Oberholzer, A microfluidic array for real-time live-cell imaging of human and rodent pancreatic islets, Lab Chip 16 (8) (2016) 1466–1472.
[72] P. Maechler, C.B. Wollheim, Mitochondrial signals in glucose-stimulated insulin secretion in the beta cell, J. Physiol. 529 (1) (2000) 49–56.
[73] R.G. Kibbey, R.L. Pongratz, A.J. Romanelli, C.B. Wollheim, G.W. Cline, G.I. Shulman, Mitochondrial GTP regulates glucose-stimulated insulin secretion, Cell Metab. 5 (4) (2007) 253–264.
[74] P. Maechler, S. Carobbio, B. Rubi, In beta-cells, mitochondria integrate and generate metabolic signals controlling insulin secretion, Int. J. Biochem. Cell Biol. 38 (5–6) (2006) 696–709.
[75] H. Cho, S. Kumar, D. Yang, S. Vaidyanathan, K. Woo, I. Garcia, H.J. Shue, Y. Yoon, K. Ferreri, H. Choo, Surface-enhanced Raman spectroscopy-based label-free insulin detection at physiological concentrations for analysis of islet performance, ACS Sensors 3 (1) (2018) 65–71.
[76] S.P. Fodor, R.A. Copeland, C.A. Grygon, T.G. Spiro, Deep-ultraviolet Raman excitation profiles and vibronic scattering mechanisms of phenylalanine, tyrosine, and tryptophan, J. Am. Chem. Soc. 111 (15) (1989) 5509–5518.
[77] J. Rogal, C. Probst, P. Loskill, Integration concepts for multi-organ chips: how to maintain flexibility?! Future Sci. OA 3 (2) (2017), FSO180.
[78] M.B. Esch, A.S. Smith, J.-M. Prot, C. Oleaga, J.J. Hickman, M.L. Shuler, How multi-organ microdevices can help foster drug development, Adv. Drug Deliv. Rev. 69 (2014) 158–169.
[79] J. Rogal, C. Binder, E. Kromidas, C. Probst, S. Schneider, K. Schenke-Layland, P. Loskill, WAT's up!?–Organ-on-a-chip integrating human mature white adipose tissues for mechanistic research and pharmaceutical applications, bioRxiv (2019), 585141. https://doi.org/10.1101/585141.
[80] K. Rennert, S. Steinborn, M. Gröger, B. Ungerböck, A.-M. Jank, J. Ehgartner, S. Nietzsche, J. Dinger, M. Kiehntopf, H. Funke, A microfluidically perfused three dimensional human liver model, Biomaterials 71 (2015) 119–131.
[81] D. Soscia, A. Belle, N. Fischer, H. Enright, A. Sales, J. Osburn, W. Benett, E. Mukerjee, K. Kulp, S. Pannu, Controlled placement of multiple CNS cell populations to create complex neuronal cultures, PLoS One 12 (11) (2017), e0188146.
[82] P. Ringer, G. Colo, R. Fässler, C. Grashoff, Sensing the mechano-chemical properties of the extracellular matrix, Matrix Biol. 64 (2017) 6–16.
[83] O.V. Kim, R.I. Litvinov, J. Chen, D.Z. Chen, J.W. Weisel, M.S. Alber, Compression-induced structural and mechanical changes of fibrin-collagen composites, Matrix Biol. 60-61 (2017) 141–156.
[84] R. Cruz-Acuña, A.J. García, Synthetic hydrogels mimicking basement membrane matrices to promote cell-matrix interactions, Matrix Biol. 57-58 (2017) 324–333.
[85] A.J. Haak, Q. Tan, D.J. Tschumperlin, Matrix biomechanics and dynamics in pulmonary fibrosis, Matrix Biol. 73 (2018) 64–76.
[86] D. Chester, A.C. Brown, The role of biophysical properties of provisional matrix proteins in wound repair, Matrix Biol. 60-61 (2017) 124–140.
[87] L.T. Lock, S.G. Laychock, E.S. Tzanakakis, Pseudoislets in stirred-suspension culture exhibit enhanced cell survival, propagation and insulin secretion, J. Biotechnol. 51 (3) (2011) 278–286.

Please cite this article as: A. Zbinden, J. Marzi, K. Schlünder, et al., Non-invasive marker-independent high content analysis of a microphysiological human pancreas-on-a-chip model, Matrix Biology, https://doi.org/10.1016/j.matbio.2019.06.008

Supplement

Hydrodynamic trapping mechanims for guided immobilization of islets

The resistance of the loop channel (Q2) must exceed that of the trap channel (Q1) such that islets will be dragged into the trap structure and immobilized. Once immobilized, the islet will block the trap channel, increasing the resistance of this fluid path to near infinite and thus subsequent islets will follow the loop channel until reaching a subsequently empty trap.

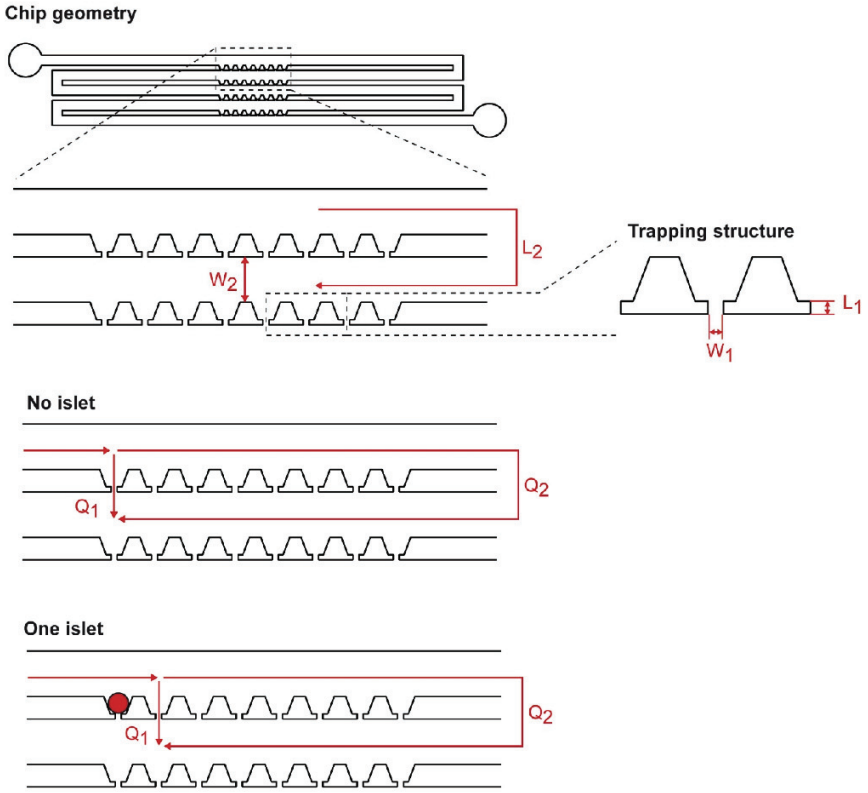

Supplemental Figure 1: Schematic of microfluidic chip and trapping structure. If the ration Q1/Q2 > 1 islets are guided into the trapping channel while other islets can bypass the occupied trap and travel along the loop channel to the next empty trap.

Trapping Efficacy

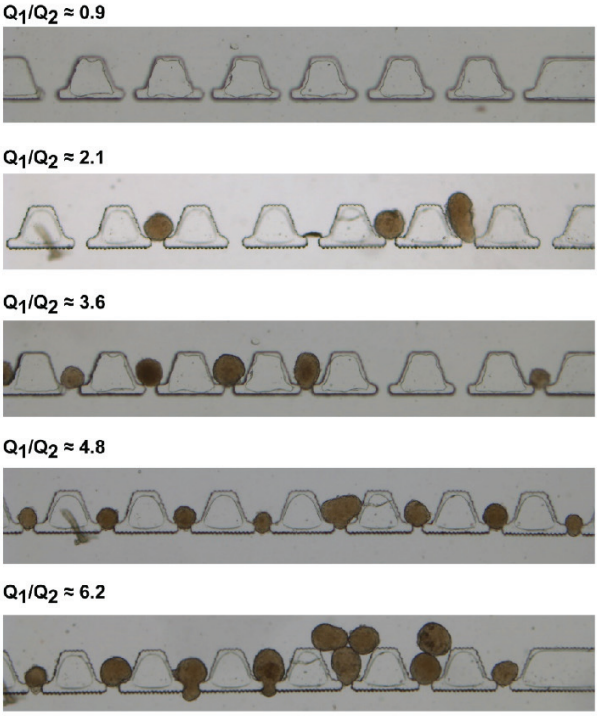

Supplemental Figure 2: Trapping efficancy at varring volumetric flow rates

Equations

As described by Takeuchi and co-workers [1], using the Darcy-Weisbach equation and thus solving the continuity and momentum equation for the Hagen-Poisueille problem we can describe the pressure drop in a microfluidic channel as

$$\Delta p = \frac{f L \rho V^2}{2D} \quad (Eq.\,1)$$

where Δp is the pressure drop, f is the Darcy friction factor, ρ is the density of the fluid, v is the average fluid velocity and D is the hydrodynamic diameter of the channel.

The Reynolds number of such a flow regime is described by:

$$Re = \frac{\rho V D}{\mu} \quad (Eq.\,2)$$

where μ is the dynamic viscosity of the fluid. Thus, by combining Eq.1 and Eq.2, one can obtain:

$$\Delta p = \frac{f L V Re \mu}{2D^2} \quad (Eq.\,3)$$

where D is described as a function of the cross sectional area A and the perimeter P:

$$D = \frac{4A}{P} \quad (Eq.\,4)$$

Thus, combining Eq.3 and Eq.4 yields:

$$\Delta p = \frac{f L V Re \mu}{\frac{32A^2}{P^2}} \quad (Eq.\,5)$$

V can further be expressed as volumetric flow rate Q and cross sectional area A:

$$V = \frac{Q}{A} \quad (Eq.\,6)$$

where Q is the volumetric flow rate and A the cross sectional area. Now, combining Eq.5 and Eq.6 gives:

$$\Delta p = \frac{f L Q \mu Re P^2}{32A^3} \quad (Eq.\,7)$$

where $f \times Re$ is a function of both the Reynolds number and the aspect ratio, $\propto$, such that $0 < \propto < 1$, and is defined as a constant $C_n(\propto_n)$:

$$C_n(\propto_n) = 96(1 - 1.3553\ \propto_n + 1.9467\ \propto_n^2 - 1.7012\ \propto_n^3 + 0.9564\ \propto_n^4 - 0.2537\ \propto_n^5) \quad (Eq.\,8)$$

Since the pressure drop between two points in a channel are equal, regardless of the route taken, $\Delta p_1 = \Delta p_2$, and hence:

$$\frac{C_1(\propto_1)L_1Q_1\mu{P_1}^2}{32{A_1}^3} = \frac{C_2(\propto_2)L_2\mu{P_2}^2}{32{A_2}^3} \quad (\text{Eq. } 9)$$

Thus,

$$C_1(\propto_1)L_1Q_1{P_1}^2{A_2}^3 = C_2(\propto_2)L_2Q_2{P_2}^2{A_1}^3 \quad (\text{Eq. } 10)$$

In order to achieve trapping, the flow rate through the trap channels Q_1 must exceed that of the loop channels Q_2. Thus, $Q_1 > Q_2$.

$$\frac{Q_1}{Q_2} = \frac{C_2(\propto_2)L_2{P_2}^2{A_1}^3}{C_1(\propto_1)L_1{P_1}^2{A_2}^3} > 1 \quad (\text{Eq. } 11)$$

and, for a non-circular channel yielding following equation:

$$\frac{Q_1}{Q_2} = f(L, W, H) = \frac{C_2(\propto_2)L_2(W_2 + H)^2{W_1}^3}{C_1(\propto_1)L_1(W_1 + H)^2{W_2}^3} > 1 \quad (\text{Eq. } 12)$$

where W is the width of the channel and H is the height.

If $Q_1/Q_2 < 1$, islets should remain in the loop channel, bypassing the traps and flowing straight to the outlet. However, if $Q_1/Q_2 > 1$, the islets are forced into the traps.

Supplemental Table 1: Values for Q1/Q2 during the sequentiel loading of islets

H (µm)	W_1 (µm)	W_2 (µm)	L_1 (µm)	L_2 (µm)	$C_1(\alpha_1)$	$C_2(\alpha_2)$	Q_1	Q_2	$\frac{Q_1}{Q_2}$
250	60	450	50	14780	73.57	60.85	9.52E+16	3.22E+16	2.96
250	60	450	50	15420	73.57	60.85	9.93E+16	3.22E+16	3.08
250	60	450	50	16060	73.57	60.85	1.03E+17	3.22E+16	3.21
250	60	450	50	16700	73.57	60.85	1.08E+17	3.22E+16	3.34
250	60	450	50	17340	73.57	60.85	1.12E+17	3.22E+16	3.47
250	60	450	50	17980	73.57	60.85	1.16E+17	3.22E+16	3.60
250	60	450	50	17340	73.57	60.85	1.20E+17	3.22E+16	3.72
250	60	450	50	16700	73.57	60.85	1.24E+17	3.22E+16	3.85
250	60	450	50	16060	73.57	60.85	1.28E+17	3.22E+16	3.98
250	60	450	50	15420	73.57	60.85	1.32E+17	3.22E+16	4.11
250	60	450	50	14780	73.57	60.85	1.36E+17	3.22E+16	4.23

References

[1] W.-H. Tan and S. Takeuchi, "A trap-and-release integrated microfluidic system for dynamic microarray applications.," *Proc. Natl. Acad. Sci. U.S.A.*, vol. 104, no. 4, pp. 1146–51, 2007.

Appendix III: Zbinden A.§, Carvajal D.A.§, Urbanczyk M., Layland S.L., Bosch M., Fliri S., Lu C., Jeyagaran A., Loskill P., Duffy G.P. & Schenke-Layland K.; *Fluorescence lifetime metabolic mapping of hypoxia-induced damage in pancreatic pseudo-islets*, Journal of Biophotonics, 2020; e202000375.

Received: 16 September 2020 | Revised: 3 October 2020 | Accepted: 4 October 2020
DOI: 10.1002/jbio.202000375

JOURNAL OF BIOPHOTONICS

FULL ARTICLE

Fluorescence lifetime metabolic mapping of hypoxia-induced damage in pancreatic pseudo-islets

Aline Zbinden[1] | Daniel A. Carvajal Berrio[1,2] | Max Urbanczyk[1] | Shannon L. Layland[1] | Mariella Bosch[1] | Sandro Fliri[1] | Chuan-en Lu[1] | Abiramy Jeyagaran[1] | Peter Loskill[1,3] | Garry P. Duffy[4] | Katja Schenke-Layland[1,2,5,6]*

[1]Department of Women's Health, Research Institute for Women's Health, Eberhard Karls University Tübingen, Tübingen, Germany

[2]Cluster of Excellence iFIT (EXC 2180) "Image-Guided and Functionally Instructed Tumor Therapies", Eberhard Karls University Tübingen, Tübingen, Germany

[3]Fraunhofer IGB, Stuttgart, Germany

[4]Anatomy and Regenerative Medicine Institute, School of Medicine, College of Medicine Nursing and Health Sciences, National University of Ireland, Galway, Ireland

[5]NMI Natural and Medical Sciences Institute at the University of Tübingen, Reutlingen, Germany

[6]Department of Medicine/Cardiology, Cardiovascular Research Laboratories, David Geffen School of Medicine at UCLA, Los Angeles, California

***Correspondence**
Katja Schenke-Layland, NMI Natural and Medical Sciences Institute at the University of Tübingen, Markwiesenstr. 55, Reutlingen 72770, Germany.
Email: katja.schenke-layland@nmi.de, katja.schenke-layland@uni-tuebingen.de

Funding information
Deutsche Forschungsgemeinschaft, Grant/Award Number: INST 2388/33-1; Horizon 2020 Framework Programme, Grant/Award Numbers: H2020-ITN 766181, H2020-NMP10-2014-645991-2; International Foundation for Ethical Research; Ministry of Science, Research and the Arts of Baden-Württemberg, Grant/Award Numbers: 33-729.55-3/214, SI-BW 01222-91

Abstract

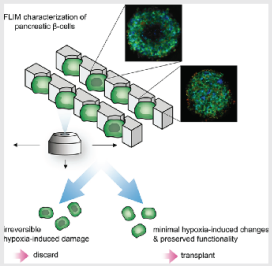

Pancreatic islet isolation from donor pancreases is an essential step for the transplantation of insulin-secreting β-cells as a therapy to treat type 1 diabetes mellitus. This process however damages islet basement membranes, which can lead to islet dysfunction or death. Posttransplantation, islets are further stressed by a hypoxic environment and immune reactions that cause poor engraftment and graft failure. The current standards to assess islet quality before transplantation are destructive procedures, performed on a small islet population that does not reflect the heterogeneity of large isolated islet batches. In this study, we incorporated

Abbreviations: BMIR, blood-mediated inflammatory reaction; ER, endoplasmic reticulum; FAD, flavin adenine dinucleotide; FDA, federal drug administration; FLIM, fluorescence lifetime imaging microscopy; GaAsP, gallium arsenide phosphide; GLUT, glucose transporter; GSIS, glucose-stimulated insulin secretion; HIF-1α, hypoxia-inducible factor 1α; MP, multiphoton; NA, numerical aperture; NADH, nicotinamide adenine dinucleotide; NADPH, nicotinamide adenine dinucleotide phosphate; NDD, nondescanned detection; PMT, photomultiplier tube; ROI, region of interest; ROS, reactive oxygen species; TCA, tricarboxylic acid; TCSPC, time-correlated single photon counting; VEGF, vascular endothelial growth factors.

Aline Zbinden and Daniel A. Carvajal Berrio contributed equally to this study.

fluorescence lifetime imaging microscopy (FLIM) into a pancreas-on-chip system to establish a protocol to noninvasively assess the viability and functionality of pancreatic β-cells in a three-dimensional in vitro model (= pseudo-islets). We demonstrate how (pre-) hypoxic β-cell-composed pseudo-islets can be discriminated from healthy functional pseudo-islets according to their FLIM-based metabolic profiles. The use of FLIM during the pretransplantation pancreatic islet selection process has the potential to improve the outcome of β-cell islet transplantation.

KEYWORDS

FLIM, hypoxia, insulin, pancreatic islet, type 1 diabetes

1 | INTRODUCTION

Islet transplantation is a promising therapy for type 1 diabetes [1]. However, insulin independency declines over time due to significant β-cell death posttransplantation [2]. Islet loss is due to multiple factors occurring pretransplantation and posttransplantation. Blood-mediated inflammatory reaction and hypoxia-associated damage are responsible for the majority of islet loss during intraportal transplantation [3, 4]. During the isolation of pancreatic islets, the pancreas is enzymatically and mechanically digested, resulting in the separation of exocrine and endocrine tissues [5, 6]. The damaged exocrine cells, including mainly acinar cells, can release proteolytic enzymes that further impair endocrine cells [7]. Moreover, the isolation process leads to the destruction of the vascular network and ultimately to the loss of oxygen supply posttransplantation. Exposure to severe hypoxia (1% oxygen) leads to β-cell dysfunction that can compromise glucose-stimulated insulin secretion (GSIS) [8]. The lack of oxygen forces β-cells to transition to anaerobic glycolysis, reducing their ability to respond to high glucose. Prolonged hypoxia permanently impacts β-cells via the hypoxia-inducible factor 1α (HIF-1α) dependent and independent pathways, resulting in ER stress and followed by apoptosis via the mitochondrial cell death pathway [9].

Regulatory bodies, such as the FDA, specify that isolated islets must meet specific standards prior to transplantation such as purity, viability, functionality and sterility [10]. Islet batch sampling may identify unsuitable batches for transplantation; however, approved batches may still contain islets that are damaged, hypoxic, or in a preapoptotic state. Moreover, the standard procedures to assess islet quality are destructive, such as immunofluorescence staining, which requires the addition of exogenous dyes [11]. Therefore, there is a need to develop noninvasive tools, which are able to rapidly assess the viability and functionality of a large batch of single islets prior to transplantation.

Fluorescence lifetime imaging microscopy (FLIM) is a powerful optical method that can probe changes in metabolic state in vitro and in vivo in real time, and can serve as diagnostic tools of pathological tissues in situ [12–14]. The time-dimensional characteristic of FLIM combined with multiphoton (MP) microscopy enables the visualization of endogenous nicotinamide adenine dinucleotide (NADH) and flavin adenine dinucleotide (FAD), and the discrimination between free and protein-bound forms based on their respective lifetimes [15]. Free NADH has a short fluorescence lifetime τ_1 (300-800 ps), while τ_2 of the protein-bound NADH is longer (1000-6500 ps). Similarly, free FAD has a longer fluorescence lifetime τ_2 (2300-2900 ps), and the lifetime of bound FAD τ_1 is shorter (300-455 ps). Based on the respective contribution of τ_1 (α_1) and the optical oxidative ratio (FAD/FAD + NADH), the metabolic equilibrium between glycolysis and oxidative phosphorylation can be evaluated in living cells. FLIM has been used to differentiate metabolic processes including proliferation, differentiation, metabolic switching in tumors, and apoptosis in various cell types [16–19]. The metabolic machineries of pancreatic β-cells are designed to sense blood glucose fluctuations and respond accordingly by the secretion of insulin [20]. β-cells uptake glucose via their transporters of the GLUT family, which is further processed by glycolysis and oxidative phosphorylation, producing NADH and FAD [21]. The increase in ATP leads to the closing of K^+ATP channels and is followed by Ca^{2+} influx, necessary for the exocytosis of insulin granules.

Here, we demonstrate that FLIM can be utilized to monitor the dynamic metabolic changes in β-cells upon glucose stimulation. By combining the detection of (pre-) hypoxic cellular response and the identification of a profile for glucose-stimulated islets, we introduce FLIM as a tool for the screening of single pancreatic pseudo-islets. Identification and exclusion of damaged and glucose nonresponsive isolated islets prior to transplantation has the potential to improve the clinical outcomes for type 1 diabetic patients receiving an islets transplant.

2 | EXPERIMENTAL SECTION

2.1 | Cell culture and pseudo-islet assembly

The EndoC-βH3 (Univercell Biosolutions, Toulouse, France) cell line was cultured as previously described [22]. We modified the protocol by seeding 2000 cells that aggregated into pseudo-islets using nonadherent 96 well U-bottom plates (Thermo Fisher Scientific, Waltham, Massachusetts). Pseudo-islets were cultured under normoxic conditions (37°C, 5% CO_2, 20% O_2) for a total period of 5 days. Hypoxic conditions were defined as 37°C, 5% CO_2 and 1% O_2. Before being subjected to hypoxia, cells were seeded and cultured for 48 hours under normoxic conditions to allow the assembly of cells into pseudo-islets. Pseudo-islets were in hypoxia for periods ranging from 3 to 48 hours. To track the pseudo-islet size over time, brightfield images were taken every 24 hours using a brightfield microscope (Zeiss, Jena, Germany). Diameters were analyzed using the software ImageJ V 1.52p.

2.2 | GSIS assay

Prior to any GSIS assay, pseudo-islets were incubated for 24 hours in starvation medium (Optiβ2, Univercell Biosolutions).

2.2.1 | Standard GSIS

Pseudo-islets were grouped by six per well and washed twice with Krebs buffer (Univercell Biosolutions), supplemented with 1% BSA (Krebs-BSA) (Thermo Fisher Scientific). Pseudo-islets were synchronized for 1 hour in Krebs-BSA and washed twice afterwards. Pseudo-islets were subsequently incubated for 1 hour with Krebs-BSA, Krebs-BSA supplemented with 20 mM glucose (Gibco, Waltham, Massachusetts), and Krebs-BSA for a second time. After each incubation, supernatants were collected and stored at −20°C until further detection of insulin with an ELISA assay (Ultrasensitive Insulin ELISA, Mercodia, Uppsala, Sweden).

2.2.2 | On-FLIM GSIS procedure

Pseudo-islets were loaded into a microfluidic chip as previously described [22]. A low-pressure four-port switching valve (IDEX Health & Science, Oak Harbor, Washington) was used to allow the switch between Krebs-BSA and Krebs-BSA supplemented with 20 mM glucose. Pseudo-islets were incubated for a total of 135 minutes with Krebs-BSA (corresponding to the synchronization phase and 1 hour under Krebs-BSA) before switching to 20 mM glucose for 327 minutes. For nonstimulated GSIS (control), the pseudo-islets were subjected to a total of 459 minutes in Krebs-BSA. The synchronization phase in Krebs-BSA was not measured. Each islet was monitored at the same focus level by acquiring FLIM images every 27 minutes continuously for the duration of the experiments.

2.3 | Immunohistological analyses

Pseudo-islets were washed with PBS (Gibco), embedded in Histogel (Thermo Fisher Scientific), fixed with 4% PFA, and subjected to paraffin-embedding using a Shandon Citadel 1000 (Thermo Fisher Scientific) according to the manufacturer's instructions. Then, 3-µm-thick sections were prepared using the microtome RM2145 (Leica, Wetzlar, Germany). Sections were deparaffinized using xylene and rehydrated by graded ethanol (100%-50%). Then, 1% Triton-X permeabilization and antigen retrieval were performed as described before utilising the following antibodies: anti-insulin: guinea-pig IgG, 1:200 dilution, A0564 (DAKO, Santa Clara, California); anti-vascular endothelial growth factor (VEGF): Rabbit IgG, 1:400 dilution, RB-9031-P (Thermo Fisher Scientific); anti-HIF-1α: rabbit IgG, 1:500 dilution, ab51608 (Abcam, Cambridge, UK) and anti-caspase-3: rabbit IgG, 1:100 dilution, ab13847 (Abcam) [23]. To visualize nuclei, sections were incubated with 4′,6-daimidin-2-phenylindol (DAPI) solution with a concentration of 2 µg/mL (Sigma-Aldrich, St. Louis, Missouri) for 10 minutes. Mounting was performed with Molecular Probes Prolong Gold Anti Fade solution (Invitrogen, Carlsbad, California). Immunofluorescence images were obtained using a Zeiss LSM 880 (Zeiss) and analyzed using Zeiss Zen Blue software and ImageJ V1.52p. Staining intensities (VEGF and caspase-3) were evaluated via the mean gray value per pixel within a region of interest (ROI) defined as $DAPI^+$ areas. HIF-1α-stained images were quantified by three independent unbiased observers. Cells were counted as HIF-1α $^+$ when nuclei were exhibiting a double staining with DAPI and HIF-1α. The ratios of HIF-$1\alpha^+$ cells were calculated by dividing the number of HIF-$1\alpha^+$ cells by the number of total $DAPI^+$ cells per pseudo-islets.

2.4 | Multiphoton imaging and FLIM data acquisition

TCSPC-based fluorescence decay measurements were performed with a Zeiss LSM 880 (Zeiss) coupled with a

Ti:Sapphire femtosecond laser (MaiTai HP Spectra Physics, Santa Clara, California) and a two-channel NDD BIG2.0 GaAsP PMT detector (Becker & Hickl GmbH, Berlin, Germany). NADH and FAD autofluorescence was induced with a two-photon excitation at a wavelength of 700 nm and 5% laser power through a ×63/1.4 NA C-plan apochromat objective (Zeiss). Emission light was filtered in the range of 450 to 490 nm for NADH, and 500 to 550 nm for FAD. Total image acquisition time was 161 seconds at a resolution of 512 × 512 pixels (524.8 μs/pixel). Instrument response function was recorded at 900 nm from crystalline urea (Sigma-Aldrich). Normoxic and hypoxic pseudo-islets were transferred either into μ-slides Angiogenesis (ibidi GmbH, Gräfelfing, Germany), or into a microfluidic chip for FLIM measurements as previously described [22]. All FLIM measurements were performed at 37°C using a microscope stage top incubation system (ibidi heating system, ibidi GmbH).

2.5 | FLIM data analysis

SPICImage (Becker & Hickl GmbH) was used to perform biexponential decay fittings with a 30% threshold of maximum photon count to remove the background. The quality of fit was decided based on a mean χ^2 value smaller than 1.1 per image. ASCII images for α, τ and χ^2 were exported for further analysis. Concentric ROI segmentation based on the outline of the islet was performed on each FLIM image using MATLAB R2020a (The MathWorks Inc., Waltham, Massachusetts). The ROIs were equally spaced at 10 μm in order to calculate mean values for cells at similar depths (MATLAB code available upon request).

2.5.1 | Optical oxidative ratio calculation

The optical oxidative ratio was defined as the total photon counts of FAD divided by the sum of FAD and NADH photon counts [24]. The calculation of the optical oxidative ratio was performed after the image processing by SPICImage and MATLAB software, which includes suppressing the background.

2.5.2 | Lumen ratio calculation

The lumen size was evaluated using an additional threshold of 25% of the total photon count images after background removal by the SPCImage software (MATLAB code available upon request).

2.6 | Statistical analyses

Statistical analyses were performed using GraphPad Prism version 6.00 for Windows (GraphPad Software, San Diego, California). Results are shown throughout the entire manuscript as mean ± standard deviation. Outliers were removed using Grubb's test with a confidence interval of 0.05. Normality was assessed using Shapiro-Wilk tests. Normal distribution was assumed for low n-number samples ($n < 8$). All n-numbers, applied tests, and corresponding significances for each result are listed in the figure legends.

3 | RESULTS AND DISCUSSION

3.1 | Human pancreatic β-cells engineered to form glucose-responsive pseudo-islets in vitro

To mimic the insulin-secretory function of endocrine pancreas, we modified a previously described protocol using human pancreatic β-cells, aggregated at 2000 cells per pseudo-islet [22]. After 5 days of culture, pseudo-islets had properly aggregated into clinically relevant spheres with a mean diameter of 101 ± 5.4 μm (Figure 1A), which were similar in size to previous studies demonstrating a relationship between islet size and functionality in vitro and in vivo in terms of survival rate after transplantation [25, 26]. Smaller rat islets (<125 μm) were superior than larger islets (>150 μm) in terms of insulin release in vitro and restoring glycemic control in a diabetic rat model [26].

The main function of pancreatic β-cells is to secrete insulin in response to glucose stimulation. Pseudo-islets were stimulated with 20 mM glucose and showed a significant increase in insulin secretion upon stimulation (0 mM: 0.63 ± 0.1 mU/L insulin/pseudo-islet vs 1.66 ± 0.6 mU/L insulin/pseudo-islets at 20 mM) (Figure 1B). After stimulation, pseudo-islets returned to their basal insulin secretion level. Immunofluorescence staining showed a homogeneous distribution of insulin throughout the pseudo-islets (Figure 1C). Altogether, these data show the dynamic response of human pseudo-islets to glucose, and their potential to mimic the functional unit of the islets of Langerhans that produce insulin.

3.2 | FLIM enables the noninvasive monitoring of hypoxia-induced cell death in vitro

Hypoxia leads to β-cell dysfunction, which is a major factor contributing to the overall poor efficiency of the Langerhans islet isolation and transplantation procedures

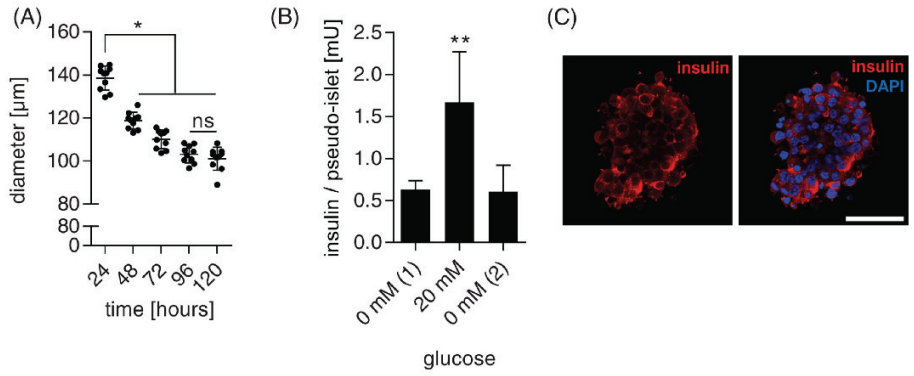

FIGURE 1 Formation of human glucose-responsive pseudo-islets to mimic the insulin-producing endocrine function of the pancreas. A, β-cell aggregation monitored by assessing the mean diameter of pseudo-islets over time. One-way analysis of variance (ANOVA) with Tukey's multiple comparisons test. n = 10. B, Standard glucose-stimulated insulin secretion (GSIS) of pseudo-islets subjected sequentially to 0, 20 and 0 mM glucose. n ≥ 4. C, Immunofluorescence staining of insulin in pseudo-islets (red) and nuclei (DAPI, blue). Scale bar equals 50 µm. *$P < .05$; **$P < .01$

[27]. Severe and prolonged hypoxia (<1% oxygen) induces nonreversible cellular changes resulting in programmed cellular death. To evaluate the impact of severe hypoxia on our pseudo-islet in vitro system, key hypoxic expression markers were evaluated over time, including vascular endothelial growth factor (VEGF), HIF-1α and cleaved caspase-3 (Figure 2).

Adult pancreatic islets continuously secrete VEGF to maintain blood vessel density and proper fenestration [28]. In response to decreased oxygen tension, pancreatic β-cells secrete VEGF as part of an adaptive response to hypoxia [29]. Here, we showed a significant increase in VEGF after 1 hour under hypoxia (Figure 2A).

Our results showed that HIF-1α, which is induced by a decrease in oxygen in the cytoplasm, significantly increased after 6 hours under hypoxia (Figure 2B). The HIF-1α protein, which is stabilized by hypoxic conditions, has a large number of target genes, including HIF-1 and VEGF [30]. Here, we observed a potentially coordinated and significant increase of HIF-1α and VEGF after 1 hour under hypoxic conditions. After 6 hours under hypoxic conditions, HIF-1α expression increased further and reached a plateau, while VEGF expression slowly decreased.

HIF-1α exerts both pro- and anti-apoptotic effects, depending on the severity of hypoxia [31]. Under severe hypoxic conditions, HIF-1α can trigger hypoxia-induced apoptosis, which can be measured by the expression of cleaved caspase-3 [32]. Here, cleaved caspase-3 was significantly upregulated from 12 to 24 hours under hypoxia (Figure 2C). These results suggest that pseudo-islets under hypoxic conditions initiate an adaptive response from 1 to 4 hours, seen by a rapid increase in VEGF. HIF-1α may exert a pro-apoptotic effect via HIF-1α between 4 and 6 hours that leads to the activation of programmed cell death via cleaved caspase-3 between 6 and 12 hours under hypoxia. Identification of dead cells (i.e. after completion of apoptosis) is possible using MP images of the endogenous NADH. The appearance of a hypoxic core, which was depicted by the loss of NADH autofluorescence intensity, can be observed in pseudo-islets at 12 hours under hypoxia (Figure 2D).

FLIM can identify metabolic changes in living cell cultures and in vivo [33]. Here, we were interested in whether FLIM has the fidelity to identify metabolic changes arising from the early adaptive response to hypoxia before the activation of cleaved caspase-3 and following nonreversible cellular changes. Therefore, FLIM images were acquired from the endogenous NADH and FAD autofluorescence of pseudo-islets under normoxia and hypoxia for 3, 6 and 12 hours. Each metabolic profile was characterized by the FLIM parameters τ_1, τ_2 and α_1 from the respective coenzymes NADH and FAD, as well as the optical oxidative ratio (FAD/FAD + NADH) (Figure 2E-J). NADH τ_1 represents the fluorescence lifetime of free NADH, whose major contribution arises from cytosolic NADH in opposition to bound NADH found in the oxidative phosphorylation chain and characterized by τ_2 [34]. NADH and FAD lifetimes are highly sensitive to changes within their microenvironment, such as pH, solvent polarity or viscosity [33]. We showed that hypoxia induced an increase in NADH τ_1 at 3 and 6 hours, while NADH τ_2 was most affected after 3 hours (Figure 2E,F). Hypoxia is known to trigger a switch from aerobic to anaerobic glycolysis, which is a protective strategy against the production of reactive oxygen species (ROS) [35]. It is also the means with which NAD^+ is recovered

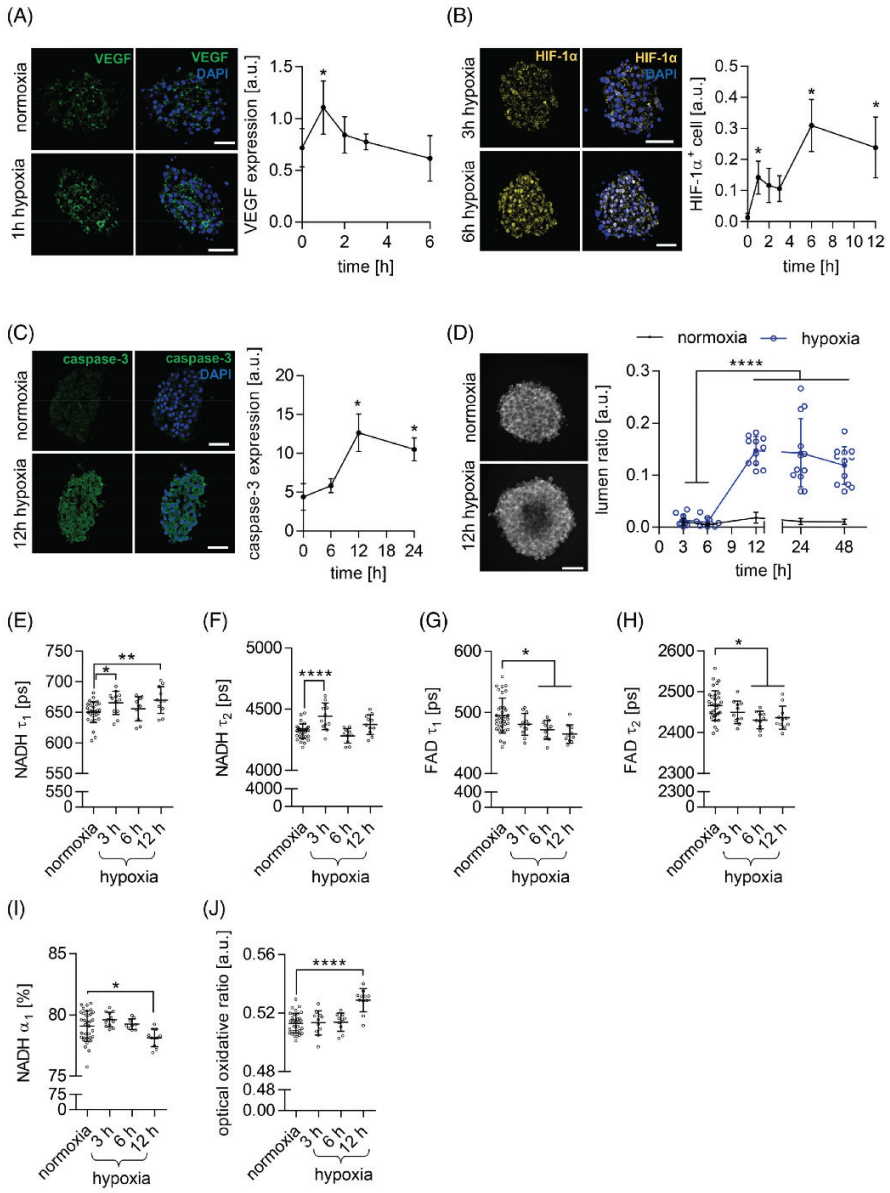

FIGURE 2 Hypoxia-induced cellular response in human pseudo-islets is detectable with fluorescence lifetime imaging microscopy (FLIM). Immunofluorescence staining of, A, vascular endothelial growth factor (VEGF), B, hypoxia-inducible factor 1α (HIF-1α) and, C, cleaved capase-3 in pseudo-islets under normoxic and hypoxic conditions and the corresponding quantification (right). n ≥ 3. D, Multiphoton (MP) imaging and quantification of the lumen size of hypoxic pseudo-islets over a time period of 12 hours. n ≥ 10. E-J, Time lapse FLIM analysis of hypoxic pseudo-islets showing, E, nicotinamide adenine dinucleotide (NADH) τ_1, F, NADH τ_2, G, flavin adenine dinucleotide (FAD) τ_1, H, FAD τ_2, I, NADH α_1 and, J, the optical oxidative ratio based on endogenous fluorescence of FAD/FAD + NADH. n ≥ 10. Scale bars equal 50 μm. One-way analysis of variance (ANOVA) with Tukey's multiple comparisons test. *$P < .05$; **$P < .01$ and ****$P < .0001$

from NADH, which is required to produce ATP. This process produces a large amount of lactic acid. The following acidification of the cytosol may be responsible for the significant change in NADH τ_1. The mitochondria produce ROS via the complexes I and III of the electron chain transporters, whose production levels increase when oxygen levels drop in a range of 5% to 0.5% [35]. Interestingly, oxidative stress arising from ROS has been shown to increase NADH τ_2, which is observed here after 3 hours under hypoxia (Figure 2F) [36]. The recovery of NADH τ_2 at 6 and 12 hours under hypoxia may reflect the activation of antioxidant pathways [37].

Under hypoxia, FAD τ_1 and τ_2 significantly decreased after 6 and 12 hours (Figure 2G,H). The majority of the endogenous fluorescence from FAD arises from the mitochondria when FAD is in a complex with lipoamide dehydrogenases and the electron transfer flavoproteins, whose contributions represent ~50% and ~25% of the total intensity, respectively [38]. The contribution from the electron change transporter is considered negligible, and the remaining 25% of the FAD intensity is not associated with metabolism. Therefore, change in FAD τ_1 and τ_2 are strongly associated with the mitochondrial microenvironment.

NADH α_1, which is the contribution of the free NADH over the total amount of photons collected, significantly decreased in pseudo-islets after 12 hours under hypoxia when compared with the normoxic controls (Figure 2I). This describes a redistribution from free to bound NADH forms to facilitate more efficient ATP production in the mitochondria. The nucleus increases its energy demands, as it prepares the cells for apoptosis [39]. Decrease in NADH α_1 has been reported in vivo in murine keratinocytes undergoing apoptosis [19]. These data are corroborated with a significant increase in optical oxidative ratio at 12 hours under hypoxia, implying that the relative amount of mitochondrial FAD (free and bound) increased when compared to NADH (free and bound) (Figure 2J).

We showed that FLIM can detect metabolic changes that are induced by the hypoxic environment in a nondestructive manner in pancreatic β-cells. Moreover, our data reveals that the NADH lifetimes τ_1 and τ_2 can be used as indicators of the early adaptive hypoxia-induced cellular response, occurring before the appearance of the major peak in HIF-1α or cleaved caspase-3.

3.3 | Spatial distribution of FLIM outputs allow the detection of early adaptive hypoxia-induced cellular response in pseudo-islets

During the isolation process, pancreatic islets are severed from their vasculature and rely on diffusive properties from the surrounding media for their oxygen and nutrient supply. The diffusion gradient is depending partially on the islet size, which is highly heterogenous in the native pancreas [40]. In addition, each islet has a different degree of vascularization and composition of α-, β-, δ-, γ- and PP-cells [41]. FLIM can be used to assess the metabolic state of single cells, which can reveal the heterogeneity within single islets or pseudo-islets. We hypothesize that FLIM can discriminate subregions within one pseudo-islet that differentially react to hypoxic conditions, either by an adaptive response to hypoxia or by initiating a programmed cell death. Therefore, we segmented FLIM acquisitions to create ROIs based on their spatial distribution (see Section 2) within the pseudo-islets as illustrated in Figure 3a. For each ROI representing a 10 μm increment in depth, NADH and FAD lifetimes τ_1 and τ_2, NADH α_1, and optical oxidative ratio were assessed (Figure 3B-G).

Under normoxic conditions, the first ROI (0-10 μm) is metabolically different than all other ROIs: a significantly higher optical oxidative ratio and lower NADH α_1 indicate that cells within the first ROI rely on higher oxidative phosphorylation rates. This is likely due to the direct contact between nutrients/oxygen and β-cells.

Under hypoxia, FLIM parameters NADH τ_1, FAD τ_2, NADH α_1 and optical oxidative ratio were significantly affected by the spatial distribution of the corresponding ROIs. Hypoxia severely impacted FLIM parameters in the central region of the pseudo-islets (30-80 μm), starting from 3 hours under hypoxia, characterized by a steady increase of NADH τ_1, decrease in FAD τ_2, decrease in NADH α_1, and increase in optical oxidative ratio (Figure 3B,E-G). In the pseudo-islet core, hypoxia is most likely <1% oxygen due to the oxygen consumption of the outer cells. Under such conditions, cellular mechanisms concentrate on antioxidant-producing pathways that come at the expense of glycolytic ATP production [37]. After a prolonged time under those severe conditions, the apoptotic cascade is activated, which may be responsible for the further increase in oxidative phosphorylation [42].

In contrast, in the outermost ROI (0-30 μm), a significant decrease in NADH α_1 was observed after 12 hours under hypoxia, while no changes were noted in either NADH τ_1 or optical oxidative ratio. FAD τ_1 and τ_2 decreased after 6 hours only in the first ROI (0-10 μm). This suggests that the cells in the first ROI may have initiated an adaptive response to hypoxia and are able to maintain their glycolytic rate for a longer period.

NADH τ_2 and FAD τ_1 were not affected by the spatial distribution within the pseudo-islets (Figure 3C,D). While NADH τ_2 oscillated during hypoxia, FAD τ_1 was only affected in the first ROI (0-10 μm). Interestingly, both

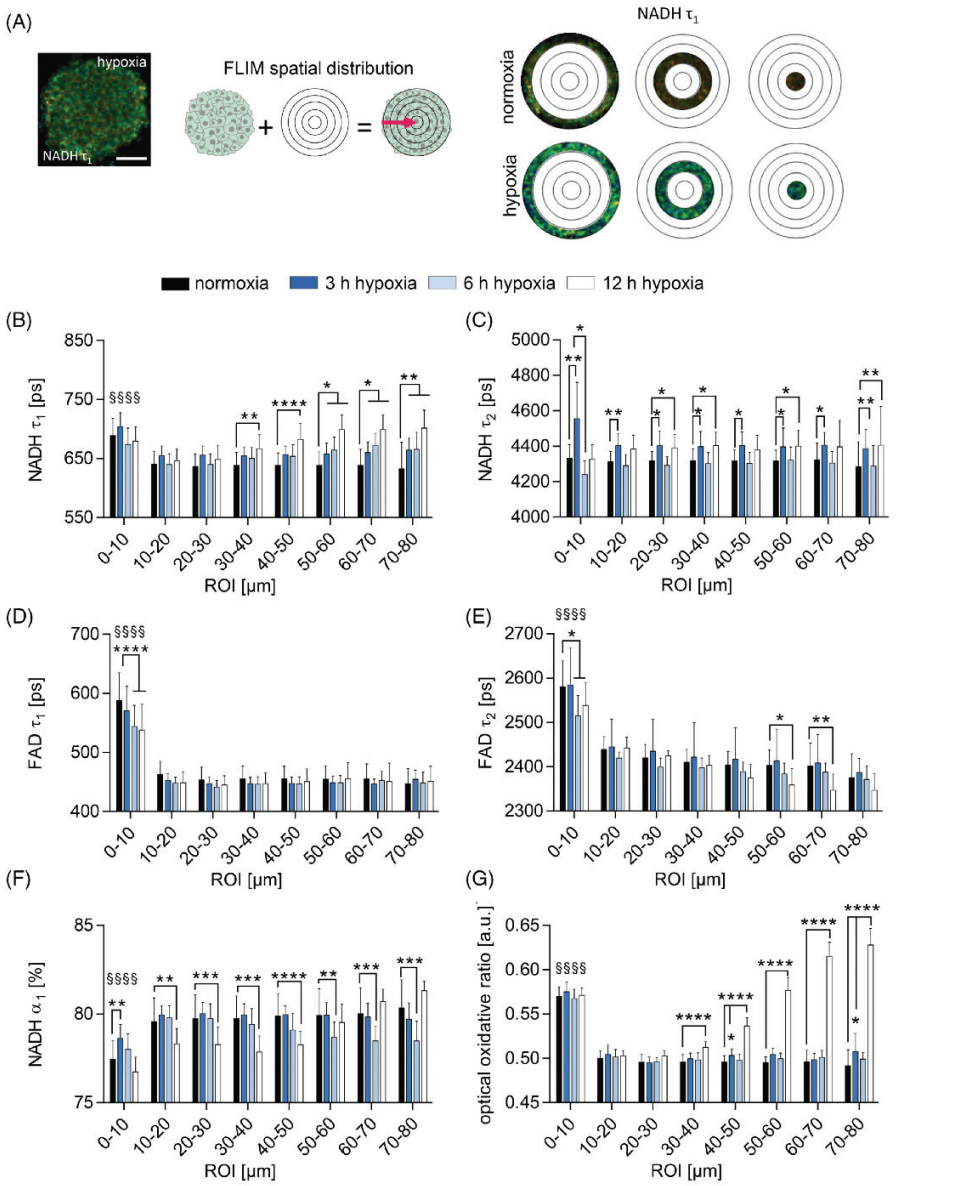

FIGURE 3 Segmentation of fluorescence lifetime imaging microscopy (FLIM) images reveal the heterogeneity of hypoxic pseudo-islets in vitro. A, Schematic illustration of the segmentation of FLIM images creating 10 µm-deep incremented regions of interest (ROIs). B-G, FLIM analysis of hypoxic pseudo-islets over time, and segmented per ROI, showing, B, nicotinamide adenine dinucleotide (NADH) τ_1, C, NADH τ_2, D, flavin adenine dinucleotide (FAD) τ_1, E, FAD τ_2, F, NADH α_1 and, G, the optical oxidative ratio based on endogenous fluorescence of FAD/FAD + NADH. n ≥ 10. Scale bar equals 50 µm. Two-way analysis of variance (ANOVA) with Dunnett's multiple comparisons test. §§§§: significant difference between ROIs $P < .0001$. *: Significant difference between groups within one ROI. *$P < .05$; **$P < .01$, ***$P < .001$ and ****$P < .0001$

NADH τ_2 and FAD τ_1 are protein-bound lifetimes within the mitochondria, which may reduce their sensitivity to microenvironmental changes.

The segmentation of FLIM outputs allowed the discrimination of surviving and apoptotic cells within a single pseudo-islet. As expected, the innermost ROIs are

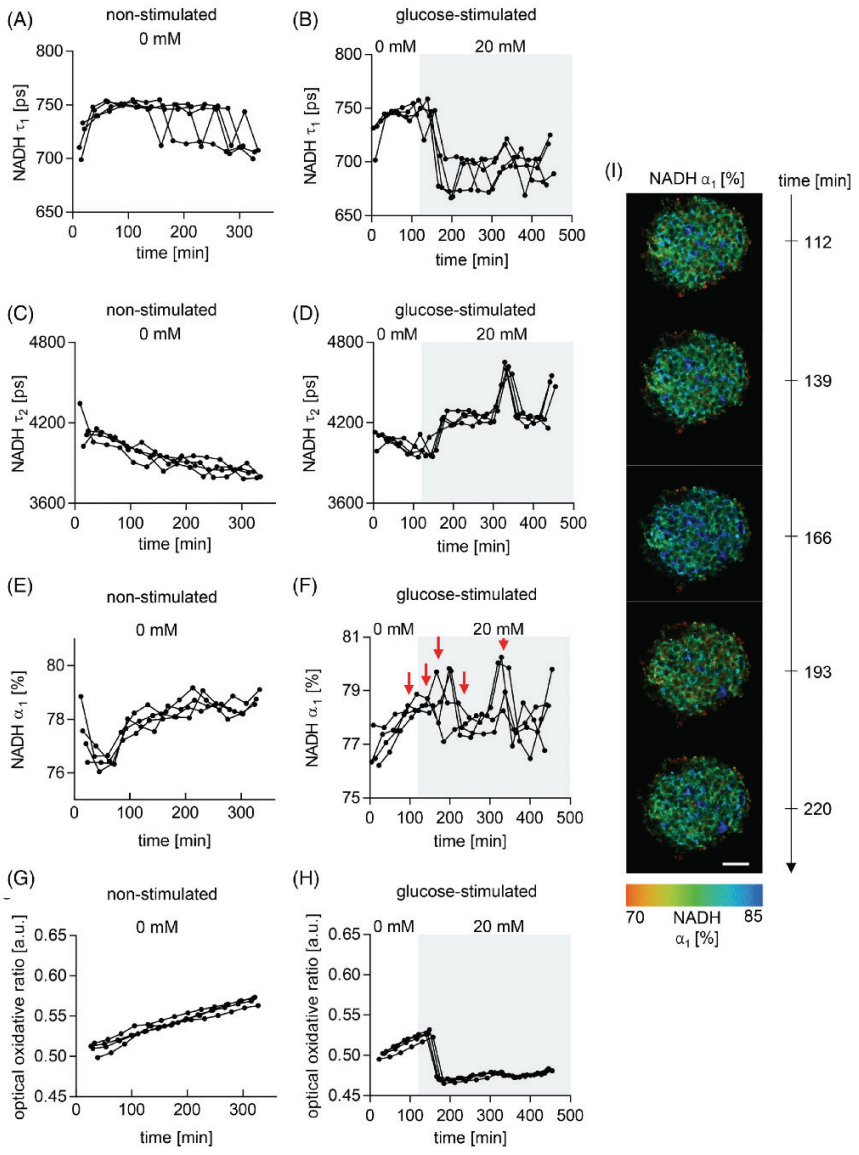

FIGURE 4 In situ fluorescence lifetime imaging microscopy (FLIM) probes glucose-responsiveness of normoxic pseudo-islets in vitro. FLIM analysis over time of nonstimulated pseudo-islets and glucose stimulation with 20 mM shows, A,B, nicotinamide adenine dinucleotide (NADH) τ_1, C,D, NADH τ_2, E,F, NADH α_1 and, G,H, the optical oxidative ratio based on endogenous fluorescence of flavin adenine dinucleotide (FAD)/FAD + NADH. I, Representative images of NADH α_1 over time during glucose stimulation. Corresponding time points are shown with red arrows in F. n = 4. Scale bar equals 50 μm

strongly affected by hypoxia, as indicated by a change in NADH lifetimes, NADH α_1, and oxidative ratio. These changes will likely lead to the nonreversible initiation of apoptosis [19, 42]. The β-cells located in the outer ROIs were characterized by a lower NADH α_1 and stable values for NADH τ_1, FAD τ_2 and optical oxidative ratio. These metabolic changes suggest that the β-cells were affected by hypoxia by redistributing free to bound NADH. However, the stable values of NADH and FAD lifetimes suggest that these β-cells have reached a metabolic equilibrium under hypoxia via an adaptive response.

3.4 | FLIM can noninvasively identify metabolic oscillations of glucose-responsive pseudo-islets

The major prerequisite of transplanted pancreatic islets is the regulation of glucose homeostasis by sensing glucose and secreting appropriate amounts of insulin [1]. Hypoxia decreases aerobic glycolysis, thus reducing the β-cell capacity to secrete insulin upon glucose stimulation [43]. Depending on the severity of the hypoxia-induced cell damage, the downstream effects of HIF-1α activation in β-cells can be transient and reversible. Therefore, assessing the metabolic changes due to glucose stimulation is essential to identify functional islets. Here, we characterized the glucose-response of functional pseudo-islets using FLIM. Normoxic pseudo-islets were stimulated with 20 mM glucose as previously described [22]. FLIM images were acquired during the glucose stimulation of single pseudo-islets over time and compared to nonstimulated pseudo-islets (Figure 4).

In the first 60 minutes of analysis without glucose, NADH τ_1 steadily increased overtime, while NADH α_1 decreased, which reflects the known metabolic changes due to glucose starvation (Figure 4A,E) [44]. Prolonged starvation resulted in NADH τ_1, FAD τ_1 and FAD τ_2 oscillations, steady decrease in NADH τ_2, and an increase in NADH α_1 and optical oxidative ratio (Figures 4A,C,E, G and S1). The absence of glucose diminishes the glycolytic flux and forces mitochondrial adaptation. Carbon sources can be provided, for instance by glutamine, which can fuel the TCA cycle and maintain ATP levels [45]. Additional pathways can be initiated to provide energy, such as the β-oxidation of fatty acids or the pentose phosphate pathway [37]. The pentose phosphate pathway produces nicotinamide adenine dinucleotide phosphate (NADPH), which may be responsible for the increase of free NADH after 60 minutes, as NADPH endogenous fluorescence is included in the NADH signals [46].

Stimulation of β-cells with glucose impacted NADH and FAD lifetimes, oscillations of NADH α_1 and led to a drop of the oxidative ratio (Figures 4B,D,F,H,I and S1). Glycolytic flux abruptly increases as glucose is transported into the cells, which was seen in our data by the immediate changes in NADH and FAD lifetimes and spiking of NADH α_1. Similarly, aerobic glycolysis produces large amounts of NADH, correlating with the decrease in oxidative ratio.

Hypoxia-induced cellular changes can be reversible depending on their severity. For instance, 6 hours under hypoxia altered the mitochondrial lifetimes of NADH and FAD, while NADH α_1 and optical oxidative ratio were stable, suggesting a moderate impact of hypoxia. To investigate the glucose-response of pseudo-islets cultured under hypoxia for 6 hours, FLIM metabolic profiles were assessed during stimulation with 20 mM glucose (Figure 5). We detected large fluctuations in NADH τ_1 and NADH α_1, which did not resemble the metabolic response of stimulated normoxic pseudo-islets (Figure 5A,C). Nevertheless, the value of NADH τ_2 before glucose stimulation under hypoxia was similar to normoxia (Figure 5B,E). Upon stimulation, NADH τ_2 under hypoxia spiked and plateaued at higher values compared with normoxia (Figure 5B). The optical oxidative ratio of hypoxic pseudo-islets, which was overall higher than in normoxia, dropped upon glucose stimulation similarly to normoxic pseudo-islets (Figure 5D). The profile of FAD lifetimes was similar to normoxia as well (Figure S2). Stimulation of pancreatic β-cells with glucose and following insulin secretion requires both glycolysis and oxidative phosphorylation [47]. After 6 hours under hypoxia, pseudo-islets were still glucose-responsive, as indicated by NADH τ_2, FAD τ_1, FAD τ_2 and the optical oxidative ratio. The stimulation lead to an increase in the total NADH compared to FAD, which most likely is produced by an increase in glycolysis. However, the high value of NADH τ_2 indicated an important change within the mitochondrial microenvironment. This change may have arisen from the increasing levels of ROS due to hypoxia and the loss of the metabolic rescue mechanisms of a functional cell, which further increased as the TCA cycle and oxidative phosphorylation are enforced during insulin secretion. Prolongated hypoxia is known to lead to β-cell dysfunction, characterized, in part, by a loss of glucose-response [43]. Here, we showed that pseudo-islets after 6 hours under hypoxia still respond to glucose based on FLIM, which was validated by a standard GSIS assay (Figure S3). However, important changes in the metabolic response of the coenzymes NADH and FAD were detected suggesting cellular

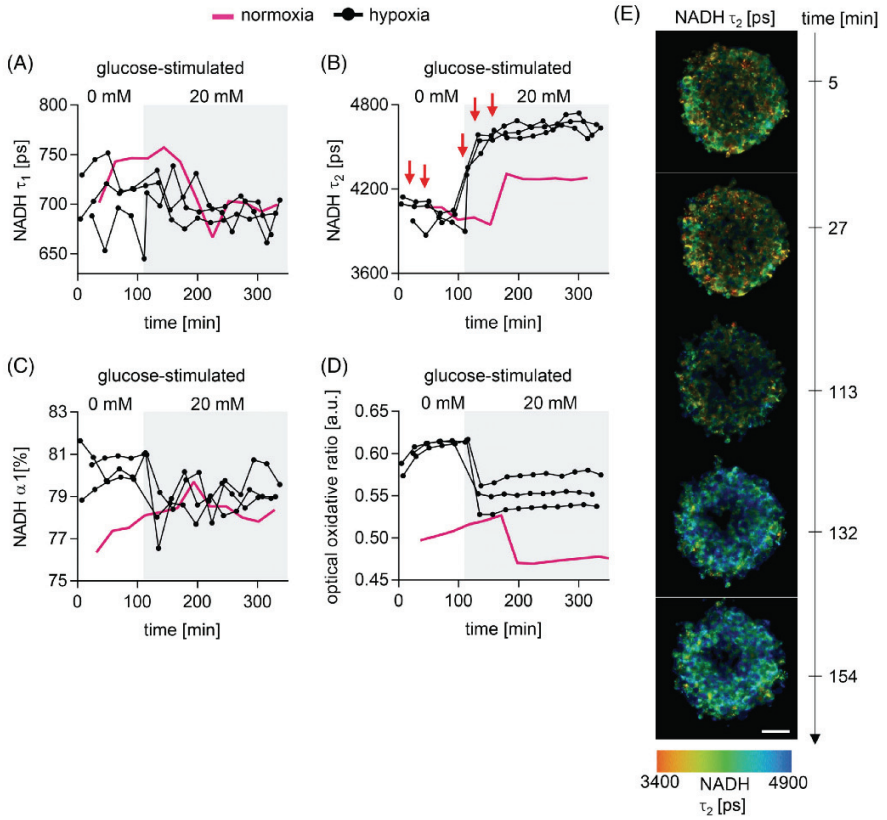

FIGURE 5 In situ fluorescence lifetime imaging microscopy (FLIM) monitors individual pseudo-islet glucose responses under hypoxic conditions for 6 hours. FLIM analysis over time during glucose stimulation with 20 mM reveals, A, nicotinamide adenine dinucleotide (NADH) τ_1, B, NADH τ_2, C, NADH α_1 and, D, the optical oxidative ratio based on endogenous fluorescence of flavin adenine dinucleotide (FAD)/FAD + NADH. Hypoxic pseudo-islets are shown in black and normoxic controls (averaged, n = 4) are shown in pink. E, Representative images of NADH τ_2 over time during glucose stimulation. Corresponding time points are highlighted with red arrows in B. n = 3. Scale bar equals 50 μm

stress. Our data demonstrates how FLIM can detect metabolic impairment in hypoxic pseudo-islets in comparison with standard methods such as GSIS assays.

4 | CONCLUSION

Developing noninvasive tools to assess the quality of isolated pancreatic islets prior implantation has the potential to improve the outcomes of Langerhans islet transplantation to treat type 1 diabetes. In this study, we used an in vitro system mimicking the insulin-producing and glucose-responsive characteristics of the islets of Langerhans and combined it with FLIM to assess pseudo-islet quality and their glucose-response under standard and hypoxic conditions. FLIM identified and discriminated between minor and severe hypoxia-induced cellular damages in β-cells. FLIM further allowed the marker-free and noninvasive detection of a metabolic response due to glucose stimulation in functional living pseudo-islets, which can be used to assess the severity of hypoxia-induced damages during insulin secretion.

ACKNOWLEDGMENTS

A. Z. and D. A. C. B. contributed equally to this work. The authors thank Katharina U. Schlünder (University of Tübingen) for her support with the pancreas-on-chip system. This work was financially supported by the European

Union (H2020-NMP10-2014-645991-2, DRIVE; H2020-ITN 766181, DELIVER to G. P. D and K. S.-L.), the International Foundation for Ethical Research (to A. Z.), as well as the Ministry of Science, Research and the Arts of Baden-Württemberg (33-729.55-3/214 and SI-BW 01222-91 to K. S.-L.) and the Deutsche Forschungsgemeinschaft (INST 2388/33-1 to K. S.-L.). Open access funding enabled and organized by Projekt DEAL.

CONFLICT OF INTEREST

The authors declare no conflict of interest.

AUTHOR CONTRIBUTIONS

Aline Zbinden, **Daniel A. Carvajal Berrio**, **Max Urbanczyk**, **Shannon L. Layland** and **Katja Schenke-Layland**: Designed the experiments and wrote the manuscript. **Aline Zbinden**, **Daniel A. Carvajal Berrio**, **Max Urbanczyk**, **Mariella Bosch**, **Sandro Fliri**, **Chuan-en Lu** and **Abiramy Jeyagaran**: Performed experiments, collected and analyzed data. **Peter Loskill** and **Garry P. Duffy**: Gave conceptual advice.

DATA AVAILABILITY STATEMENT

The main data supporting the findings of this study are available within the article and its supplementary information. The raw data generated in this study are available from the corresponding author upon reasonable request.

ORCID

Katja Schenke-Layland https://orcid.org/0000-0001-8066-5157

REFERENCES

[1] M. R. Rickels, R. P. Robertson, *Endocr. Rev.* **2019**, *40*, 631.
[2] E. A. Ryan, B. W. Paty, P. A. Senior, D. Bigam, E. Alfadhli, N. M. Kneteman, J. R. T. Lakey, A. M. J. Shapiro, *Diabetes* **2005**, *54*, 2060.
[3] Q. Zhou, D. A. Melton, *Nature* **2018**, *557*, 351.
[4] W. Bennet, C. G. Groth, R. Larsson, B. Nilsson, O. Korsgren, *Ups. J. Med. Sci.* **2000**, *105*, 125. https://doi.org/10.1517/03009734000000059.
[5] M. Giuliani, W. Moritz, E. Bodmer, D. Dindo, P. Kugelmeier, R. Lehmann, M. Gassmann, P. Groscurth, M. Weber, *Cell Transplant.* **2005**, *14*, 67.
[6] R. M. Spiers, J. Marzi, E. M. Brauchle, S. E. Cross, R. H. Vaughan, P. A. Bateman, S. J. Hughes, K. Schenke-Layland, P. R. V. Johnson, *Acta Biomater.* **2019**, *99*, 269.
[7] G. Loganathan, R. K. Dawra, S. Pugazhenthi, Z. Guo, S. M. Soltani, A. Wiseman, M. A. Sanders, K. K. Papas, K. Velayutham, A. K. Saluja, D. E. R. Sutherland, B. J. Hering, A. N. Balamurugan, *Transplantation* **2011**, *92*, 1222.
[8] M. Garcia-Contreras, A. Tamayo-Garcia, K. L. Pappan, G. A. Michelotti, C. L. Stabler, C. Ricordi, P. Buchwald, *J. Proteome Res.* **2017**, *16*, 2294. https://doi.org/10.1021/acs.jproteome.7b00160.
[9] X. Zheng, X. Zheng, X. Wang, Z. Ma, V. Gupta Sunkari, I. Botusan, T. Takeda, A. Björklund, M. Inoue, S. B. Catrina, K. Brismar, L. Poellinger, T. S. Pereira, *Cell Death Dis.* **2012**, *3*, e322.
[10] E. Linetsky, C. Ricordi, *Transplant. Proc.* **2008**, *40*, 424.
[11] J. D. Carter, S. B. Dula, K. L. Corbin, R. Wu, C. S. Nunemaker, *Biol. Proced. Online* **2009**, *11*, 3.
[12] P. H. Lakner, M. G. Monaghan, Y. Möller, M. A. Olayioye, K. Schenke-Layland, *Sci. Rep.* **2017**, *7*, 1.
[13] J. Li, A. J. Bower, Z. Arp, E. J. Olson, C. Holland, E. J. Chaney, M. Marjanovic, P. Pande, A. Alex, S. A. Boppart, *J. Biophotonics* **2018**, *11*, e201700195.
[14] A. J. Walsh, R. S. Cook, M. E. Sanders, L. Aurisicchio, G. Ciliberto, C. L. Arteaga, M. C. Skala, *Cancer Res.* **2014**, *74*, 5184. https://doi.org/10.1158/0008-5472.CAN-14-0663.
[15] J. R. Lakowicz, H. Szmacinski, K. Nowaczyk, M. L. Johnson, *Proc. Natl. Acad. Sci. U. S. A.* **1992**, *89*, 1271.
[16] I. A. Okkelman, R. I. Dmitriev, T. Foley, D. B. Papkovsky, *PLoS One* **2016**, *11*, e0167385. https://doi.org/10.1371/journal.pone.0167385.
[17] A. V. Meleshina, V. V. Dudenkova, A. S. Bystrova, D. S. Kuznetsova, M. V. Shirmanova, E. V. Zagaynova, *Stem Cell Res. Ther.* **2017**, *8*, 15.
[18] M. Wang, F. Tang, X. Pan, L. Yao, X. Wang, Y. Jing, J. Ma, G. Wang, L. Mi, *BBA Clin.* **2017**, *8*, 7.
[19] A. J. Bower, M. Marjanovic, Y. Zhao, J. Li, E. J. Chaney, S. A. Boppart, *J. Biophotonics* **2017**, *10*, 143.
[20] P. E. MacDonald, J. W. Joseph, P. Rorsman, *Philos. Trans. R. Soc. B: Biol. Sci.* **2005**, *360*, 2211.
[21] L. J. McCulloch, M. van de Bunt, M. Braun, K. N. Frayn, A. Clark, A. L. Gloyn, *Mol. Genet. Metab.* **2011**, *104*, 648. https://doi.org/10.1016/j.ymgme.2011.08.026.
[22] A. Zbinden, J. Marzi, K. Schlünder, C. Probst, M. Urbanczyk, S. Black, E. M. Brauchle, S. L. Layland, U. Kraushaar, G. Duffy, K. Schenke-Layland, P. Loskill, *Matrix Biol.* **2020**, *85–86*, 205.
[23] K. Schenke-Layland, J. Xie, E. Angelis, B. Starcher, K. Wu, I. Riemann, W. R. MacLellan, S. F. Hamm-Alvarez, *Matrix Biol.* **2008**, *27*, 53.
[24] O. I. Kolenc, K. P. Quinn, *Antioxidants Redox Signal.* **2019**, *30*, 875.
[25] R. Lehmann, R. A. Zuellig, P. Kugelmeier, P. B. Baenninger, W. Moritz, A. Perren, P. A. Clavien, M. Weber, G. A. Spinas, *Diabetes* **2007**, *56*, 594. https://doi.org/10.2337/db06-0779.
[26] W. Li, R. Zhao, J. Liu, M. Tian, Y. Lu, T. He, M. Cheng, K. Liang, X. Li, X. Wang, et al., *J. Diabetes Res.* **2014**, *2014*, 192093. https://doi.org/10.1155/2014/192093.
[27] K. E. Dionne, C. K. Colton, M. L. Yarmush, *Diabetes* **1993**, *42*, 12.
[28] J. D'Hoker, N. de Leu, Y. Heremans, L. Baeyens, K. Minami, C. Ying, A. Lavens, M. Chintinne, G. Stangé, J. Magenheim, et al., *Diabetes* **2013**, *62*, 4165. https://doi.org/10.2337/db12-1827.
[29] K. S. Sankar, S. M. Altamentova, J. V. Rocheleau, *PLoS One* **2019**, *14*, e0222424.
[30] G. L. Semenza, *Biochem. Pharmacol.* **2002**, *64*, 993.
[31] J. P. Piret, D. Mottet, M. Raes, C. Michiels, *Biochem. Pharmacol.* **2002**, *64*, 889.
[32] A. E. Greijer, E. van der Wall, *J. Clin. Pathol.* **2004**, *57*, 1009.
[33] J. V. Chacko, K. W. Eliceiri, *Cytom. Part A* **2019**, *95*, 56.

[34] K. Suhling, L. M. Hirvonen, J. A. Levitt, P. H. Chung, C. Tregidgo, A. Le Marois, D. A. Rusakov, K. Zheng, S. Ameer-Beg, S. Poland, et al., *Med. Photonics* **2015**, *27*, 3.
[35] G. Solaini, A. Baracca, G. Lenaz, G. Sgarbi, *Biochim. Biophys. Acta - Bioenerg.* **2010**, *1797*, 1171.
[36] A. Chorvatova, S. Aneba, A. Mateasik, D. Chorvat, B. Comte, *J. Biomed. Opt.* **2013**, *18*, 067009.
[37] E. Mullarky, L. C. Cantley, *Innovative Medicine*, Springer, Tokyo, Japan **2015**, p. 3.
[38] W. S. Kunz, W. Kunz, *BBA - Gen. Subj.* **1985**, *841*, 237. https://doi.org/10.1016/0304-4165(85)90064-9.
[39] J. M. Levitt, A. Baldwin, A. Papadakis, S. Puri, J. Xylas, K. Münger, I. Georgakoudi, *J. Biomed. Opt.* **2006**, *11*, 064012.
[40] A. A. Elayat, M. M. El-Naggar, M. Tahir, *J. Anat.* **1995**, *186*(Pt 3), 629.
[41] G. da Silva Xavier, *J. Clin. Med.* **2018**, *7*, 54. https://doi.org/10.3390/jcm7030054.
[42] K. L. Eales, K. E. R. Hollinshead, D. A. Tennant, *Oncogenesis* **2016**, *5*, e190.
[43] J. Cantley, S. T. Grey, P. H. Maxwell, D. J. Withers, *Diabetes Obes. Metab.* **2010**, *12*, 159.
[44] Z. Liu, D. Pouli, C. A. Alonzo, A. Varone, S. Karaliota, K. P. Quinn, K. Mönger, K. P. Karalis, I. Georgakoudi, *Sci. Adv.* **2018**, *4*, eaap9302. https://doi.org/10.1126/sciadv.aap9302.
[45] A. Varone, J. Xylas, K. P. Quinn, D. Pouli, G. Sridharan, M. E. McLaughlin-Drubin, C. Alonzo, K. Lee, K. Münger, I. Georgakoudi, *Cancer Res.* **2014**, *74*, 3067. https://doi.org/10.1158/0008-5472.CAN-13-2713.
[46] P. M. Schaefer, S. Kalinina, A. Rueck, C. A. F. von Arnim, B. von Einem, *Cytom. Part A* **2019**, *95*, 34.
[47] S. Jitrapakdee, A. Wutthisathapornchai, J. C. Wallace, M. J. MacDonald, *Diabetologia* **2010**, *53*, 1019.

SUPPORTING INFORMATION

Additional supporting information may be found online in the Supporting Information section at the end of this article.

How to cite this article: Zbinden A, Carvajal Berrio DA, Urbanczyk M, et al. Fluorescence lifetime metabolic mapping of hypoxia-induced damage in pancreatic pseudo-islets. *J. Biophotonics*. 2020;e202000375. https://doi.org/10.1002/jbio.202000375

Supplement

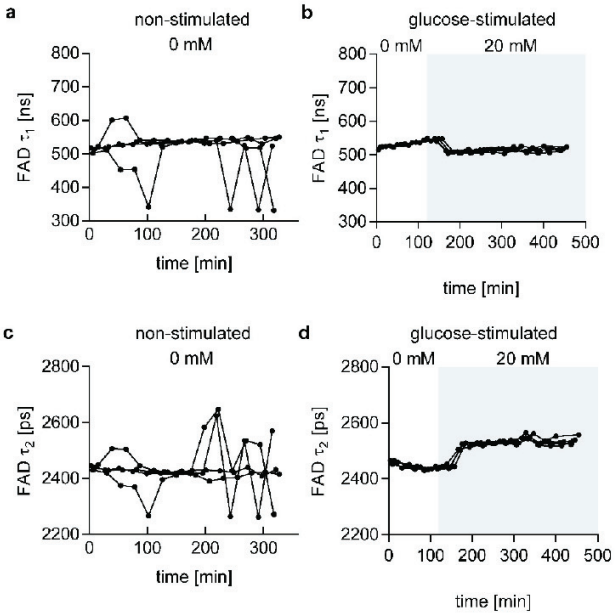

FIGURE S1 In situ FLIM analysis of normoxic pseudo-islets. FLIM analysis over time of non-stimulated pseudo-islets and glucose stimulation with 20 mM showing (a-b) FAD τ_1 and (c-d) FAD τ_2.

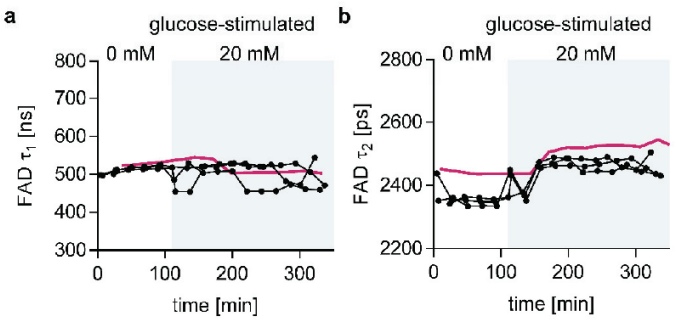

FIGURE S2 In situ FLIM analysis of pseudo-islets cultured under hypoxic conditions for 6 hours. FLIM analysis over time during glucose stimulation with 20 mM showing (**a**) FAD τ_1 and (**b**) FAD τ_2. Hypoxic pseudo-islets are shown in black and a normoxic control is shown in pink.

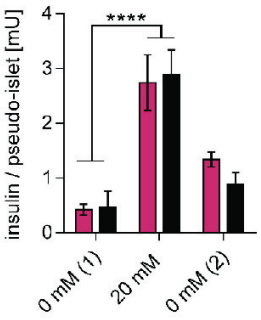

FIGURE S3 Standard GSIS of pseudo-islets under hypoxia (6 hours, pink) and normoxia (black). Pseudo-islets were subjected to subsequent incubation with 0 mM, 20 mM and 0 mM glucose. n = 5. Two-way ANOVA with Dunnett's multiple comparisons test. ****$p < 0.0001$.

Appendix IV: Zbinden A.§, Layland S.L.§, Urbanczyk M., Carvajal D.A., Marzi J., Zauner M., Hammerschmidt A., Brauchle E.M., Sudrow K., Fink S., Templin M., Liebscher S., Klein G., Deb A., Duffy G.P., Crooks G.M., Eble J.A., Mikkola H.K.A., Seifert M. and Schenke-Layland K.; *Nidogen-1 Mitigates Ischemia and Promotes Tissue Survival and Regeneration*, Advanced Science, 2021; 8(4): 2170016.

FULL PAPER

ADVANCED SCIENCE Open Access

www.advancedscience.com

Nidogen-1 Mitigates Ischemia and Promotes Tissue Survival and Regeneration

*Aline Zbinden, Shannon L. Layland, Max Urbanczyk, Daniel A. Carvajal Berrio, Julia Marzi, Monika Zauner, Anne Hammerschmidt, Eva M. Brauchle, Katrin Sudrow, Simon Fink, Markus Templin, Simone Liebscher, Gerd Klein, Arjun Deb, Garry P. Duffy, Gay M. Crooks, Johannes A. Eble, Hanna K. A. Mikkola, Ali Nsair, Martina Seifert, and Katja Schenke-Layland**

Ischemia impacts multiple organ systems and is the major cause of morbidity and mortality in the developed world. Ischemia disrupts tissue homeostasis, driving cell death, and damages tissue structure integrity. Strategies to heal organs, like the infarcted heart, or to replace cells, as done in pancreatic islet β-cell transplantations, are often hindered by ischemic conditions. Here, it is discovered that the basement membrane glycoprotein nidogen-1 attenuates the apoptotic effect of hypoxia in cardiomyocytes and pancreatic β-cells via the $\alpha v\beta 3$ integrin and beneficially modulates immune responses in vitro. It is shown that nidogen-1 significantly increases heart function and angiogenesis, while reducing fibrosis, in a mouse postmyocardial infarction model. These results demonstrate the protective and regenerative potential of nidogen-1 in ischemic conditions.

1. Introduction

Ischemic injury due to the disruption of blood flow can lead to irreversible tissue injury precipitating to neurologic stroke, limb ischemia or myocardial infarction (MI).[1] Ischemic conditions also disrupt regenerative and protective therapies to attenuate cell death and restore organ function, particularly in applications where cell engraftment is required. Strategies to protect cells, modulate the immune response, and repair the tissue milieu within ischemic environments are therefore of critical importance.

The current clinical and preclinical stage strategies that seek to restore organ function post-ischemia include the injection of

A. Zbinden, S. L. Layland, M. Urbanczyk, D. A. Carvajal Berrio, Dr. J. Marzi, S. Liebscher, Prof. K. Schenke-Layland
Department of Bioengineering
Eberhard Karls University Tübingen
Tübingen 72076, Germany
E-mail: katja.schenke-layland@uni-tuebingen.de

A. Zbinden, S. L. Layland, M. Urbanczyk, D. A. Carvajal Berrio, Dr. J. Marzi, Dr. M. Zauner, A. Hammerschmidt, Dr. E. M. Brauchle, S. Liebscher, Prof. K. Schenke-Layland
Department of Women's Health
Research Institute for Women's Health
Eberhard Karls University Tübingen
Tübingen 72076, Germany

D. A. Carvajal Berrio, Dr. J. Marzi, Dr. E. M. Brauchle, Prof. K. Schenke-Layland
Cluster of Excellence iFIT (EXC 2180) "Image-Guided and Functionally Instructed Tumor Therapies"
Eberhard Karls University Tübingen
Tübingen 72076, Germany

The ORCID identification number(s) for the author(s) of this article can be found under https://doi.org/10.1002/advs.202002500

DOI: 10.1002/advs.202002500

Dr. J. Marzi, Dr. E. M. Brauchle, S. Fink, Dr. M. Templin, Prof. K. Schenke-Layland
NMI Natural and Medical Sciences Institute at the University of Tübingen
Reutlingen 72770, Germany

K. Sudrow, Prof. M. Seifert
Institute of Medical Immunology
Charité Universitätsmedizin Berlin
corporate member of Freie Universität Berlin
Humboldt-Universität zu Berlin
Berlin 10117, Germany

K. Sudrow, Prof. M. Seifert
Charité Universitätsmedizin
Berlin Institute of Health (BIH) Center for Regenerative Therapies Berlin (BCRT)
Berlin 10178, Germany

Prof. G. Klein
Center for Medical Research
Department of Medicine II
Eberhard Karls University Tübingen
Tübingen 72076, Germany

Prof. A. Deb, Prof. H. K. A. Mikkola
Department of Molecular
Cell and Developmental Biology
UCLA
Los Angeles CA 90095, USA

cells, growth factors, small molecules, hydrogels or decellularized extracellular matrix (ECM) proteins.[2–4] The ECM is the 3D noncellular component of tissues and organs. It consists of mostly water, proteins, and polysaccharides, and provides the biophysical scaffolding for tissues. The ECM also offers important biochemical and mechanical cues influencing cell homeostasis and differentiation.[5] Ischemia leads to pathological ECM remodeling, resulting in fibrosis due to the deposition of fibrillar proteins, such as collagens type I (COL1) and III, leading to fibrotic scarring.[6] The alteration of ECM proteins can lead to cellular mutations, transdifferentiation or apoptotic death.[7] Basement membranes (BMs) are crucial ECM structures created by networks of collagen type IV (COL4) and laminins (LAM), which are linked by nidogen-1 (NID1). Other macromolecules integrate into BMs to give them unique functions in different tissues.[8] BMs are essential for tissue development and homeostasis.[9] In previous work, we demonstrated the cardiogenic effect of COL4 and LAM in vitro,[10] as well as the role of NID1 in human embryonic stem cell (hESC) assembly.[11] Therefore, we asked whether a single BM protein could have a functional impact on tissue protection or regeneration.[12]

To address the condition of MI, we analyzed the expression of BM proteins during heart development to identify candidates that could protect cardiac tissues during ischemia and support regeneration. NID1, also known as entactin-1,[13] was selected as the lead candidate as it was the most prominent BM protein in hESC-derived cells that were differentiated to the cardiovascular lineages. In vitro and in vivo studies uncovered a novel protective function of NID1 in the cardiovascular system. We also documented a beneficial effect of NID1 on immune cells, which is an essential component of the regenerative process for therapeutic approaches.

To test if NID1 may have a similar effect on other organ systems, therefore potentially supporting a regenerative therapy that is otherwise hindered by ischemic conditions, we choose a model of pancreatic beta cell transplantation, which is a therapy for type 1 diabetes where up to 60% of beta-cell-containing islets fail to engraft due to ischemia at the transplant location and the adverse reaction of the immune system.[14] Here, we demonstrated the protective and functional effect of NID1 on pancreatic beta cells in an ischemia model. Our studies uncovered a novel protective function of NID1 in multiple organ systems in vitro and in vivo and elucidate potential integrin-driven mechanisms of action.

2. Results

2.1. NID1 Is Identified as a Candidate for Cardiovascular Regenerative Approaches

To identify potential therapeutic cardiovascular candidates, the expression of ECM BM proteins was investigated in differentiating hESC-derived embryoid bodies (EBs). We used a modified cardiovascular differentiation protocol for the formation of EBs from the H9 hESC line (Figure S1, Supporting Information).[15,16] Semiquantification of ECM immunofluorescence (IF) staining within spontaneously beating day-10 EBs showed a significantly higher expression of NID1 compared with other well-investigated ECM proteins such as fibronectin (FN), periostin (POSTN), LAM, COL4, and COL1 (**Figure 1**A).[10–18] In addition, NID1 gene expression significantly increased during cardiovascular differentiation (Figure 1B).

To assess if NID1 has a beneficial effect during cardiovascular differentiation, we produced recombinant full length human NID1, available upon request, (Figure S2, Supporting Information) and supplemented it to hESCs that were differentiating toward the cardiovascular lineages. The supplementation of NID1 increased gene expression for cardiac (cardiac troponin T (*TNNT2*)) and smooth muscle (smooth muscle α2-actin (*ACTA2*)) cell markers (Figure 1C). Image-Stream analyses revealed the presence of a significantly higher number of cardiac muscle troponin T $(CTNT)^+$ cells within the NID1-treated cultures when compared with the controls, indicating a potential cardioinductive or cardioprotective effect of NID1 (Figure 1D–F).

The presence of NID1 in native human cardiac tissue was verified both during development (9-, 12-, 17-week embryonic) and in the adult (18 and 51 years) by IF staining (Figure 1G,F; Figure S3A, Supporting Information). The positive correlation of NID1 with cardiovascular development and its presence in human cardiac tissue nominated NID1 as a potential candidate for regenerative and reparative therapies.

2.2. NID1 Improves Heart Function Post Myocardial Infarction

Regenerative and remodeling approaches for post-MI therapies, to modulate infarction size and scar formation, aim to protect

Prof. A. Deb, Prof. G. M. Crooks, Prof. H. K. A. Mikkola, Prof. A. Nsair
Eli and Edythe Broad Stem Cell Research Center
UCLA
Los Angeles CA 90095, USA
Prof. A. Deb, Prof. H. K. A. Mikkola
Molecular Biology Institute
UCLA
Los Angeles CA 90095, USA
Prof. A. Deb, Prof. G. M. Crooks, Prof. H. K. A. Mikkola
Jonsson Comprehensive Cancer Center
UCLA
Los Angeles CA 90024, USA
Prof. A. Deb, Prof. A. Nsair, Prof. K. Schenke-Layland
Department of Medicine/Cardiology
Cardiovascular Research Laboratories
David Geffen School of Medicine at UCLA
Los Angeles CA 90095, USA
Prof. G. P. Duffy
Anatomy and Regenerative Medicine Institute
School of Medicine
College of Medicine Nursing and Health Sciences
National University of Ireland Galway
Galway H91TK33, Ireland
Prof. G. M. Crooks
Department of Pathology and Laboratory Medicine, and Pediatrics
David Geffen School of Medicine at UCLA
UCLA
Los Angeles CA 90095, USA
Prof. J. A. Eble
Institute of Physiological Chemistry and Pathobiochemistry
University of Münster
Münster 48149, Germany
Prof. M. Seifert
DZHK (German Centre for Cardiovascular Research)
partner site Berlin Berlin 10117, Germany

ADVANCED SCIENCE NEWS
www.advancedsciencenews.com

ADVANCED SCIENCE Open Access
www.advancedscience.com

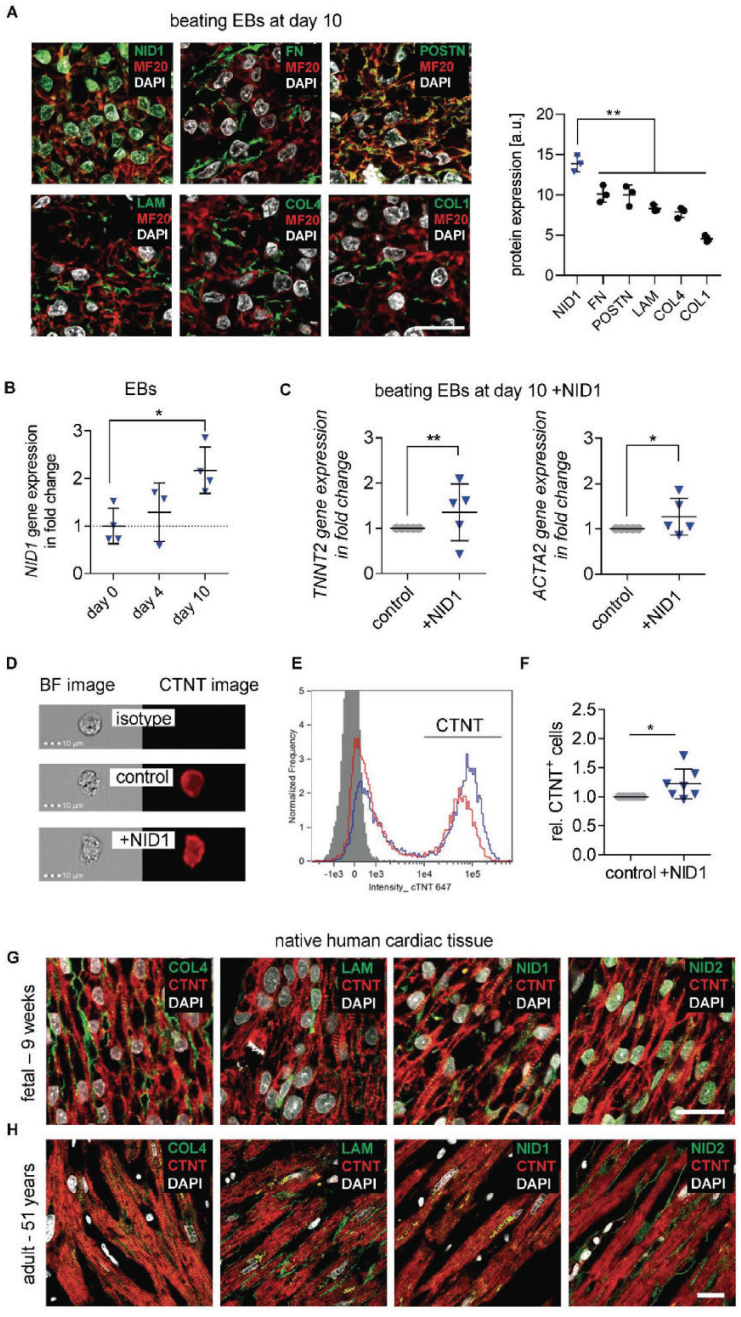

cardiovascular cells from the ischemic environment. We thus asked whether the potential remodeling properties of NID1 could improve the outcome of an MI and reperfusion (MI/R) mouse model. Ischemia/reperfusion was conducted through the ligation of the left anterior descending (LAD) artery in C57BL/6J mice as previously described.[19] Directly after reperfusion, three groups of mice received a single treatment of five injections in the infarct border zone of either saline as a procedure control, the hyaluronic acid (HA) gel carrier as a carrier control, or NID1 within the HA carrier gel (NID1 + HA).

Echocardiography 28 days post MI/R revealed a significant increase of heart ejection fraction (EF) by 19.7% (NID1 + HA 44.6% ± 1.6% versus saline 25% ± 4.8%, $p < 0.001$) (**Figure 2A**) and fractional shortening (FS) by 9.6% (NID1 + HA 21.1% ± 0.8% versus saline 11.5% ± 2.3%, $p < 0.01$) (Figure 2B). Left ventricular (LV) volume and diameter (end-systolic volume (ESV), left ventricle end-systolic diameter (LVES), and left ventricular internal dimension at end -systole (LVIDs)) were all significantly improved in the NID1 + HA-treated hearts when compared with the controls ($p < 0.0001$) (Figure 2C). Significant differences between NID1 + HA and HA treatments were found in EF and FS, as well as in LV volume and diameter. Strikingly, NID1 + HA treatment resulted in a complete recovery in end-diastolic volume (EDV), left ventricular end-diastolic diameter (LVED), and left ventricular internal dimension at end -diastole (LVIDd) when compared with the pre-MI/R baseline (Table S1, Supporting Information); however, the HA-treated hearts also showed a recovery in these values, which should be taken into consideration as the HA carrier gel may have contributed to the positive effect in these parameters.

Mouse hearts from the HA and NID1 + HA-treated groups were excised after the final echocardiography and processed. Russel–Movat pentachrome staining identified qualitative differences between the ECM-rich infarct zone and the surrounding tissue with intact cardiac muscle (Figure 2D–I). Picrosirius Red and Fast Green staining of serial sections throughout the whole heart (Figure 2J,K) were analyzed to identify and quantify scar tissue formation based on hue, saturation, and value (HSV) histograms (Figure S3B, Supporting Information). Scar tissue constituted 13.9% ± 2.6% of the HA-treated hearts and 8.8% ± 1.5% of the NID1 + HA-treated hearts, which is a 37% absolute reduction of scar tissue in the entire heart, not only the LV (Figure 2L).

IF staining of α-smooth muscle actin (αSMA) and CD31 was performed to study the effect of the NID1 + HA treatment on angiogenesis within the infarct zone (Figure 2M–P). The density of $\alpha SMA^+/CD31^+$ vessels in the scar area was significantly increased in the NID1 + HA treatment group when directly compared with the baseline and HA-treated tissues (Figure 2Q).

It has been recently demonstrated that reinnervation is critical for mammalian cardiac regeneration.[20] We used the neuronal marker β-tubulin 3 (TuJ1) to investigate the potential of NID1 + HA to increase nerve protection and innervation of infarcted tissue (Figure 2R–U). Interestingly, we identified a significant twofold increase of $TuJ1^+$ cells in the infarct area of the NID1 + HA-treated hearts compared with the baseline and HA-treated hearts (Figure 2V).

To investigate the scar tissue quality in the infarct areas, Raman microspectroscopy and Raman imaging were employed as noninvasive marker-free techniques to differentiate biochemical spectral fingerprints as previously demonstrated by our group.[21] True component analysis (TCA) and principal component analysis (PCA) identified molecular differences and spatial distribution of spectral information corresponding to myocardium, DNA, and scar tissue (Figure S4A,B, Supporting Information). Interestingly, PCA analysis of the scar fingerprint of the NID1 + HA-treated mice showed peaks associated with glycogen (497 cm^{-1}), porphyrin (1513, 1557, and 1612 cm^{-1}), and DNA (1093 cm^{-1}), while the scar fingerprint of the control mice was dominated by peaks assigned to collagens (858, 940, and 1248 cm^{-1}), which indicates that the scar tissue in the treated mice resembled the molecular fingerprint of the noninfarcted myocardium connective tissue (Extended Data in Figure S4C–G and Table S2, Supporting Information). Taken together, these data demonstrate that NID1 positively affects heart function, angiogenesis, scar size, and scar tissue quality in a therapeutic model.

2.3. NID1 Protects Cardiovascular Cells in an Ischemia In Vitro Model

To elucidate the therapeutic effect of NID1 in vitro, human induced-pluripotent stem cell-derived (hiPSC) iCell cardiomyocytes (CMs) were investigated in a hypoxia (1% oxygen) ischemia-like in vitro model. For two days, NID1-treated and control hiPSC-CMs were cultured under normoxic and hypoxic conditions and evaluated for cell death via the expression of cleaved caspase-3 and the number of $TUNEL^+$ cells (**Figure 3A,B**). NID1-treated hiPSC-CMs had a significantly lower expression of cleaved caspase-3 and a reduced the number of $TUNEL^+$ cells in hypoxic conditions when compared with nontreated controls. No changes were observed in normoxic cultures in the presence of NID1.

PCR array analysis of the expression of human ECM and adhesion molecules in NID1-treated hiPSC-CMs identified several significantly up and downregulated genes (Figure 3C). In hypoxic conditions, NID1-treated hiPSC-CMs showed significantly

Figure 1. ECM BM protein NID1 is identified as a candidate for regenerative approaches. A) IF staining and semiquantification of BM proteins NID1, FN, POSTN, LAM, COL4, and COL1, as well as DAPI and MF20 in day-10 beating EBs. Gray value intensities (GVI) of IF images were normalized to the laser intensity ($n = 3$), one-way ANOVA with Tukey's multiple comparisons test. B) qPCR analysis of *NID1* expression on day 0 (undifferentiated hESCs), and after 4 and 10 days (beating EBs) of cardiovascular differentiation. Data are normalized to the average of day 0 and shown as fold change ($n = 3$–4); one-way ANOVA with Tukey's multiple comparisons test. C) qPCR analysis of *TNNT2* and *ACTA2* gene expression within EBs at day 10 of cardiovascular differentiation without (control) and with NID1 ($n = 5$); Kolmogorov–Smirnov *t*-test. D) Bright field (BF) and CTNT IF images of single cells derived from EBs that were cultured for 10 days without (control) and with NID1 acquired with 40× magnification using imaging flow cytometry. An isotype control is provided. E) Representative histogram of cells that were cultured for 10 days with (blue) or without (red) NID1. The isotype control is shown in gray. F) Quantification of the data obtained by imaging flow cytometric analysis showing the relative amount of $CTNT^+$ cells derived from EBs that were cultured for 10 days without (control) and with NID1 ($n = 7$); Kolmogorov–Smirnov *t*-test. G,H) IF staining of BM proteins COL4, LAM, NID1, NID2, as well as DAPI and sarcomeric myosin CTNT within human (G) fetal heart sections (9 weeks postgestation) and (H) adult heart tissue (51 years). Scale bars: 20 μm. $^*p < 0.05$, $^{**}p < 0.01$, $^{***}p < 0.001$, and $^{****}p < 0.0001$.

ADVANCED SCIENCE NEWS
www.advancedsciencenews.com

ADVANCED SCIENCE Open Access
www.advancedscience.com

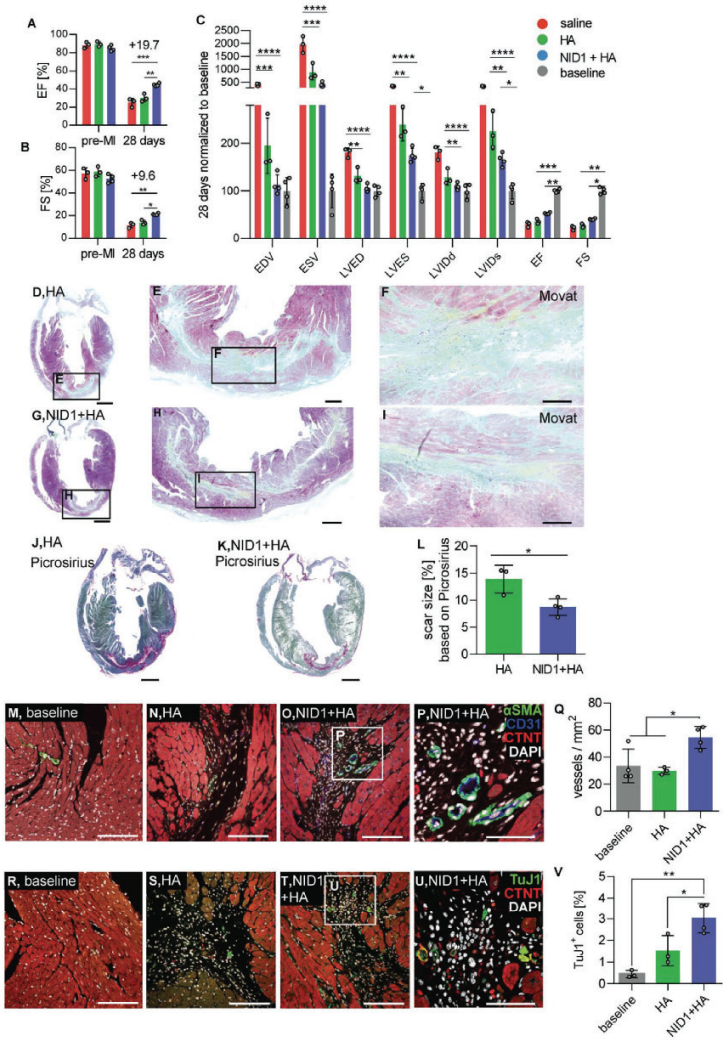

Figure 2. NID1 increases heart function post-MI. A–C) Echocardiography analysis: absolute values of (A) EF and (B) FS after intracardiac injections of saline, HA and 50 µg mL^{-1} NID1 + HA at 28 days post-MI/R, and C) parameters were normalized to the baseline at 28 days post-MI/R. Echocardiography data were analyzed by one-way ANOVA with Tukey's multiple comparisons test. D–I) Movat pentachrome staining of representative sections of (D–F) HA- and (G–I) NID1 + HA-treated hearts after 28 days post-MI/R with scar tissue stained in green and yellow. Scale bars: (D,G) 1 mm, (E,H) 200 µm, and (F,I) 100 µm. J,K) Picrosirius Red and Fast Green staining of representative (J) HA- and (K) NID1 + HA-treated heart sections with scar tissue stained in pink. Scale bars: 1 mm. L) Quantification of scar size in Picrosirius Red- and Fast Green-stained serial sections. Whole-heart scans of every tenth slide throughout the whole heart were analyzed. M–P) Confocal images of αSMA, CD31, and CTNT IF staining of representative (M) baseline, (N) HA-, and (O) NID1 + HA-treated heart sections obtained with a 25× magnification (scale bar: 100 µm), and with a P) 63× magnification (scale bar; 50 µm). Q) Quantification of vessel density within the infarct area using images obtained with a 25× magnification. R–U) Images of TuJ1 and CTNT IF staining of representative (R) baseline, (S) HA-, and (T) NID1 + HA-treated tissue sections obtained with a 25× magnification (scale bar equal 100 µm), and a (U) 63× magnification (scale bar: 50 µm). V) Quantification of TuJ1^{+} cells within the infarct area. For all MI/R studies saline mice ($n = 3$), HA mice ($n = 3$), NID1 + HA-treated mice ($n = 4$) were used, unpaired t-test. *$p < 0.05$, **$p < 0.01$, ***$p < 0.001$, ****$p < 0.0001$. LVIDd: left ventricular internal dimension at end diastole, LVIDs: left ventricular internal dimension at end-systole, LVED: left ventricle end-diastolic diameter, LVES: left ventricle end-systolic diameter, EDV: end-diastolic volume, ESV: end-systolic volume, EF: ejection fraction, FS: fractional shortening.

ADVANCED SCIENCE NEWS
www.advancedsciencenews.com

ADVANCED SCIENCE Open Access
www.advancedscience.com

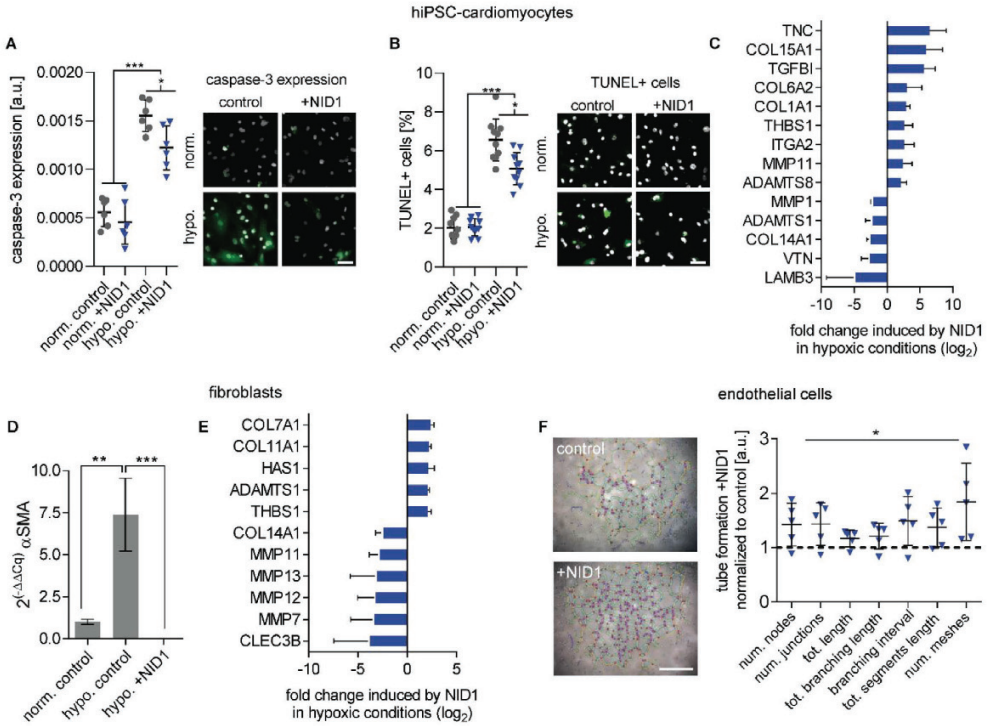

Figure 3. NID1 mitigates the effects of hypoxia on cardiovascular cells. A,B) Protective effect of NID1 on hiPSC-CMs shown by (A) cleaved caspase-3 staining and semiquantification ($n = 6$) and (B) by number of TUNEL$^+$ cells over total cell number ($n = 10$); one-way ANOVA with Tukey's multiple comparisons test. C) qPCR array analysis of NID1-treated hiPSC-CMs under hypoxic conditions with a focus on matrix production, degradation, and regulation ($n = 3$). D) qPCR analysis for the expression of αSMA in control fibroblasts under normoxic and hypoxic conditions, as well as for NID1-treated fibroblasts under hypoxic conditions ($n = 3$). One-way ANOVA with Tukey's multiple comparisons test. E) qPCR array analysis of NID1-treated fibroblasts under hypoxic conditions (identical qPCR array as in (C)) ($n = 3$). F) Tube formation assay performed using 1.5×10^4 HUVECs/0.32 cm^2 with serum-reduced Matrigel without (control) or with NID1 ($n = 4$–5). Quantification of different tube formation parameters using the angiogenesis analyzer of the ImageJ software. Data are normalized to the Matrigel control (set as 1), one-way ANOVA with Tukey's multiple comparisons test. For qPCR, gene regulation by NID1 is shown when fold-regulation > |2|, p-value < 0.05. *$p < 0.05$; **$p < 0.01$, ***$p < 0.001$, and ****$p < 0.0001$. Scale bars: 50 µm.

upregulated expression levels for *TNC*, *THBS1*, *ITGA2*, *ADAMTS8*, *MMP11*, and several collagens such as *COL1A1*, *COL6A2*, and *COL15A1*. Interestingly, *TGFB1* was significantly upregulated in both normoxic and hypoxic NID1-treated hiPSC-CMs (Figure S5A, Supporting Information). *LAMB3*, *VTN*, *COL14A1*, *ADAMTS1*, and *MMP1* were significantly downregulated in NID1-treated hiPSC-CMs under hypoxic conditions. Of the transcriptional changes in ECM-associated genes in hiPSC-CMs induced by hypoxic conditions, 28 genes out of a total of 89 genes tested were significantly differentially expressed compared to the normoxic groups. In NID1-treated hiPSC-CMs, transcriptional changes induced by hypoxia were minimal with only one differentially expressed gene (*COL14A1*) (Figure S5B, Supporting Information).

Hypoxia is known to induce a phenotypic switch from fibroblasts to myofibroblasts, which is the cell population producing the majority of the structural ECM proteins during fibrosis.[22] The phenotypic switch to myofibroblasts can be assessed by α-SMA expression and was observed in our control fibroblasts (Figure 3D). Interestingly, the expression of α-SMA was significantly reduced in NID1-treated fibroblasts. Gene expression analysis of fibroblasts showed that *MMP7*, *MMP11*, *MMP12*, *MMP13*, *COL14A1*, and *CLEC3B* were significantly downregulated by NID1; and *COL7A1*, *COL11A1*, *HAS1*, *ADAMTS1*, and *THBS1* were significantly upregulated by NID1 (Figure 3E). Exposure to hypoxic conditions resulted in significant up- or downregulation of 26 genes in the control group, while only 11 genes were impacted in NID1-treated fibroblasts (Figure S5C, Supporting Information).

The MI/R model data showed an increased number of αSMA$^+$/CD31$^+$ vessels in the NID1-treated infarcted hearts. To test the angiogenic potential of NID1, a human umbilical vein

endothelial cell (HUVEC) tube formation assay was performed. NID1 significantly increased a variety of angiogenesis parameters including the total segment length, number of meshes, and total mesh area, as well as number of segments (Figure 3F).

Our data shows that NID1 supports angiogenesis and cardiovascular cell homeostasis during hypoxia and provides an antifibrotic effect on fibroblasts, elucidating the cellular events underlying the positive functional effect of NID1 in the therapeutic model.

2.4. NID1 Protects Pancreatic β-Cells and Increases Insulin Secretion in an In Vitro Ischemia Model

We next asked if the protective and antifibrotic effect of NID1 during ischemia is organ-specific or would be of benefit in other noncardiac therapeutic areas, such as islet transplantation, where ischemia and the survival of transplanted islets are a major therapeutic roadblock. The presence of BM proteins COL4, LAM, NID1, and nidogen-2 (NID2) was confirmed in human 11-week fetal and 64-year adult pancreatic tissues by IF staining (**Figure 4**A,B). Interestingly, in adult tissues, NID1 was spatially confined to insulin-producing β-cells in contrast to other BM proteins, suggesting that NID1 has a specific function in β-cells (Figure 4C).

To determine if NID1 impacts β-cell functionality, we established an in vitro hypoxia model using β-cell aggregates, so-called pseudoislets, using the conditionally immortalized human EndoC-βH3 cell line (Figure S6A–I, Supporting Information). The impact of dosages of 20, 30, and 40 µg mL^{-1} NID1 on pseudoislet function was first assessed under normoxic conditions. NID1-treated pseudoislets significantly increased insulin secretion at all dosages; with 30 µg mL^{-1} reaching the maximum effect, which was the dosage chosen for all further pseudoislet experiments (Figure 4D). IF staining of NID1-treated pseudoislets cultured under normoxic conditions showed a significant increase in E-cadherin when compared with the controls (Figure 4E). NID1 had no effect on cell death under normoxic conditions, assessed by the quantification of TUNEL$^+$ cells and cleaved caspase-3 staining (Figure 4F). In hypoxic conditions, NID1 rescued the loss of insulin secretion that was lost in control cultures, preserved the significant increase in E-cadherin seen in normoxia, and significantly reduced cell death (Figure 4G–I).

Raman imaging with TCA analysis and multivariate curve resolution confirmed that NID1 enhances β-cell function in hypoxia, particularly in the pseudoislet core, by an increase in mitochondrial function, insulin, and insulin-transporting lipid vesicles (Figure S6J–P, Table S2, Supporting Information).[23] These data demonstrate the protective and stimulative effect of NID1 on pancreatic β-cells.

2.5. NID1 Modulates Immune Cell Responses toward Regeneration

Our data nominated NID1 as a potential therapeutic candidate. Therefore, its interaction with immune cells of the innate and adaptive system was evaluated in vitro utilizing a previously described human-based assay.[24] Briefly, a chemotaxis assay was performed to measure the impact of NID1 on human CD14$^+$ blood monocyte migration (**Figure 5**A). CD14$^+$ blood monocyte migration is an important process to clear the tissue of debris from apoptotic cells and disrupted ECM, thereby inducing normal tissue remodeling. Significant migration was detected for the 50 µg mL^{-1} NID1-treated CD14$^+$ monocytes compared with the negative control. Measuring the induced short-term tumor necrosis factor alpha (TNFα) release from human monocytes showed negligible TNFα levels for a NID1 dosage up to 50 µg mL^{-1} compared with the lipopolysaccharide (LPS) control (Figure 5B).

To determine the influence of NID1 on macrophage polarization, unpolarized M0 macrophages were exposed to NID1 for 24 h. The macrophages were of rounded morphology with a tendency to arrange in clusters. This appearance was qualitatively more similar to an alternatively activated/regenerative (M2) macrophage, since classically activated/proinflammatory (M1) macrophages have a more elongated cell shape (Figure 5C). Flow cytometry studies detecting the surface molecules HLA-DR, CD80, CD206, and CD163 confirmed that NID1-treated macrophages did not develop an M1 phenotype (Figure 5D). Cytokine analysis of supernatants from NID1-treated macrophages confirmed the absence of M1 macrophage induction. Rather, a profile was detected that is characteristic for M0 or M2 macrophages with low levels of IL-6 and TNFα (Figure 5E).

T cell subsets with diverse functions can also influence the inflammatory milieu and the remodeling process, for example, post-MI in heart tissue.[25] Therefore, we studied the impact of NID1 on preactivated T cells by measuring its effect on anti-CD3 (aCD3)-induced proliferation of classical T cell subsets. NID1 provided an additional trigger to CD4$^+$ T cells, but not to the cytotoxic CD8$^+$ T cell fraction (Figure 5F). The release of the proinflammatory cytokines TNFα and IFNγ was significantly reduced in 5-day cultures of NID1-treated aCD3-activated immune cells (Figure 5G). A standardized cytotoxicity test was performed according to EN ISO 10993. With this test, we assessed the metabolic activity of primary-isolated human dermal fibroblasts to determine a potential cytotoxic effect of NID1 as requested by certification bodies such as the European Medicines Agency (Figure 5H). As a complementary test, cytotoxicity of NID1 was also investigated using human primary-isolated cardiac fibroblasts (Figure 5I). We observed no cytotoxic effect due to NID1 exposure in the tested concentrations of 50, 100, and 200 µg mL^{-1}. Interestingly, we noted an increased metabolic activity of both dermal and cardiac fibroblasts in the NID1-treated groups compared with controls. These data show the regenerative immunomodulatory effect of NID1 in a human in vitro system and the safety of NID1 at dosages up to 50 µg mL^{-1}, supporting the therapeutic potential of NID1.

2.6. NID1 Signals via Integrin $\alpha v\beta 3$ and Activates the MAPK Pathway

Understanding the mechanistic function of a therapeutic biomolecule is required before entering clinical trials. Here, we sought to elucidate the mechanisms driving the function of NID1 during hypoxic events. The integrin $\alpha v\beta 3$ has been reported as a binding partner for NID1 and is expressed on the cells of human Langerhans islets and on CMs.[26 28] NID1 and $\alpha v\beta 3$

ADVANCED SCIENCE NEWS
www.advancedsciencenews.com

ADVANCED SCIENCE Open Access
www.advancedscience.com

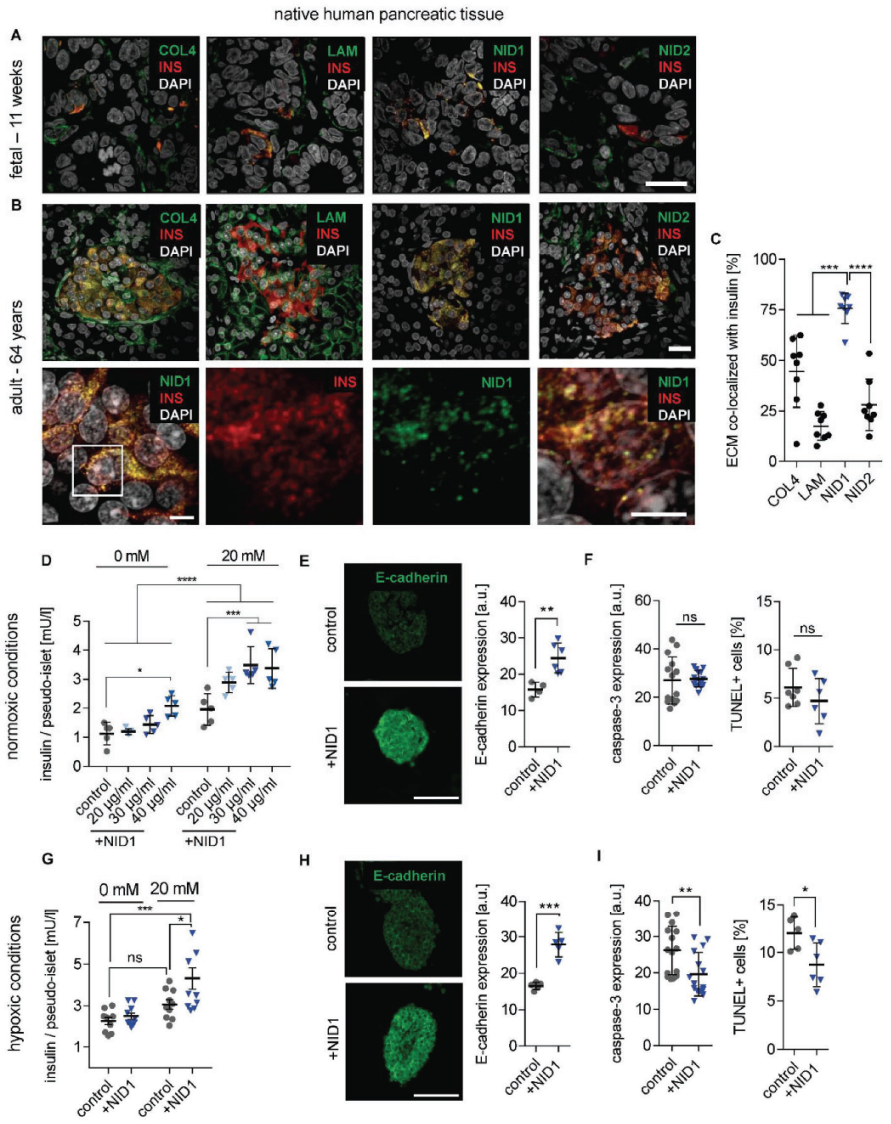

Figure 4. NID1 mitigates the effects of hypoxia on pancreatic β-cells and increases insulin secretion. A,B) Expression pattern of BM proteins, insulin (INS), and DAPI in human (A) fetal (11 weeks postgestation) and (B) adult pancreas (64 years). Scale bars: 20 µm. Highly magnified images show the colocalization of NID1 with INS in native adult pancreas. Scale bar: 5 µm. C) Quantification of the colocalization of ECM proteins with INS ($n = 10$), one-way ANOVA with Tukey's multiple comparisons test. D) GSIS response (with 0×10^{-3} and 20×10^{-3} M glucose) under normoxic conditions of human NID1-treated pseudoislets in suspension at different concentrations: 20, 30, 40 µg mL^{-1} when compared with the control (PBS) ($n = 5$); two-way ANOVA with Tukey's multiple comparisons test. E) E-cadherin expression under normoxic conditions ($n \geq 5$). F) Cell death under normoxic conditions via the detection of cleaved caspase-3 ($n = 14$) and TUNEL$^+$ cells ($n = 7$). G) GSIS response (with 0×10^{-3} and 20×10^{-3} M glucose) under hypoxic conditions of NID1-treated pseudoislets at 30 µg mL^{-1} and normalized by live cells ($n = 10$); two-way ANOVA with Tukey's multiple comparisons test. H) E-cadherin expression under hypoxic conditions ($n \geq 5$ M; unpaired t-test. I) Protective effect of NID1 assessed by cleaved caspase-3 expression ($n \geq 7$). and via detection of TUNEL$^+$ cells ($n \geq 4$); unpaired t-test. $^*p < 0.05$; $^{**}p < 0.01$, $^{***}p < 0.001$, and $^{****}p < 0.0001$.

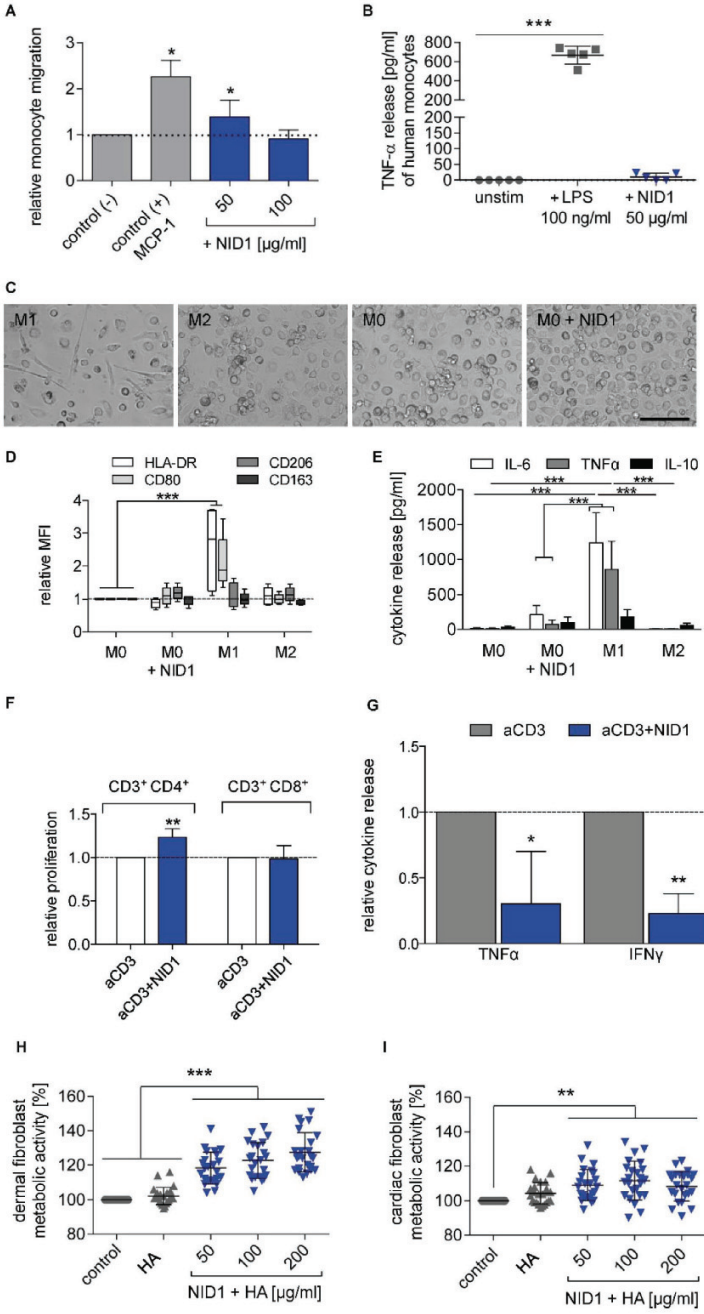

binding was confirmed at the protein level by titration of immobilized $\alpha v\beta 3$ with soluble NID1 (**Figure 6**A). No fixation was employed, as this would have altered the protein binding. Coating of 4 μg mL^{-1} of $\alpha v\beta 3$ was sufficient to have a specific ELISA signal of bound NID1 in the presence of Mn^{2+} when compared with NID1 in EDTA, indicating a divalent cation-dependent interaction of NID1 and $\alpha v\beta 3$ integrin. In addition, the binding was dose-dependent as a specific ELISA signal was detected starting between 25 and 50 μg mL^{-1} of NID1 (corresponding to ≈0.167×10^{-6} M to 0.334×10^{-6} M).

Blocking of the $\alpha v\beta 3$ integrin on pseudoislets and hiPSC-CMs was performed to investigate whether the positive effect of NID1 is mediated through the activation of the $\alpha v\beta 3$ integrin (Figure 6B–D). Blocking of NID1-treated pseudoislets with an $\alpha v\beta 3$ antibody inhibited the increase in insulin secretion under normoxia (Figure 6B). Blocking $\alpha v\beta 3$ integrin in NID1-treated hiPSC-CMs under hypoxic conditions negated the decrease in apoptosis seen in nonblocked NID1-treated hiPSC-CMs in caspase-3 staining and TUNEL assay (Figure 6C,D). These data indicate that $\alpha v\beta 3$ is involved in mediating the interaction of NID1 with β-cells and CMs.

A novel high-throughput digital Western blot platform (DigiWest) was employed to investigate the specific biological pathways that are mediated by NID1 in β-cells and CMs cultured under hypoxic conditions.[29] NID1-treated β-cells showed a significantly upregulated expression of EpCAM, Erk 2, pFyn, p21, Src, pSrc, Wnt3, and a trend toward the upregulation of pMEK1/2 (Figure 6E,F). NID1 treatment of hiPSC-CMs led to an upregulation of Bax, pErk 1/2, SAPK, MOB1, Rac1/cdc42, and Wnt3 (Figure 6G,H) Downregulation was observed for b-Raf, pFAK, and Notch2. Bax and SAPK protein contents were normalized by Bcl2 and Erk1,2 in order to determine whether proapoptotic pathways have been activated. Ratios of Bax/Bcl2 and SAPK/Erk1,2 showed no significant difference between NID1-treated and control cultures (Figure 6I,J), which indicates that the increase in Bax and SAPK in the NID1-treated hiPSC-CMs had been offset by an increase in Bcl2 and Erk.[30,31] All target proteins tested and the resulting protein regulation are shown as heatmaps in Figure S7 of the Supporting Information. The hypothetical pathways associated with NID1 are proposed in Figure 6K. Here, we have shown that NID1 binds and signals through integrin $\alpha v\beta 3$ as seen by the upregulation of pFyn, Src, pSrc, and Rac1/cdc42. This leads to the activation of the mitogen-activated protein kinases (MAPK) pathway, including the kinases extracellular signal-regulated kinase 1/2 (Erk 1/2) and mitogen-activated protein kinase 1/2, which is driving the protective effects of NID1 both on β-cells and CMs.

3. Discussion

In this study, we report the protective and immune-modulatory effects of NID1 on cells and tissues of the cardiovascular, pancreatic, and immune system. We demonstrate the therapeutic efficacy of NID1 by a significant improvement in heart function post-MI/R in a preclinical mouse model and discovered a promising new avenue to improve the outcome of β-cell transplantation. We propose that the effect of NID1 is mediated by the $\alpha v\beta 3$ integrin leading to the activation of the MAPK pathway in both CMs and β-cells.

NID1 is an underinvestigated ECM BM protein that is mostly recognized as a linker protein of COL4 and LAM.[32] It has been suggested to play a role in angiogenesis, hepatic regeneration, and regenerative axon growth and guidance.[33–36] Here, the identification of NID1 as the highest expressed BM component during cardiovascular differentiation, and the important role of BM proteins in organogenesis suggested that NID1 may have a regenerative or protective effect on the ischemic heart. The heart has a highly limited capacity for regeneration; therefore, current treatment strategies seek to restore cardiac function by methods such as cell injections into the infarct border zone, and delivering growth factors and small molecules or ECM proteins to activate or modify native cardiac cells.[37,38] Despite promising results, many of these approaches have questionable or unknown safety profiles, hindering their clinical translation. We propose a simplified strategy of one ECM protein that has a potential supportive effect on immune cells, as opposed to an inflammatory effect. The therapeutic ability of NID1 was demonstrated by an improved heart function in a post-MI/R mouse model as demonstrated by elevated EF and FS, as well as the recovery of EDV, LVED, and LVIDd. Moreover, in vitro studies showed that NID1 suppresses the transdifferentiation of fibroblasts into fibrillar ECM-secreting myofibroblasts, potentially enhancing the significant reduction of fibrosis seen in vivo. The ECM protein agrin was previously shown to improve heart function post-MI through CM division and proliferation.[39] Our findings are unique as we show that NID1 improves heart function by the protection of CMs and potential regeneration of other heart cells. Interestingly, both NID1 and agrin activate the MAPK pathway in CMs; however, NID1 ligates the $\alpha v\beta 3$ integrin and agrin ligates Dag1.

Figure 5. NID1 modulates immune cells. A) CD14$^+$ monocyte migration in the presence of different NID1 concentrations (50, 100 μg mL^{-1}) and the control protein MCP-1 after 3 h. Cell migration is shown relative to the control (–) ($n = 3$ experiments with 9 single values); one-way ANOVA with Dunnett's multiple comparison test. B) Potential endotoxin contamination was tested by adding 50 μg mL^{-1} NID1 or 100 ng mL^{-1} LPS in a monocyte culture for 24 h. Released TNFα was measured by ELISA ($n = 5$); Friedman test with Dunn's multiple comparison test. C) Representative images of M1- and M2-type macrophages, unstimulated M0-type macrophages and NID1-treated M0-type macrophages. Scale bar: 100 μm. D) Expression of polarization markers (HLA-DR, CD80, CD206, CD163) was determined for M0-type macrophages cultured for 24 h with 50 μg mL^{-1} NID1, M0, M1, and M2-type macrophages. Mean fluorescence intensity (MFI) is shown relative to the untreated M0 macrophage control (set as 1) ($n = 5$); two-way ANOVA with Dunnett's multiple comparison test. E) Release of IL-6, TNFα, and IL-10 after 24 h culture of M0 macrophages with NID1 (50 μg mL^{-1}) and M0, M1 or M2 type cultures ($n = 5$); two-way ANOVA with Tukey's multiple comparison post-test. F) T cell proliferation after 5 days culture of human PBMCs with low-dose aCD3 alone or combined with NID1 (50 μg mL^{-1}) was tested in a CFSE-based assay and measured by flow cytometry. Shown is the relative proliferation level of CD3$^+$ CD4$^+$ and CD3$^+$ CD8$^+$ T cells compared to the aCD3 control. G) Relative TNFα and IFNγ release of PBMC cultures after 5 days with either aCD3 alone or combined with NID1 (50 μg mL^{-1}). Data for proliferation and cytokine release were analyzed by Kolmogorov–Smirnov *t*-test, relative to the aCD3 control ($n = 6$). H) Cytotoxicity test using human dermal fibroblasts (EN ISO 10993) or I) cardiac fibroblasts. Cell viability was measured after treatment with control medium, HA hydrogel, and HA-supplemented with NID1 (50, 100, and 200 μg mL^{-1}) for 24 h. Cell viability is shown relative to the control (set as 100% viability) ($n \geq 22$); one-way ANOVA with Tukey's multiple comparisons test: $^*p < 0.05$, $^{**}p < 0.01$, $^{***}p < 0.001$, and $^{****}p < 0.0001$.

ADVANCED SCIENCE NEWS
www.advancedsciencenews.com

ADVANCED SCIENCE Open Access
www.advancedscience.com

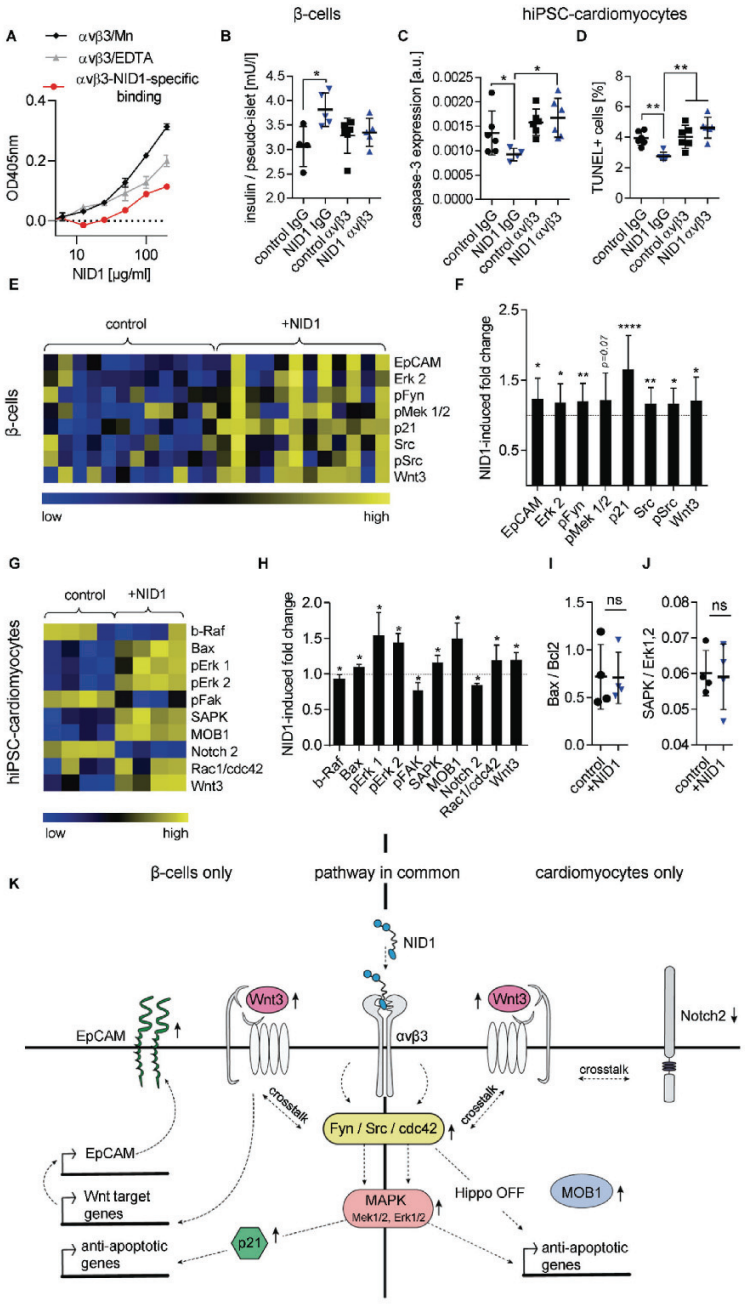

Our functional data suggest that NID1 is also applicable in other therapeutic applications where ischemia and fibrosis hinder therapeutic efficacy, such as in islet β-cell transplantation. During the first week of islet transplantation, fibrosis encapsulates the transplant delivery device, and the lack of oxygen supply causes the loss of β-cell mass, restricting the patient's insulin independency.[40] Interestingly, NID1 was the only BM protein to have a specific spatial distribution that exclusively colocalized with insulin-producing β-cells. In vitro data showed that NID1 has a protective effect on β-cells under hypoxic conditions and has a direct impact on insulin secretion in a dose-dependent manner. This suggests that NID1 could be used as a protective and functional molecule during islet transplantation as it could enhance angiogenesis and reduces fibrosis around the device while improving β-cell function and survival within.

We discovered that full length human NID1 binds to human integrin $\alpha v\beta 3$ in a divalent cation-dependent way, and that $\alpha v\beta 3$ is the primary binding ligand driving the therapeutic effect of NID1 on CMs and β-cells. The combination of gene and protein expression analysis confirmed the activation and downstream signaling of the $\alpha v\beta 3$ via the MAPK pathway in hiPSC-CMs and β-cells. MAPK effectors such as Erk 1/2 are expressed following oxidative stress in CMs, which protect them from apoptosis in vitro and in vivo.[41] In addition, the MAPK pathway is essential for glucose-stimulated insulin secretion in β-cells.[42] In CMs, an additional protective mechanism may be provided by shutting down the Hippo pathway, which has been described to inhibit adult cardiac regeneration.[43] Wnt signaling, which may arise through $\alpha v\beta 3$ downstream signaling, is involved in β-cell insulin secretion, as well as cellular survival in both cell types.[44,45] The MAPK and Wnt pathways as well as the stimulation of the $\beta 3$ integrin are known activators of *TNC* expression.[46] *TNC* is involved in CM detachment from the ECM that allows surviving CMs to reorganize and rebind to the ECM thus protecting CMs from anoikis.[47] *TNC* and *THSP1* are known activators of TGF-β signaling, which regulates the inflammatory response in the postinfarcted heart and the deposition of fibrous tissue.[48] Taken together, our data uncovered the key mechanisms of NID1 action in vitro, providing insight into the therapeutic function of NID1 seen in vivo.

It is well established that the ECM has a modulatory function on a variety of immune cells. Monocytes migrate to injured tissue and polarize to distinct macrophage phenotypes depending on the surrounding tissue milieu.[49] We identified in vitro a significant migration of CD14+ monocytes in the presence of NID1 and the influence of macrophage polarization toward a phenotype with characteristics of both the M0 and the regenerative M2 phenotype, but not the pro-inflammatory M1 phenotype. It was previously shown that NID1 binds to natural killer cells via NKp44, mediating an inhibitory effect seen by the reduction of cytokine release such as IL-2 and IFNγ.[50] We demonstrated a similar reduction of proinflammatory cytokine secretion such as TNFα and IFNγ in activated T cells by NID1, indicating the anti-inflammatory potential of NID1. Taken together with recent research showing that macrophages contribute collagen to scar formation, the NID1-mediated modulation of macrophages may play an important role in the reduction of scar tissue seen in this study.[51]

4. Conclusion

In summary, in our study, in vitro and in vivo models demonstrated that NID1 increases cardiogenesis, angiogenesis, and cell survival, while beneficially modulating immune responses and reducing fibrosis. Mechanistically, NID1 was shown to ligate the $\alpha v\beta 3$ integrin to activate the Erk 1/2-MAPK and Wnt pathways in cardiomyocytes and pancreatic β-cells. In a preclinical mouse model, a single treatment with an NID1-functionalized gel significantly increased heart function post-MI. These data demonstrate the positive effect of NID1 on ischemic cells and tissues from different organs, suggesting that it may have multiple clinical applications as an off-the-shelf product.

5. Experimental Section

hESC Cultures and Cardiovascular Differentiation: The use of hESCs (H9, passages 36–60, WiCell) was approved by the Robert Koch-Institute, Berlin, Germany (AZ: 3.04.02/0086). hESCs were maintained according to WiCell feeder-dependent Pluripotent Stem Cell Protocols, SOP-SH-001, version G, on mouse embryonic fibroblasts (AMS Biotechnology (Europe) LTD) in stem cell growth medium. For EB generation, 3×10^4 cells of an H9 single cell suspension in mTeSR1 (STEMCELL Technologies), supplemented with 10 ng mL^{-1} BMP4 and 10 ng mL^{-1} ROCK inhibitor Y-27632 (Sigma-Aldrich), were centrifuged per 96-well (nontreated, conical bottom, Thermo Fisher Scientific) at 1000 rpm for 5 min and incubated overnight. Two previously described protocols were modified for cardiovascular differentiation.[15,16] On day 1, after the overnight incubation, up to 200 EBs were transferred to one ultralow attachment 6-well well (Corning Inc.) in 3 mL of stage 1 media (StemPro 34 (Life Technologies), 3 ng mL^{-1} activin A, 5 ng mL^{-1} bFGF, 10 ng mL^{-1} BMP4). On day 4, the floating EBs were transferred to a 6-well plate, coated with 0.1% gelatin or 0.1% gelatin-supplemented with or without 50 µg mL^{-1} nidogen-1 (NID1) and cultured in 2 mL^{-1} of stage 1 media + 5×10^{-6} M inhibitor of WNT response-1 (IWR-1). The EBs were incubated for 24 h to allow attachment. The attached EBs were differentiated in stage 2 media (StemPro 34, 5 ng mL^{-1} VEGF, 10 ng mL^{-1} bFGF, 5×10^{-6} M IWR-1) from day 5 to day 10.

Figure 6. NID1 signals via $\alpha v\beta 3$ and activates the MAPK pathway in β-cells and cardiomyocytes. A) Divalent cation-dependent and dose-dependent binding of $\alpha v\beta 3$ with NID1. B) Blocking of $\alpha v\beta 3$ in NID1-treated and control pseudoislets under normoxic conditions. Functionality assessment by glucose stimulation at 20×10^{-3} M glucose ($n \geq 4$); one-way ANOVA with Tukey's multiple comparisons test. c,d) Blocking of $\alpha v\beta 3$ in NID1-treated and control hiPSC-CMs by a $\alpha v\beta 3$ antibody under hypoxic conditions. Protective effect of NID1 assessed by C) cleaved caspase-3 ($n \geq 4$) and D) TUNEL assay ($n = 6$); one-way ANOVA with Tukey's multiple comparisons test. E–H) DigiWest-based protein expression analysis of significantly regulated proteins in NID1-treated E,F) pseudoislets ($n = 12$) and G,H) hiPSC-CMs ($n = 4$) under hypoxic conditions compared with their respective controls. Data are (E,G) shown as column-wise and color-coded heatmap from the lowest (blue) to the highest (yellow) expression for each analyte; and (F,H) quantified as fold change induced by NID1. Nonparametric Wilcoxon Rank sum test. I,J) Protein ratios of (I) Bax to Bcl2 and (J) SAPK to Erk1,2 ($n = 4$); unpaired t-test. K) Proposed common and separate mechanisms of action of NID1 for CMs and β-cells in vitro. Middle: common pathway, NID1-$\alpha v\beta 3$ ligation upregulating Fyn/Src in β-cells and cdc42 in CMs, which stimulates Wnt3 and the MAPK pathway. Left: β-cells, Fyn/Src activates the MAPK pathway, upregulating p21, which can be antiapoptotic. Fyn/Src crosstalks with Wnt3 and EpCAM, which enhances insulin secretion. Right: CMs, cdc42 downregulates the Hippo pathway as shown by an upregulation of MOB1. Pathways specific for each cell type are shown either on the left for β-cells and on the right for CMs. $^*p < 0.05$; $^{**}p < 0.01$, $^{***}p < 0.001$, and $^{****}p < 0.0001$.

Media changes were required every two days throughout cardiovascular differentiation. Attached EBs typically started beating on day 7 and were harvested for further analysis on day 10.

Ethics Information: This study was performed in accordance with institutional guidelines and was approved by the local research ethics committees (University of California, Los Angeles IRB #05-10-093; University Tübingen IRB #356-2008BO2, #406-2011BO1, and #495-2018BO2; Landesärztekammer Baden-Württemberg, IRB #F-2012-078 and #F-2011-068; and the Charité Universitätsmedizin Berlin #EA/226/14).

Human first trimester and second trimester tissues were obtained from electively aborted fetuses following informed consent and de-identification. Normal adult heart sections were obtained from post-mortem autopsy samples (expiration due to noncardiac cases, with no history or evidence of cardiac disease on post-mortem inspection), which were provided by the department of pathology, David Geffen School of Medicine at UCLA, Los Angeles, USA.

All mouse surgeries were performed under the supervision and with approval of the UCLA Animal Review Committee (#2011-042 and #2013-057).

Histology, Histochemistry, Immunofluorescence Staining, and Quantification: Fetal tissues were freshly fixed in 4% PFA and embedded in paraffin using a Shandon Citadel 1000 (Thermo Fisher Scientific). The pseudoislets and EBs were fixed in 4% PFA, placed in Histogel (American MasterTech) and processed for paraffin embedding. All paraffin-embedded cells and tissue were sectioned (3 µm sections) using a microtome HM340E (Thermo Fisher Scientific). Sections of adult pancreas (3 µm sections) were commercially obtained (NBP2-30191, Novus Biologicals). Sections of adult human heart tissue were provided by UCLA as stated in the Ethics section.

Histological and histochemical staining was performed on deparaffinized and hydrated serial sections of explanted mouse hearts, 28 days post MI/R. Russell-Movat pentachrome staining visualized collagens (yellow), muscle tissue (red), proteoglycans/ glycosaminoglycans (blue-green), mature elastic fibers (black), and cell nuclei (dark red). Bright field (BF) images were acquired using a Zeiss Axio Observer Z1 (Carl Zeiss). Picrosirius Red and Fast Green stain visualized the collagen-rich scar (red) and the myocardium (green). In detail, deparaffinized and hydrated sections were incubated for 5 min in 0.5% acidified water (acetic acid, Carl Roth) and subsequently for 1 h in a solution of 0.1% Fast Green FCF at pH 2 (Sigma-Aldrich) and 0.1% Picrosirius Red in saturated picric acid (Morphisto) at a 1:1 ratio. The sections were cleaned twice in acidified water for 2 min, dehydrated using graded ethanol washes (70–100% v/v), and then mounted. High definition images were acquired with the glass slide scanner Opticlab H850 (Plusteck) and saved as TIFF. The glass scale bar 1972-50 peak (GWJ Co) was used to scale the collected images. A MATLAB algorithm was developed to identify and quantify the image components based on their HSV histograms. Valves and vessels of the outflow tract were stained red and cropped out of the image to determine the true scar areas. All areas calculated were normalized to the total tissue area.

For immunofluorescence staining, the paraffin sections were stained as previously described.[24–53] Briefly, antigen retrieval was performed consecutively in Tris-EDTA (pH = 9.0) and citrate buffer (pH = 6.0) in a steam cooker. For the intracellular antigens, the sections were treated with 1% Triton X-100. A goat block solution was used to block unspecific binding sites. Antibodies were diluted in antibody dilution buffer (PBS containing 1% BSA, 0.1% TritonX-100, 0.1% cold-water Fish Skin Gelatin, 0.05% Tween20) and samples were incubated overnight at 4 °C. After several washes, the secondary antibody was applied to the samples and incubated for 30 min at room temperature, and after several washes the sections were exposed to a DAPI solution (5 µg mL^{-1} in PBS, Roche). Fluorescence images were acquired using a confocal laser scanning microscope (LSM 880 with Airyscan, Carl Zeiss Microscopy GmbH, Germany). The images acquired were processed with Adobe Photoshop CS5 (Adobe System Inc.). Semiquantitative analyses of IF images were conducted by detecting the gray value intensity (GVI) using ImageJ software. All GVI data were normalized to the laser power. Quantification of E-cadherin and caspase-3 staining of pseudoislets was conducted utilizing images obtained with a 63× magnification on a Zeiss Axio Observer Z1 (Carl Zeiss). The entire pseudoislet was selected as region of interest (ROI). GVI quantification of the ROI was conducted using ImageJ, version 1.52p. TUNEL assay was performed using the Click-iT Alex Fluor Imaging Assay kit (Thermo Fisher Scientific). Sections were mounted with Prolong Gold Anti Fade solution (Thermo Fisher Scientific). TUNEL images were evaluated in a double-blinded study by two unbiased observers. Cells were identified as $TUNEL^+$ when a clear green and blue staining was exhibited. The ratio was calculated by dividing $TUNEL^+$ cells by total number of $DAPI^+$ cells per pseudoislet. Images were obtained using a 63× magnification on a Zeiss Axio Observer Z1 (Carl Zeiss). Quantification of the vessel density in αSMA/CD31/CTNT-stained mouse infarct scar area sections was conducted by counting αSMA+/CD31+ vessels utilizing images taken with a 25× objective ($n = 6$). The scar area of each image was measured using the ImageJ software. To quantify colocalization, a macro was designed using Microsoft Excel, version Office 365. Briefly, the algorithm compares GVI values of pixels of the simultaneously obtained NID1 and insulin channels. Colocalization was counted when the GVI of a specific pixel exceeded a set threshold on both channels and normalized by the total amount of pixels exceeding the threshold value in the NID1 channel. TuJ1 was used for the assessment of neuronal cells in the infarct area. 10 IF images per heart were taken with a 63× objective. $TuJ1^+$ and total cells were counted.

NID1 Production Plasmid: The inducible NID1 production plasmid was constructed from several sections of commercially available vectors. The main backbone consisted of the pcDNA3.1 vector. The inducible TRE promotor for NID1 expression was taken from the pTRE3G vector and DHFR expression was controlled by the TK promoter from the pGL4.74(hRluc/TK) vector. A codon-optimized sequence of human NID1 (GenBank accession number: BC045606.1, 5406 bp) with a histidine/asparagine tag at the C-terminus was synthesized from GeneArt (Life Technologies).

Stable NID1 Production Clone Generation and Production Induction: CHO DHFR-negative mutant cells (DSMZ no.: ACC 126) were transfected with the pCMV-Tet3G plasmid (631166, Clontech Laboratories) and selected for Geneticin (G418, Calbiochem) resistance. Selected activator clones were transfected with the NID1 production plasmid and cultured for two weeks in selection media (MEM α, 10% FBS dialyzed, 500 µg mL^{-1} of G418), which does not support the growth of DHFR-negative cells. Single cell cloning was conducted and clones were treated with 100 ng mL^{-1} doxycycline hydrochloride (Dox) (Thermo Fisher Scientific) to induce NID1 production. Secreted NID1 was measured using an ELISA (DY2570, R&D Systems). Clones with the highest measured levels of NID1 underwent selection rounds with rising levels of methotrexate (MTX) for genomic amplification. During MTX selection, ELISA, q-RT-PCR, and q-PCR were performed to measure NID1 protein levels and assess the relative levels of NID1 mRNA and the relative copy number of genome amplified NID1. The best production clones were adapted to suspension growth in Erlenmeyer flasks with serum-reduced media (DMEM/Ham's F12 basal medium, 0.5% FBS dialyzed, 2.5×10^{-6} M MTX, 2×10^{-3} M L-Glutamine, 1% penicillin–streptomycin (Pen/Strep), 250 µg mL^{-1} G418) in an incubation shaker (Minitron, Infors GmbH) at 37 °C and 5% CO_2 at 85 rpm. NID1 expression was induced with 100 ng mL^{-1} Dox and the media with secreted NID1 was harvested 4–5 days later and stored before NID1 purification at −20 °C.

NID1 Purification: The IMAC purification of the histidine/asparagine-tagged human NID1 was performed with a HisPrep FF 16/10 affinity chromatography column (GE Healthcare), controlled by the FPLC system Äkta Explorer 10 (GE Healthcare). NID1 elution was indicated by the increased absorption at the wavelengths 280 and 256 nm. Protein-containing elution fractions were pooled and desalted using a HiPrep 26/10 desalting column (GE Healthcare), controlled by the Äkta Purifier 100 (GE Healthcare). Subsequently, the protein solution was washed and concentrated with ultrafiltration units (Vivaspin 20, Sartorius), sterile filtered (SCGP00525, Millipore), and stored at −80 °C until further use.

SDS-PAGE and Western Blot: All protein samples were mixed with 4× Roti-Load (Carl Roth) and denatured at 90 °C for 5 min. The samples were run on a NuPAGE Novex 3–8% Tris-Acetate gel (EA03752BOX, Life Technologies) under denaturing conditions. The HiMark Pre-Stained Protein Standard was used for easy band identification. After SDS-PAGE, the

proteins were transferred to a nitrocellulose membrane (Whatman) in an electrical field (30 V, 60 min) in the XCell II Blot Module (Life Technologies). For an unspecific protein staining, the nitrocellulose membrane was incubated in a Ponceau-Red solution (Sigma-Aldrich) for 5 min at room temperature. Images were acquired and the membrane was discolored in a 0.1 M NaOH solution for later specific protein immunodetection. The membrane was blocked using 5% skim milk powder (Sigma-Aldrich) in TBS-T and then incubated with the primary antibodies overnight at 4 °C while shaking. After several washes with TBS-T, the membrane was incubated with the secondary antibody in TBS-T with 5% skim milk powder for 1 h at room temperature. After washing with TBS-T, SuperSignal West Dura Extended Duration Substrate (Thermo Fisher Scientific) was applied onto the membrane, drained after few seconds and the developed chemiluminescence was detected in the Luminescent Image Analyzer LAS-1000 plus (FujiFilm).

NID1 Deglycosylation: Purified NID1 was deglycosylated with an enzyme mix (P6039S, New England Biolabs) as instructed by the manufacturer. In addition to the 4 h incubation time described by the manufacturer, an identical reaction mix was incubated for 20 h. The control sample was treated accordingly, except for the addition of the deglycosylation enzymes, and incubated for 4 h. NID1 deglycosylation was analyzed by the mobility shift of the NID1 bands to a lower protein size on the SDS-PAGE gel.

Co-Immunoprecipitation (Co-IP): The protocol for Co-IP was modified from previously published studies.[54,55] The interaction partners NID1 (1 µg) and LAM 511 (0.5 µg, LN511-02, BioLamina) were mixed in 500 µL of a dilution and washing buffer (0.1 M NaCl, 0.05 M Tris/HCl pH 7.4 containing 0.04% Tween-20 and 1% BSA) and were agitated gently on a rotisserie mixer overnight. 6 µg of the antibody against LAM (ab11575, Abcam) was added to the protein mix and incubated for 24 h for Co-IP. This antibody was not added in the negative control (unspecific background control). Protein A magnetic beads (LSKMAGA02, Millipore) were added and gently agitated on the rotisserie mixer with the protein complexes ± the LAM antibody for 2.5 h at 4 °C and another 30 min at room temperature. After washing off the magnetic beads using a magnetic stand (LSKMAGS08, Millipore), the protein complexes were eluted from the beads and denatured in 30 µL of 1× Roti-Load (K929.2, Carl Roth) via heating for 10 min at 90 °C. Detection of the specific protein bands occurred after SDS-PAGE and Western blot.

qPCR and Expression Profiling Using RT2 Profiler PCR Array: RNA extraction of dermal fibroblasts was performed on lysed cells. Briefly, RNA was isolated using sequential incubation and centrifugation of the lysate with chloroform (Sigma-Aldrich), isopropanol (Carl Roth), and 75% ethanol (Applichem). RNA was resuspended in nuclease free-water and heated for 10 min at 55 °C prior to RNA quantification. RNA was reverse transcribed according to the manufacturer's instructions (RNeasy Micro Kit, Omniscript RT Kit, Qiagen). qPCR of EBs was performed on the LightCycler 480 II (Roche) with the 480 SYBR Green I Master (04887352001, Roche) for the primers NID1, p53 and β-actin for normalization and reference as listed in Extended Data in Table S4 of the Supporting Information. qPCR was performed using a Bio-Rad CFX96 system and the QuantiFast SYBR Green PCR Kit (Qiagen) for the primers *TNNT2* (QT00089782, Qiagen) and *ACTA2* (QT00088102, Qiagen).

qPCR on dermal fibroblasts was performed using ACTA2 (QT00088102, Qiagen), GAPDH (QT01192646, Qiagen) and the QuantiNova SYBR green PCR Kit (208052, Qiagen). All samples were performed as triplicates. The $2^{-\Delta\Delta Ct}$ method was applied for qPCR data quantification.

For expression profiling using RT^2 profiler PCR Array (Qiagen), RNA extraction was performed according to manufacturer's instructions (RNeasy Micro Kit, Omniscript RT Kit, Qiagen). RNA was reverse transcribed to cDNA using RT2 First Strand Kit (SABiosciences, Qiagen). The Human Extracellular Matrix & Adhesion Molecules RT^2 Profiler PCR Array (PAHS-013ZD; Qiagen) was used to measure expression levels of 84 individual genes important for cell–cell and cell–matrix interactions. For all RNA and DNA quantifications, absorbance was measured using a NanoQuant Plate in combination with Infinite 200 PRO (Tecan). If not mentioned otherwise, qPCR measurements were performed using a Bio-Rad CFX96 system and data analysis was performed using the Qiagen data analysis center online tool.

Imaging Flow Cytometry: EBs were harvested at day 10 of the cardiovascular differentiation protocol to conduct flow cytometry analyses using a standard staining protocol.[56] Briefly, cells were incubated with Zombie Red dye (BioLegend) to exclude dead cells and CD29-PE (MCA2298PE, AbD Serotec, UK) for 25 min at 4 °C protected from light. After washing, the Foxp3 Staining Buffer Kit (421403, BioLegend) was used to fix the cells for 30 min on ice, followed by washing and permeabilization for 15 min at 4 °C. After blocking with BSA for 10 min, cells were incubated with CTNT primary antibody (ab8295, Abcam) for 35 min at 4 °C, washed and blocked with 5% BSA for 10 min at room temperature to avoid unspecific binding. The secondary anitbody (rat antimouse IgG1-AF647, 406617, BioLegend) was added for 25 min at 4 °C, protected from light. For the analysis using the ImageStreamx mkII (Amnis Corporation, USA) with the INSPIRE instrument controller software with 40× magnification, 1×10^4 single cells were acquired per sample. Data were analyzed with IDEAS Image analysis software. All samples were gated on single cells that were Zombie Red-negative. The percentage of CTNT+ cells was determined and a control sample (stained with the same antibodies except the primary antibody) was used to set the background fluorescence.

In Vivo Mouse MI/R Model and NID1 Injections: A mouse MI/R model was used to identify the effect of myocardial NID1 injections post MI.[19] All surgeries were performed at UCLA. In detail, 8 weeks old female C57BL/6J mice, strain DLAMb6, were anesthetized using 2.0% isoflurane (Butler Schein), placed on a heated surgical board and given 2.5 mg kg^{-1} flunixin (Flunixin Meglumine, Schering-Plough Animal Health) subcutaneously. Under a dissecting microscope, a midline cervical incision was made to expose the trachea for intubation with a PE-90 plastic catheter (Stoelting Company). The catheter was connected to a Harvard minivent (Harvard Apparatus) supplying oxygen with a tide volume of 225–250 µL and a respiratory rate of 130 strokes per minute. Surgical plane anesthesia was subsequently maintained with 1–1.5% isoflurane. A lateral incision was made in the fourth intercostal space. The heart was exposed and the left anterior descending coronary artery (LAD) was ligated intramurally 2 mm from its origin with a 9-0 nylon suture (Ethicon). The suture was tied around a small piece of plastic tubing (PE-10) to occlude the coronary artery while allowing an easier and safer relief of the occlusion. This occlusion occurred for 45 min. During this time, a moist gauze pad was placed over the incision to maintain a sterile atmosphere. Ischemia was verified by the regional paleness of the myocardium that was no longer supplied with blood by the left coronary artery. Reperfusion was allowed by cutting the knot on the PE-10 tube and could be verified by the appearance of hyperaemia in the previously pale region. Reperfusion caused the infarcted region to change into a normal pinkish red color. This procedure was conducted on five mice for the NID + HA treatment group, five mice for the HA carrier gel group, and three mice for the saline control group. Samples sizes were determined for statistical power and in accordance to the EU 3Rs regulation for the reduction of animal studies. After confirming that there was no bleeding, the animals received injections in the MI border zone. Three animals in the control group were injected with 50 µL of saline solution. Five animals were injected with a total of 50 µL of HyStem hyaluronic acid (HA) hydrogel (Glycosan BioSystems) in PBS per animal. In the NID1 + HA group, five animals received 50 µL injections of HA in PBS with 50 µg mL^{-1} NID1. For each mouse, the 50 µL total injection volume was divided into 10 µL injections at five sites in the LV myocardial infarction border zone. The mouse chests were closed in two layers. The ribs (inner layer) were closed with 6-0 coated vicryl sutures (Ethicon) in an interrupted pattern. The skin was closed using 6-0 nylon or silk sutures (Covidien) in a subcuticular manner. The anesthesia was stopped and the mice were allowed to recover for several minutes before the endotracheal tube was removed. The mice received intraperitoneal injections of 2.5 mg kg^{-1} Banamine postsurgery for the alleviation of pain. One mouse in the NID1 + HA treatment group died of arrhythmia after surgery, which lead to the total number of four animals in this group. Two animals from the HA carrier gel group (HA controls) had to be excluded due to incomplete ischemia, giving the final number of three for this group.

Hydrogel Preparation with and Without Supplementation of NID1: All procedures for control and NID1 + HA injections were conducted under sterile conditions. The HA hydrogel was prepared according to the manufacturer's instructions (HyStem) and was further diluted to 2:13. For each mouse, a total of 50 µL HA in PBS ± 50 µg mL^{-1} NID1 was needed; therefore, due to possible residues in the preparation tube or in the syringe, 70 µL were prepared per mouse (HA: PBS ± 50 µg mL^{-1} NID1).

Echocardiography: Conscious echocardiography was conducted on three different time points. A baseline echocardiography measurement was conducted on each mouse prior to the MI/R procedure. In serial nature, further echocardiography measurements were conducted 2 days and 28 days after the MI/R and myocardial injection procedure to track cardiac function. For noninvasive echocardiographic imaging of the conscious mice in vivo, the high-frequency ultrasound imaging system Vevo 2100 (VisualSonics) was applied with the MS400 transducer 18–38 MHz. Myocardial performance was assessed via the Vevo LAB software. The mice were sacrificed after the 28-day echocardiography, and their hearts were explanted for histological and immunofluorescence assessment.

Raman Imaging of Mouse Heart Sections and Pseudoislets: Islets were prepared as previously described.[24] Briefly, hypoxic NID1-treated and control pseudoislets were placed in a microfluidic chip for noninvasive in situ Raman imaging as previously performed.[24,57] Spectral mapping was performed on a customized inverted WITec Raman system (WITec GmbH) equipped with a green laser (532 nm) and a CCD spectrograph with a grating of 600 g mm^{-1}. Images were acquired at a laser power of 50 mW, an integration time per spectrum of 0.5 s, a pixel resolution of 1 × 1 µm and at least as triplicates. Based on Movat staining, representative sections were selected from each heart and deparaffinized. The sections were kept at 4 °C in PBS until measurement. The spectra were collected with a 63× dipping objective (W Plan-apochromat; Carl Zeiss), a laser power of 60 mW and an integration time of 0.05 s (per pixel). In order to locate the scar, an overview image of 1000 × 1700 µm was collected from the apex of the heart with 1 µm image resolution. Within this scan, 3 ROIs of 200 × 200 µm were acquired with a resolution of 0.5 µm.

Multivariate Data Analysis: Raman images were processed and analyzed by TCA using the Project FIVE 5.2 software (WITec GmbH).[23] Briefly, TCA is a non-negative matrix factorization-based MVA tool that elaborates spectral components that predominantly occur in the data set and allows the identification and localization of these components by false color intensity distribution heatmaps. GVI per pixel were determined in ImageJ to semiquantify the distribution of the spectral components in both conditions. Furthermore, TCA allowed the preselection of ROIs of similar spectral information, which were extracted for further in-depth analysis of the molecular composition by PCA using Unscrambler X (Camo). Moreover, MCR analysis was applied to define the local spectral composition within the islet periphery and islet core of the pseudoislets. NID1 core, control core, NID1 periphery and control periphery were defined by the islet area and compared to determine the protective effect of NID1 on the pseudoislets.

hiPSC-Derived Cardiomyocyte Cell Culture: iCell Cardiomyocytes2 (cat: #R1057, Cellular Dynamics) culture was performed according to the manufacturer's specifications. Briefly, 96-well plates were coated with 0.1% porcine gelatin solution for 1 h. hiPSC-CMs were seeded at a density of 2 × 10^4 cells mL^{-1}. At day 9, hiPSC-CMs were treated with 50 µg mL^{-1} NID1 and placed in normoxic or hypoxic conditions for 48 h. At day 9, hiPSC-CMs were treated with 50 µg mL^{-1} NID1, or PBS as control, and placed in normoxic or hypoxic conditions for 48 h. Cells were either fixed in 4% PFA for IF staining, lysed in TRI-Reagent (Sigma-Aldrich) for RNA isolation and qPCR or prepared for DigiWest evaluation. For DigiWest evaluation, the cells were detached using TrypIE (Gibco), washed five times on ice and snap frozen in liquid nitrogen.

Fibroblast Cultures: Fibroblasts were isolated from adult skin and myocardial biopsies after informed consent was given (Landesärztekammer Baden-Württemberg, IRB #F-2012-078 and #F-2011-068) as previously reported.[58,59] Fibroblasts were cultured until 90% confluency. Prior to seeding, 3.5 mm dishes (glass bottom µ-Dish, ibidi) were coated with 0.1% porcine gelatin coating (Sigma-Aldrich) for 1 h. 1 × 10^5 cells per dish were seeded in media containing 50 µg mL^{-1} NID1 and placed in normoxic or hypoxic conditions for 48 h. After incubation, cells were either fixed in 4% PFA for IF staining or lysed in TRI-Reagent (Sigma-Aldrich) for RNA isolation and qPCR.

Tube Formation Assay: HUVECs (single donor cells, C2517A, Lonza) were thawed and cultured in EGM-2 medium per manufacturer's instructions (CC-4176, Lonza) at 37 °C and 5% CO_2. One day before the tube formation assay, the cells were equilibrated in low-serum EGM2 medium (0.5% FBS and no other supplements). HUVECs were seeded in a cell density of 1.5 × 10^4 cells/96-well well (1.5 × 10^4 cells/ 0.32 cm^2) in triplicates on serum-reduced Matrigel only, or serum-reduced Matrigel supplemented with 50 µg mL^{-1} NID1. All materials for the coating were precooled and the coating was performed with 75 µL per 0.32 cm^2. Following 75 µL low serum EGM-2 medium, 100 µg mL^{-1} NID1 were added to the respective wells and allowed to equilibrate at 37 °C and 5% CO_2 for 30 min. 75 µL of the cell suspension was added per 96-well and incubated for 2 h. HUVEC tubular structure formation was assessed with a Zeiss Axio Observer Z1 (Carl Zeiss). Quantification of different tube formation parameters was performed using the angiogenesis analyzer of ImageJ Version 1.50 g, which allows for the automated visual recognition of different tube formation parameters.

EndoC-βh3 Cell Culture and Pseudoislet Formation: The conditionally immortalized human pancreatic beta cell line EndoC-ßH3 was cultured per manufacturer's instructions. After 21 days, pseudoislets were formed as previously described.[24] After 48 h in standard culture, pseudoislets were incubated for an additional 72 h under hypoxic (37 °C, 5% CO_2, and 1% O_2) or normoxic (37 °C, 5% CO_2, and 21% O_2) conditions. NID1 was supplemented in the media 72 h after seeding and for an additional 48 h at 20, 30, and 40 µg mL^{-1}. PBS was used as negative control. After 72 h, pseudoislets were either subjected to a glucose-stimulated insulin secretion (GSIS) assay, fixed in 4% PFA (Sigma-Aldrich) for IF staining or prepared for DigiWest evaluation. For DigiWest evaluation, pseudoislets were grouped and washed five times on ice, centrifuged at 700 x *g* and snap frozen in liquid nitrogen.

Pseudoislet Size Tracking: A minimum of 10 pseudoislets were imaged every 24 h with a brightfield microscope (Carl Zeiss). Images were further processed with the ImageJ software, version 1.52p, where the average area was evaluated and subsequent average diameter calculated.

GSIS Assays: Prior to all GSIS assays, pseudoislets were incubated with NID1- or PBS- OPTIβ2 (Univercell Biosolutions) medium for 24 h in normoxic or hypoxic condition. GSIS assays were performed after 5 days as previously described, except otherwise mentioned.[23,60] Pseudoislets were grouped by 6 to 8 per well and washed twice with β-Krebs (Univercell Biosolutions) and 1% BSA (Thermo Fisher Scientific). Pseudoislets were preincubated for 1 h with Krebs-BSA and the supernatant was discarded. 20 × 10^{-3} M glucose (Thermo Fisher Scientific) solution was prepared in Krebs-BSA, and pseudoislets were incubated with either Krebs-BSA or 20 × 10^{-3} M glucose solution for 1 h. The supernatant was collected and stored at −20 °C. An ultrasensitive insulin ELISA (Mercodia) was performed and the GSIS index was calculated by dividing the amount of secreted insulin during high glucose treatment by the amount of secreted insulin during basal state.

NID1 Cytotoxicity Test: A standardized cytotoxicity test according to EN ISO 10993 was performed using primary isolated human dermal fibroblasts (IRB #F-2012-078). An additional cytotoxicity test was performed utilizing primary isolated human cardiac fibroblasts (IRB #F-2011-068). 2 × 10^4 cells were seeded per 96-well well. In parallel, sterile solutions containing 50, 100, and 200 µg mL^{-1} NID1 were prepared in Dulbecco's modified Eagle medium (DMEM, Life Technologies). After 24 h, 200 µL of the NID1 solution was pipetted into each well and incubated for another 24 h. The cytotoxic substance SDS, which induces cell death, served as the positive control, and DMEM was used as the negative control. After incubation, the medium was removed and an MTS assay was performed. The cells of each well were incubated with a solution of 20 µL MTS (CellTiter 96 AQueous One Solution Cell Proliferation Assay, Promega) mixed with 100 µL DMEM. The absorbance was measured at 492 nm (Infinite 200 PRO, Tecan) after 45 min and the percentage of viable cells was calculated relative to the negative control, which was set to 100%. In all samples, cell numbers were counted.

Isolation of Human Immune Cells: Peripheral blood mononuclear cells (PBMCs) were isolated from buffy coats (DRK, Berlin, Germany, IRB #EA/226/14) as previously described.[61] Briefly, blood was diluted (1:2) with PBS (Biochrom, Germany), layered on Biocoll Separation Solution (Biochrom) and centrifuged for 30 min at 800 x *g* at room temperature. PBMCs were isolated and washed three times with PBS. PBMCs were used to isolate $CD14^+$ monocytic cells by CD14 MicroBeads (Miltenyi Biotec) according to manufacturer's instructions with MACS separation columns (Miltenyi Biotec). Labeling with CD14 PerCP/Cy5.5 (BioLegend) confirmed a purity of 95–98%.

Cultures of Human Macrophages with NID1: 1×10^6 monocytes per well or 7×10^5 M0-macrophages per well were seeded in 24-well culture plates and were treated with NID1 at 50 μg mL^{-1} in VLE-RPMI (Biochrom) containing 10% AB-Serum (Sigma-Aldrich) 1% penicillin/streptomycin (Life Technologies) and 1% glutamine (Life Technologies) at 37 °C in a 5% CO2 incubator for 7 days or 24 h, respectively. Monocytes (2×10^6 mL^{-1}) were differentiated into M0-type macrophages for 7 days in 6-well culture plates using 50 ng mL^{-1} M-CSF (Miltenyi Biotec) in complete VLE-RPMI. M0-type macrophages were polarized for 24 h either toward M1 macrophages by adding 20 ng mL^{-1} IFN-γ (Miltenyi Biotec) and 100 ng mL^{-1} LPS from *E. coli* O127:B4 (Sigma-Aldrich) or into M2 macrophages by adding 20 ng mL^{-1} IL-4 (Miltenyi Biotec) according to the recently described method.[54] Representative images were obtained using a bright-field microscope (Carl Zeiss).

Macrophage Flow Cytometry Analyses: As described above, macrophages were harvested using 1% (v/v) trypsin/EDTA (Life Technologies), washed with PBS and labeled with a master mix of fluorophore-labeled human-specific antibodies CD163-FITC, CD80-PE, HLA-DR-PE/Cy7, CD206-APC (all BioLegend), CD14-APC/Cy7 (BD Biosciences), and a Live/Dead violet fixable staining kit (Molecular Probes).[54,61] Samples were measured with FACS Canto II (BD Biosciences) and analyzed using FlowJo Version 8.8.6 (TreeStar Inc.). Surface marker expression levels were normalized to the unstimulated controls (set as 1).

Immune Cell Proliferation Assay: Modulation of NID1-treated T cell subset proliferation was analyzed with a CFSE-based proliferation assay as described previously.[24] Briefly, 96-well culture plates were coated with 0.05 μg mL^{-1} anti-CD3 antibody (OKT3, Janssen-Cillag) overnight at 4 °C. Wells were washed three times with PBS, coated with 50 μg mL^{-1} NID1 for 6 h at room temperature and washed again with PBS. Isolated PBMCs were labeled with 2.5×10^{-6} M 5,6-CFDA-SE and seeded at a cell density of 3×10^5 cells per well in complete VLE-RPMI in wells coated with anti-CD3 and NID1, anti-CD3 alone (positive control) or they were used uncoated (unstimulated control). After 5 days of culture at 37 °C and 5% CO_2, PBMCs were harvested and labeled with human-specific antibodies CD8-PE and CD4-APC (both Miltenyi Biotec) as well as CD3-APC/Cy7 (BioLegend) and Live/Dead violet fixable staining kit. Samples were processed using a FACS Canto II and data were analyzed using FlowJo Version 8.8.6. MFI of all markers were normalized to the anti-CD3 control MFI level (set to 1).

Cytokine Detection Assays: Supernatants of NID1-treated macrophage cultures (24 h or 5 days) and NID1-treated PBMC proliferation assays (5 days) were collected for detection of released cytokines IFNγ, TNFα, IL-6, and IL-10 using ELISA kits (BioLegend) according to the manufacturer's instructions. Samples were measured on a Micro-plate reader (Bio-Rad).

Monocyte Chemotaxis Assay: To analyze chemotaxis, a specific 96-well cell migration system (Neuro Probe) was applied as previously described.[54] Briefly, the chemotactic stimulus was added in a volume of 37.5 μL per well. A membrane filter with 5 μm pores was placed onto the plate. 3×10^4 cells in 40 μL diet medium consisting of VLE-RPMI (Biochrom) and 0.1% autologous serum were added on the membrane. Chemotaxis was induced by 50 or 100 μg mL^{-1} NID1 or without stimulus (negative control). MCP-1 (50 ng mL^{-1}, Miltenyi Biotec) served as positive control. After incubation for 3 h at 37 °C in a 5% CO_2 incubator, the membrane was carefully removed. Monocytes that adhered to the membrane were fixed with methanol (Merck) and labeled with Hemacolor staining kit (Merck). After microscopic documentation using ProgRes CapturePro 2.8.8 (Jenoptik), the number of migrated monocytes was determined using ImageJ Version 1.4.3.67 (National Institutes of Health). The number of migrated cells was normalized to the negative control.

Endotoxin Test: $CD14^+$ monocytes (1×10^6) were incubated alone (negative control), with 100 ng mL^{-1} LPS O127:B4 (Sigma-Aldrich, positive control) or with 50 μg mL^{-1} NID1 in 24-well plates in 1 mL^{-1} of VLE-RPMI (Biochrom). After 24 h, the supernatant was collected and tested for TNFα by ELISA (BioLegend). In addition, a Pierce Chromogenic LAL Endotoxin quantification kit (Thermo Fisher Scientific) was employed according to the manufacturer's instructions.

Integrin Binding Assays: Binding assays were performed as previously described.[62] Microtiter plates (Costar Half Area plate) were coated overnight at 4 °C with 50 μLper well and 4 μg mL^{-1} $\alpha v\beta 3$ (R&D Systems) in TBS containing 2×10^{-3} M $MgCl_2$ or TBS with 2×10^{-3} M $MgCl_2$ and 1×10^{-3} M $CaCl_2$, respectively. Plates were washed twice with the respective buffers. Blocking of nonspecific binding was performed for 1 h at room temperature with 1% BSA/TBS/$MgCl_2$ or 1% BSA/TBS/ $MgCl_2$/$CaCl_2$. Serial dilutions of NID1 were prepared on ice. For $\alpha v\beta 3$, NID1 serial dilutions were prepared in 1% BSA/TBS/$MgCl_2$ and 1×10^{-3} M $MnCl_2$, or in 1% BSA/TBS/$MgCl_2$ and 10×10^{-3} M EDTA-buffer for nonspecific binding. Reaction was stopped using 1.5 M NaOH solution. OD determination was performed at 405 nm. Three independent experiments were performed, each of them with duplicates.

Blocking of Integrin $\alpha v\beta 3$: Mouse IgG (Vector Laboratories) and $\alpha v\beta 3$ (Novus Biologicals) were used at a concentration of 10 μg mL^{-1} in PBS. Pseudoislets at 48 h and CMs at 9 days, respectively, were washed twice with PBS and incubated with the blocking antibody or control for 1 h under standard culture conditions. Pseudoislets and CMs were washed twice with PBS. The respective NID1-treated culture media or control were added to the pseudoislet or CM culture. Pseudoislets were culture for an additional 72 h and CMs for an additional 48 h before evaluation via IF staining or GSIS assay, respectively.

DigiWest: DigiWest assays (NMI Reutlingen, Germany) were performed as recently described.[30] Briefly, gel electrophoresis and blotting onto PVDF membranes was performed using the NuPAGE system as recommended by the manufacturer (Life Technologies, Carlsbad, CA, USA). Blots were washed in PBST, proteins were biotinylated on the membranes using NHS-PEG12-Biotin (50×10^{-6} M) in PBST for 1 h followed by washing in PBST and drying. Individual sample lanes were cut into 96 molecular weight fractions (0.5 mm each) and proteins were eluted in 96-well plates using 10 μL elution buffer per well (8 M urea, 1% Triton-X100 in 100×10^{-3} M Tris-HCl pH 9.5). Eluted proteins from each molecular weight fraction were loaded onto color-coded, neutravidin coated Luminex bead sets (MagPlex, Luminex, Austin, TX, USA). 384 Luminex bead sets were employed and the protein loaded beads from four different sample lanes were pooled into one bead-mix resulting in 6 bead mixes for the 24 samples. The bead-mixes were sufficient for 100 antibody incubations (see Extended Data in Table S5, Supporting Information). Aliquots of the DigiWest bead-mixes (1/100th per well) were added to 96-well plates containing 50 μL per well assay buffer (Blocking Reagent for ELISA supplemented with 0.2% milk powder, 0.05% Tween-20, and 0.02% sodium azide, Roche). Beads were briefly incubated in assay buffer and the buffer was discarded. Antibodies were diluted in an assay buffer and 30 μL were added per well. After overnight incubation at 15 °C on a shaker, the bead-mixes were washed twice with PBST and PE-labeled (Phycoerythrin) secondary antibodies (Dianova) were added and incubated for 1 h at 23 °C. Beads were washed twice prior to readout on a Luminex FlexMAP 3D. Secondary antibodies were either diluted in an assay buffer or in a polymer buffer (Blocking Reagent for ELISA supplemented with 4% PVP 360.000, 1% milk powder, 0.05% Tween-20, and 0.02% sodium azide, Roche). For quantification of the antibody specific signals the DigiWest analysis tool (version 3.8.6.1, Excel-based) was employed. This tool uses the 96 values for each initial lane obtained from the Luminex measurements on the 96 molecular weight fractions, identifies the peaks at the appropriate molecular weight, calculates a baseline using the local background and integrates the peaks. The values are based on relative fluorescence (accumulated fluorescence intensity). For analysis, data (measured signal intensity) was normalized to the total protein amount corresponding to the sample, median centered

and $\log_2$-transformed. The software package MEV 4.8.1 was used for data visualization, clustering, and nonparametric statistical analysis.

Statistical Analysis: The relevant statistical tests, sample sizes, replicate types, and *p*-values are described in the corresponding figures and tables of the Supporting Information. Each *n* represents a distinct sample. Statistical tests were two-sided if not mentioned otherwise. Data are presented as mean ± SD and as dot plots every time possible. All data sets were tested for normality. Statistical analysis was performed using Prism, version 6.07 (GraphPad Software). Statistical significance was defined at $p < 0.05$.

Supporting Information

Supporting Information is available from the Wiley Online Library or from the author.

Acknowledgements

The authors thank the flow cytometry core facility of the BCRT and Simone Pöschel from the ImageStream Core Facility at the University Tübingen for support with the cell analyses, Kristin Fröhlich for her help with the chemotaxis assays, and Maria Schneider for performing the LAL test (both BCRT), Yan Lu (UCLA, CVRL) for her support with the MI/R experiments, as well as Mariella Bosch, Madeleine Waltner, Svenja Hinderer, Peter Loskill, Germano Piccirillo (all University Tübingen), and Nam Che (UCLA, CVRL) for their technical support and scientific input. The authors thank Frank Zaucke (University Frankfurt) for providing the NID1 and NID2 antibodies. This work was financially supported by the European Union (H2020-NMP10-2014-645991-2, DRIVE, and FP7 NMP3-SME-2013-604531, AMCARE, to K.S.-L. and G.P.D.), CIRM (RB3-05086 to A.N.), the BMBF (0316059 to K.S.-L., 1315848A to M.S.), Boehringer Ingelheim Fonds (to M.Z.), the International Foundation for Ethical Research (to A.Z.), the Ministry of Science, Research and the Arts of Baden-Württemberg (33-729.55-3/214 and SI-BW 01222–91 to K.S.-L.) and the Deutsche Forschungsgemeinschaft (SCHE701/14-1, INST 2388/33-1 and Germany's Excellence Strategy-EXC 2180 to K.S.-L; SFB1009 A09 to J.A.E.).

Open access funding enabled and organized by Projekt DEAL.

Conflict of Interest

A.Z., S.L.L., G.P.D., and K.S.-L. are inventors on patent application EP19154849.4 associated with this work and owned by the University Tübingen. S.L.L., M.Z., and K.S.-L. are inventors on patents (EP3027201B1 and CN105517564A), and patent applications (US20160158314A1, CA2916614A1, JP2016530532A, and KR20160037170A) associated with this work and owned by the NMI, Reutlingen.

Author Contributions

A.Z. and S.L.L. contributed equally to this work. A.Z., S.L.L., M.U., M.Z., H.K.A.M., A.N., M.S., and K.S.-L. designed the experiments and wrote the manuscript. A.Z., S.L.L., M.U., D.A.C.B., J.M., M.Z., A.H., E.B., K.S., S.F., M.T., S.L., J.A.E., and M.S. performed experiments, collected and analyzed data. G.M.C., A.D., G.P.D., and G.K. provided reagents and gave conceptual advice.

Keywords

diabetes, ischemia, myocardial infarction, nidogen-1, pancreatic β-cells

Received: July 2, 2020
Revised: October 25, 2020
Published online:

[1] H. K. Eltzschig, T. Eckle, *Nat. Med.* **2011**, *17*, 1391.
[2] T. Su, K. Huang, H. Ma, H. Liang, P.-U. Dinh, J. Chen, D. Shen, T. A. Allen, L. Qiao, Z. Li, S. Hu, J. Cores, B. N. Frame, A. T. Young, Q. Yin, J. Liu, L. Qian, T. G. Caranasos, Y. Brudno, F. S. Ligler, K. Cheng, *Adv. Funct. Mater.* **2019**, *29*, 1803567.
[3] M. Kapnisi, C. Mansfield, C. Marijon, A. G. Guex, F. Perbellini, I. Bardi, E. J. Humphrey, J. L. Puetzer, D. Mawad, D. C. Koutsogeorgis, D. J. Stuckey, C. M. Terracciano, S. E. Harding, M. M. Stevens, *Adv. Funct. Mater.* **2018**, *28*, 1800618.
[4] S. B. Seif-Naraghi, J. M. Singelyn, M. A. Salvatore, K. G. Osborn, J. J. Wang, U. Sampat, O. L. Kwan, G. M. Strachan, J. Wong, P. J. Schup-Magoffin, R. L. Braden, K. Bartels, J. A. DeQuach, M. Preul, A. M. Kinsey, A. N. DeMaria, N. Dib, K. L. Christman, *Sci. Transl. Med.* **2013**, *5*, 173ra25.
[5] C. Frantz, K. M. Stewart, V. M. Weaver, *J. Cell Sci.* **2010**, *123*, 4195.
[6] T. A. Wynn, T. R. Ramalingam, *Nat. Med.* **2012**, *18*, 1028.
[7] S. F. Badylak, *Nat. Rev. Urol.* **2019**, *16*, 389.
[8] R. Jayadev, D. R. Sherwood, *Curr. Biol.* **2017**, *27*, R207.
[9] A. Kumar, J. K. Placone, A. J. Engler, *Development* **2017**, *144*, 4261.
[10] K. Schenke-Layland, A. Nsair, B. Van Handel, E. Angelis, J. M. Gluck, M. Votteler, J. I. Goldhaber, H. K. Mikkola, M. Kahn, W. R. MacLellan, *Biomaterials* **2011**, *32*, 2748.
[11] D. Evseenko, K. Schenke-Layland, G. Dravid, Y. Zhu, Q. L. Hao, J. Scholes, X. C. Wang, W. R. MacLellan, G. M. Crooks, *Stem Cells Dev.* **2009**, *18*, 919
[12] C. Bonnans, J. Chou, Z. Werb, *Nat. Rev. Mol. Cell Biol.* **2014**, *15*, 786.
[13] B. Carlin, R. Jaffe, B. Bender, A. E. Chung, *J. Biol. Chem.* **1981**, *256*, 5209.
[14] Q. Zhou, D. A. Melton, *Nature* **2018**, *557*, 351.
[15] L. Yang, M. H. Soonpaa, E. D. Adler, T. K. Roepke, S. J. Kattman, M. Kennedy, E. Henckaerts, K. Bonham, G. W. Abbott, R. M. Linden, L. J. Field, G. M. Keller, *Nature* **2008**, *453*, 524.
[16] E. Willems, S. Spiering, H. Davidovics, M. Lanier, Z. Xia, M. Dawson, J. Cashman, M. Mercola, *Circ. Res.* **2011**, *109*, 360.
[17] F. Monte, R. J. Hajjar, Y. Chang, D. Lebeche, S. Arab, M. T. Keating, *Nature* **2007**, *13*, 962.
[18] K. Schenke-Layland, K. E. Rhodes, E. Angelis, Y. Butylkova, S. Heydarkhan-Hagvall, C. Gekas, R. Zhang, J. I. Goldhaber, H. K. Mikkola, K. Plath, W. R. MacLellan, *Stem Cells* **2008**, *26*, 1537.
[19] J. Duan, C. Gherghe, D. Liu, E. Hamlett, L. Srikantha, L. Rodgers, J. N. Regan, M. Rojas, M. Willis, A. Leask, M. Majesky, A. Deb, *EMBO J.* **2012**, *31*, 429.
[20] A. I. Mahmoud, C. C. O'Meara, M. Gemberling, L. Zhao, D. M. Bryant, R. Zheng, J. B. Gannon, L. Cai, W.-Y. Choi, G. F. Egnaczyk, C. E. Burns, C. G. Burns, C. A. MacRae, K. D. Poss, R. T. Lee, *Dev. Cell* **2015**, *34*, 387.
[21] M. G. Monaghan, M. Holeiter, E. Brauchle, S. L. Layland, Y. Lu, A. Deb, A. Pandit, A. Nsair, K. Schenke-Layland, *Tissue Eng., Part A* **2017**, *24*, 57.
[22] N. G. Frangogiannis, *J. Clin. Invest.* **2017**, *127*, 1600.
[23] A. Zbinden, J. Marzi, K. Schlünder, C. Probst, M. Urbanczyk, S. Black, E. M. Brauchle, S. L. Layland, U. Kraushaar, G. Duffy, K. Schenke-Layland, P. Loskill, *Matrix Biol.* **2020**, *85–86*, 205.
[24] S. Hinderer, M. Schesny, A. Bayrak, B. Ibold, M. Hampel, T. Walles, U. A. Stock, M. Seifert, K. Schenke-Layland, *Biomaterials* **2012**, *33*, 5259.
[25] U. Hofmann, S. Frantz, *Eur. Hear. J.* **2016**, *37*, 873.
[26] X.-Y. Yi, E. A. Wayner, Y. Kim, A. J. Fish, *Cell Adhes. Commun.* **1998**, *5*, 237.
[27] K. Y. Peng, Y. H. Liu, Y. W. Li, B. L. Yen, M. L. Yen, *J. Cell. Mol. Med.* **2017**, *21*, 1572.
[28] M. Riopel, W. Stuart, R. Wang, *Acta Biomater.* **2013**, *9*, 8140.

[29] F. Treindl, B. Ruprecht, Y. Beiter, S. Schultz, A. Döttinger, A. Staebler, T. O. Joos, S. Kling, O. Poetz, T. Fehm, H. Neubauer, B. Kuster, M. F. Templin, *Nat. Commun.* **2016**, *7*, 12852.
[30] J. Misao, Y. Hayakawa, M. Ohno, S. Kato, T. Fujiwara, H. Fujiwara, *Circulation* **1996**, *94*, 1506.
[31] Z. Xia, M. Dickens, J. Raingeaud, R. J. Davis, M. E. Greenberg, *Science* **1995**, *270*, 1326.
[32] J. W. Fox, U. Mayer, R. Nischt, M. Aumailley, D. Reinhardt, H. Wiedemann, K. Mann, R. Timpl, T. Krieg, J. Engel, *EMBO J.* **1991**, *10*, 3137.
[33] R. F. Nicosia, E. Bonanno, M. Smith, P. Yurchenco, *Dev. Biol.* **1994**, *164*, 197.
[34] A. Martinez-Hernandez, P. S. Amenta, *FASEB J.* **1995**, *9*, 1401.
[35] H. K. Lee, I. A. Seo, D. J. Suh, H. T. Park, *J. Korean Med. Sci.* **2009**, *24*, 654.
[36] G. Wolfstetter, I. Dahlitz, K. Pfeifer, U. Töpfer, J. A. Alt, D. C. Pfeifer, R. Lakes-Harlan, S. Baumgartner, R. H. Palmer, A. Holz, *Development* **2019**, *146*, 168948.
[37] M. Bechtel, M. V. Keller, W. Bloch, T. Sasaki, P. Boukamp, F. Zaucke, M. Paulsson, R. Nischt, *FASEB J.* **2012**, *26*, 3637.
[38] M. Montgomery, S. Ahadian, L. Davenport Huyer, M. Lo Rito, R. A. Civitarese, R. D. Vanderlaan, J. Wu, L. A. Reis, A. Momen, S. Akbari, A. Pahnke, R.-K. Li, C. A. Caldarone, M. Radisic, *Nat. Mater.* **2017**, *16*, 1038.
[39] E. Bassat, Y. E. Mutlak, A. Genzelinakh, I. Y. Shadrin, K. Baruch Umansky, O. Yifa, D. Kain, D. Rajchman, J. Leach, D. Riabov Bassat, Y. Udi, R. Sarig, I. Sagi, J. F. Martin, N. Bursac, S. Cohen, E. Tzahor, *Nature* **2017**, *547*, 179.
[40] G. G. Nair, J. S. Liu, H. A. Russ, S. Tran, M. S. Saxton, R. Chen, C. Juang, M. lan Li, V. Q. Nguyen, S. Giacometti, S. Puri, Y. Xing, Y. Wang, G. L. Szot, J. Oberholzer, A. Bhushan, M. Hebrok, *Nat. Cell Biol.* **2019**, *21*, 263.
[41] S. R. Adderley, D. J. Fitzgerald, *J. Biol. Chem.* **1999**, *274*, 5038.
[42] M. A. Kalwat, D. C. Thurmond, *Exp. Mol. Med.* **2013**, *45*, 37.
[43] J. Wang, S. Liu, T. Heallen, J. F. Martin, *Nat. Rev. Cardiol.* **2018**, *15*, 672.
[44] C. Rallis, S. M. Pinchin, D. Ish-Horowicz, *Development* **2010**, *137*, 3591.
[45] H. J. Welters, R. N. Kulkarni, *Trends Endocrinol. Metab.* **2008**, *19*, 349.
[46] J. Golledge, P. Clancy, J. Maguire, L. Lincz, S. Koblar, *Cardiovasc. Res.* **2011**, *92*, 19.
[47] K. Imanaka-Yoshida, *Circ. J.* **2012**, *76*, 2513.
[48] N. G. Frangogiannis, *J. Thorac. Dis.* **2017**, *9*, S52.
[49] K. L. Spiller, T. J. Koh, *Adv. Drug Delivery Rev.* **2017**, *122*, 74.
[50] S. Gaggero, M. Bruschi, A. Petretto, M. Parodi, G. Del Zotto, C. Lavarello, C. Prato, L. Santucci, A. Barbuto, C. Bottino, G. Candiano, A. Moretta, M. Vitale, L. Moretta, C. Cantoni, *Oncoimmunology* **2018**, *7*, 1470730.
[51] F. C. Simões, T. J. Cahill, A. Kenyon, D. Gavriouchkina, J. M. Vieira, X. Sun, D. Pezzolla, C. Ravaud, E. Masmanian, M. Weinberger, S. Mayes, M. E. Lemieux, D. N. Barnette, M. Gunadasa-Rohling, R. M. Williams, D. R. Greaves, L. A. Trinh, S. E. Fraser, S. L. Dallas, R. P. Choudhury, T. Sauka-Spengler, P. R. Riley, *Nat. Commun.* **2020**, *11*, 600.
[52] M. Votteler, D. A. Carvajal Berrio, A. Horke, L. Sabatier, D. P. Reinhardt, A. Nsair, E. Aikawa, K. Schenke-Layland, *Development* **2012**, *140*, 2345.
[53] A. Zbinden, M. Urbanczyk, S. L. Layland, L. Becker, J. Marzi, M. Bosch, P. Loskill, G. Duffy, K. Schenke-Layland, *Tissue Eng., Part A* **2020**.
[54] S. Hinderer, K. Sudrow, M. Schneider, M. Holeiter, S. L. Layland, M. Seifert, K. Schenke-Layland, *Sci. Rep.* **2018**, *8*, 110.
[55] S. Puch, S. Armeanu, C. Kibler, K. R. Johnson, C. A. Müller, M. J. Wheelock, G. Klein, *J. Cell Sci.* **2001**, *114*, 1567.
[56] N. Shen, A. Knopf, C. Westendorf, U. Kraushaar, J. Riedl, H. Bauer, S. Pöschel, S. L. Layland, M. Holeiter, S. Knolle, E. Brauchle, A. Nsair, S. Hinderer, K. Schenke-Layland, *Stem Cell Rep.* **2017**, *9*, 122.
[57] A. Zbinden, D. A. Carvajal Berrio, M. Urbanczyk, S. L. Layland, M. Bosch, S. Fliri, C. Lu, A. Jeyagaran, P. Loskill, G. P. Duffy, K. Schenke-Layland, *J. Biophotonics* **2020**.
[58] G. Piccirillo, M. V. Ditaranto, N. F. S. Feuerer, D. A. Carvajal Berrio, E. M. Brauchle, A. Pepe, B. Bochicchio, K. Schenke-Layland, S. Hinderer, *J. Mater. Chem. B* **2018**, *6*, 6399.
[59] E. Brauchle, H. Johannsen, S. Nolan, S. Thude, K. Schenke-Layland, *Biomaterials* **2013**, *34*, 7401.
[60] M. Urbanczyk, A. Zbinden, S. L. Layland, G. Duffy, K. Schenke-Layland, *Tissue Eng., Part A* **2019**, *26*, 387.
[61] M. Stolk, F. Klatte-Schulz, A. Schmock, S. Minkwitz, B. Wildemann, M. Seifert, *Sci. Rep.* **2017**, *7*, 9801.
[62] J. A. Eble, K. W. Wucherpfennig, L. Gauthier, P. Dersch, E. Krukonis, R. R. Isberg, M. E. Hemler, *Biochemistry* **1998**, *37*, 10945.

WILEY-VCH

ADVANCED SCIENCE
Open Access

Supporting Information

for *Adv. Sci.*, DOI: 10.1002/advs.202002500

Nidogen-1 Mitigates Ischemia and Promotes Tissue Survival and Regeneration

*Aline Zbinden, Shannon L. Layland, Max Urbanczyk, Daniel A. Carvajal Berrio, Julia Marzi, Monika Zauner, Anne Hammerschmidt, Eva M. Brauchle, Katrin Sudrow, Simon Fink, Markus Templin, Simone Liebscher, Gerd Klein, Arjun Deb, Garry P. Duffy, Gay M. Crooks, Johannes A. Eble, Hanna K. A. Mikkola, Ali Nsair, Martina Seifert, and Katja Schenke-Layland**

Supporting Information

Nidogen-1 Mitigates Ischemia and Promotes Tissue Survival and Regeneration

Authors

*Aline Zbinden[1], Shannon L. Layland[1], Max Urbanczyk[1], Daniel A. Carvajal Berrio[1,2], Julia Marzi[1,3], Monika Zauner[1], Anne Hammerschmidt[1], Eva M. Brauchle[1,2,3], Katrin Sudrow[4,5], Simon Fink[3], Markus Templin[3], Simone Liebscher[1], Gerd Klein[6], Arjun Deb[7,8,9,10,11], Garry P. Duffy[12], Gay M. Crooks[8,10,13], Johannes A. Eble[14], Hanna K. A. Mikkola[7,8,9,10], Ali Nsair[8,11], Martina Seifert[4,5] and Katja Schenke-Layland[1,2,3,11]**'*

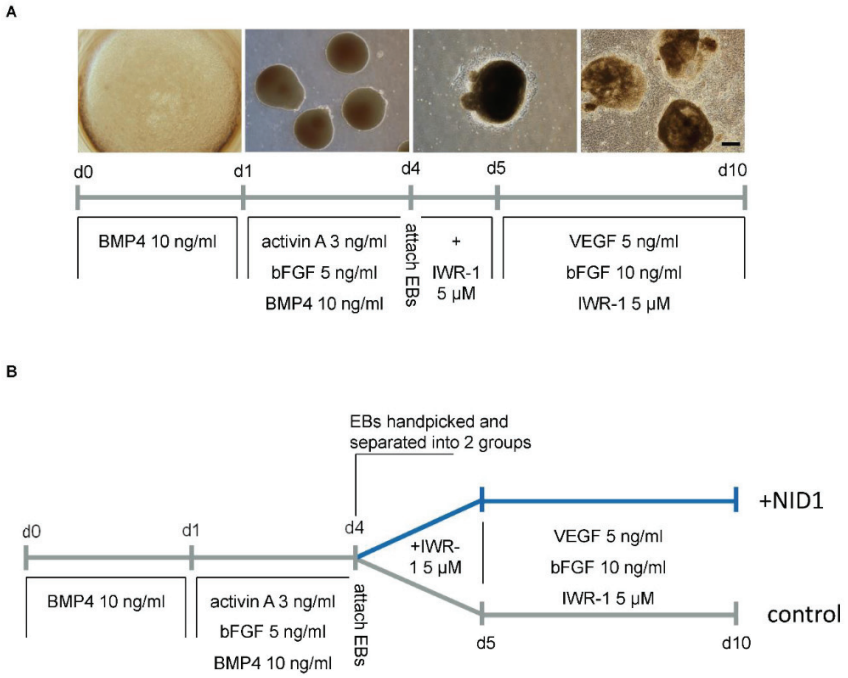

Figure S1. Schematic illustration of the modified cardiovascular differentiation protocol. EBs were derived from hESCs (line H9). **(A)** The differentiation protocol timeline is shown together with the stage-specific additives to the medium. Scale bar equals 100 µm. **(B)** The differentiation protocol using NID1 from day 4 (d4) and control are shown together with the stage-specific additives in the medium.

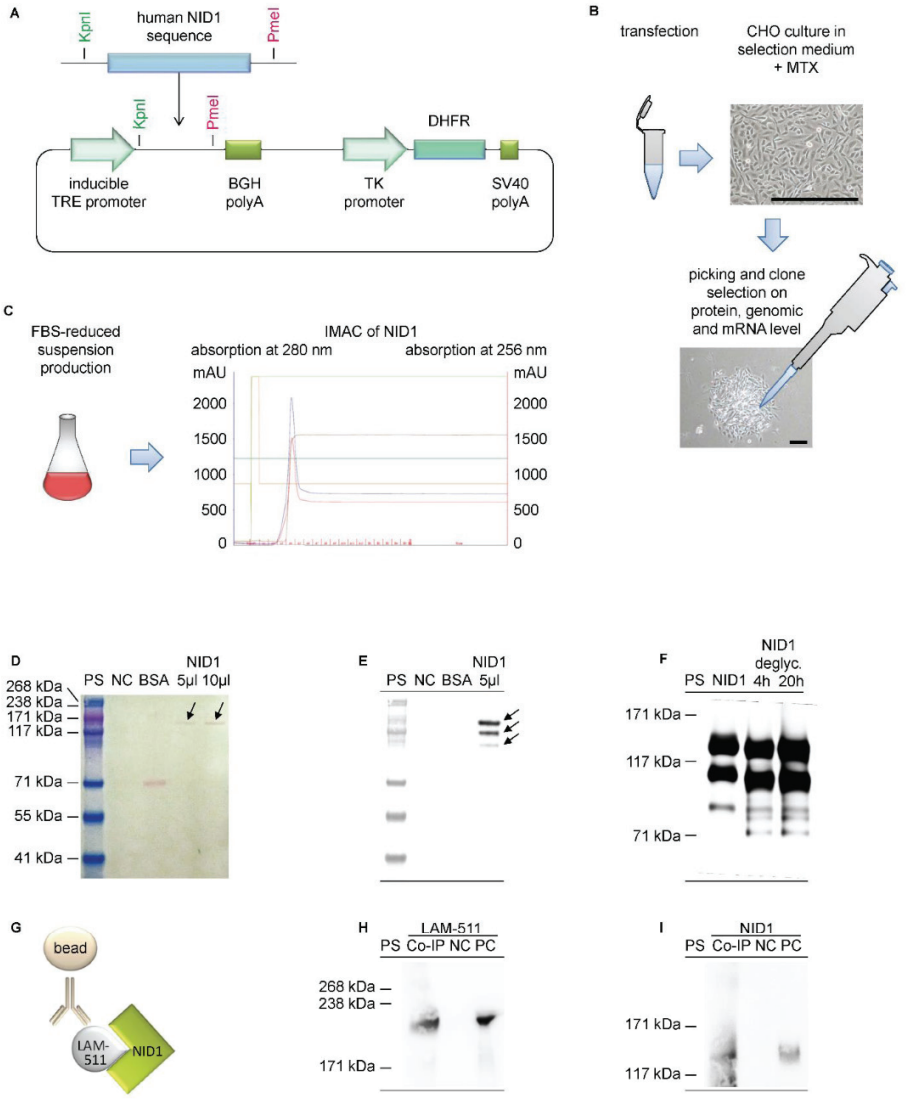

Figure S2. Recombinant NID1 production and characterization. (A) Schematic representation of NID1 production plasmid generation with main components for genomic amplification strategy. **(B)** Schematic depiction of CHO culture transfection with the NID1 production plasmid, MTX selection and clone analysis. Scale bars equal 200 µm. **(C)** Schematic depiction of production clone adaptation to FBS-reduced suspension culture and purification of secreted NID1 using immobilized-metal affinity chromatography (IMAC). Characteristic protein absorption is shown at 280 nm (blue line) and 256 nm (red line) in milli absorption unit (mAU). **(D)** Ponceau-Red staining of a nitrocellulose membrane with IMAC eluates: negative control (NC, 10 µl IMAC eluate of media with 1% FBS, dialyzed), BSA (10 µl IMAC eluate of media with 1% BSA) and 5

or 10 µl IMAC eluate of NID1-containing cell culture media with originally 0.5% FBS, dialyzed. **(E)** Same membrane after discoloring and specific immunodetection of NID1. Arrows indicate 3 NID1 bands at about 140 kDa, 110 kDa and 90 kDa. **(F)** Specific immunodetection of NID1 deglycosylated for 4 hours and for 20 hours shows a shift of the characteristic NID1 bands to lower molecular weight compared to a NID1 control that was not treated with the deglycosylation enzyme, proving the glycosylated state of the recombinant NID1. **(G)** Schematic of Co-IP between interaction partners NID1 and LAM-511. **(H)** Specific immunodetection of the ß1 and ɣ1 chain of LAM-511 in Co-IP, NC (Co-IP w/o LAM antibody) and positive control (PC, LAM-511). **(I)** Specific immunodetection of NID1 in Co-IP, NC (Co-IP w/o LAM antibody) and PC (NID1). The HiMark pre-stained protein standard (PS) was used in all blots.

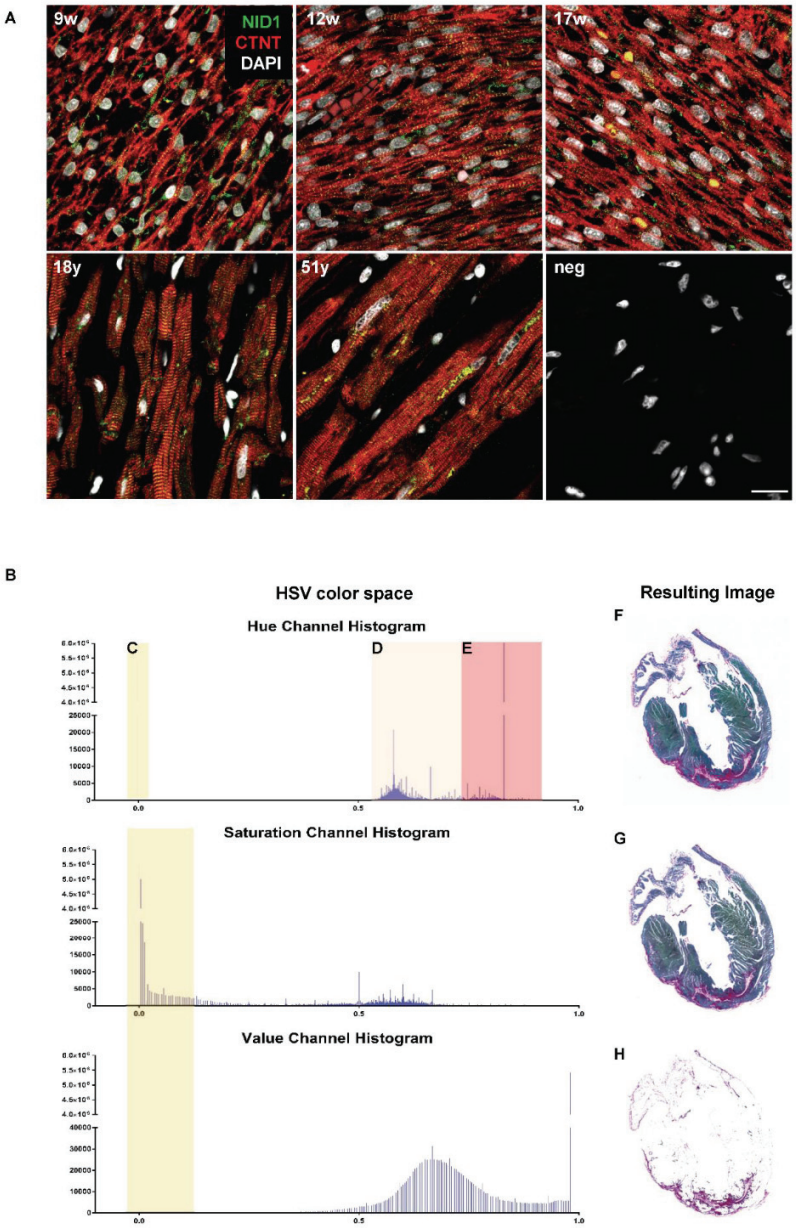

Figure S3. Identification of NID1 as crucial ECM protein in fetal and adult hearts by IF staining & Myocardial scar quantification. (A) NID1 (green) was detected in fetal heart sections 9, 12 and 17 weeks post-fertilization as well as in sections of 18 and 51 year old adult heart tissue. CTNT (red) was used to detect CMs. Cell nuclei were visualized with DAPI (white).

Scale bar equals 20 μm. **(B-H)** HSV color segmentation was performed using a customized MATLAB code. The HSV histogram bands responsible for the background are shown in **(C)**, the Fast Green-positive region labeling the myocardium is shown in **(D)** and, the Picrosirius Red-stained areas corresponding to the scar content are shown in **(E)**. By subtracting band **(C)** from an image of Picrosirius Red and Fast Green **(F)**, an image without background is generated **(G)** and, comparably, the removal of bands **(C)** and **(D)** yields an image of only the scar component **(H)**.

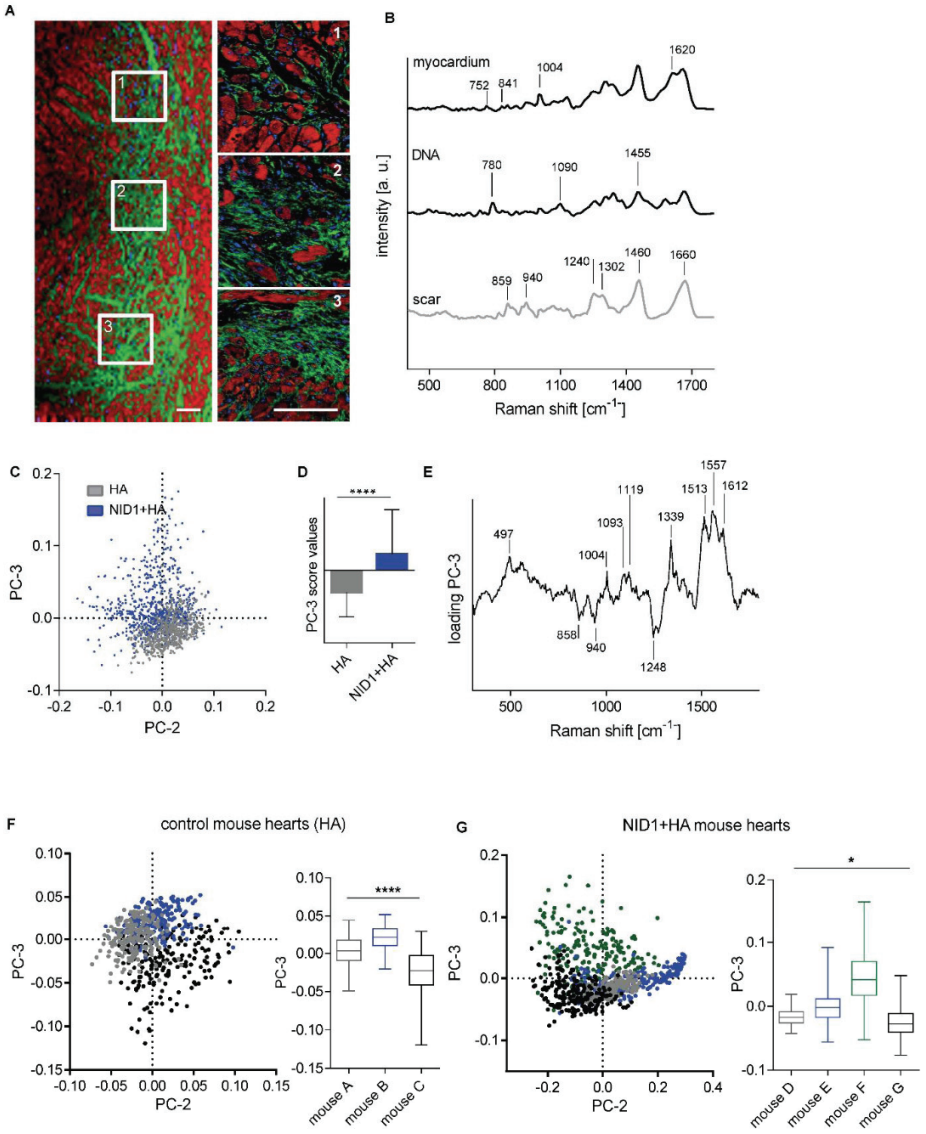

Figure S4. Raman imaging and multivariate analysis of infarcted mouse hearts and single animals. (A) Representative overview of Raman images showing DNA (blue), myocardium (red) and the scar (green). Three regions within the scar area (rectangular boxes: 1-3) were selected for high-resolution Raman images. **(B)** Spectra-associated to the color-coding shown in **(A)**. Based on the signal patterns, the specific ECM composition for the scar area was detected. Scale bar equals 100 µm. **(C,D)** PCA of Raman spectra revealed molecular and structural differences in the scar area of NID1+HA and control hearts. PC score values of spectra from NID1+HA and control

hearts were significantly different, unpaired t-test. **(E)** The loading plot displays typical porphyrin vibrations (1513, 1557, 1612 cm^{-1}) seen in the NID1+HA heart tissue. Collagen peaks (858 and 1248 cm^{-1}) were assigned to the control hearts. PCA of TCA scar component of **(F)** control (HA) and **(G)** NID1+HA mouse hearts. Significant differences between animals are detected in both groups. Kruskal-Wallis test with Dunn's multiple comparisons test. Results are shown as standard box plot diagram. *p<0.05, **p<0.01, ***p<0.001 and ****p<0.0001.

8

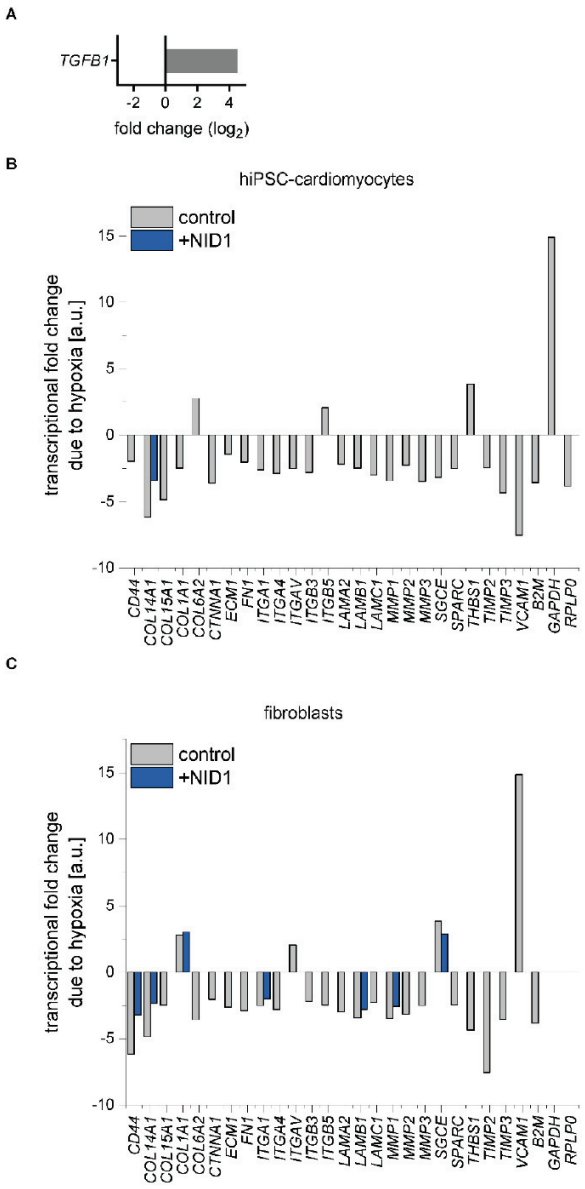

Figure S5. Translational changes in ECM production, degradation and regulation due to hypoxic conditions. (A) Transcriptional changes of *TGFB1* in NID1-treated hiPSC-CMs under normoxic conditions. **(B,C)** Transcriptional changes in gene expression after hypoxic conditions without (control) and with NID1 **(B)** hiPSC-CMs and **(C)** dermal fibroblasts. Gene regulation are shown when fold-regulation > |2|, p-value < 0.05.

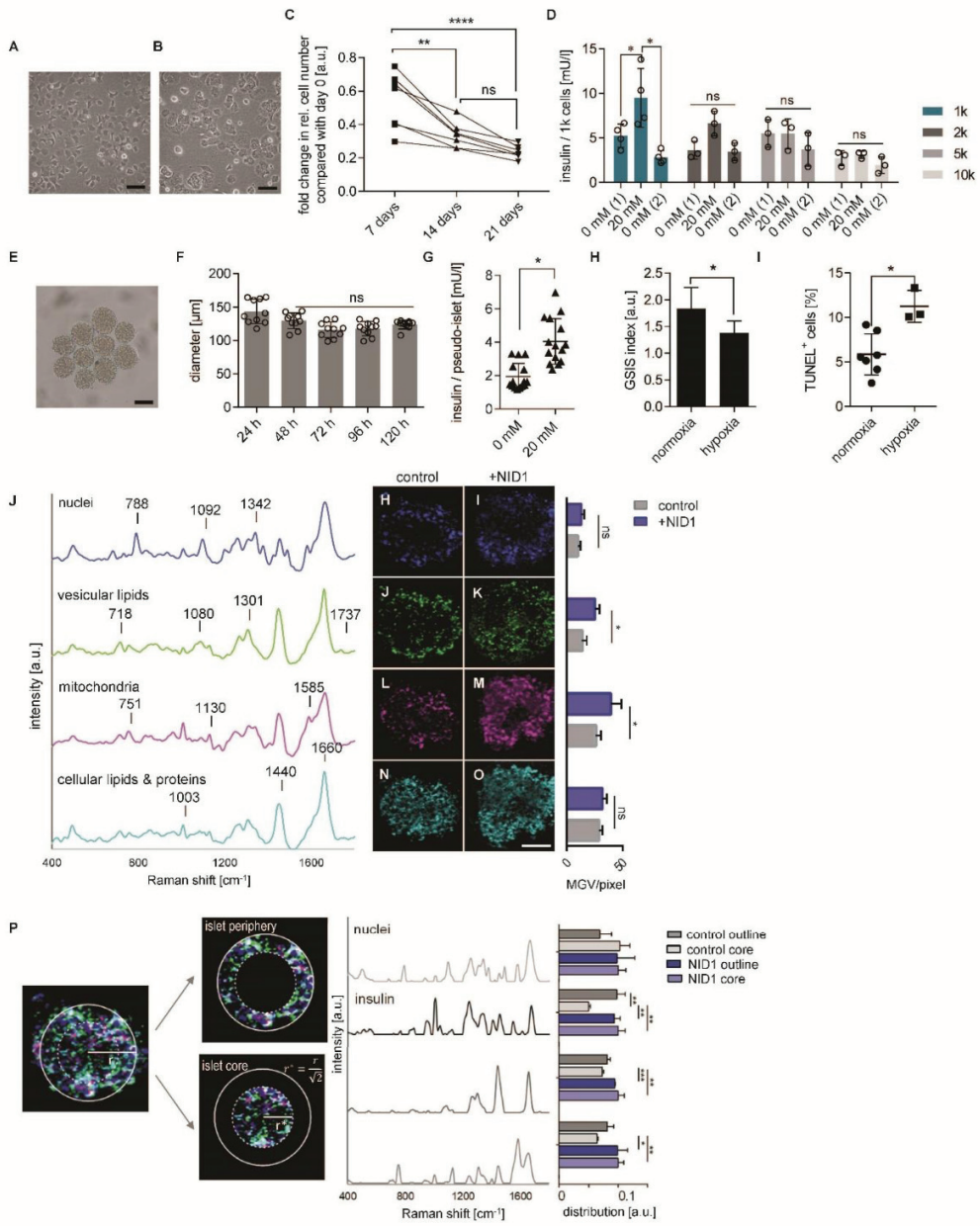

Figure S6. Human pseudo-islet functionality under hypoxic conditions and characterization by in situ Raman imaging and multivariate analysis. (A) Unexcised and **(B)** excised EndoC-βH3 morphology. Scale bars equal 100 µm. **(C)** Reduced cell number over time due to the excision of the proliferation transgene over 21 days. **(D)** GSIS assay (with 0 and 20 mM glucose) of pseudo-islets composed of 1000 (1k), 2000 (2k), 5000 (5k) and 10000 (10k) cells/ pseudo-islet

after 5 days of culture under normoxic conditions. **(E)** 1k pseudo-islet morphology. Scale bar equals 100 µm **(F)** Pseudo-islet size, described as pseudo-islet diameter, is stable from 72h until 5 days under normoxic conditions (n = 10); one-way ANOVA, *p<0.05. **(G)** GSIS assay (with 0 and 20 mM glucose) of pseudo-islets under normoxic conditions at 5 days (n = 15); unpaired t-test, *p<0.05 **(H)** Significant loss of glucose responsiveness under hypoxic conditions, described as the GSIS index (fold increase in insulin release due to the transition from Krebs buffer (0 mM glucose) to 20 mM glucose (n = 10); one-way ANOVA, *p<0.05. **(I)** DNA fragmentation under hypoxic conditions determined by the quantification of $TUNEL^-$ cells (n = 3-7); unpaired t-test. **(J)** True component analysis (TCA) identified four major spectral components assigned to nuclei (blue), insulin-transporting lipid vesicles (green), mitochondrial activity (pink) and cellular lipids and proteins (light blue). **(H-O)** False color intensity distribution images for each spectral component in (**H,J,L,N**) PBS controls and (**I,K,M,O**) NID1-treated pseudo-islets. Semi-quantitative analysis by definition of the mean gray value intensity/pixel demonstrated a significant increase in the vesicular lipids and the mitochondrial activity in NID1-treated islets. **(P)** Multivariate curve resolution (MCR) analysis was performed for in-depth analysis of the molecular composition in the periphery and core region of the hypoxic pseudo-islets. Most relevant, components related to nuclei, insulin, lipids and mitochondria were identified and their distribution within both regions were compared in PBS controls and NID1-treated pseudo-islets. The control core region showed a significant decrease in insulin, lipids and mitochondria, whereas the NID1-treated core region showed levels comparable to the peripheral regions (n = 4); *p<0.05, **p<0.01, ***p<0.001.

11

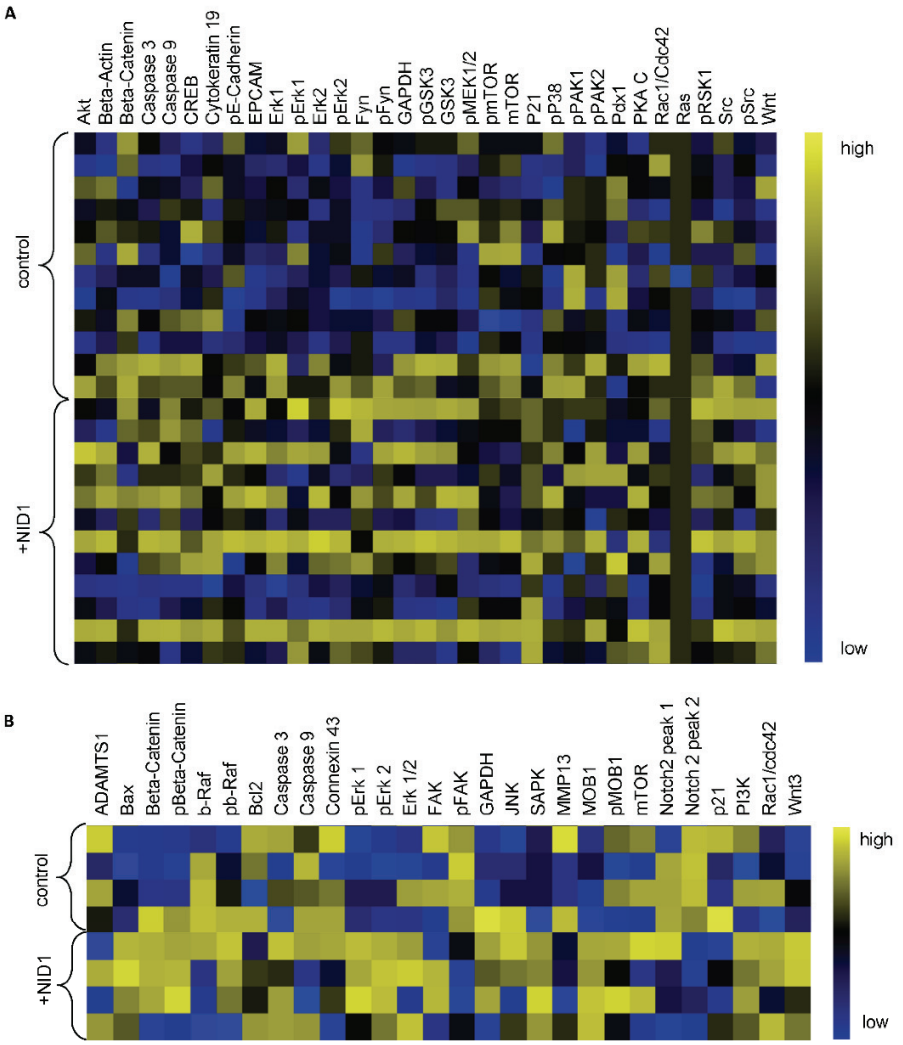

Figure S7. Change in protein expression in NID1-treated cultures. DigiWest®-based protein expression analysis of all tested proteins in (a) NID1-treated pseudo-islets (n = 12) and (b) NID1-treated hiPSC-CMs (n = 4) under hypoxic conditions compared with their respective controls. Data are shown as column-wise and color-coded heatmap from the lowest (blue) to the highest (yellow) expression for each analyte.

	baseline	saline	HA	NID1 + HA
Heart Rate^{min}	605 ± 46	675 ± 18	549 ± 46*	539 ± 45*
LVIDd^{mm}	2.65 ± 0.40	4.77 ± 0.36	3.40 ± 0.44**	2.90 ± 0.18***
LVIDs^{mm}	1.30 ± 0.22	4.29 ± 0.31	2.93 ± 0.51**	2.15 ± 0.18****,#
LVAWd^{mm}	0.73 ± 0.10	0.49 ± 0.01	0.48 ± 0.05	0.51 ± 0.06
LVAWs^{mm}	1.12 ± 0.14	0.52 ± 0.03	0.49 ± 0.04	0.60 ± 0.10
LVPWd^{mm}	0.71 ± 0.03	0.61 ± 0.17	0.53 ± 0.11	0.61 ± 0.07
LVPWs^{mm}	0.98 ± 0.03	0.79 ± 0.17	0.58 ± 0.03	0.70 ± 0.08
LVED^{mm}	2.67 ± 0.31	4.82 ± 0.26	3.52 ± 0.42**	2.82 ± 0.21****
LVES^{mm}	1.27 ± 0.20	4.26 ± 0.30	3.04 ± 0.43**	2.22 ± 0.18****,#
EDV$^{\mu L}$	26.89 ± 7.50	108.80 ± 13.57	52.39 ± 15.62***	30.30 ± 5.69****
ESV$^{\mu L}$	4.18 ± 1.49	81.83 ± 13.34	36.91 ± 13.01***	16.86 ± 3.57****
EF$^{\%}$	84.88 ± 3.08	24.96 ± 4.75	30.17 ± 4.31	44.63 ± 1.57***,##
FS$^{\%}$	52.56 ± 3.70	11.54 ± 2.34	13.80 ± 2.10	21.12 ± 0.78**,#

Table S1. Echocardiography analysis 28 days after MI/R. Baseline is the pre-MI/R measurement of the NID1+HA mice. Data are presented as means ± standard error of the mean (SEM). *p<0.05, **p<0.01, ***p<0.001, ****p<0.0001 saline vs. HA and NID1+HA, $^{\#}$p<0.05, $^{\#\#}$p<0.01 HA vs. NID1+HA; individual one-way ANOVA with Tukey's multiple comparison test, baseline (n = 4), saline (n = 3), HA (n = 3), NID1+HA (n = 4). LVIDd: left ventricular internal dimension at end diastole, LVIDs: left ventricular internal dimension at end-systole, LVAWd: left ventricular anterior wall thickness in diastole, LVAWs: left ventricular anterior wall thickness in systole, LVPWd: left ventricular posterior wall dimensions in diastole, LVPWs: left ventricular posterior wall dimensions in systole, LVED: left ventricle end-diastolic diameter, LVES: left ventricle end-systolic diameter, EDV: end-diastolic volume, ESV: end-systolic volume, EF: ejection fraction, FS: fractional shortening.

Raman shift [cm^{-1}]	Assignment
497	glycogen
718	C-N / nucleotide peak
751	mitochondrial DNA
752	porphyrin
780	DNA
788	DNA
841	Polysaccharides
858-9	proline, hydroxyproline
940	C-C backbone
1003	phenylalanine
1004	phenylalanine
1080	typical phospholipids
1090-3	phosphodioxy / DNA
1119	C-C stretch in lipids
1130	phospholipid structural changes / Mitochondrial activity
1240	lipids
1247-8	collagens, amide III
1301	lipids, fatty acids, triglycerides
1302	collagens
1339	tryptophan, CH2, CH3 wagging - bending in lipids/proteins
1342	guanine (DNA/RNA)
1440	CH2, CH3 deformation (lipids)
1455	deoxyribose
1460	CH2, CH3 deformation of lipids and collagen
1513	cytosine, porphyrin
1557	porphyrin ν(C=C)
1585	mitochondria /mitochondrial activity
1612	C=C stretching (ring)
1620	porphyrin ν(C=C)
1660	amide I
1737-8	lipids

Table S2. Raman-associated peaks. Raman peaks in cm^{-1} and their assigned molecular structure.

antibodies for DigiWest	species	order information
Beta-Actin	rabbit IgG	A1978, Sigma
ADAMTS1	rabbit IgG	12897, Cell Signaling
Akt	rabbit IgG	4685, Cell Signaling
Bax	rabbit IgG	2772, Cell Signaling
Bcl2	rabbit IgG	2872, Cell Signaling
Beta-Catenin	rabbit IgG	8480, Cell Signaling
Beta-Catenin	rabbit IgG	8814, Cell Signaling
Beta-Catenin - phospho Ser552	rabbit IgG	9566, Cell Signaling
b-Raf	rabbit IgG	07-683, Upstate
b-Raf - phospho Ser445	rabbit IgG	2896, Cell Signaling
Caspase 3	rabbit IgG	9662, Cell Signaling
Caspase 9	mouse IgG1	9508, Cell Signaling
Connexin 43	rabbit IgG	3512, Cell Signaling
CREB - phospho Ser133	rabbit IgG	9196, Cell Signaling
EpCAM	rabbit IgG	3599, Cell Signaling
Erk1/2 (MAPK p44/42)	rabbit IgG	4695, Cell Signaling
Erk1/2 (MAPK p44/42) - phospho Thr202/Tyr204	rabbit IgG	4370, Cell Signaling
E-cadherin	rat IgG	sc-59778, Santa Cruz
E-cadherin – phospho Ser838/Ser840	rabbit IgG	2239-1, Epitomics
FAK1	rabbit IgG	3285, Cell Signaling
FAK1 - phospho Tyr397	rabbit IgG	8556, Cell Signaling
Fyn	rabbit IgG	4023, Cell Signaling
Fyn – phospho Tyr530	rabbit IgG	orb99261, biorbyt
GAPDH	rabbit IgG	5174, Cell Signaling
GSK3 alpha/beta - phospho Ser21/Ser9	rabbit IgG	9331, Cell Signaling
GSK3 beta	rabbit IgG	9315, Cell Signaling
GSK3 beta - phospho Ser9	rabbit IgG	9336, Cell Signaling
JNK/SAPK	rabbit IgG	9252, Cell Signaling
MEK1/2 - phospho Ser217/Ser221	rabbit IgG	9154, Cell Signaling
MMP13	mouse IgG1	MAB511, R&D Systems
MOB1	rabbit IgG	3863, Cell Signaling
MOB1 - phospho Thr35	rabbit IgG	8699, Cell Signaling
mTOR (FRAP)	rabbit IgG	2983, Cell Signaling
mTOR (FRAP) - phospho Ser2448	rabbit IgG	2971, Cell Signaling
Notch 2	rabbit IgG	5732, Cell Signaling
P21	rabbit IgG	2947, Cell Signaling
P38 MAPK - phospho Thr180/Tyr182	rabbit IgG	4511, Cell Signaling
PAK 1/2 - phospho Ser144/Ser141	rabbit IgG	2606, Cell Signaling
Pdx1	rabbit IgG	5679, Cell Signaling
PI3-kinase p85 a pha	rabbit IgG	ab40755, abcam
PKA C a pha	rabbit IgG	4782, Cell Signaling
Rac1/Cdc42	rabbit IgG	4651, Cell Signaling
Ras	rabbit IgG	8955, Cell Signaling
RSK 1 (p90RSK) - phospho Thr573	rabbit IgG	ab62324, abcam
Src	rabbit IgG	2108, Cell Signaling
Src – phospho Tyr527	rabbit IgG	2105, Cell Signaling
Wnt3A	rabbit IgG	09-162, Millipore
antibodies for DigiWest	**species**	**order information**
dk-a-rb IgG (H+L) - RPE		#711-116-152, Jackson
dk-a-ms IgG (H+L) - RPE		#715-116-15', Jackson
gt-a-rt IgG (H+L) - RPE		#112-116-143, Jackson
Streptavidin - RPE		#016-110-084, Jackson

antibodies for IF staining	species	dilution	order information
NID1	rabbit IgG	1:100	Sc-33141, Santa Cruz
NID1	rabbit IgG	1:1000	kind gift from F. Zaucke
NID2	rabbit IgG	1:1000	kind gift from F. Zaucke
FN	rabbit IgG	1:500	A0245, Dako
POSTN	rabbit IgG	1:100	HPA012308, Sigma-Aldrich
LAM	rabbit IgG	1:50	ab11575, Abcam
COL4	rabbit IgG	1:250	ab6586, Abcam
COL1	rabbit IgG	1:75	R1038, Acris
αSMA-FITC	mouse IgG2a	1:500	F3777, Sigma-Aldrich
CD31	rat IgG2a	1:20	DIA-310, Dianova
MF20	mouse IgG2b	1:50	MF20, Developmental Studies Hybridoma Bank
CTNT	rabbit IgG	1:3000	HPA015774, Sigma-Aldrich
CTNT	mouse IgG1	1:600	NB200-412, Novus Biologicals
TUJ1	rabbit IgG	1:2000	802001, BioLegend
NESTIN	rabbit IgG	1:200	839801, BioLegend
MAP2	rabbit IgG	1:500	ab5622, Merck-Millipore
INS	guinea-pig IgG	1:200	A0564, Dako
E-cadherin	mouse IgG2a	1:250	ab76055, Abcam
CASP-3	rabbit IgG	1:100	ab13847, Abcam
rabbit IgG-AF488	goat	1:250	A-11034, Invitrogen
rat IgG2a-AF647	goat	1:250	A-21247, Invitrogen
mouse IgG1-AF594	goat	1:250	A-21125, Invitrogen
mouse IgG2a-AF488	goat	1:250	A-21131, Invitrogen
mouse IgG2b-AF594	goat	1:250	A-21145, Invitrogen
guinea-pig IgG-AF594	goat	1:250	A-11076, Invitrogen
antibodies for WB	**species**	**dilution**	**order information**
NID1	rabbit IgG	1:400	sc-33141, Santa Cruz
LAM	Rabbit IgG	1:500	ab11575, Abcam
anti-rabbit IgG-HRP	goat	1:4000	ab6721, Abcam

Primer		Sequence
Human NID1 5'	QhNID1-389F QhNID1-495R	CCGCTCAGTCCCTCCACACA GTCCCGAGAAGGGCCCTGGT
Human NID1 3'	QhNID1-2016F QhNID1-2160R	CCACCGCCTGCCATACCAACGCCG CC CAGGATGTGCTCTCTCTCGTGCTG G
Hamster β-Actin	QhamB-Actin-F QhamB-Actin-R	GGCGCTTTTGACTCAGGACTTTA GGGATGTTTGCTCCAACCGA
Hamster p53	Qham-p53-F Qham-p53-R	CATGCCGAATACCTGGATGACAAG GCAAATCAAACCCTGTCTTCAACC
human αSMA	Hs_ACTA2_1_SG	Qiagen, QT00088102
human GAPDH	Hs_GAPDH_2_SG	Qiagen, QT01192646
RT² Profiler PCR Arrays	Extracellular Matrix & Adhesion Molecules	Qiagen, PAHS-013Z

Table S3. List of antibodies and primer sequences.